HAL
open science

# Josephson effect and high frequency emission in a carbon nanotube in the Kondo regime

Raphaëlle Delagrange

## To cite this version:

Raphaëlle Delagrange. Josephson effect and high frequency emission in a carbon nanotube in the Kondo regime. Mesoscopic Systems and Quantum Hall Effect [cond-mat.mes-hall]. Université Paris Saclay (COmUE), 2016. English. NNT : 2016SACLS319 . tel-01392964

**HAL Id: tel-01392964**

**https://theses.hal.science/tel-01392964v1**

Submitted on 5 Nov 2016

**HAL** is a multi-disciplinary open access archive for the deposit and dissemination of scientific research documents, whether they are published or not. The documents may come from teaching and research institutions in France or abroad, or from public or private research centers.

L'archive ouverte pluridisciplinaire **HAL**, est destinée au dépôt et à la diffusion de documents scientifiques de niveau recherche, publiés ou non, émanant des établissements d'enseignement et de recherche français ou étrangers, des laboratoires publics ou privés.

NNT : 2016SACLS319

# THESE DE DOCTORAT
# DE
# L'UNIVERSITE PARIS-SACLAY
# PREPAREE A
# L'UNIVERSITE PARIS-SUD

ÉCOLE DOCTORALE N°564
Physique en Île-de-France
Spécialité de doctorat : Physique

Par

**Raphaëlle Delagrange**

Josephson effect and high frequency emission in a carbon nanotube in the Kondo regime

**Thèse présentée et soutenue à Orsay, le 6 octobre 2016 :**

**Composition du Jury :**

| | | |
|---|---|---|
| M Pascal Simon | Pr Université Paris-Sud | Président du jury |
| M Ramòn Aguado | DR, ICMM, Madrid | Rapporteur |
| M Silvano De Franceschi | Chercheur CEA, Grenoble | Rapporteur |
| M Philippe Joyez | Chercheur CEA, Saclay | Examinateur |
| M Christian Schönenberger | Pr. Université de Bâle | Examinateur |
| M Richard Deblock | CR, LPS, Orsay | Directeur de thèse |
| Mme Hélène Bouchiat | DR, LPS, Orsay | Invitée |

# Table des matières

**Remerciements** **i**

**Résumé de la thèse** **v**
0.1 Effet Josephson dc dans un nanotube de carbone . . . vii
0.1.1 Présentation de l'expérience . . . vii
0.1.2 Relations courant-phase . . . viii
0.2 Bruit haute fréquence dans le régime Kondo . . . xiv
0.2.1 Présentation de l'expérience . . . xiv
0.2.2 Résultats expérimentaux . . . xvi
0.2.3 Conclusion . . . xix
0.3 Effet Josephson AC dans un nanotube de carbone dans le régime Kondo . . . xx
0.3.1 Principe de l'expérience . . . xx
0.3.2 Résultats expérimentaux . . . xx

**Introduction** **1**

**I Kondo effect and carbon nanotube quantum dots** **3**

**1 The Kondo effect in condensed matter** **5**
1.1 The Kondo problem . . . 5
1.1.1 Phenomenological description . . . 5
1.1.2 Renormalization of the problem . . . 6
1.2 The problem of impurities in metals . . . 8
1.2.1 Anderson Hamiltonian . . . 8
1.2.2 Equivalence with the Kondo problem . . . 9
1.2.3 Virtual bound states and phase shift . . . 10
1.3 Kondo effect in quantum dots . . . 10
1.3.1 Introduction to quantum dots and link with the Anderson hamiltonian 11
1.3.2 Comparison of Kondo effect in QD and in metals . . . 12
1.4 Some aspects of the Kondo effect investigated in this thesis . . . 12
1.4.1 Out-of-equilibrium decoherence of the Kondo effect . . . 12
1.4.2 High frequency dynamics of the Kondo effect . . . 13
1.4.3 Interplay with superconductivity . . . 14

1.5 Conclusion and summary . . . . . 16

**2 Carbon nanotubes as quantum wires and quantum dots 19**

2.1 Carbon nanotube wires . . . . . 19

2.1.1 Geometrical structure . . . . . 19

2.1.2 Mesoscopic transport in a carbon nanotube . . . . . 22

2.1.3 Breaking of degeneracy and magnetic field dependence . . . . . 26

2.1.4 Conclusion . . . . . 30

2.2 Carbon nanotubes quantum dots and Coulomb blockade regime . . . . . 32

2.2.1 Contact transparency and transport regime . . . . . 32

2.2.2 Electron transport in a CNT quantum dot . . . . . 35

2.2.3 Conclusion . . . . . 41

2.3 Kondo effects in carbon nanotube quantum dots . . . . . 42

2.3.1 SU(2) spin Kondo effect . . . . . 42

2.3.2 Two-level Kondo effects . . . . . 47

2.3.3 Conclusion . . . . . 51

**3 Experimental techniques 53**

3.1 Making samples . . . . . 53

3.1.1 Fabrication of metallic contacts : electronic lithography technique . . . 53

3.1.2 Carbon nanotubes samples (CNT) . . . . . 55

3.1.3 Making tunnel junctions . . . . . 58

3.2 Measuring samples . . . . . 59

3.2.1 Cryogenic cooling . . . . . 59

3.2.2 Wiring and filtering . . . . . 60

3.2.3 Electronic measurements . . . . . 61

**II Josephson effect in a carbon nanotube 63**

**4 Josephson effect in a carbon nanotube QD : state of the art 65**

4.1 Superconducting proximity effect . . . . . 65

4.1.1 Superconductivity : important notions . . . . . 65

4.1.2 Superconducting proximity effect . . . . . 68

4.2 Josephson effect in a carbon nanotube quantum dot . . . . . 76

4.2.1 Qualitative description . . . . . 76

4.2.2 Proximity effect and single-impurity Anderson model . . . . . 80

4.2.3 Josephson effect in a two-level quantum dot . . . . . 86

4.2.4 0-$\pi$ transitions . . . . . 89

4.3 Conclusion . . . . . 94

**5 Current-phase relation measurement in a carbon nanotube quantum dot 97**
5.1 Current-phase relation : experimental setup . . . 97
5.1.1 Principle of measurement . . . 97
5.1.2 Experimental setup . . . 103
5.2 Characterization of the sample in the normal state . . . 105
5.2.1 Differential conductance in the normal state . . . 105
5.2.2 Determination of the QD's parameters . . . 107
5.3 Superconducting state : Current-phase relation measurements . . . 111
5.3.1 Superconducting state : Gate controlled 0 or $\pi$-junction and two-level physics. . . . 111
5.3.2 Current-phase relation in the single-level regime . . . 112
5.3.3 Effect of the two-level regime on the 0-$\pi$ transition . . . 119
5.3.4 Toward a $\varphi_0$-junction ? . . . 122
5.4 Supplementary measurements . . . 123
5.4.1 Spectroscopy of Andreev Bound states. . . . 123
5.4.2 SU(4) Kondo effect ? . . . 125
5.5 Conclusion . . . 126

**III Noise measurements in the Kondo regime 129**

**6 Noise in a mesoscopic system 131**
6.1 Definition and different regimes . . . 131
6.1.1 Definition of noise . . . 131
6.1.2 Noise in a quantum system . . . 132
6.1.3 Equilibrium noise . . . 132
6.2 Shot noise in a mesoscopic system . . . 135
6.2.1 Fluctuations due to charge carriers discreteness . . . 135
6.2.2 Noise in the scattering matrix formalism . . . 136
6.2.3 Low frequency limit . . . 139
6.3 Low frequency noise measurement in Kondo regimes . . . 142
6.3.1 Experimental setup . . . 142
6.3.2 Linear noise . . . 144
6.3.3 Effective charge due to Kondo effect . . . 146

**7 High frequency noise measurement 149**
7.1 High frequency noise measurements . . . 149
7.1.1 How to measure non-symmetrized noise at high frequency ? . . . 149
7.1.2 SIS junction detector . . . 151
7.1.3 Coupling through a resonator . . . 157
7.1.4 Characterization of the experimental setup . . . 158
7.2 High frequency noise in a QD : general problematic and theoretical expectations 164
7.2.1 In the scattering matrix formalism (non-interacting theories) . . . 164

7.2.2 Finite frequency noise in the Kondo regime . . . . . 168
7.2.3 Non-interacting theories and Kondo effect ? . . . . . 172
7.3 Experimental results : finite frequency noise in carbon nanotube quantum dot 175
7.3.1 Noise in the Kondo SU(2) regime . . . . . 175
7.3.2 Noise in other regimes . . . . . 184
7.3.3 Conclusion . . . . . 186

**IV AC Josephson effect in a carbon nanotube in the Kondo regime 187**

**8 AC Josephson effect in a carbon nanotube in the Kondo regime 189**
8.1 Why measuring AC Josephson effect ? . . . . . 189
8.1.1 Definition and experimental manifestation . . . . . 189
8.1.2 AC Josephson effect used as a probe of the Josephson effect . . . . . 191
8.1.3 AC Josephson effect in a superconducting QD . . . . . 195
8.2 AC Josephson effect measurement . . . . . 197
8.2.1 Experimental setup . . . . . 197
8.2.2 Detail of one measurement . . . . . 199
8.2.3 Quantitative analysis and attempts of explanations . . . . . 203
8.3 Conclusion . . . . . 208

**Conclusion 211**

**List of publications 215**

**Bibliography 216**

# Remerciements

Acknowledgments are probably the most delicate task in writting a thesis, because it is the only part that will be read by a significative number of persons, non-necessary physicists. That's why they will be written mainly in French (but not only).

Si ces trois années de thèse ont été si intenses, passionnantes et agréables, c'est parce que j'ai eu la chance de tomber dans le groupe Méso. Un groupe où l'on fait de la physique pour la physique, dans une ambiance de bienveillance et d'entraide qui donne à la fois les moyens et l'envie de travailler ! (si on peut appeler "travail" la recherche telle que je l'ai vécue ici...). Cette ambiance m'a conquise dès ma première visite au LPS et l'a largement emporté sur les petites irrégularité du RER [1] !

J'aimerais en particulier remercier Richard, à qui je dois le plus et qui a eu à me supporter quasiment à temps plein. Quand j'étais petite [pendant mon stage de M2 et durant les premiers mois de la thèse], tu m'as tout appris : après m'avoir patiemment et inlassablement montré et expliqué les manips, tu as surveillé mes premiers pas jusqu'à ce que je sois à peu près autonome. Je pense que cela a été un apprentissage efficace qui m'a permis d'adopter dès le début tes bonnes habitudes de prudence qui m'ont fait gagner un temps précieux par la suite ! Puis, quand j'étais capable de faire moi même, tu as toujours été très présent quand j'avais besoin d'aide et d'avis, toujours en suggérant, jamais en imposant. D'autre part, je crois que je penserai longtemps à toi à chaque fois que je mangerai des crêpes dentelle au chocolat et que j'entendrai parler de construction de maison ;-).

C'est ensuite à Hélène que j'aimerais exprimer ma reconnaissance. Sans toi, cette thèse n'aurait probablement pas été ces trois années de pure physique, certainement les plus riches intellectuellement que j'ai vécues jusqu'à présent. Je ne me souviens pas d'une seule de nos discussions qui ne m'ait pas proposé de nouvelles pistes, amenée à me poser de nouvelles questions ou aidée à mieux poser les anciennes. Tes avis étaient généralement tellement pertinents que j'ai suivis tous tes conseils de lecture, et pas seulement concernant la physique... [2]. Sur le plan humain, c'est également toujours un grand plaisir d'échanger avec toi !

Un grand merci également à Meydi, le groupe-Méso-délocalisé-au-Japon. Evidemment suite à

[1] Qui m'ont également été dévoilées dès cette première visite.

[2] J'ai même essayé l'omelette à la banane. Mais ça, je regrette un peu...

mon séjour au Japon (voir plus loin), mais également par nos échanges de mails et lors de tes visites en France, très denses en enseignements et nouvelles idées ! Je n'ose pas imaginer ce qu'aurait été ma compréhension des effets Kondo dans les nanotubes sans tes explications et conseils de lecture... Ton soucis de comprendre en profondeur la physique et de l'expliquer avec des mots simples est aussi pour moi une grande source d'inspiration.

Merci également à Sophie, avec qui j'ai moins travaillé mais qui m'a quand même fait bénéficier de son intérêt et de son enthousiasme ! Ta volonté de ne rien laisser incompris et tes exigences de pédagogie ont mené à des discussions passionnantes qui m'ont poussée à la remise en question et, je l'espère, à l'amélioration. Aussi, ce fût le plus souvent un plaisir de débattre avec toi sur une grande variété de sujets, qu'ils soient scientifiques ou pas ! [3]

Merci aussi[4] à Sandrine qui a toujours été présente pour m'aider quand il s'agissait de cryogénie, de câblage ou de conseils pratiques en tous genres ! Ta gentillesse et ton écoute m'ont aussi été très précieuses.

Et puis merci à Alexei qui en plus de ses remarques physiques toujours pertinentes m'a initiée aux usages tokyoites : payer pour jouer avec des chats, vénérer un radis doré géant et manger des sushis aux trois nuances de thons. Anil, mon co-bureau pendant la majeure partie du temps, pour ses lottes de jeux de mots ! Alik, notre assurance contre les fuites de joint de graisse, toujours prêt à nous motiver pour un café sur la terrasse. Shamashis, pour m'avoir fait découvrir l'Inde auditivement et gustativement ! Taro, dont l'apprentissage éclair du français devrait lui permettre de lire ces lignes sans aucun soucis... Et puis Chuan, qui même depuis les Pays-Bas me prodigue conseils et expérience, quand elle ne me fait pas découvrir la Chine dans le 13ème ou à New York ! Et enfin Bastien, dont les blagues résonnent encore dans le bureau... [air de violon triste]... Cela dit, heureusement que tu n'y est pas resté pendant toute ma rédaction, sinon j'y serais encore ;-).

Au delà du groupe Méso, j'aimerais remercier Pascal Simon pour nos nombreuses discussions, parfois autour de la machine à café, qui ont constitué une précieuse étape dans l'interprétation de nos mesures. Merci également de tes contacts et de ton expérience concernant l'enseignement. Merci aussi à Raphaël Weil pour son aide constante pour tout ce qui est nanofabrication, ce fut aussi un plaisir d'enseigner Scilab avec toi ! Merci à Miguel de m'avoir également accueillie dans le module de mécanique. J'espère ne pas avoir squatté trop souvent le fauteuil invité de votre bureau ;-). Merci aux utilisateurs de la salle nano, en particulier le groupe NS2 (Cyril, Alexis, Pierre, Gianluca), avec qui j'ai pu partager mon désespoir lié à la mort de mes échantillons (surtout celle de mes délicates et malheureuses jonctions tunnel). Merci à Julien Basset, mon prédécesseur de thèse, d'avoir si bien préparé le terrain. Merci à Jean-Pierre Dalac, Gilles Guillier et Pascale Senzier qui se sont démenés pour que nous ayons toujours l'hélium dont nous avions besoin. Merci à Christophe Nicolosi puis à Ciham Zaabhoul, nos

[3] Me contacter tout de même pour connaître la liste des sujets non-scientifiques à n'aborder qu'après une solide préparation ;-)

[4] Je commence à être à sec sur les formules d'accroche...

gestionnaires, qui ont aplani toutes les formalité liées à l'organisation des voyages, ainsi qu'à toute l'équipe d'administration du labo.

I would like as well to thank Kobayashi-san for giving me the opportunity to spend one month in Japan. This stay was for me a great experience, and not only from the scientific point of view, it was also a great human experience. This has been made possible by all the members of the team who wonderfully took care of me, from housing to food and touristic advices ! I specially thank Arakawa-san, Yoshii-san and Hata-san for that, but also all the students of the group. And of course, thanks to Meydi for supervising me at this time, from both scientific and touristic point of view. It was a pleasure to visit some places in Japan benefiting from your insights into Japanese culture !

J'aimerais remercier les thésards du labo (passés et présents) avec qui j'ai découvert les bars du quartier latin et les pique niques au bord du lac d'Orsay. C'était aussi bien agréable d'aller discuter en dehors du groupe Méso, pour se changer les idées, collecter les potins et râler ;-) (merci Alexis, Arnaud, Cyril, Émilie, Pierre et tous les autres !).

J'ai également eu la chance de pouvoir participer à un certain nombre d'écoles/conférences dans des endroits très sympathiques : (dans le désordre) Aussois, Sherbrooke, San Sebastian, Strasbourg, Baltimore, la Laponie. A chaque fois, j'y ai fait des rencontres très intéressantes/plaisantes/enrichissantes, même quand je m'y attendais le moins[5]. Je remercie toutes ces personnes rencontrées et espère recroiser leur chemin !

Il me faut également remercier ma famille, en particulier Maman et Nicolas qui ont stoïquement écouté le récit de la mort de chacun de mes échantillons (et ils sont nombreux...). Merci à tous de votre soutien, qui a toujours été très important pour moi.

Thanks to Ramòn Aguado, Silvano de Franceschi, Philippe Joyez, Christian Schönenberger and Pascal Simon for accepting to be in my PhD jury. I don't thank Richard and Hélène for that, because they had no choice, but I am particularly grateful to them for reading and correcting this (too ?) long manuscript...

Finally, thanks to those who will take some interest in reading this text (if they exist). Most of the time, it was a pleasure to write it, this pleasure would be multiplied ten fold if anybody would learn anything by reading it !

[5]Même à la conférence en Laponie remplie de russes qui viennent pour faire des igloos.

# Résumé de la thèse

## Introduction

L'objectif de cette thèse est de contribuer à l'exploration de la physique quantique dans des systèmes conducteurs de petite taille à très basse température. En l'occurrence, nous nous sommes intéressés aux boîtes quantiques, qui sont des systèmes de taille si petite que leurs niveaux d'énergie sont quantifiés, formant ainsi de véritables atomes artificiels dont il est possible de contrôler le nombre d'électrons par une grille électrostatique. Lorsqu'une telle boîte quantique est connectée à des réservoirs métalliques (ou, comme nous le verrons, supraconducteurs), il est possible de déterminer son spectre électronique par des mesures de conductance différentielle et d'accéder à une large variété de phénomènes caractéristiques de la physique des corrélations électroniques aux échelles nanomètriques quantiquement cohérents.

En particulier, à basse température, la boîte quantique va permettre d'étudier un effet de grand intérêt en matière condensée : l'effet Kondo. Il s'agit d'un effet qui a été initialement observé dans des alliages dilués où des impuretés magnétiques sont réparties dans un réseau métallique. Les électrons proches de l'énergie de Fermi forment alors un état collectif fortement corrélé afin d'écranter le moment magnétique de l'impureté, donnant lieu à une résonance dans la densité d'état. Cet effet a une grande importance théorique puisqu'il s'agit d'une des premières applications des théories de groupe de renormalisation. Il s'agit également d'un phénomène assez général puisqu'il est présent dès qu'un degré de liberté quantique localisé se trouve couplé à un réservoir d'électrons délocalisés : c'est pour cela qu'on le trouve dans les boîtes quantiques, où un spin 1/2 localisé est couplé à des réservoirs métalliques, mais il existe aussi des effet Kondo de charge [1] ou topologiques [2]. Si la physique de cet effet commence à être bien comprise à l'équilibre, son comportement hors équilibre ainsi que sa dynamique ont été très peu étudiés expérimentalement et constituent une des questions importantes qui ont été abordées dans cette thèse par l'intermédiaire de l'émission haute fréquence d'une boîte quantique dans le régime Kondo.

Nous nous sommes également intéressés à la coexistence de cet effet Kondo avec des corrélations supraconductrices. En effet, même si la boîte quantique n'est pas intrinsèquement supraconductrice, en la contactant à des réservoirs supraconducteurs il va être possible d'y induire de telles corrélations grâce à ce qu'on appelle l'effet de proximité. On y observe

alors l'effet Josephson, se manifestant par un courant non dissipatif induit non pas par une différence de tension mais par une différence de phase supraconductrice. La supraconductivité résulte de l'appariement d'électrons en paires de spin total nul et ouvre un gap d'énergie au niveau de Fermi, comment cela peut-il se concilier avec la formation d'un singulet Kondo avec les électrons autour de l'énergie de Fermi ? Ce sera également une des questions majeures évoquées dans cette thèse. Le système que nous avons choisi comme boîte quantique pour ce travail de thèse est un nanotube de carbone. Cette molécule a l'avantage de se connecter relativement facilement à des contacts métalliques et de pouvoir être considéré comme un conducteur cohérent et balistique sur des distances de l'ordre du micron. Les nanotubes ont, de plus, une structure électronique particulière : chaque niveau d'énergie, en plus d'être dégénéré en spin, possède une dégénérescence orbitale (correspondant au sens dans lequel l'électron tourne autour du nanotube). Ils peuvent également présenter de l'interaction spin-orbite. Ils constituent ainsi un système parfait pour étudier les problématiques évoquées plus haut, enrichies par les spécificités du nanotube.

La première partie décrit notre étude de l'effet Josephson dans un nanotube de carbone. Nous avons inséré un nanotube de carbone dans un SQUID afin d'en mesurer le supercourant en fonction de la différence de phase supraconductrice à ses bornes. Lorsque les corrélations Kondo et supraconductrices sont du même ordre de grandeur, nous montrons que l'état du système, singulet ou doublet (correspondant à une transition d'une jonction 0 à $\pi$), peut être contrôlé par la phase, induisant une relation courant-phase fortement anharmonique. Nous avons aussi montré que, si un deuxième niveau d'énergie participe au transport des paires de Cooper, la transition 0-$\pi$ observée est tout à fait différente.

Dans la deuxième partie de la thèse, le nanotube est couplé, aux fréquences déterminées par un résonateur, à une jonction tunnel supraconductrice qui sert de détecteur on-chip de bruit haute fréquence. Ceci nous a permis de mesurer le bruit en émission de la boîte quantique dans le régime Kondo avec des couplages aux réservoirs plus ou moins symétriques. Nos mesures posent le problème de l'asymétrie spatiale du bruit mesuré et montrent que, plus le couplage aux réservoirs est symétrique, plus la résonance Kondo est affaiblie dans une situation hors d'équilibre.

Enfin, ce dispositif a été utilisé afin de mesurer l'émission Josephson AC d'un nanotube de carbone avec des électrodes supraconductrices, afin d'étudier ce qu'il advient de la compétition entre l'effet Kondo et la supraconductivité à haute fréquence.

## 0.1 Effet Josephson dc dans un nanotube de carbone

### 0.1.1 Présentation de l'expérience

#### 0.1.1.1 Contexte scientifique

Dans cette première expérience, il s'agit d'étudier une boîte quantique constituée d'un nanotube de carbone dans laquelle sont induites des corrélations supraconductrices. Ce système peut être vu comme une jonction Josephson et est traversé par un supercourant qui est, d'une manière générale, une fonction périodique et impaire de la phase supraconductrice à ses bornes, que l'on nommera $\varphi$. La forme exacte de cette relation courant-phase (en particulier son contenu en harmoniques) est, quant à elle, fortement dépendante du système considéré.

Dans le cas du nanotube de carbone formant une boîte quantique et se trouvant dans le régime de blocage de Coulomb, la situation est particulièrement intéressante. En effet, il s'agit de faire passer de manière cohérente une paire de Cooper à travers un système sur lequel le nombre d'électrons est fixé. Ceci n'est possible que par l'intermédiaire de processus de cotunneling, qui autorisent l'entrée d'un électron dans la boîte quantique à la condition qu'un électron du système en sorte. Ces processus sont fortement dépendants du nombre de niveaux d'énergie disponibles dans le système ainsi que de leurs nombres occupations et peuvent mener à un renversement de l'ordre des spins dans la paire de Cooper. Ceci se manifeste par un déphasage de $\pi$ de la relation courant-phase et est caractéristique de ce qu'on appelle une jonction-$\pi$, par opposition avec le cas habituel, la jonction 0 [3, 4].

Dans ce travail, nous nous sommes intéressés spécifiquement au comportement de la relation courant-phase à la transition entre ces états 0 et $\pi$, dans deux cas distincts. Le premier est la transition 0-$\pi$ induite par la compétition entre l'effet Kondo et la supraconductivité, qui correspond à une transition singulet-doublet associée à un croisement de niveau. Le deuxième est une transition 0-$\pi$ qui se produit sans changement d'état magnétique du système, possible quand au moins deux niveaux d'énergie participent au transport. Ces deux situations, ayant des origines physiques très différentes, donnent lieu à des relations courant-phase à la transition tout aussi distinctes.

#### 0.1.1.2 Dispositif expérimental et principe de mesure

Le contrôle de la phase supraconductrice aux bornes de la jonction Josephson à nanotube est réalisé en l'insérant dans une boucle supraconductrice traversée par un champ magnétique. Une jonction tunnel supraconductrice est insérée dans la boucle, formant un SQUID (Superconducting Quantum Interference Device). Si le courant critique de la jonction tunnel est grand devant celui de la jonction à nanotube, alors la mesure du courant critique du SQUID en fonction du champ magnétique donne une mesure directe de la relation courant phase de

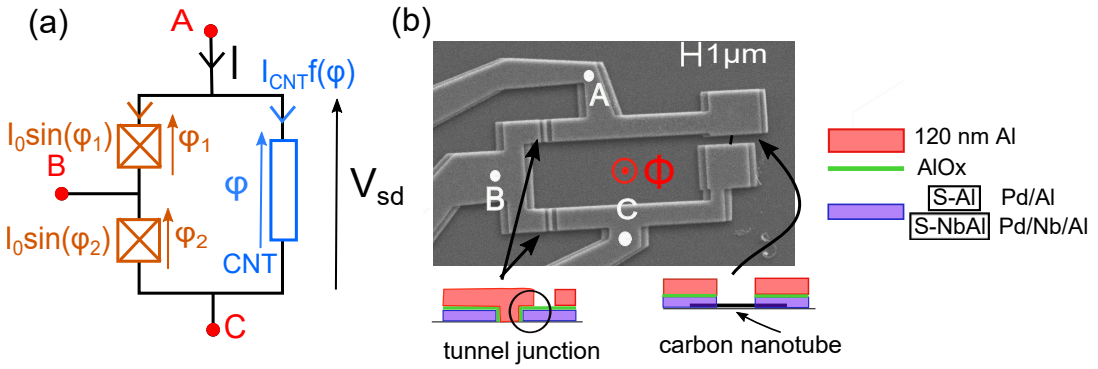


FIGURE 1 – (a) Schéma du dispositif expérimental, un SQUID asymétrique dans lequel deux jonction tunnel supraconductices sont en parallèle avec la jonction à nanotube de carbone. (b) Image au microscope électronique à balayage de l'échantillon, avec indiqué la composition des couches utilisées pour fabriquer les jonctions tunnel et les contacts du nanotube. La première couche est formée de Pd(7 nm)/Al(70 nm) pour un des échantillons et de Pd(7 nm)/Nb(20 nm)/Al(40 nm) pour l'autre. $\Phi = B \times S$ est le flux magnétique à travers la boucle.

la jonction Josephson [5].

Le dispositif expérimental que nous avons utilisé est celui représenté sur la figure 1. Il s'agit d'un SQUID asymétrique comme décrit ci-dessus sauf qu'au lieu d'une jonction tunnel de grand supercourant, il y en a deux en parallèle du nanotube, avec un fil de mesure entre les deux. L'avantage de ce design est de pouvoir mesurer indépendamment chacune des trois jonctions du SQUID [6]. Avec un tel échantillon, il est possible de mesurer à la fois la relation courant-phase du nanotube de carbone, sa conductance dans l'état supraconducteur, ainsi que sa conductance dans l'état normal si les corrélations supraconductrices sont détruites par un champ magnétique. Les résultats obtenus vont maintenant être présentés.

### 0.1.2 Relations courant-phase

A partir de la mesure de conductance de l'échantillon dans l'état normal, on montre qu'il s'agit d'un nanotube "propre", dans le sens où la manière dont les diamants de Coulomb se succèdent est caractéristique d'une dégénerescence de niveaux d'ordre 4. Le motif un gros diamant/4 petits est typique des nanotubes de carbone où les niveaux d'énergie, en plus d'être dégénérés en spin, sont quasiment dégénérés orbitalement [7]. Cette mesure permet de déterminer les paramètres du système en tant que boîte quantique : l'énergie de charge $U$, la levée de dégénérescence des niveaux orbitaux $\delta E$ et le couplage $\Gamma$. Dans la suite vont être présentées des mesures de relation courant-phase dans deux zones de tension de grille différentes, pour lesquelles la boîte quantique est occupée par un nombre impair d'électrons et présente de l'effet Kondo. Ces diamants correspondent à la même couche d'énergie du nanotube (occupée avec respectivement 1 et 3 électrons) mais le comportement du supercourant y est

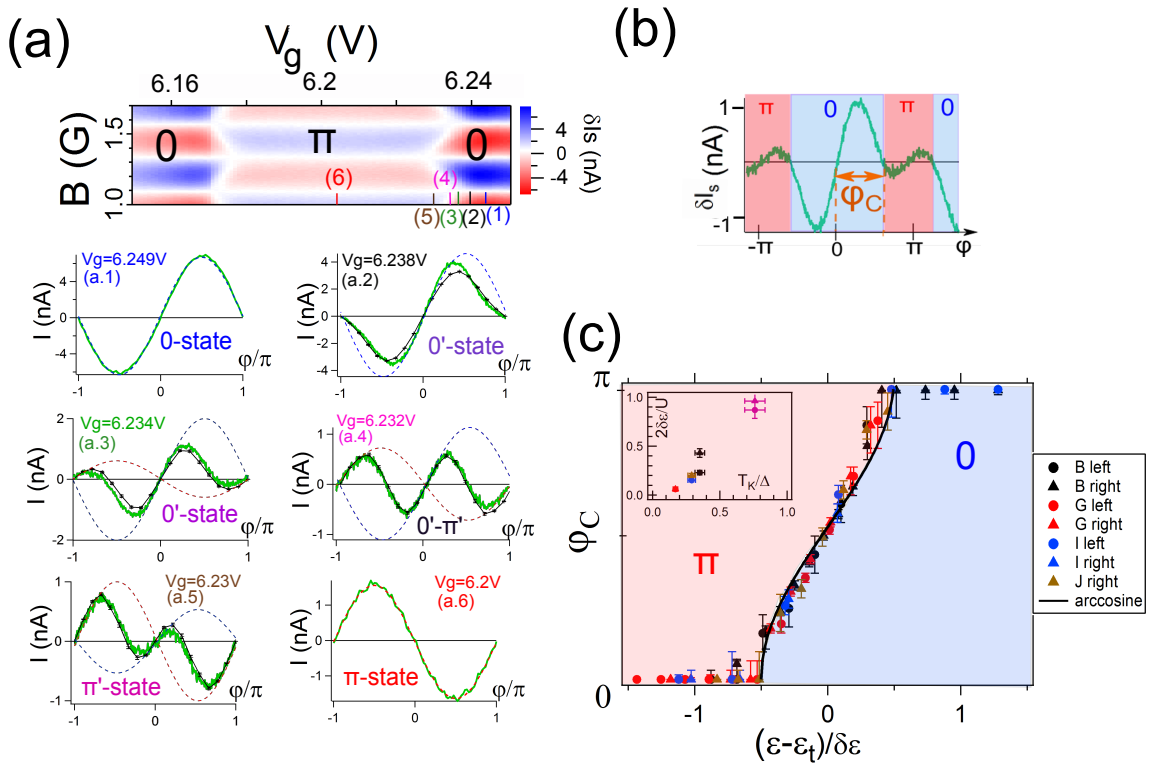


FIGURE 2 – Relation courant-phase dans le régime à un seul niveau. (a) Graphe 2d : Modulation du supercourant dans le nanotube en fonction du champ magnétique B et de la tension de grille $V_g$. $B$ est proportionnel à $\varphi$, la différence de phase aux bornes du nanotube, et la plage de tension de grille considérée correspond au diamant correspondant à un remplissage $N = 1$. En dessous sont extraites les relations courant-phase pour les tensions de grilles indiquées sur le graphe 2D (lignes vertes) superposées aux prédictions réalisées avec un calcul Monte Carlo quantique (lignes avec des points noirs). Les lignes pointillées sont des indicateurs donnant qualitativement la contribution du singulet (jonction 0, en bleu) et du doublet (jonction $\pi$, en rouge). (b) Définition de la phase critique $\varphi_c$ à laquelle la jonction passe de 0 à $\pi$. C'est la phase, dans l'intervalle $]0, \pi[$, à laquelle le supercourant s'annule. (c) Universalité du diagramme de phase à la transition : $\varphi_c$ est tracé en fonction de $(\epsilon - \epsilon_t)/\delta\epsilon$ pour les deux bords de quatre diamants différents. En noir est représenté un fit en arccosinus. Inset en haut à gauche : largeur en énergie de la transition $\delta\epsilon$, renormalisée par $U/2$, en fonction du rapport $T_K/\Delta$. Cela montre que $2\delta E/U$ varie linéairement avec $T_K/\Delta$, rapport qui contrôle la transition 0-$\pi$.

pourtant radicalement différent. Nous attribuons cela au fait que, suivant les cas, un ou deux niveaux d'énergie participent au transport des paires de Cooper, c'est ce qui va être détaillé maintenant (et a été publié dans les ref. [8, 9]).

#### 0.1.2.1 Boîte quantique à un niveau : transition 0-$\pi$ singulet-doublet induite par la phase supraconductrice

Commençons par détailler la mesure de relation courant phase dans le diamant de Coulomb correspondant à une occupation de la plus haute couche électronique disponible par un seul électron ($N = 1$).

**Transition singulet-doublet contrôlée par la phase** La modulation du courant critique du SQUID en fonction du champ magnétique (proportionnel à la différence de phase supraconductrice) et de la tension de grille est représentée sur la figure 2 (a), pour l'ensemble du diamant de Coulomb. En dessous, la relation courant phase est également extraite pour les tensions de grilles indiquées sur le graphe 2D.

La première constatation que l'on peut faire est qu'au centre du diamant, la relation courant-phase est déphasée de $\pi$ par rapport à celle sur les bords du diamant. De plus, la position en grille de cette transition 0-$\pi$ est à peu près symétrique par rapport au centre du diamant. Cette transition est contrôlée par le rapport $\Delta/T_K$, qui dépend des forces relatives des corrélations supraconductrices et Kondo. Quand l'effet Kondo est faible par rapport à la supraconductivité, ce qui est le cas au milieu du diamant dans une boîte quantique dans laquelle un seul niveau d'énergie participe au transport, le système est dans un état doublet, associé à une jonction $\pi$. En revanche, quand l'effet Kondo est fort par rapport à la supraconductivité, ce qui est le cas sur les bords du diamant, le moment magnétique de l'électron non-apparié sur le nanotube est écranté par l'effet Kondo. Le système est alors dans un état singulet/jonction-0.

Cette transition 0-$\pi$ contrôlée par la grille avait déjà été observée à de nombreuses reprises. En revanche, la relation courant-phase à la transition, bien que prédite théoriquement, n'avait jamais été mesurée. Dans la partie basse de la figure 2 (a), cette relation courant-phase est extraite du graphe 2D à tous les stades de la transition. Cela donne des courbes fortement anharmoniques, ce qui peut être interprété comme suit : autour de $\varphi = 0$, la relation courant-phase ressemble au sinus d'une jonction 0 alors qu'aux alentours de $\varphi = \pi$ c'est plutôt un $-\sin(\varphi)$, une jonction $\pi$ (voir les pointillés sur les figures, servant de guides pour les yeux). Autrement dit, il s'agit d'une transition $0 - \pi$, qui se trouve être également une transition singulet-doublet, contrôlée par la phase supraconductrice. Selon la proportion de 0 ou de $\pi$ dans la relation courant-phase, ces états intermédiaires sont nommés $0'$ et $\pi'$. Sur ces mêmes courbes sont superposés en noir les résultats d'un calcul Monte Carlo quantique dans un modèle d'hamiltonien d'Anderson à un seul niveau [10], réalisé par David Luitz and Volker

Meden dans le cadre d'une collaboration [8]. Ces calculs reproduisant exactement la forme des courbes mesurées, ils confirment bien l'origine physique de la transition.

**Diagramme de phase de la transition : une propriété universelle de la transition**
Afin d'étudier plus finement cette transition contrôlée par la phase supraconductrice, nous avons extrait des mesures précédentes la phase critique $\varphi_c$, définie sur la figure 2 (b), à laquelle le système passe de 0 à $\pi$ dans les états $0'$ et $\pi'$. Cette quantité a été tracée sur la figure 2 (c) pour trois diamants différents, et deux transitions par diamant (une à chaque bord) en fonction de $(\epsilon - \epsilon_t)/\delta\epsilon$, le niveau d'énergie dans la boîte quantique centré sur la transition $\epsilon_t$ et renormalisé par sa largeur $\delta E$. Ceci permet de prendre en compte le fait que suivant les diamants, et donc les paramètres du système, la transition 0-$\pi$ peut se faire à des positions en grille différentes et avec un étalement plus ou moins grand. On peut ainsi constater que toutes ces données se superposent sur une même courbe, qui peut être modélisée par un arcosinus (ligne noire sur le graphe). Ce diagramme de phase constitue donc une caractéristique universelle de la transition 0-$\pi$ pilotée par la phase supraconductrice.

#### 0.1.2.2 Boîte quantique à deux niveaux : transition 0-$\pi$ entre deux états doublets

Voici maintenant les mesures de relation courant-phase obtenues dans le diamant de Coulomb occupé par un nombre impair d'électron faisant immédiatement suite à celui de la section précédente. La plus haute couche occupée comporte donc $N = 3$ électrons.

Ces résultats sont présentés sur la figure 3. On observe, de même que dans le cas précédent, un changement de signe du supercourant dans le diamant, signalant une transition 0-$\pi$. Ce qui est en revanche très différent, c'est d'abord l'amplitude du courant dans la jonction $\pi$, qui est très petite, ainsi que la brisure de symétrie entre les deux côtés du diamant. En effet, toute la partie gauche du diamant est dans l'état 0, alors que le côté droit est dans l'état $\pi$. De plus, la transition se produisant au milieu du diamant (à la tension de grille numérotée (4) sur le graphe) se fait par l'intermédiaire d'une annulation du courant critique, sans les anharmonicités observées précédemment, alors que la transition en (7) présente les caractéristiques des états $0'$ et $\pi'$.

Cette dépendance en grille du supercourant est prédite quand deux niveaux d'énergie participent au transport. En effet, il est alors attendu que le supercourant soit symétrique par rapport à la demi-occupation de ces niveaux, qui est alors au centre du diamant $N = 2$ et non plus par au centre du diamant considéré, comme c'est le cas quand un seul niveau est impliqué dans le transport. Une conséquence notable est que la transition 0-$\pi$ se produisant au milieu du diamant est alors une transition entre deux états doublets et non entre un doublet et un singulet comme c'est le cas dans le régime à un seul niveau. L'existence de cet état doublet/jonction-0 est rendue possible par le chemin alternatif qu'offre le second

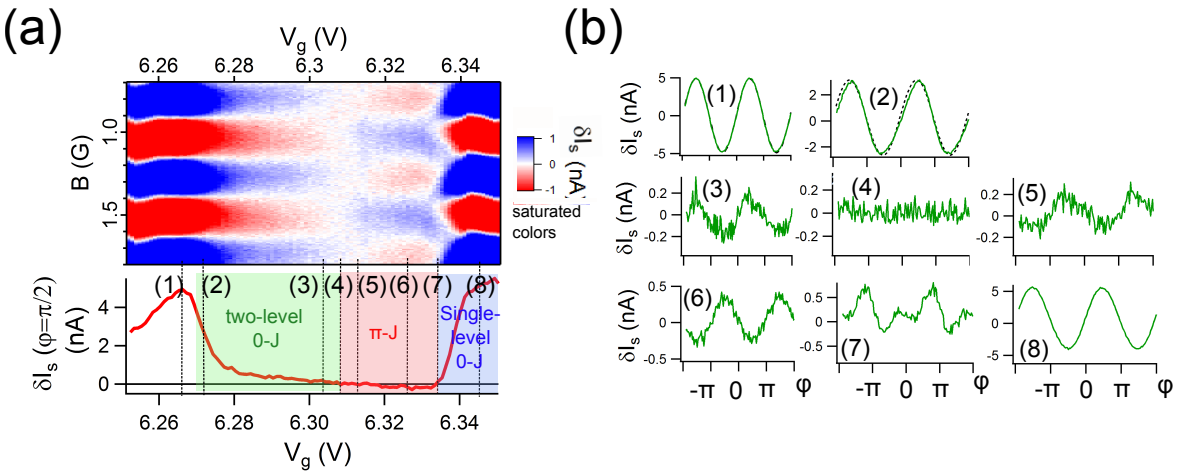


FIGURE 3 – (a) Modulation du courant de switching du SQUID en fonction du champ magnétique, quantité proportionnelle à la relation courant phase, en fonction de la tension de grille $V_g$ dans le diamant de Coulomb correspondant à une occupation N=3. Le supercourant à la transition étant très petit, l'échelle de couleur est saturée. En dessous est tracé le supercourant à une phase de $\varphi = \pi/2$ fixée en fonction de $V_g$. (b) Relation courant phase aux tensions de grilles indiquées sur le graphe 2D. On peut remarquer qu'à la transition (4), le courant critique s'annule, et pas à la transition (7).

niveau aux paires de Cooper, qui autorise des processus donnant des contributions positives au supercourant malgré la présence d'un électron non apparié (et en l'absence d'effet Kondo).

#### 0.1.2.3 Conclusion

Nous avons donc mesuré la relation courant-phase à la transition 0-$\pi$ dans deux cas très différents :

- Dans le régime à un seul niveau, la transition 0-$\pi$ révèle une transition entre un état doublet, où la boîte quantique est occupée par un seul électron, et un état singulet Kondo-BCS, où le moment magnétique de cet électron non apparié est écranté grâce à l'effet Kondo. Cette transition a pour origine un croisement de niveau, ce qui en fait une transition de phase quantique du premier ordre. Cela se manifeste par une discontinuité dans le courant critique (voir figure 4 (a)) ainsi qu'une transition 0-$\pi$ contrôlée par la phase supraconductrice (figure 4 (b)).

- Dans le régime à deux niveaux, une des deux transitions se produit au milieu du diamant, sans changement d'état magnétique puisque l'occupation électronique est constante dans le diamant, l'électron non-apparié formant un doublet puisque l'effet Kondo est trop faible pour former un état singulet sur tout le diamant. On montre qu'à cette transition, le courant critique s'annule et qu'il n'y a pas d'états composite $0'$ ou $\pi'$ : elle n'est clairement pas de la même nature que la transition du premier ordre singulet/doublet.

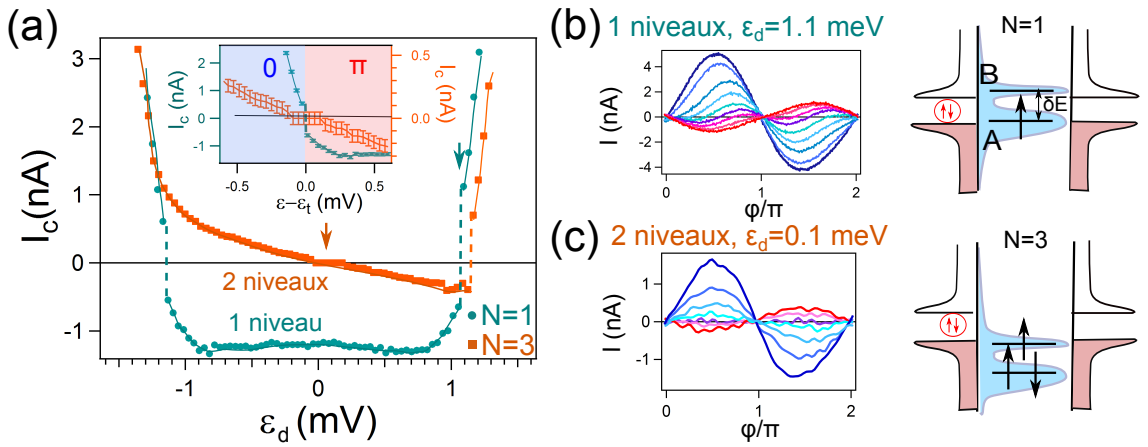


FIGURE 4 – (a) Courant critique $I_c$, défini comme le maximum de la relation courant-phase, en fonction de la position des niveaux d'énergie $\epsilon_d$. $I_c$ est choisi positif pour une jonction 0, négatif pour une jonction $\pi$. Cette quantité est tracée pour les deux diamants étudiés, celui au remplissage électronique N=1 (points bleus), dans le régime à un seul niveau, et celui à N=3 (carrés oranges), où les deux niveaux participent au transport. Les lignes pointillées matérialisent la discontinuité de $I_c$ quand la transition est induite par un croisement de niveaux. Inset : zoom sur deux transitions 0-$\pi$, centrées sur $\epsilon_t$ avec $\epsilon_t = -1.1$ meV pour la bleue et $\epsilon_t = 0.1$ meV pour la orange. (b) Relation courant phase au cours de la transition dans le régime à un niveau, dans le diamant N=1, ainsi qu'un schéma de l'occupation électronique que nous supposons. (c) Même chose pour le régime à deux niveaux dans le diamant N=3.

La différence entre les deux régimes est résumée sur la figure 4 (a) : la transition doublet/doublet au milieu du diamant se fait de manière continue par une annulation du courant critique, alors que les transitions singulet/doublet donnent lieu à une discontinuité du courant critique (voir le fig. 4 (b) pour les relations courant-phase correspondantes).

Il reste cependant un point d'importance : pourquoi ces deux diamants correspondant à la même couche électronique présentent des régimes de conduction aussi différents ? Notre hypothèse est que cela est dû à une différence de couplage entre les deux niveaux concernés (appelés A et B sur les figures 4 (b) et (c)). Pour l'occupation N=1, l'électron non apparié est dans un niveau qui est mieux couplé que celui qui est vide, de sorte que ce dernier ne participe pas au transport. En revanche, pour l'occupation N=3, l'électron non-apparié est dans le niveau le moins couplé, qui participe donc au transport en même temps que le mieux couplé.

Pour aller plus loin dans la compréhension de l'effet Josephson dans les boîtes quantiques à deux niveaux, il pourrait être utile de reproduire cette expérience dans des régimes de couplage différents, de manière à observer les riches diagrammes de phases prédits théoriquement [11, 12]. D'autre part, en présence d'interactions spin-orbite comme il en existe dans les nanotubes [13], il serait possible d'observer des comportements intéressants en présence d'un champ magnétique (comme par exemple des jonctions $\varphi_0$ [14]).

## 0.2 Bruit haute fréquence dans le régime Kondo

Cette partie résume l'expérience que nous avons réalisée afin de mesurer le bruit haute fréquence dans un nanotube de carbone dans le régime Kondo.

### 0.2.1 Présentation de l'expérience

#### 0.2.1.1 Quel intérêt y a-t-il à mesurer le bruit haute fréquence ?

On appelle "bruit" d'un signal ses fluctuations autour de sa valeur moyenne. Si à haute température ou quand le dispositif expérimental est bruyant, ces fluctuations sont indésirables, elles peuvent être très riches en informations dans le cas inverse. En particulier, si le système est assez petit, les fluctuations de courant induites par une tension sont sensibles à la granularité des porteurs de charge, il s'agit du bruit de grenaille (shot noise en anglais). A basse fréquence, la mesure de ce bruit de grenaille apporte donc des informations sur la charge des porteurs, mais également sur les interactions et corrélations ou bien encore le régime de transport dans lequel se trouve le système [15, 16, 17, 18].

A haute fréquence ($h\nu > k_B T$), il devient intéressant de considérer le bruit en terme d'émission et d'absorption de photons : on peut choisir une convention telle que le bruit à fréquence négative corresponde à l'émission d'un photon par le système dans l'environnement, alors que le bruit à fréquence positive correspond à l'absorption d'un photon de l'environnement par le système. Ces deux quantités contiennent *a priori* des informations différentes, en particulier sur la dynamique du système. Dans le cas d'une boîte quantique dans le régime Kondo, on peut s'attendre à ce que le bruit aux fréquences de l'ordre de grandeur de la température Kondo nous fournissent des informations sur la dynamique de l'effet Kondo. C'est la motivation initiale de notre travail.

#### 0.2.1.2 Dispositif de mesure

Distinguer les processus d'émission et d'absorption dans une mesure de bruit n'est pas évident : dans la majorité des expériences, il est difficile de dire si ce qui est mesuré est un bruit symétrisé, la somme de l'émission et de l'absorption ou bien seulement l'un de ces processus. Pour y parvenir, nous avons utilisé un détecteur placé sur le même échantillon que le système à mesurer ("on-chip" en anglais), qui permet de mesurer l'émission et l'absorption haute fréquence grâce à une mesure de courant DC dans une jonction tunnel supraconductrice placée à proximité.

Le dispositif expérimental est représenté sur la figure 5 (a) et (b). La source de bruit, un nanotube de carbone contacté avec 20 nm de palladium, est connectée au bout de la ligne centrale d'un résonateur supraconducteur avec une géométrie de ligne à transmission coplanaire. Le détecteur de bruit, une jonction tunnel supraconductrice (jonction SIS, fabriquée

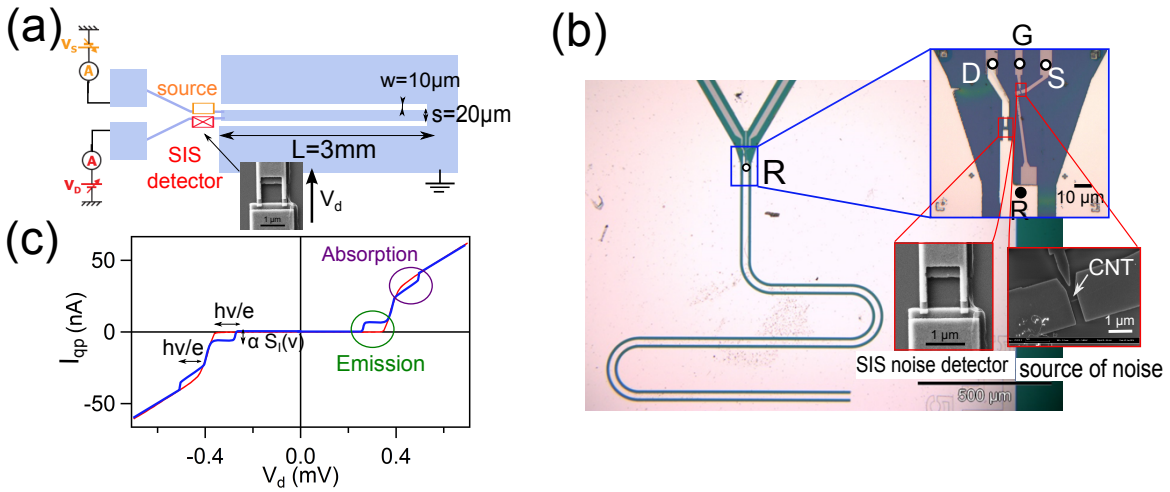


FIGURE 5 – (a) Schéma du dispositif expérimental, où la source de bruit est connectée au détecteur-jonction SIS par l'intermédiaire d'un résonateur à guide d'onde coplanaire. (b) Image en microscopie optique et électronique de l'échantillon utilisé pour la mesure de bruit haute fréquence. (c) En rouge : caractéristique I(V) du détecteur SIS, dans lequel toute contribution des paires de Cooper a été supprimée grâce à la géométrie de SQUID. En bleu : allure qualitative de cette caractéristique en présence d'une émission ou d'une absorption de photons par la source de bruit (voir texte).

en aluminium) est connecté sur la même ligne, de sorte que la source et le détecteur sont couplés uniquement aux fréquences de résonance du circuit, en l'occurrence des fréquences de l'ordre de $\nu_0 = 12$ GHz, $\nu_1 = 31$ GHz et $\nu_2 = 51$ GHz (le couplage par les harmoniques supérieures est très faible).

Le principe de la détection de bruit est basé sur la mesure du courant tunnel de quasi-particules dans la jonction SIS, photo-assisté par l'émission ou l'absorption de photons par la source de bruit. La jonction SIS est particulièrement adaptée pour cela car, si elle est polarisée sous le gap supraconducteur, le seul courant de quasi-particules possible est photo-assisté. Afin d'éliminer toute contribution due au passage par effet tunnel des paires de Cooper, le détecteur est en fait un SQUID dont on peut supprimer le supercourant global en appliquant un flux approprié. La caractéristique I(V) correspondante, en l'absence d'absorption on d'émission de photons, est représentée en rouge sur la figure 5 (c). En bleu est représentée qualitativement la modification de cette caractéristique en présence d'émission ou d'absorption de photons par la source de bruit.

Si la tension $V_d$ utilisée pour polariser la jonction SIS est telle que $|V_d| < 2\Delta/e$, un courant de quasi-particules est possible si des photons de fréquence $h\nu > 2\Delta - |V_d|$ sont émis par la source et absorbés par le détecteur. Il apparaît alors une marche de courant photo-assisté dans la I(V), de largeur $h\nu/e$ et dont la hauteur est proportionnelle au bruit en émission de la source. Il est possible de mesurer également les photons absorbés par la source, en polarisant la jonction au delà du gap ($|V_d| > 2\Delta/e$), ce qui se traduit par une réduction du courant

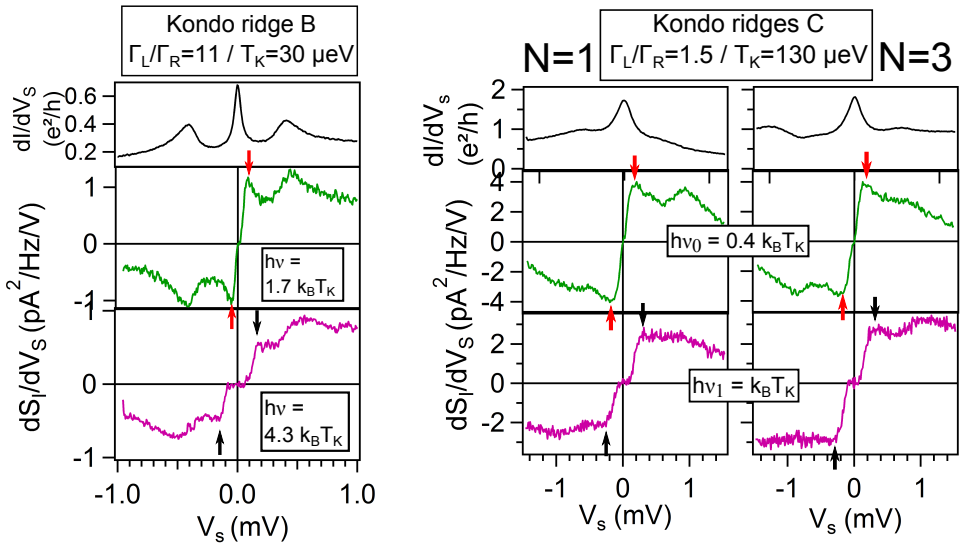


FIGURE 6 – Mesure de la dérivée du bruit en émission du nanotube de carbone en fonction de sa tension de polarisation, aux deux premières fréquences de résonance du résonateur : $\nu_0 = 12$ GHz en vert, et $\nu_1 = 31$ GHz en rose. Cette mesure est donnée pour trois valeurs de tension de grille différentes, correspondant aux centres de trois diamants de Coulomb présentant de l'effet Kondo (dont les caractéristiques, $T_K$ et asymétrie des contacts, sont indiquées sur la figure). La conductance correspondante du nanotube est représentée en noir. Les flèches rouges indiquent des singularités dans le bruit, dues à l'effet Kondo. Les flèches noires indiquent là où ces singularités ont disparu (voir texte).

de quasi-particules. Toutefois, ce signal de bruit en absorption est beaucoup plus difficile à obtenir que celui en émission. Dans le cadre de cette thèse, nous ne sommes pas parvenus à mesurer ce type de bruit sur le nanotube de carbone.

### 0.2.2 Résultats expérimentaux

Grâce à ce dispositif, nous avons donc pu mesurer le bruit en émission d'une boîte quantique à nanotube de carbone à 12 et 31 GHz. Je présente dans la suite trois valeurs de tension de grille, correspondant aux centres de trois diamants de Coulomb où est observé de l'effet Kondo. La conductance correspondant à ces trois effets Kondo est représentée sur la figure 6, en noir.

La première zone Kondo, appelée B, correspond à une température Kondo $T_K = 30$ $\mu$eV et un des réservoirs est 11 fois mieux couplé au nanotube que l'autre. Les deux autres zones ont en les mêmes paramètres et sont nommées zone C : $T_K = 130$ $\mu$eV et les réservoirs sont quasiment identiquement couplés au nanotube ($\Gamma_L/\Gamma_R = 1.5$).

La dérivée du bruit par rapport à la tension de polarisation $V_s$ du nanotube est tracée en fonction de $V_s$, dans chacune de ces zones Kondo, aux deux premières fréquences de résonance du système : $\nu_0 = 12$ GHz et $\nu_1 = 31$ GHz. Comme les températures Kondo ne sont pas les

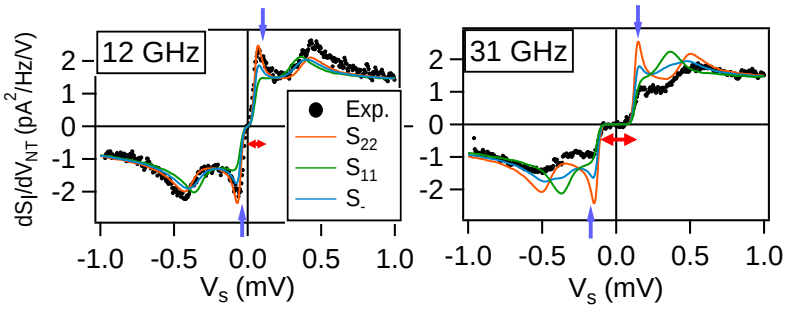


FIGURE 7 – Comparaison, pour la zone B, entre les données expérimentale de dérivée du bruit en fonction de $eV_s/k_BT_K$ et les différents termes prédits par une théorie basée sur la dépendance en énergie de la transmission du système [20]. En supposant que le réservoir de droite est celui qui est dix fois plus couplé que l'autre, les bruits intra-contacts que l'on attend dans chacune des électrodes (à "gauche" $S_{LL}$ et à "droite" $S_{RR}$) sont tracés, ainsi que $S_-$, qui est en quelque sorte à la fois le bruit à gauche et à droite, et est relié aux fluctuations du courant net calculé dans la référence [21].

mêmes dans les zones B et C, les rapports $\nu/T_K$ ne sont pas les mêmes non plus.

Qu'attend-t-on de ces mesures, réalisées à fréquence finie $\nu$ ? Tout d'abord, il s'agit de bruit en émission, qui n'existe pas si la tension appliquée $V_s$ ne fournit pas l'énergie nécessaire à l'émission d'un photon d'énergie $h\nu$ (*i.e.* si $V_s < h\nu$). C'est pour cela qu'il y a un plateau de bruit autour de $V_s = 0$, visible surtout dans la mesure à 31 GHz. Pour $V_s > h\nu$, s'il s'agissait d'une jonction tunnel avec une transmission indépendante de l'énergie, on attendrait un bruit linéaire en tension, de dérivée constante. En présence d'effet Kondo, la transmission devient fortement dépendante de l'énergie, avec l'apparition d'une résonance au niveau de Fermi. Ceci se manifeste dans le bruit par une augmentation logarithmique du bruit à $eV_s = h\nu$, et donc un pic dans sa dérivée. C'est ce pic qui nous intéresse, puisqu'il nous renseigne sur la dynamique de la résonance Kondo à la fréquence $\nu$. Il ne faut cependant pas oublier que le système est également soumis à une tension $V_s$, et se trouve donc hors d'équilibre. D'après une première expérience de ce type réalisée en 2012 par Basset et al. [19], il semblerait que ce soit justement le comportement hors équilibre qui affecte le plus la résonance et non la dynamique de l'effet Kondo : la mesure de bruit en émission à fréquence $\nu$ nous permet donc de sonder la résonance Kondo quand une tension $V_s = h\nu/e$ est appliquée entre les réservoirs.

Dans notre expérience, ce pic dû à la résonance Kondo est présent pour la zone B, à 12 GHz (qui correspond à $1.7T_K$), alors qu'il disparaît à 31 GHz ($4.3T_K$). Dans la zone C, on voit également une structure à 12 GHz($0.4T_K$). Le fait qu'elle soit moins marquée que dans la zone B est dû à la présence d'un fond de conductance autour de $e^2/h$, très bruyant. Ce qui est frappant, c'est que cette structure disparaît à 31 GHz, qui correspond cette fois à $1T_K$. Ces observations qualitatives sont confirmées par l'analyse plus quantitative présentée sur les figures 7 et 8. Sur la figure 7 sont présentées les mêmes données de bruit que précédemment

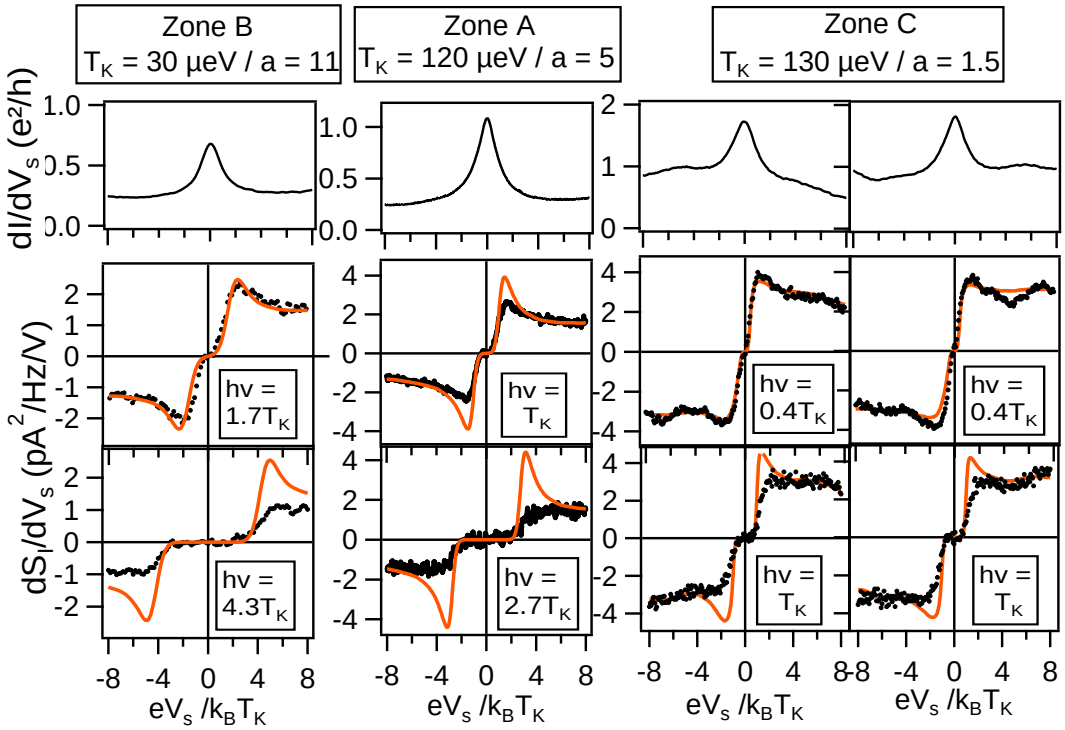


FIGURE 8 – Comparaison des données expérimentales de dérivée du bruit en fonction de $eV_s/k_BT_K$ dans les zones B et C ainsi que dans la A (mesurée en 2012) avec les prédictions de la théorie basée sur la dépendance en énergie de la transmission du système [20]. La quantité $a = \Gamma_L/\Gamma_R$ désigne l'asymétrie des contacts.

pour la zone B, mais comparées à des prédictions théoriques faisant intervenir la dépendance en énergie de la transmission du système, déduite de la mesure de conductance. On notera que ces prédictions ne prennent pas en compte l'effet Kondo directement (comme dans [22]) mais par l'intermédiaire de la dépendance en énergie de la transmission du système, obtenue par une mesure de conductance DC. Cette théorie ne peut donc pas prendre en compte la dynamique de l'effet Kondo et la décohérence hors équilibre, mais elle donne justement le bruit attendu en l'absence de tous ces effets. De plus, il s'agit de la seule prédiction qui permet de prendre en compte la contribution d'un éventuel fond de conductance dû au blocage de Coulomb, en plus de l'effet Kondo. Nous nous sommes appuyés pour cela sur la référence [20].

Dans le cas de la zone B, il est à noter que, comme la symétrie entre les deux réservoirs est brisée (puisqu'un des deux est beaucoup mieux couplé que l'autre) et qu'il s'agit d'une mesure à fréquence finie, le bruit n'est a priori pas le même suivant le contact dans lequel il est mesuré [20]. Ne sachant pas lequel nous mesurons, les deux composantes intra-contact du bruit (à "gauche" $S_{LL}$ et à "droite" $S_{RR}$), on été tracées en prenant comme convention que le contact de droite était le mieux couplé. Ainsi, à 12 GHz, $S_{LL}$ le bruit dans le contact le moins bien couplé rend très bien compte de la mesure, contrairement à celui à $S_{RR}$ : il semblerait

que ce soit celui là que nous mesurons. Le bon accord expérience/théorie nous dit que la résonance Kondo n'est pas du tout affaiblie alors qu'il y a une tension $eV_s = 1.7T_K$ entre les deux réservoirs. En revanche, à $eV_s = 4.3T_K$, cette résonance est complètement détruite.

La même analyse est réalisée avec les mesures de l'expérience de 2012 [23] (nommée zone A), présentée sur la figure 8, avec une conclusion similaire.

Pour la zone C, où les contacts sont couplés symétriquement au nanotube, il n'y a plus ce problème de la brisure de symétrie spatiale. La comparaison entre les mesures et le calcul est présentée sur la figure 8. Pour $eV_s = 0.4T_K$, notre théorie reproduit plutôt bien les mesures. En revanche, pour $eV_s = 1T_K$, nous mesurons moins de bruit qu'attendu : la résonance Kondo est fortement affaiblie.

En résumé, pour la zone B, il faut appliquer une tension supérieure à $1.7T_K$ sur le système pour que la signature dans le bruit de la résonance Kondo soit détruite par la décohérence hors équilibre. En revanche, pour la zone C, la résonance Kondo est déjà fortement affectée quand une tension équivalente à $T_K$ est appliquée. Ce qui différencie ces zones c'est que la B correspond à des réservoirs couplés de manière très asymétrique, puisqu'un des deux est dix fois plus couplé que l'autre à la boîte quantique, alors que la zone C correspond à des couplages quasiment symétriques. Il ressort donc de notre expérience que plus les contacts sont symétriques, plus la signature de la résonance Kondo est facilement détruite par l'application d'une tension. Ceci peut se comprendre de la manière suivante. Quand les réservoirs sont couplés symétriquement à l'impureté Kondo, le singulet se forme également sur les deux contacts : si ces contacts ne sont pas au même potentiel, l'état Kondo va être fortement affecté. En revanche, si un des contacts est beaucoup mieux couplé que l'autre, le singulet Kondo va se former majoritairement avec ce réservoir et est moins affecté si le contact mal couplé est à un potentiel différent.

### 0.2.3 Conclusion

En résumé, ces mesures de bruit en émission haute fréquence nous ont permis de mieux comprendre comment est affectée la résonance Kondo lorsqu'elle est mise hors équilibre par une tension appliquée entre les deux réservoirs. Nous avons en particulier mis en évidence le fait que, si les réservoirs sont couplés à la boîte quantique de manière asymétrique, la résonance Kondo est beaucoup moins affectée que si les deux réservoirs sont équivalents. Ceci renvoie au fait que, dans ce cas, le singulet Kondo n'implique que le mieux couplé des réservoirs.

Cette expérience soulève également la question de la brisure de symétrie spatiale du bruit à fréquence finie en cas d'asymétrie du système : le bruit n'est pas nécessairement le même suivant le contact dans lequel on le mesure. Qu'est ce qui est mesuré exactement dans les expériences ? Est-il possible de détecter une telle asymétrie spatiale du bruit ? Ceci demanderait de plus amples investigations expérimentales et théoriques.

## 0.3 Effet Josephson AC dans un nanotube de carbone dans le régime Kondo

### 0.3.1 Principe de l'expérience

L'idée de cette étude est de reproduire exactement la même expérience que dans la partie précédente, à savoir de coupler un nanotube de carbone à un détecteur de radiation haute fréquence à travers un résonateur, mais cette fois le nanotube est contacté par des électrodes supraconductrices. L'objectif est d'étendre l'étude de l'effet Josephson DC décrite dans la première partie aux hautes fréquences, en particulier pour voir ce qu'il advient de la compétition entre l'effet Kondo et la supraconductivité dans ce régime. De même que dans la deuxième partie, cette étude à haute fréquence pourrait également nous en apprendre plus sur la dynamique de l'effet Kondo.

Pour cela, un échantillon très similaire à celui de la figure 5 (b) est réalisé, la différence étant qu'au lieu d'être contacté avec du palladium, le nanotube est contacté avec un tri-couche dans le même esprit que celui décrit sur la figure 1 : Pd(8 nm)/Nb(11 nm)/Al(50 nm) (après oxydation de cette couche, 100 nm d'aluminium sont ajoutés pour former la jonction tunnel du détecteur). Cette fois, la phase supraconductrice aux bornes de l'échantillon ne peut être contrôlée, il est cependant toujours possible de polariser le nanotube par une tension $V_s$. De par ce qu'on appelle l'effet Josephson AC, la phase varie alors telle que $d\varphi/dt = 2eV_s/\hbar$ de sorte qu'il s'établit dans la jonction un courant alternatif à la fréquence Josephson $\nu_J = 2eV_s/h$ (plus d'éventuelles harmoniques ou sous-harmoniques en fonction de la relation courant-phase et de la dynamique du système). L'amplitude de ce courant alternatif est a priori proportionnelle au courant critique. Le courant photo-assisté de quasi-particules mesuré dans le détecteur est donc proportionnel au carré de l'amplitude de l'émission Josephson à 11 et à 31 GHz (qui sont les fréquences de résonance de ce dispositif).

Avant de décrire les résultats expérimentaux, il est à noter qu'il faut être prudent lorsque l'on interprète des mesures d'effet Josephson AC. En effet, comme la phase varie très rapidement, des effets de dynamiques, telles que des transitions Landau-Zener, peuvent modifier l'émission Josephson, en particulier sa fréquence [24]. D'autre part, il faut garder en tête que, de même que lors de la mesure de bruit quantique en émission, il s'agit d'une mesure hors d'équilibre.

### 0.3.2 Résultats expérimentaux

Un aperçu des résultats expérimentaux est présenté sur la figure 9, où l'amplitude de l'émission Josephson est tracée, pour les deux fréquences de mesure 11 et 31 GHz, en fonction de la tension de grille. La conductance dans l'état normal en fonction de la tension de polarisation est également présentée sur la même plage de tension de grille, montrant la présence de quatre diamants de Coulomb présentant une conductance non-nulle à tension nulle, caractéristique de

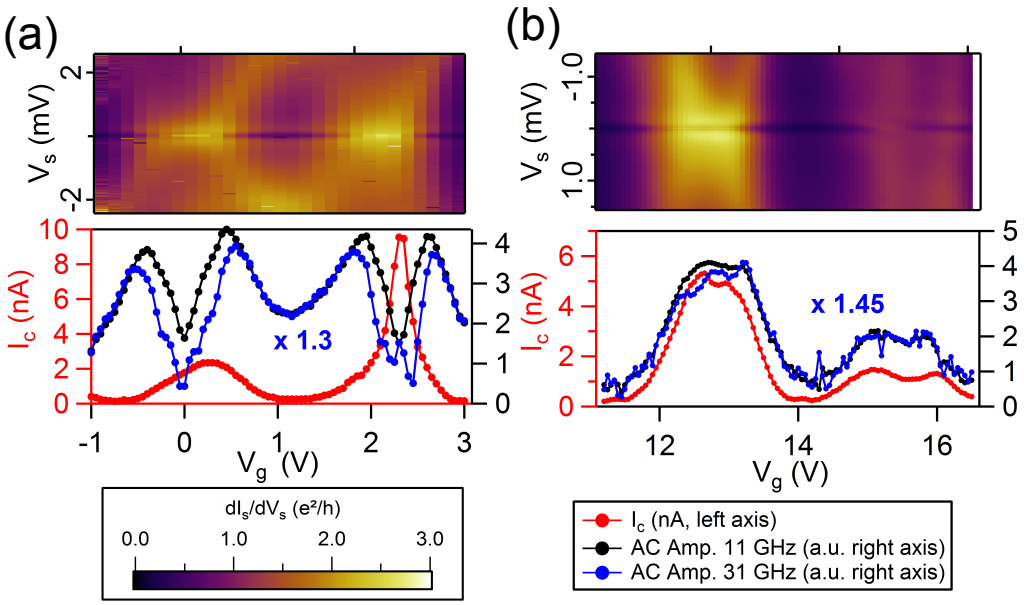


FIGURE 9 – (a) et (b) Amplitudes de l'émissions Josephson AC à 11 GHz (courbes noires) et 31 GHz (courbes bleues) en fonction de la tension de grille, comparées au courant de switching (courbes rouges), dans quatre diamants qui manifestent de l'effet Kondo. Au dessus est représentée la conductance différentielle dans l'état normale (en présence d'un champ de 1 T), en fonction de la tension de polarisation $V_s$, pour les mêmes tensions de grille. Les amplitudes AC sont tracées en unités arbitraires, qui sont cependant les mêmes pour toutes les courbes et indiquées sur les axes de droite. L'amplitude à 31 GHz a cependant été renormalisée par un facteur écrit en bleu sur les courbes, pour prendre en compte le fait que le facteur de calibration reliant le courant photo-assisté dans le détecteur à l'amplitude Josephson dépend de la fréquence.

l'effet Kondo. Il faut tout de même noter que les contacts utilisés comportent du niobium qui a un champ critique au delà de 1T, la valeur maximale de champ que l'on peut appliquer avec notre bobine (et au delà de laquelle l'effet Kondo peut être dramatiquement affecté). C'est pour cela qu'un creux de conductance est observé à tension nulle pour toutes les tensions de grilles, ce qui rend difficile l'extraction des paramètres de l'effet Kondo.

Dans l'état supraconducteur, pour cette gamme de tension de grille, le courant de switching est tracé en rouge. Dans les diamants occupés par un nombre impair d'électron où il y a de l'effet Kondo, deux comportements peuvent être observés en fonction du rapport $\Delta/T_K$, quantifiant la force des corrélations supraconductrices par rapport à l'effet Kondo. Si $\Delta/T_K \gg 1$, alors il n'y a pas d'électrons disponibles au niveau de Fermi pour former le singulet Kondo : l'état du système est un doublet, qui mène à une jonction $\pi$. En revanche, si $\Delta/T_K \ll 1$, la formation d'un singulet BCS/Kondo est possible, donnant lieu à une jonction 0 donc le supercourant est amplifié par les processus de cotunneling associés à l'effet Kondo. C'est dans ce dernier régime que se trouve notre système, le supercourant augmentant dans les zones Kondo. La question est de savoir s'il est possible de détecter cette jonction 0, rendue possible par l'effet Kondo, dans l'effet Josephson AC ? Va-t-elle survivre à la fois à la dynamique de l'effet Josephson et

de l'effet Kondo ?

Pour tenter de répondre à cette question, regardons les mesures d'amplitude de l'effet Josephson AC, présentées sur la même figure.

- Pour les zones Kondo du panneau (a), l'émission Josephson décroît fortement lorsque le supercourant est maximum, et de manière plus marquée à 31 qu'à 11 Ghz. Ce constat est étonnant : il est tout à fait inhabituel d'avoir en même temps un maximum de supercourant et un minimum d'émission Josephson. Ceci ne semble pas s'expliquer par des transitions Landau-Zener qui modifieraient la fréquence d'émission, puisqu'aucun signal n'est observé aux autres fréquences (données non montrées ici). Cela pourrait signifier que l'effet Kondo et la supraconductivité n'arrivent plus à coopérer, que ce soit à cause de leurs dynamiques ou de l'aspect hors équilibre, restaurant une jonction $\pi$.
- Pour les zones Kondo du panneau (b), les choses sont en revanche très différentes : l'émission Josephson a la même allure que le supercourant, on n'observe pas d'écroulement du supercourant dans la zone Kondo.

Quelle est la différence entre ces deux zones ? Malheureusement, l'état normal n'est pas suffisamment clair pour pouvoir trancher sur les valeurs de températures Kondo. Un seul indice nous est donné par la conductance dans l'état supraconducteur (non montrée) : la diminution de l'émission Josephson AC est corrélée à une absence de structures dues aux réflexions d'Andreev multiple, ce qui est en général le signe d'une transmission proche de 1. Mais globalement, dans l'état actuel, nous ne comprenons pas pourquoi ces zones Kondo ont des comportements si différents et à quoi ils sont dûs.

Pour éclaircir la situation, il est nécessaire de réaliser des expériences complémentaires avec des contacts sans niobium, afin de mieux caractériser le nanotube dans l'état normal.

## Conclusion

En conclusion, ce travail de thèse nous a permis, à travers trois expériences impliquant des boîtes quantiques formées dans des nanotubes de carbone, d'explorer l'effet Kondo dans une boîte quantique, ainsi que sa coexistence avec l'effet Josephson.

Grâce à la mesure de relation courant-phase dans un nanotube, nous avons pu mettre en évidence deux types de transitions 0-$\pi$ différentes. Une première résultant d'un croisement de niveau induit par la compétition entre un état singulet BCS/Kondo et un doublet, l'autre entre deux doublets qui, grâce à la participation d'un second niveau d'énergie, donnent des contribution au courant de signes opposés. Chacune de ces situations conduit à des relations courant-phase très différentes à la transition.

En mesurant le bruit quantique en émission dans un nanotube de carbone, nous avons pu sonder la décohérence hors équilibre de l'effet Kondo, et ainsi montrer de quelle manière elle dépend de la symétrie des contacts. Ainsi, plus les contacts sont symétriques, plus la résonance Kondo est affaiblie lorsqu'une tension est appliquée entre les deux réservoirs. Nous avons également soulevé le problème de l'influence de la brisure de symétrie des contacts sur le bruit à fréquence finie : il est alors prédit que le bruit est différent selon le contact dans lequel on le mesure. Est-ce réellement le cas dans nos expériences ? Ce point est à approfondir expérimentalement.

Enfin, nous nous sommes intéressés à la compétition entre effet Kondo et l'effet Josephson, mais cette fois à haute fréquence, en mesurant l'émission Josephson AC d'une jonction supraconductrice à nanotube de carbone. Cette mesure est délicate à interpréter à cause des effets de dynamique et hors d'équilibre. Elle semble toutefois indiquer que lorsque l'effet Kondo coopère avec la supraconductivité pour donner une jonction 0 avec un supercourant important, l'effet Josephson AC, lui, peut s'écrouler, comme s'il s'agissait d'une jonction $\pi$. Il semblerait donc qu'à cause de la dynamique de la phase, de l'effet Kondo, et/ou de la tension appliquée sur le système, la jonction 0 en DC puisse se transformer en jonction $\pi$ en AC. Des mesures complémentaires seront nécessaires pour déterminer dans quelles conditions cela se produit.

# Introduction

How to introduce a mesoscopic physics PhD thesis without talking about the recent progresses of electronics and nanofabrication, which have been made possible by the reduction of the size of the electronic components to a few tens of nanometers ? How not to mention the next step, quantum computing, the new expected technological revolution ?

Actually, we are not so much interested in these technological achievements. If we study electronic transport in small systems at low temperature, it is first because of the extraordinary rich physics that is unveiled by the vanishing of thermal fluctuations and the appearance of interference and confinement effects.

One of these quantum effects we are interested in is the Kondo effect, that can be found in dilute alloy where magnetic impurities are embedded in a metal. The electrons around the Fermi energy cooperate collectively to screen the magnetic moment of the impurity, giving rise to a resonance in the density of states. The Kondo effect has a significant theoretical importance since it has been one of the first application of the renormalization group theory. However, several aspects of Kondo effect remain unexplored (in particular from the experimental point of view), as for example its behavior out-of-equilibrium or its dynamics.

Another very famous quantum phenomenon is superconductivity, which exists thanks to attractive interactions between electrons that induce their pairing in Cooper pairs and a flow of non-dissipative currents driven by a superconducting phase instead of a voltage. An interesting point is that these superconducting correlations can be induced in a non-superconducting material (provided that it is phase coherent) : this is the Josephson effect. What happens if superconductivity is induced in a Kondo system ? This is one of the questions we address in this work.

This PhD work is centered on the investigation of electronic transport in a mesoscopic realization of the Kondo effect : carbon nanotubes contacted to metallic (and eventually superconducting) reservoirs.

The first part of the manuscript is dedicated to the presentation of carbon nanotubes and their physics, starting by a general introduction on the Kondo effect. We show that this effect, generally considered in bulk metals, also exists in a single impurity localized on a quantum

dot weakly coupled to macroscopic leads. This system provides a tunable Kondo resonance, through which electronic transport can be investigated. The second chapter describes in details the carbon nanotube system, mainly seen as a quantum dot in the Coulomb blockade regime, which enables the observation of the Kondo effect. Besides, nanotubes are shown to be very special quantum dots since each energy level should be, in addition to the spin degeneracy, orbitally degenerated, so that they can be seen as two-level quantum dots, where more exotic Kondo effects are expected. In the third chapter, I explain how are made the nanotube samples, and how they are measured.

The second part deals with the Josephson effect in a carbon nanotube : what happens when superconducting correlations compete with Coulomb interactions and Kondo effect ? While chapter 4 exposes the basics of the superconducting proximity effect and the state of the art in quantum dots, chapter 5 presents our experimental results. In this experiment, a carbon nanotube is embedded in an asymmetric superconducting loop, so that it is possible to measure the supercurrent in the system as a function of the superconducting phase. We have measured this relationship in a regime where the superconducting and Kondo correlations are of the same order of magnitude and shown that the ground state of the system, singlet or doublet, can be controlled by the superconducting phase. We then compare this phase-driven transition to what happens when two energy levels participate to the transport of Cooper pairs.

The third part is about the fluctuations of current in a carbon nanotube quantum dot in the Kondo regime. In chapter 6, an overview of out-of-equilibrium noise, also called shot noise, is presented. In particular, I present a measurement of shot noise in a carbon nanotube performed in Osaka with nanotube samples that we made in Orsay. This experiment enables to show that the Fermi liquid description of the Kondo effect extends to out-of-equilibrium situations. Chapter 7 focuses on the other major problematic of my PhD : high frequency shot noise measurements, expected to probe the out-of equilibrium dynamics of the Kondo effect. In this experiment, the carbon nanotube has normal contacts and is coupled, at some frequencies determined by a resonator, to a superconducting tunnel junction used as an on-chip high frequency noise detector. This allowed us to measure the emission noise of the quantum dot in the Kondo regime with possible asymmetric coupling with the two reservoirs. These measurements address the issue of the spatial asymmetry of the measured signal and show that, when the contacts are symmetrically coupled to the dot, the Kondo resonance is more easily weaken by an out-of-equilibrium situation than asymmetrical contacts.

Finally, the fourth part presents an experiment which mixes the two aspects investigated before : a carbon nanotube is coupled to an on-chip high frequency noise detector but it is contacted with superconducting electrodes. Then, if it is voltage biased, the system emits an AC radiation whose harmonic content and amplitude depend on the current-phase relation. Measured in the Kondo regime, this should give insights into the competition between the Kondo effect and superconductivity at high frequency and out of equilibrium. Experimental results are presented together with possible interpretations.

# Part I

# Kondo effect and carbon nanotube quantum dots

# 1 The Kondo effect in condensed matter

This chapter is dedicated to the Kondo effect, that will be mentioned all over this manuscript. Indeed, the main results of this PhD work are related to the Kondo effect realized in a carbon nanotube quantum dot, through essentially two aspects. The first one is how this effect can coexist and compete with superconductivity, the second concerns its high frequency emission.

In order to understand the importance of these results, this chapter aims at describing the underlying framework of the Kondo effect and more generally the problem of impurities in metals, before introducing the associated issues that will be investigated in the thesis.

## 1.1 The Kondo problem

### 1.1.1 Phenomenological description

Generally, when the temperature of a metal is lowered, its resistance decreases due to the smaller importance of inelastic scattering (electron-phonon, electron-electron etc.). For superconducting metals, the resistance can even fall to zero. But in the 50's, the resistance of some alloys with magnetic impurities have been found to increase at low temperature [25]. This was surprising and remained unexplained until 1964 when Jun Kondo, a Japanese theoretician, noticed that this increase of resistance was correlated to the presence of localized magnetic moments in the alloys [26]. He proposed to describe formally the problem as an exchange interaction between the localized impurities (called $d$ electrons) and the conduction electrons of the Fermi sea, giving the so-called Kondo hamiltonian [27]:

$$H_K = \sum_{\vec{k}\sigma} \epsilon_{\vec{k}} n_{\vec{k}\sigma} - J_K \vec{S_d}.\vec{s_c(0)} \tag{1.1}$$

The key parameter is $J_K$, the exchange coupling between the spins of itinerant electrons and the one of the localized impurity. Kondo has shown that, provided that $J_K$ is negative, this hamiltonian gives rises to the measured increase of resistance. That's why his name has

been given to the effect. The Kondo effect refers now more generally to the coherent and many-body interaction of the Fermi sea of a metal, composed by delocalized electrons, with localized magnetic moments. This effect happens for temperatures lower than the so-called Kondo temperature, whose connection with $J_K$ will be shown in the following.

Beyond its predictive interest, this interpretation allows to go qualitatively further. Since the system behaves as a magnetic moment antiferromagnetically coupled to the conduction electrons, it tends to form a singlet state [1] to minimize its energy. This singlet state is made possible by the screening of the magnetic moments by the conduction electrons : this is called the Kondo screening (see Fig. 1.1 for a naive representation). When going through a sample, the conduction electrons scatter on the "Kondo clouds" formed by the electrons correlated with the impurity, making the resistance increase.

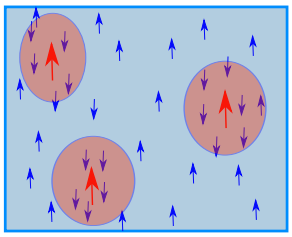

FIGURE 1.1 – Schematic representation of magnetic localized impurities in a metal that are screened due to Kondo effect.

But actually, the explanation given by Kondo raised new questions. For example, this model does not explain why the parameter $J_K$ is negative. Most of all, the perturbative approach gives a logarithmic divergence of the resistance at low temperature, showing that the problem was not solved at all.

### 1.1.2 Renormalization of the problem

#### 1.1.2.1 Why does the perturbative approach fail ?

The "Kondo problem" is the fact that perturbative calculations give a divergence of the physical quantities at low temperature. This is due to the nature of the impurity, which has a quantum degree of freedom (generally a spin 1/2). Indeed, if the impurity has a spin up at a given time, due to the Pauli exclusion principle, only spin down electrons of the Fermi sea are involved in spin-flip scattering with the impurity. This produces correlations between the scattering events, implying a collective participation of the conduction electrons. In other words, the conduction electrons should not be considered as independent particles but as a many-body entity [28, 29]. These correlated electrons, which interact with the impurity, form

[1] "Singlet state" describes a state with zero spin (S=0). For a spin S=1/2 system, we speak of a "doublet state" because it is doubly degenerated ($m = \pm 1/2$). A "triplet state" is a spin 1 system originating from the combination of two 1/2 spins, it is degenerated three times.

the Kondo cloud [30].

The degenerated nature of the spin and the fact that it is conserved during scattering processes are fundamental. Note that Kondo effect is also possible with other quantum degrees of freedom : orbital [31], topological[2] or charge [1] Kondo effect are also possible. In the case of a four fold degenerated degree of freedom, a richer Kondo effect arises : SU(4) Kondo effect (while the usual one described above is called SU(2)). As it will be discussed in chapter 2, this situation can be found in carbon nanotubes.

#### 1.1.2.2 Scaling methods

The solution to the Kondo problem came from renormalization, in a first version by P. W. Anderson (the "poor man's scaling" [32]) and then by K. Wilson (Nobel prize in 1982 for the renormalization group method). In fact, it was the first complete realization of renormalization [28], even though this method is more famous for its application to phase transitions.

As explained by Wilson himself [28], the idea is to solve the hamiltonian successively for various "shells" of the conduction band. At each step, the electrons involved are closer and closer to the Fermi level (chosen such that $\epsilon_F = 0$) [2], but still taking into account the coupling of the further energy states to the impurity (from the previous iterations). In other words, the hamiltonian is solved at smaller and smaller energy scales. At each step, a new effective coupling constant $\tilde{J_K}$ is calculated, giving what is call a flow diagram (see Fig. 1.2).

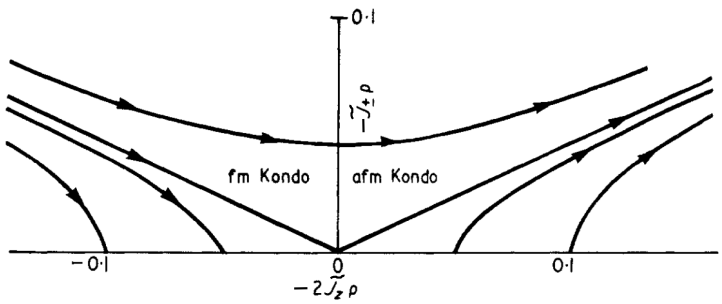


FIGURE 1.2 – Flow diagram in Anderson's poor man's scaling, taken from Ref. [32]. Note that for any negative initial coupling $J_K$, the fixed point is $\tilde{J_K} = -\infty$.

For any negative initial coupling $J_K$, one shows that the flow goes toward the fixed point $\tilde{J_K} = -\infty$ : the smaller is the energy scale, the stronger is the effective coupling to the impurity. Qualitatively, this is why the electrons closer to the Fermi energy are more involved in the Kondo effect, giving rise to a peak in the density of states around the impurity. This so-called Kondo resonance, pinned to the Fermi energy, is another characteristic feature of the Kondo effect (see fig. 1.3).

[2] Or, equivalently, further and further from the impurity in space.

Another result of this kind of calculation is the evaluation of the Kondo temperature $T_K$, characteristic energy of the effect and scale invariant of the problem. As a function of the coupling $J_K$ and the density of states $N_0$, it can be expressed as :

$$k_B T_K \propto e^{-\frac{1}{N_0|J_K|}} \tag{1.2}$$

If $T > T_K$, the electrons involved in the correlated state are likely to be excited by fluctuations due to temperature, bringing decoherence in the system and a weakening of the Kondo resonance (see fig. 1.3). It worth noting as well the exponential dependence of the Kondo energy in the exchange coupling $|J_K|$.

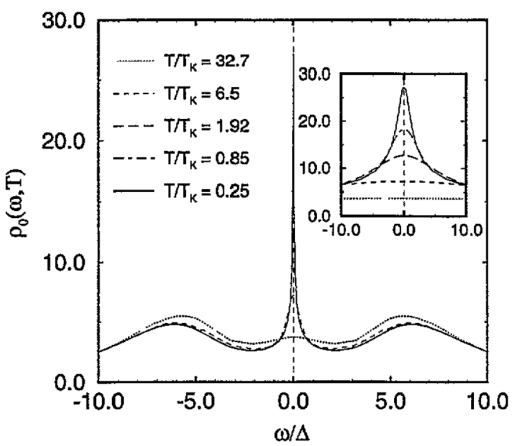


FIGURE 1.3 – Kondo resonance in the density of states and its temperature dependence for the Anderson model from numerical renormalization group (NRG) calculations at $\epsilon_d = -U/2$. The quantity called $\Delta$ represents the width of the impurity level $\Gamma$. Taken from [33].

## 1.2 The problem of impurities in metals

### 1.2.1 Anderson Hamiltonian

The Kondo problem is actually a particular case of the more general problem of impurities in metals, as it as been developed in the 60's by P. W. Anderson and J. Friedel's team in Orsay.

Such systems are simply modeled by the so-called Anderson hamiltonian [34]:

$$H_A = H_0 + H_{at} + H_{coupl} \tag{1.3}$$

- $H_0 = \sum_{\vec{k},\sigma} \epsilon_{\vec{k}} a^\dagger_{\vec{k},\sigma} a_{\vec{k},\sigma}$ represents the unperturbed energy of the conduction electrons.
- $H_{at} = \epsilon_d \sum_\sigma a^\dagger_{d,\sigma} a_{d,\sigma} + U n_{d\uparrow} n_{d\downarrow}$ is the energy associated to the impurity level if it is isolated. The first term is the energy of a single electron in the energy level, the second

one takes into account the Coulomb repulsion $U$ in case of double occupancy. This latter term is the one coupling spin up and down, allowing spin-flip processes.

- $H_{coupl} = \sum_{\vec{k},\sigma} (V_{\vec{k}d} a_{\vec{k},\sigma} a^{\dagger}_{\vec{d},\sigma} + h.c.)$ is the coupling between the conduction electrons and the impurity.

To visualize the meaning of the parameters $U$ and $\epsilon_d$, the limit case of an isolated impurity ($H_{coupl} = 0$) is represented on Fig. 1.4. The impurity can bare a local moment only for

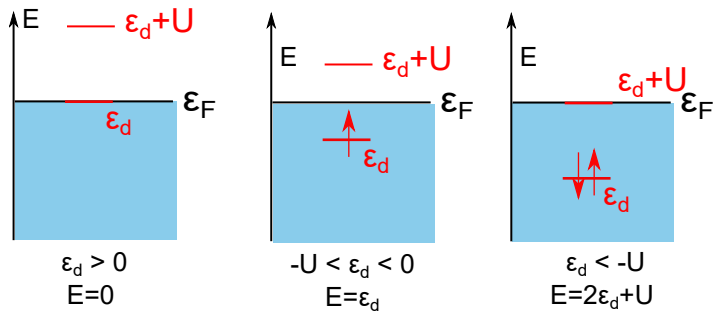


FIGURE 1.4 – Schematic representation of an impurity in a metal in the case of an isolated atom (no coupling impurity/conduction electrons).

$-U < \epsilon_d < 0$ (corresponding to average single occupation). $\epsilon_d = -U/2$ is a specially interesting case since the levels $\epsilon_d$ and $\epsilon_d + U$ are symmetric compared to the Fermi energy : it is the electron-hole symmetry point. All the issue of impurities in metals is to understand, in the case of a non-zero coupling with the conduction electrons, if there is indeed a local moment or not [27].

### 1.2.2 Equivalence with the Kondo problem

In the case of the local moment ($-U < \epsilon_d < 0$), it was shown by Schrieffer and Wolff [35] that the Anderson Hamiltonian was equivalent to the Kondo one. This is valid provided that $U \gg \Gamma$, $\Gamma$ being the width of the impurity level $\Gamma = \pi N_0 |V_{kd}|^2$ [3]. It is then possible to express the $J_K$ parameter of the hamiltonian as a function of the Anderson parameters, giving :

$$J_K N_0 = \frac{2\Gamma U}{\pi \epsilon_d (U + \epsilon_d)} \tag{1.4}$$

In our limit $-U < \epsilon_d < 0$, $J_K$ is indeed negative, as expected from the experiment. It is interesting to note that the antiferromagnetic nature of the coupling comes from the charge fluctuations, that are naturally not included in the Kondo hamiltonian [36].

[3] This comes from the Fermi Golden rule. Note the convention : there is no factor 2 as in some definitions.

From equation 1.2, we get for the Kondo temperature[4] :

$$k_B T_K = \sqrt{\frac{U\Gamma}{2}} e^{\frac{\pi}{2}\epsilon_d(\epsilon_d+U)/(U\Gamma)} \tag{1.5}$$

Note that the minimum value of $|J_K|$ (*i.e.* the minimum value of $T_K$) is obtained at the electron/hole symmetry point, $\epsilon_d = -U/2$. The maximum $|J_K|$ is found on the edges of the $-U < \epsilon_d < 0$ zone ($\epsilon_d \to 0, -U$).

### 1.2.3 Virtual bound states and phase shift

The problem of impurities has been also described by Friedel in terms of virtual bound state. Unlike a bound state, a virtual bound state is not attractive enough to trap electrons, but can retain them during a time of the order of $1/\Gamma$ ($\Gamma$ as defined previously) [27]. This creates an extra density of state and affects the conduction electrons by dephasing their wave-function. One result obtained by Friedel is that this phase-shift at the Fermi level, $\delta(0)$ only depends on the average occupancies of the impurity by spins $\uparrow$ and $\downarrow$ ($N_\uparrow$ and $N_\downarrow$), through what is called the Friedel sum rule [38]:

$$\delta(0) = \pi(N_\uparrow + N_\uparrow) \tag{1.6}$$

This formula is particularly useful since it can be generalized for any value of $U$ and $\Gamma$ [27]. In the case we are interested in, the Kondo effect, the impurity is globally occupied by one electron $< N_\uparrow > + < N_\uparrow >= 1$, the Kondo resonance induces a $\delta = \pi/2$ phase-shift on the conduction electrons. This will be of practical interest in the next chapter, to determine the expected conductance in a quantum dot in the Kondo regime.

This phase-shift description is of great importance to describe the Kondo effect as a Landau Fermi liquid, as it is possible at low energy (*i.e.* in the strong coupling limit) [39]. This aspect of the Kondo effect will be addressed in chapter 6.3, through shot noise measurements.

## 1.3 Kondo effect in quantum dots

Until now, we addressed implicitly Kondo effect in bulk metals, containing many localized magnetic impurities, which were real atomic levels. We move now to another realization of the Kondo effect : quantum dots (QD) in the Coulomb blockade regime. Here is a brief presentation of this system, in order to show its specificities as a Kondo system. Quantum dots (made of carbon nanotubes) and their various transport regimes are described in details in chapter 2.

[4] Actually, the prefactor before the exponential comes from the exact resolution of the Anderson model using what is called the Bethe Ansatz [37]. That is why some people call this formula "the Bethe formula".

### 1.3.1 Introduction to quantum dots and link with the Anderson hamiltonian

Coulomb blockade happens in a system that is so cold and weakly coupled to the environment that electrons are localized on it : adding or removing a single electron requires more energy than what can provide thermal fluctuations. In addition, if it is small enough is is referred as a quantum dot where, thanks to confinements, the single particle levels are quantized. This is realized typically in 2D electron gas or, as in this work, in carbon nanotubes. This kind of system, can therefore provide a localized impurity.

Generally, a quantum dot is connected to two reservoirs, between which a voltage $V$ can be applied. An electrostatic gate can be placed nearby, in order to shift the energy levels of the dot (see Fig. 1.5). The number of electrons in the system is then controlled by both the bias and the gate voltage. We call $U$ the charging energy, the electrostatic energy needed to add an electron on the dot.

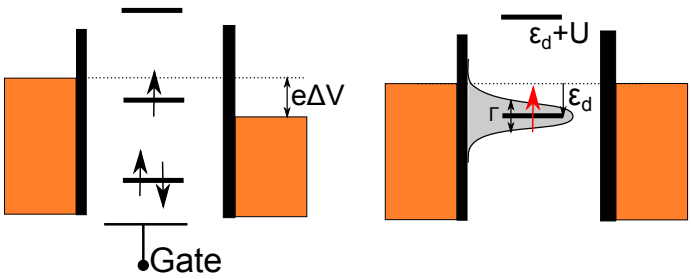


FIGURE 1.5 – Schematic representation of a quantum dot and definition of the QD's parameters.

How to describe a quantum dot with the Anderson model ?

- In the case of large single particle level spacing $\Delta E$, one can consider that only one energy level is involved. If the total number of electrons is odd, then this level should carry a spin 1/2 magnetic moment. Its position can be assimilated to the impurity energy $\epsilon_d$ in the Anderson model, and can be tuned by the gate voltage.
- The charging energy $U$, in both descriptions, represents the Coulomb interaction which comes up when two electrons are on the same level.
- In this context, $\Gamma$ represents the coupling between the dot and the reservoirs, *i.e.* the coupling between the localized impurity and conduction electrons (as in Anderson model). It is as well the width of the impurity level.

As shown by Glazman and Raikh [40], an analog of Kondo effect is indeed possible in this system. Note that in a quantum dot weakly coupled to the electrodes (*i.e.* in the Coulomb Blockade regime), there is *a priori* no current except at the charge degeneracy points. The Kondo effect, making possible due to Coulomb blockade, gives rise to a resonance at the

Fermi level independently of the position of the levels of the dot and thus restores the current suppressed by the Coulomb blockade.

### 1.3.2 Comparison of Kondo effect in QD and in metals

Since the impurity is coupled to two reservoirs (instead of one), there should be two coupling constants J between the dot and the leads, and thus two channels. It is shown [38] that these two channels generally do not correspond to each reservoir, they are *a priori* a linear combination of both. But, at the end of the calculation, provided that the two reservoirs are coherently coupled [5], one of the channel decouples from the dot. That is why, at zero bias, the thermodynamic properties of a QD in the Kondo regime are identical to those described in the single channel Kondo effect.

The specificity of QDs arises when they are voltage biased, allowing transport measurements. Due to the appearance of the Kondo resonance in the density of states, a well transmitted channel is opened in the dot which, otherwise, would be in a Coulomb blockade regime with an almost zero transmission (see next chapter). The measurement of transport through the impurity itself thus gives rise to an increase of the conductance (up to $2\frac{e^2}{h}$ if the two reservoirs are equally coupled to the dot), instead of an increase of the resistance as in bulk Kondo effect.

## 1.4 Some aspects of the Kondo effect investigated in this thesis

The Kondo effect in QD's has been first realized experimentally in 1998 at the MIT [42] and in Delft [43], in 2D electron gas (2DEG) where the quantum dot is defined by electrostatic gating. In 2000, the Copenhagen group measured the Kondo effect in carbon nanotubes [44], and in semi-conducting nanowires in 2006 [45]. Since then, the DC transport properties have been quite well understood as a function of temperature, voltage and magnetic field (see chapter 2 for a more involved discussion). However several points are less understood, I introduce now the ones investigated in this PhD : the out-of-equilibrium decoherence of the Kondo effect, its dynamics and its interplay with superconductivity.

### 1.4.1 Out-of-equilibrium decoherence of the Kondo effect

The specificity of a quantum dot realization of Kondo effect is that a bias voltage $V$ can be applied between the two reservoirs : the Kondo system can be easily driven out-of-equilibrium. Then, a finite current flows in the system inducing a noise that dephases the coherent spin-flip

[5] In a QD where the electronic levels are well resolved, this condition is fulfilled. When it is not, this gives rise to two-channel Kondo effect [41]. In practice, this two-channels situation can be obtained with a large metallic islands, where $\Delta E \ll k_B T$, but this is not that easy.

processes [46]. This inelastic scattering of electrons is thus a source of decoherence that weakens the Kondo resonance as soon as $eV \approx k_B T_K$ [6].

From the experimental point of view, the decoherence induced by a bias voltage cannot be probed directly from conductance measurements and is thus very poorly investigated experimentally. A way of probing the Kondo resonance out of equilibrium is the measurement of emission noise, as in ref. [23]: this is the purpose of one of the experiments described in this thesis, subject of chapter 7. In particular, we aim at investigating experimentally the influence of the asymmetry of coupling between the reservoirs on the decoherence of the Kondo effect.

### 1.4.2 High frequency dynamics of the Kondo effect

Another question, experimentally open, is the dynamics of the Kondo effect. Let's consider the situation described in [48] (but not performed experimentally), where a QD in which the impurity level $\epsilon_d$ is shifted "instantaneously" to a value that allows Kondo effect. Nordlander *et al.* demonstrate that the Kondo effect develops in a time of the order of $\hbar/(k_B T_K)$. One can then expect a modification of the Kondo resonance when it faces processes at frequencies of the order of $\nu = k_B T_K$. How to test experimentally the high frequency dynamics of the Kondo effect ?

In an experiment performed in 2004, Kogan *et al.* [49] measured the DC conductance in the Kondo regime in presence of a high frequency irradiation. Two effects were predicted by theory [50]: the first one is the appearance of satellite peaks in the density of states at bias $V = \pm nh\nu/e$. This can be seen as the excitation of electrons from the Kondo resonance at $h\nu$, followed by the tunneling of the excited electrons in the other lead. Secondly, this effect is damped by the decoherence induced by the microwave excitation itself, resulting from spin-flip excitations due to irradiation. This decoherence is actually of similar nature as the out-of-equilibrium decoherence, and does not really probe the dynamics of the Kondo effect itself.

To our knowledge, the only experiment addressing the high frequency response (and not the dc response to an high frequency excitation) in the Kondo regime is the high frequency noise measurement done by Basset *et al.* [23] (this thesis is the following of this work). Unfortunately, with this experiment, we are currently only able to measure the emission noise, which is as well an ou-of-equilibrium measurement. The dynamics itself is thus difficult to reach, and may be affected by the bias voltage. This problematic is investigated in chapter 7.

In chapter 8, we propose a new experiment to probe the dynamics of the Kondo effect, in competition with superconducting correlations : the measurement of the AC Josephson emission of a carbon nanotube in the Kondo regime contacted with superconducting electrodes.

[6] It is interesting to note that the effect of finite voltage is not, even formally, equivalent to an increase of temperature [47]: it cannot be described by an effective temperature.

### 1.4.3 Interplay with superconductivity

#### 1.4.3.1 Survival basics of superconductivity

Here is a very rapid presentation of superconductivity, before a more involved discussion in chapter 4.

At low temperature, below a temperature called $T_c$, the resistance of some metals becomes equal to zero : they can be traversed by a non-dissipative current. This phenomenon is a quantum macroscopic effect resulting from the pairing of electrons, in what is called Cooper pairs, through interactions with the lattice (at least for the most common superconductors, the type 1 ones). These pairs of electrons have a net spin equal to zero and a pairing energy $\Delta$. Their formation leads to the condensation of electrons into a many body quantum state, that carries the current without dissipation. A gap of width $2\Delta$ around the Fermi energy opens in the density of states. The phase of the macroscopic order parameter is called superconducting phase, it is the quantity whose gradient induces a current in the superconductor.

#### 1.4.3.2 Competition with the Kondo effect

The question is how superconductivity could co-exist with the Kondo effect ? Is it possible and in which conditions ? Whether from the point of view of the Kondo effect or the superconductivity, the question deserves being asked :

- The Kondo effect results from the screening of magnetic impurities by conduction electrons. If the conduction electrons are gathered in zero-spin pairs, how this screening is still possible ? Another way to express the problem is that if a gap opens around the Fermi energy, there is no conduction electron available for the Kondo screening...
- The superconductivity is strongly reduced in the presence of magnetic impurities, that have a pair-breaking effect [51, 52] (since magnetic impurities tend to align the spins of the Cooper pair). But when there is Kondo effect, the impurities moments are screened. How the Kondo screening affects the superconductivity ?

In bulk metals, the situation has been tackled a long time ago [53]. In these systems, the question is how the critical temperature [7] depends on the concentration of impurities in the alloy. The main effect of magnetic impurities is to break the Cooper pairs and thus to reduce $T_c$, the effect being particularly strong for high concentrations (see fig. 1.6 left). In presence of the Kondo effect, since the magnetic impurities are screened, this behavior is modified. If $T_K/T_c > 1$, the decay curve has a positive curvature and the higher is the ratio $T_K/T_c$ (*i.e.* the stronger is the Kondo effect), the less the pair breaking effect is important, decreasing the curvature of the curve (see fig. 1.6 and ref. [53, 55]). This shows that superconductivity

[7] $T_c$ is directly related to the superconducting gap at zero temperature by $\Delta = 1.76 k_B T_C$ [54].

and Kondo effect can coexist. The case $T_K/T_c < 1$ is more complex, with a S-shape of the $T_c = f(c)$ curve.

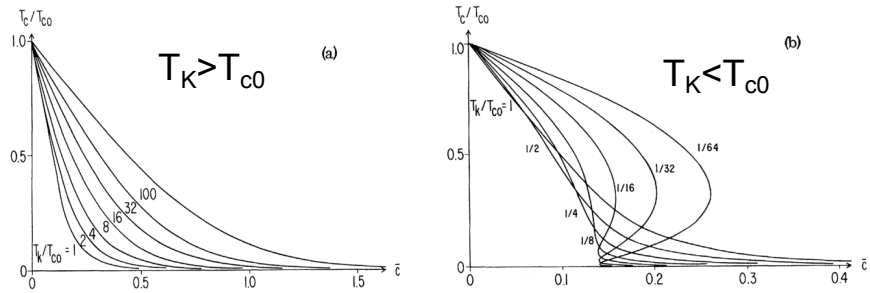


FIGURE 1.6 – Critical temperature, characterizing the superconductivity in the material, as a function of the concentration in magnetic impurities, for both situations $T_K < T_C$ and $T_K > T_1$.

Another kind of experiment possible consist in depositing some magnetic molecules on a superconducting substrate, and to probe the electronic state of the surface with a low temperature STM, as done by Franke *et al.*[56]. In a regime of strong competition between the Kondo effect and superconductivity ($k_B T_K \approx \Delta$), they show that superconductivity and magnetism alternate at length scales of the order of the nanometer.

#### 1.4.3.3 Competition between Kondo effect and superconductivity in a quantum dot

In a carbon nanotube, the issues addressed are quite differents since the superconductivity has to be induced in the system, that is not intrinsically superconductor. This is made possible by contacting it with a superconducting metal : this is the so-called proximity effect, that will be detailed in chapter 4. What is then investigated is the supercurrent through the Kondo impurity itself, bringing new physics.

The main issue in quantum dots in the Coulomb blockade regime is that the only way of transferring an electron from one lead to the other is cotunneling processes, where the condition for one electron to enter the QD is that another leaves it. To have a Cooper pair pass through the dot, one has to transfer both electrons coherently, which is *a priori* very unlikely, in particular when there is an odd number of electrons on the system. However, the presence of the Kondo effect can radically modify the situation. We can distinguish two limit cases :

- If $k_B T_K \ll \Delta$, the Kondo effect cannot develop due to the lack of electrons at the Fermi level (see fig. 1.7). The cotunelling processes are very unlikely : the supercurrent is low and undergoes a sign reversal.
- If $k_B T_K \gg \Delta$, the Kondo singlet can form and enhances the cotunneling processes : the supercurrent is high and without sign reversal. Not only the Kondo effect and the

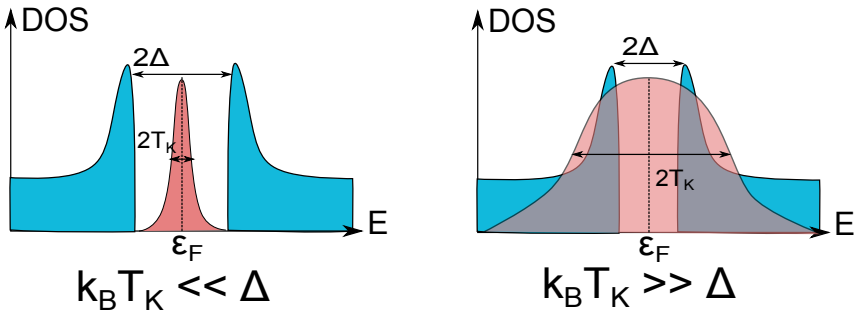


FIGURE 1.7 – Schematic representation of the superconducting density of states superimposed with the Kondo resonance as it would be in the normal state. Comparing the energy scales, one can see that if $k_B T_K \ll \Delta$, the electrons that could participate to the screening are not available because of the superconducting gap. But if $k_B T_K \gg \Delta$, both the Kondo effect and superconductivity can, *a priori*, coexist.

superconductivity coexist, but they also cooperate to induce a high supercurrent in the dot.

In this thesis, we will focus on the intermediate regime $k_B T_K \approx \Delta$, where the nature of the supercurrent is shown to depend on the superconducting phase. This can be rephrased saying that the magnetic state of the QD, Kondo singlet or doublet, is predicted to be controlled by the superconducting phase. This phenomenon is specific to quantum dot since, in the present state of knowledge, this is the only system where it is possible to impose the phase difference across a single impurity.

The experimental demonstration of this will be the subject of chapter 5 using DC measurements, and chapter 8 for an high frequency version of the study.

## 1.5 Conclusion and summary

- The Kondo effect is a many body effect arising from the antiferromagnetic coupling between localized magnetic moments and delocalized conduction electrons. It results in the screening of the localized magnetic moment.
- Using renormalization technics, it is shown that the effective antiferromagnetic coupling increases for electrons close to the Fermi level. This is why a resonance, of width of the order of $T_K$ and pinned to the Fermi energy, appears in the density of states.
- A very tunable Kondo effect can be realized in a quantum dot, where it is also possible to investigate the electronic transport through a single impurity. In particular, this opens the possibility to probe the Kondo effect out-of-equilibrium (chapter 7).
- This kind of sample enables as well to investigate the competition of the Kondo effect

and the superconducting proximity effect as a function of the superconducting phase (chapter 5 for the DC study, chapter 8 for the AC counterpart).

# 2 Carbon nanotubes as quantum wires and quantum dots

This chapter aims at describing the system that I have been investigating all over my PhD, a quantum dot made of a carbon nanotube. First, the nanotube as a molecule is presented, as well as the specificities of its band structure, electronic configuration and mesoscopic transport. Then, I will focus on electronic transport in connected carbon nanotubes, in particular in the Coulomb blockade regime, leading to the Kondo effect. The various Kondo effects that can be found in a nanotube will be reviewed.

## 2.1 Carbon nanotube wires

### 2.1.1 Geometrical structure

#### 2.1.1.1 A graphene wrap

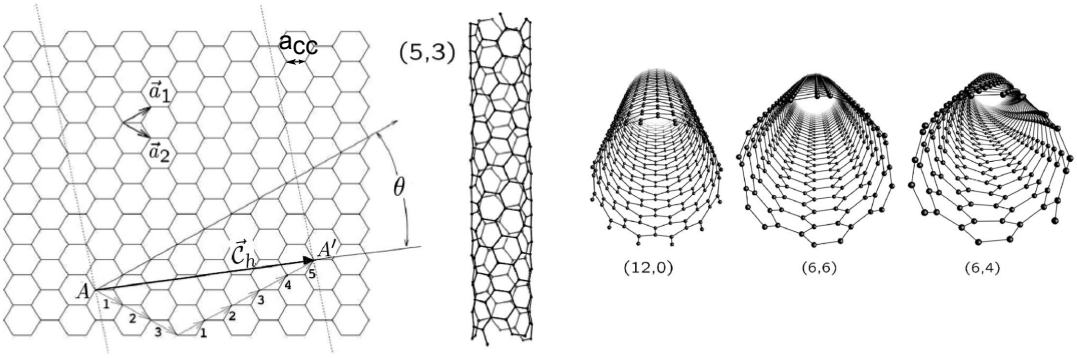


FIGURE 2.1 – Atomic structure of carbon nanotubes seen as a sheet of graphene wrapped as a tube. The way of wrapping the graphene is defined by the vector $\vec{C_h}$. The tube is obtained by superposition of the points A and A'. Taken from [57]. Right : examples respectively of zigzag, armchair and chiral carbon nanotubes.

A carbon nanotube (CNT) is a tube, made of carbon, whose diameter is of the order of a

few nanometers. To understand its atomic structure, we can imagine that it is made from a graphene layer, a two-dimensional hexagonal lattice of carbon atoms, rolled up in a tube. The way of wrapping the layer is defined by the so-called chiral vector $\vec{C_h}$, representing the circumference of the nanotube (see fig. 2.1). $\vec{C_h}$ can be expressed as a function of the lattice vectors $\vec{a_1}$ and $\vec{a_2}$ : $\vec{C_h} = n\vec{a_1} + m\vec{a_2}$. The couple of integers (n,m) describes unambiguously the atomic structure of the carbon nanotube and thus its structural and electronic properties (see [57] for a review on the subject). They are often divided in three classes (see also fig. 2.1) :

- (n,0), zigzag nanotubes, which have some C-C bonds parallel to the nanotube axis.
- (n,n), armchair nanotubes, with some C-C bonds orthogonal to the tube axis.
- (n,m) with $m \neq n \neq 0$. Contrary to the previous classes, these tubes do not have extra symmetry, they are said to be chirals.

Some nanotubes are made of only one tube of graphene, these are single-wall carbon nanotubes (SWCNT), to be opposed with multi-wall nanotubes (MWCNT) made of several tubes wrapped around the others. In the following, unless specified, we will implicitly consider SWCNT.

#### 2.1.1.2 Dispersion relation

To establish the dispersion relation of carbon nanotubes, one needs the one of graphene, that can be obtained from a tight-binding calculation [58] and is represented on fig. 2.2 left.

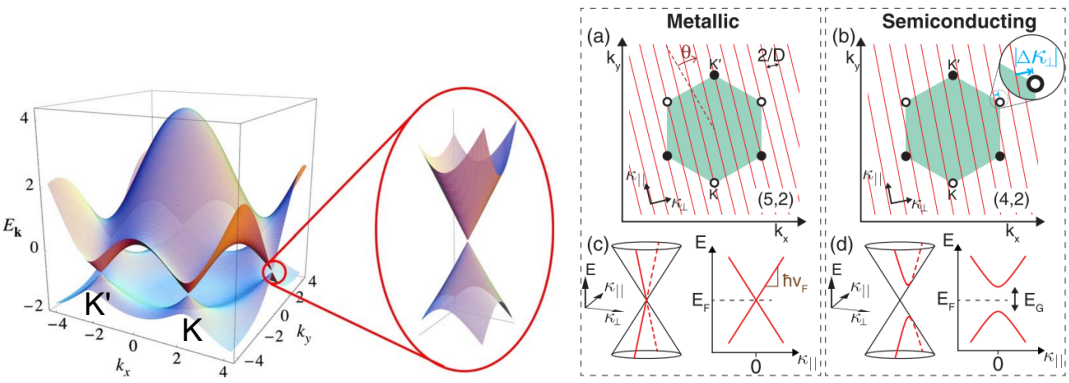


FIGURE 2.2 – Left : Dispersion relation of graphene, calculated from a tight-binding calculation. Taken from [58]. Right : Illustration of the zone-folding model to obtain the dispersion relation of a carbon nanotube. Taken from [59].

This dispersion relation, direct consequence of the two-dimensional hexagonal lattice, is very peculiar since the Fermi surface is reduced to six points in the Brillouin zone. At low energy around these points, the electrons have an effective mass equal to zero and are described by

the relativistic Dirac equation : the dispersion relation is linear $E_{\vec{k}} = \pm\hbar|\vec{k} - \vec{k}_{K,K'}|v_F$. For these reasons, the points forming the Fermi surfaces are called Dirac points. Because of the symmetries of the system, only two of them are not equivalent : K and K', defining two valleys with different helicities [58].

Graphene has various very interesting properties and applications, it is a subject of intense publications in the literature, far beyond the scope of this chapter (see for example [58]). We are going now to focus on carbon nanotubes.

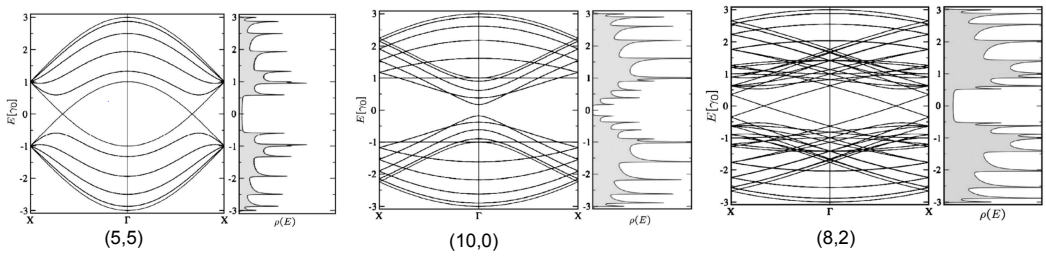


FIGURE 2.3 – Example of dispersion relations and density of states for three different chiralities. Taken from [57]. Note the linear dispersion relation at the Fermi level for metallic nanotubes (5,5) and (8,2).

The difference between graphene and carbon nanotubes comes from the confinement in one direction induced by the tubular structure. The component of the wave-vector orthogonal to the tube axis takes quantized values $k_\perp = \frac{2\pi}{C_h}p$ ($p$ being an integer), that are represented by red lines on fig. 2.2 right and superimposed with the dispersion relation of graphene. The zone-folding approximation consists in neglecting the effects of curvature such that the dispersion relation of the nanotube is given by the cut of the one of graphene along the quantization lines. If one of the red lines crosses a Dirac point, the nanotube is metallic, otherwise it is semi-conducting (see fig. 2.3 for examples of such dispersion relations). These considerations enable to show that a nanotube is metallic provided that $n - m = 3l$ (with l an integer) and semi-conducting otherwise ($n - m = 3l \pm 1$) [57].

This description allows the determination of numerous other electronic properties of nanotubes, such as the density of states, the gap and effective mass in the case of a semi-conductor, etc. See ref. [57] for a detailed review.

#### 2.1.1.3 Synthesis of carbon nanotubes

Historically, CNT were produced in large quantities by electric discharge between graphite electrodes or laser ablation of graphite. It was difficult to obtain individual CNT with these processes, which mostly produce ropes of ten to one hundred nanotubes. For transport measurements, it turned out to be more adequate to start from an organic gas such as acetylene that is decomposed into carbon at high temperature.

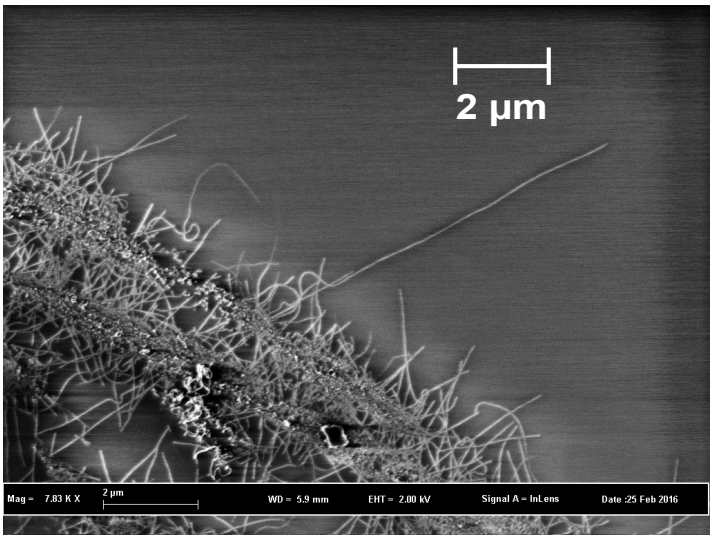


FIGURE 2.4 – Scanning Electron Microscop image of nanotubes synthetized in our group, such as the one measured in this thesis. The image has been taken with an inlens detector, sensitive to the charge of the nanotube. Therefore, the apparent diameter of the nanotube does not represent its real size.

The synthesis process used in the group has been developed by Alik Kasumov [60]. The process consists, first, in depositing a thin layer of iron catalyst on a silicon substrate. Then, the wafer is introduced in an oven, that is pumped at a vacuum around $10^{-6}$ mbar and heated around $900°C$. Then, a small pressure of pure acetylene is introduced (around a few mbar) during 9 s, before being removed. See chapter 3.1.2 for a more involved description of the fabrication of samples.

This process produces a small number of single wall nanotubes of length around a few microns, with a reduced number of defects and a quite clean surface (see fig. 2.4 for an example of synthesized CNT). The diameter of the tubes obtained by this method is around 1-5 nm.

### 2.1.2 Mesoscopic transport in a carbon nanotube

We now focus on electronic transport in carbon nanotubes. Because of their small size, quantum effects might be relevant, especially at low temperature. We start by defining the main concepts and length scales related to mesoscopic transport before considering the case of our favorite system.

#### 2.1.2.1 Characteristic length scales and main concepts

Mesoscopics Physics deals with the physics happening in a system that is so small that the wave nature of electrons becomes crucial to describe its behavior. These effects, of course, come from quantum mechanics, and are due to the confinement or interferences of the electronic

wave-function. To decide if a sample is "small", one needs to compare its size, say its length $L$, to the characteristic length scales of the system. The main ones are defined here, as well as some essential concepts.

**Confinement and Fermi wavelength** When the size of the sample is of the order of the wavelength of electrons, confinement effects arise and induce the quantization of the energies of the electrons in the system. In conductors such as the ones investigated in mesoscopic physics and at sufficiently low temperature, the electrons that contribute to the transport are the one close to the Fermi surface : their wavelength is typically the Fermi wave-length $\lambda_F$.

Within a simple model of a particle in a box, writing that the wavelength $\lambda$ satisfies $L = n\lambda/2$ and assuming that, nevertheless, $\lambda$ stays close to $\lambda_F$, one finds that the spacing between single particle energy levels is typically $\Delta E = \frac{hv_F}{2L}$.

**Electronic interference and coherence length** Just as beams of light, that can interfere provided that they are coherent, electronic interference effects occur if the electrons conserve their phase coherence in the sample. This condition is fulfilled if the sample has a length $L$ smaller than the coherence length $L_\Phi$ ($L < L_\Phi$). Decoherence is associated to irreversibility and is generally due to inelastic processes. In practice, at low temperature ($T < 1$ K), the coherence is limited by electron-electron interactions and magnetic impurities [61].

**Disorder and transport** Generally, conductors may contain defects of various nature, that can modify the trajectories of electrons. We call elastic mean free path $l_e$ the distance that an electron can cover before undergoing such an elastic collision. Note that these collisions do not affect the coherence. If $L < l_e$, the sample is called ballistic, otherwise ($L > l_e$) it is diffusive. If we call $D$ the diffusion coefficient, an electron goes from one side of the sample to the other in a time of the order of $\tau_D = \frac{L^2}{D}$.

**Aharonov-Bohm effect** The simplest way of modifying the phase of an electron in order to observe electronic interferences is the Aharonov-Bohm effect. We consider the situation represented on fig. 2.5, where the electrons can reach the same point through two paths, enclosing a magnetic flux $\Phi = \iint \vec{B}.d\vec{S} = \oint \vec{A}.d\vec{l}$.

To understand simply the effect, we consider a free electron as a plane wave $\Psi \propto e^{i\vec{k}.\vec{r}}$ that acquires a phase $\delta = \int \frac{1}{\hbar}\vec{p}.d\vec{l}$ during its propagation. In the presence of a vector potential $\vec{A}$, as the generalized momentum becomes $\vec{p} - e\vec{A}$, the electron acquires a phase $\delta = \int \frac{\vec{p}.d\vec{l}}{\hbar} - \frac{e}{\hbar}\int \vec{A}.d\vec{l}$ ( with $e = 1.6.10^{-19}C$). The dephasing between the two paths due to the vector potential is thus :

$$\Delta\delta = \frac{e}{\hbar}\oint \vec{A}.d\vec{l} = 2\pi\frac{\Phi}{\Phi_0} \tag{2.1}$$

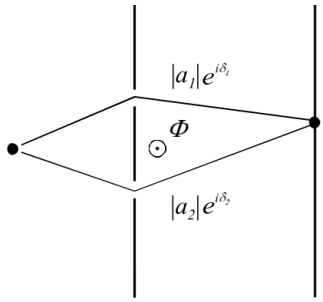


FIGURE 2.5 – Equivalent of the "two slits experiment" for electrons. A magnetic flux $\Phi$ is enclosed by the two trajectories. From ref. [62].

Just as in a optical Young slits experiment, provided that $L < L_\Phi$, the conductance oscillates with the magnetic field. This effect has been put forward experimentally by R. Webb *et al.* [63].

**Landauer-Büttiker formula** From a macroscopic point of view, the resistance of a material is due to the scattering processes that prevent the current to pass, the conductance $G$ of a sample is thus proportional to its section $S$ and inversely proportional to its length $L$. But this description falls down if the sample is very small, ballistic for example : then is no scattering process and thus $G$ should not depend on the length. The Landauer formalism allows to consider this situation.

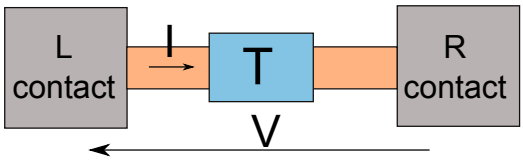


FIGURE 2.6 – Situation investigated in the Landauer formalism in the case of one channel of transmission T.

This formalism consists in modelizing a mesoscopic conductor by a channel of transmission T, or by M channels of transmissions $T_m$ (fig. 2.6). The value of the transmission T is a global quantity that includes both the transmission inside the mesoscopic sample itself and the coupling between the sample and the reservoirs. It is then possible to show that, at zero temperature, the conductance is equal to [64, 65]:

$$G = s\frac{e^2}{h}\sum_m T_m \tag{2.2}$$

With $s$ being the degeneracy of the channels (2 for spin 1/2 e.g.). In the particular case of one perfectly transmitted channel (T=1) this yields $G = 2\frac{e^2}{h}$. The dissipation, responsible for

| System | CNT | Metal [66] | AlGaAs [67] | InAs NW [68] |
|---|---|---|---|---|
| $n$ | $V_g$ and (n,m) dep. | $10^{28} - 10^{29}$ m$^{-3}$ | 1-5 $10^{15}$ m$^{-2}$ | $(2-10).10^{24}$ m$^{-3}$ |
| $\lambda_F$ (nm) | $\approx 0.7$ [69] | 0.5-1 | 30-80 | 10 |
| $m^*$ ($m_e$) | $\approx 0 - 0.5$ | $\approx 1$ | 0.06 | 0.02 [70] |
| $v_F$ ($m.s^{-1}$) | $8.10^5$ [57] | $1.10^6$ | $2.10^5$ | $6.10^5$ |
| $l_e$ ($\mu m$) <1K | 0.5-10 [71] | 0.02 | 10-100 | 0.01-0.1 |
| $L_\Phi$ ($\mu m$) <1K | >L | a few $\mu m$ | a few $\mu m$ | 10 |

TABLE 2.1 – Typical value of some characteristic scales in four different mesoscopic systems : in a carbon nanotube, in a metal, in a two-dimensional electron gas (where a QD can be defined with electrostatic gates) and in an InAs nanowire. The quantities are the density of carriers $n$, the Fermi wave-length $\lambda_F$, the effective mass $m^*$, the Fermi velocity $v_F$, the mean free path $l_e$ and the coherence length $L_\Phi$. Some of these quantities have been deduced one from the other from the relations $v_F = \frac{\hbar}{m^* \lambda_F}$ and $\lambda_F^{3D} = 2\pi(3n\pi^2)^{-1/3}$.

the non-zero resistance, cannot occur in the ballistic channel : it happens in the reservoir and is due to the fact that the current is carried by a lot of channels in the leads, for only one in the sample [64]. The resulting dissipation is due to what is called the contact resistance, equal to $\frac{h}{e^2}$ for one reflection-less contacts.

Note that the non-perfection of the conductor can be included in the transmission $T$, that can be afterward related to other quantities : for example, in a diffusive system, this leads to $G \approx \frac{2e^2}{h} M \frac{l_e}{L}$ [65].

Typical value of the above quantities are given in table 2.1 for carbon nanotubes and, for comparison, some materials than can be used to make quantum dot.

#### 2.1.2.2 Electronic transport in a carbon nanotube

**A ballistic coherent conductor** Typically, in this thesis, the contacts of the nanotubes are separated by $L = 0.4$ $\mu$m. For most nanotubes, metallic or semi-conductor, this is lower than the mean free path $l_e \approx 0.5 - 10$ $\mu$m, they can be considered as ballistic as well as coherent.

**One channel four-fold degenerate** In a bulk wire of section $S$, the number of channels propagating along the axis direction is of the order of $M \approx S/\lambda_F^2$. But in a nanotube, this simple picture does not work anymore, because of its specific band structure, inherited from

the Dirac cones of graphene. Indeed, around the Fermi energy there are very few levels available (see fig. 2.7) : often, provided that the tube diameter is not too large, only one energy level is accessible. But, as in graphene, this level corresponds either to a K or a K' valley : it is said to be orbitally degenerate. This orbital degeneracy is added to the spin one, giving a total of four : (K↑, K↓, K'↑ and K'↓). That is why nanotubes are generally said to sustain only one four-fold degenerate channel.

The K and K' states can be seen as two ways of propagating along the tube and correspond, in this context, to electrons moving clockwise or anti-clockwise around the nanotube (see fig. 2.7).

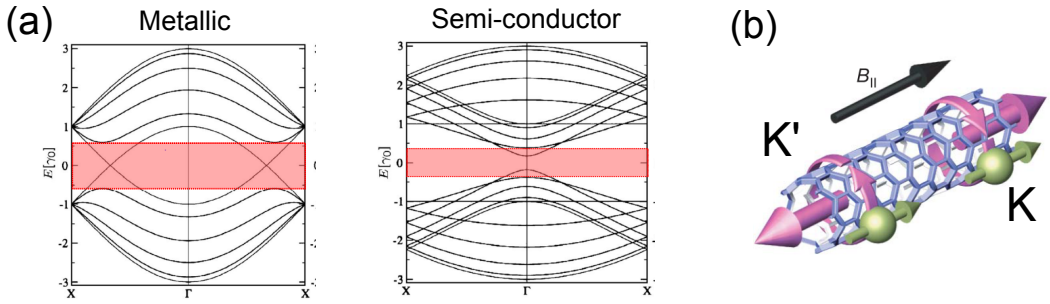


FIGURE 2.7 – (a) Examples of dispersion relations, with $\gamma_0 \approx 2.9$ meV [57]. In the red zones, there is no more than one energy level available for transport. (b) Schematic representation of the two way of propagating along the nanotube : clockwise (K') and anti-clockwise (K). Taken from [72].

If it is flawless, the maximal value of conductance in such a four-fold degenerate nanotube is $G = 4\frac{e^2}{h}$, corresponding to a minimal value of resistance of $R \approx 6.4$ kΩ .

### 2.1.3 Breaking of degeneracy and magnetic field dependence

From above, the energy states in a carbon nanotube are four-fold degenerated in the four following states : (K↑), (K↓), (K'↑) and (K'↓). We show here that, generally, this degeneracy is broken by spin-orbit interactions and/or orbital level mixing.

#### 2.1.3.1 Spin-orbit coupling in carbon nanotubes

**Basics of spin-orbit coupling in carbon nanotubes** Spin-orbit (SO) interactions refer to any coupling between the spin moment of a particle (written $-g_s\mu_B\vec{S}$) and its motion through the orbital moment $\vec{L}$.

In condensed matter, this coupling is induced by the motion of an electron in an electric field $\vec{E}$, due to relativistic effects. According to Lorentz transformation the effective magnetic field felt by an electron moving with a velocity $\vec{v}$ is $\vec{B} = -\frac{\vec{v}\times\vec{E}}{c^2}$ (that is sometimes called $\vec{B_{SO}}$). The energy associated to the spin magnetic moment is then $H_{SO} = \vec{B}.\vec{S}$ which yields, for a

radial electric field :

$$H_{SO} = \Delta_{SO}\vec{L}.\vec{S} \tag{2.3}$$

Where does this electric field comes from ? In materials made of heavy atoms, provided that there is a breaking of the inversion symmetry, $\vec{E}$ is induced by the ions of the lattices. In graphene, this atomic spin-orbit is negligible but, in carbon nanotubes, it is enhanced by the curvature, that breaks the symmetry of the surface. $\vec{S}$ represents the spin of the electron, $S_{\uparrow,\downarrow} = \pm\frac{1}{2}$, and $\vec{L}$ is the orbital moment, whose sign depends on the valley K or K' : $L_{K,K'} = \pm 1$.

Because of $H_{SO}$, the two degrees of freedom are coupled and the four degenerated states become two degenerate Kramers doublets : (K↑, K'↓) and (K↓, K'↑) (fig. 2.8) at energy $\pm\Delta_{SO}/2$. Note that the system is still invariant by the transformation (K↔K') and (↑↔↓) and therefore that spin-orbit coupling preserves time reversal symmetry.

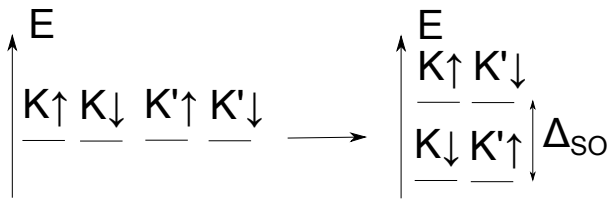


FIGURE 2.8 – Breaking of degeneracy in presence of spin-orbit coupling and formation of Kramers doublets.

**"Real life" spin-orbit coupling in CNT** Actually, spin-orbit in carbon nanotubes is substantially more complicated, and can be decomposed in two components, both induced by the curvature (see ref. [59]). At the end of the calculation, the zero-field splitting is :

$$\Delta_{SO} \approx 2(\Delta^0_{SO} \mp \Delta^1_{SO}) \tag{2.4}$$

- The first component, $\Delta^0_{SO} = -\frac{0.3\ \text{meV}}{D\ (\text{nm})}\cos(3\theta)$ [1]. This component is related to the chirality and disappears for armchair nanotubes ($\theta = \pi/6$).
- The second component is $\Delta^1_{SO} = -\frac{0.3\ \text{meV}}{D\ (\text{nm})}$. The important point is that this contribution does not depend on chirality and breaks the electron-hole symmetry.

The presence of SO coupling in carbon nanotubes has been proven experimentally, in particular by Kuemmeth *et al.* [72] and Jespersen *et al.* [13]. The latter have shown as well the gate

[1] D the tube diameter and $\theta$ an angle that depends on the chirality : $\theta(n,m) = \frac{\sqrt{3}m}{2n+1}$

dependence of $\Delta_{SO}$. Depending on samples, $\Delta_{SO}$ goes from 0.15 to 3 meV, often without any correlation with theoretical predictions (in particular, values above 1 meV are one order of magnitude larger than theoretical predictions) [59]. For the comparison, in semi-conducting nanowires $\Delta_{SO} \approx 0.3$ meV [73, 74] and reaches 100 meV in topological insulators.

#### 2.1.3.2 Orbital mixing

Spin-orbit is a "clean" way of breaking the degeneracy in carbon nanotubes, in the sense that the orbital levels K and K' are shifted and coupled to the spin, but not mixed. The breaking of the degeneracy can also be associated to a mixing of the orbital levels, which occurs for a large range of nanotubes.

Marganska *et al.* [75] have shown that nanotubes can be arranged in two classes : zigzag-like (Z) and armchair-like nanotubes (A). While Z-nanotubes are not affected by the boundary conditions , A-ones undergo orbital mixing as soon as they have a finite size. Then, the four-fold degenerated state of A-CNT becomes two energy states degenerated : (A↑, B↓) and (C↑, D↓), separated by $\Delta_{KK'}$ (A, B, C and D are combinations of orbital states K and K'). If there is, in addition, spin-orbit coupling, the levels are separated by $\delta E = \sqrt{\Delta_{KK'}^2 + \Delta_{SO}^2}$. Note that this orbital mixing can as well be induced simply by disorder in the nanotube [75].

For a given nanotube, the orbital degeneracy is thus very likely to be broken, and it is *a priori* difficult to know exactly the reason : SO, boundary conditions or disorder. To have a clearer picture, a magnetic field investigation is needed.

#### 2.1.3.3 Magnetic field dependence

At zero magnetic field, the energy levels are found at $\pm\delta E$, $\delta E$ being the energy that breaks the orbital degeneracy. When a magnetic field is applied, the two degrees of freedom of the nanotube, spin and orbital, can be affected, strongly modifying the position of the energy levels.

**Effect of a magnetic field on the spin degree of freedom** Whatever its direction, when a magnetic field is applied, the spin of the electrons tend to align along the direction of the field and the ↑ and ↓ states are split by the Zeeman energy $E_z = 2g_s\mu_B B$. $g_s$ is the Landé factor, $g_s = 2$ for electrons.

**Effect of a magnetic field on the orbital degree of freedom** Only a magnetic field parallel to the nanotube axis is able to affect the orbital degree of freedom, by changing the periodic boundary conditions due to Aharonov-Bohm effect.

Without magnetic field, the geometric boundary condition gives for the component of the

wave-vector perpendicular to the axis $k_\perp = m\frac{2\pi}{|\vec{C_h}|}$. But if a magnetic flux $\Phi$ is applied through the section of the nanotube, an electron propagating around the nanotube acquires an additional phase $2\pi\Phi/\Phi_0$, giving [57]:

$$k_\perp(\Phi) = \frac{2\pi}{|\vec{C_h}|}(m + \frac{\Phi}{\Phi_0}) = \frac{2\pi}{|\vec{C_h}|}m + \frac{|\vec{C_h}|B_{//}}{2\Phi_0} \tag{2.5}$$

The dispersion relation can then be written as a function of the magnetic field. The orbital magnetic moment is obtained from the derivative of the energy with respect to $B_{//}$, giving, for low energy electrons [59]:

$$\mu_{orb} = \pm\tau\frac{|\vec{C_h}|ev_F}{8\pi} \tag{2.6}$$

The sign of $\mu_{orb}$ depends on the valley ($\tau = \pm 1$) and is different for electrons or holes, since the sign of the Aharonov-Bohm phase depends on the direction of rotation around the nanotube and of the charge of the carrier.

If we define the orbital factor $g_{orb} = \frac{\mu_{orb}}{\mu_B}$, we get $g_{orb} \approx 1.1|\vec{C_h}|(nm)$. For nanotubes of diameter of 1-5 nm, this is much larger than $g_s = 2$ : applying a parallel magnetic field is more efficient than a perpendicular one for energy level splitting.

One could naively expect that, to observe directly interferences due to the Aharonov-Bohm effect, one needs to apply $\Phi_0$ in the surface of the nanotube, which corresponds to 1000 T for a CNT of diameter 1 nm. Actually, thanks to the chirality of the nanotubes that increases the dephasing of one orbital compared to the other, a modulation of Aharonov-Bohm oscillations has been observed at a scale of 10T by Cao *et al.* [76].

**Global magnetic field dependence** Zeeman effect is also induced by parallel magnetic field, therefore in absence of SO coupling and orbital mixing, the level are shifted by (with $s = \pm 1/2$ the spin) :

$$E(B_{//}) = (g_s s \mp g_{orb}\tau)\mu_B B_{//} \qquad E(B_\perp) = g_s s \mu_B B_\perp \tag{2.7}$$

The general case is obtained through more involved calculations and is represented on fig. 2.9 for various values of spin-orbit interactions and valley mixing. When possible, the nature of the levels (↑, ↓, K and K') is indicated, unless they are combinations of these states.

Some interesting points to note [59]:

- In presence of spin-orbit coupling, the Kramers pairs are not affected by a weak perpendicular magnetic field (2.9 (b)). This is due to the fact that the spin is locked to the valley, that is itself not affected by a perpendicular field.

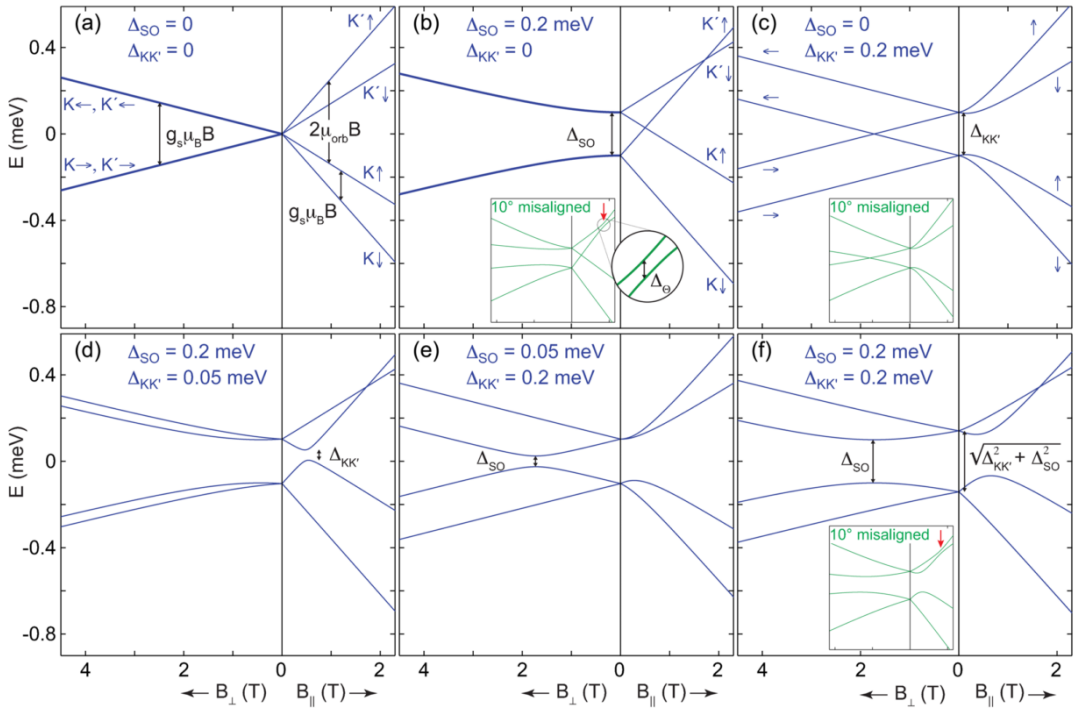


FIGURE 2.9 – Magnetic field dependence (both parallel and perpendicular) of energy levels in a carbon nanotube for various values of spin-orbit coupling $\Delta_{SO}$ and orbital mixing $\Delta_{KK'}$. The green panels represent the $\vec{B}$ dependence if the magnetic field has a misalignment of $10^o$. Taken from [59].

- If there is no spin-orbit but only orbital mixing, a weak parallel magnetic field modifies the energy levels, but for high values of $B_{//}$, the situation of $\Delta_{KK'} = \Delta_{SO} = 0$ is recovered (2.9 (c)).
- In case of both SO interactions and level mixing, crossing between levels are avoided, creating anti-crossings and giving rise to complex patterns.
- A misalignment of the magnetic field gives rise to additional anti-crossings.

From the experimental point of view, this level spectroscopy is realized by measuring the magnetic field dependence of cotunneling inelastic peak of the nanotube in Coulomb blockade regime (see part 2.2.2.2), as for example in ref. [77].

### 2.1.4 Conclusion

- Carbon nanotubes of length about 1 $\mu$m can be seen as ballistic, coherent conductors.
- Generally, only one channel can propagate in the nanotube. It is *a priori* orbitally degenerated in addition to the spin degeneracy : the maximal conductance of a carbon nanotube is $4e^2/h$.

- This orbital degeneracy can be lifted either by spin-orbit interactions, that couples the spin and the valley, or by boundary conditions and defects, that induce valley mixing.
- The magnetic field dependence of the energy levels gives insights into the nature of these levels.

## 2.2 Carbon nanotubes quantum dots and Coulomb blockade regime

Investigating electronic transport in carbon nanotubes requires contacting them with metallic electrodes. In this section, we show that the transport regime is dramatically affected by the quality of these contacts.

### 2.2.1 Contact transparency and transport regime

As developed in section 2.1.2.2, the maximum conductance of a carbon nanotube is $4\frac{e^2}{h}$ (or a minimum resistance of 6.5 k$\Omega$) since only one four-fold degenerated channel can propagate. But generally, the transmission of the contacted system is lower than 1, for mainly two reasons : disorder, that reduces the transmission of the nanotube itself, and bad contact resistances that reduce the coupling of the nanotube with the reservoirs.

The disorder in nanotubes is difficult to control and, in general, is not the main cause of transmission lowering. We focus here on the contact resistance.

#### 2.2.1.1 What does define the contact resistance of a nanotube ?

Making theory about contacts between a metal and a carbon nanotube is not easy, since the transparency strongly depends both on the metal chosen and of the nanotube, whose properties vary strongly from one nanotube to the other and are not easy to control.

When a nanotube is contacted to metallic electrodes, their Fermi levels may not coincide, leading to the bending of the energy bands in the nanotube (see fig. 2.10) and to the formation of Schottky barriers at the interface (that depends also on nature of the chemical bounds). This phenomenon is more important in semi-conductor nanotubes, where the Fermi level is in the gap, and can be complicated by interface states forming inside the semi-conducting gap.

A rigorous description of Schottky barriers is beyond the scope of this thesis, the important point is that this kind of barrier can considerably modify the transparency of the contacts, depending on the position of the Fermi energy. In particular, tuning the Fermi level of the nanotube with an electrostatic gate voltage [2], one can drastically modify the transparency of the contacts (see for example fig. 2.10, from ref. [78]), it is therefore possible to access different regimes in the same sample.

Experimentally, palladium or rhenium contacts provide good transparency, while aluminum gives very high contact resistances. Titanium is able to make good contacts as well, but is more dependent on the surface preparation (heating). The quality of palladium contacts comes

[2] The electrostatic gate and the nanotube form a capacitor. If $V_g < 0$, one adds holes to the system, if $V_g > 0$, one adds electrons. This constitute a very convenient way of doping the CNT.

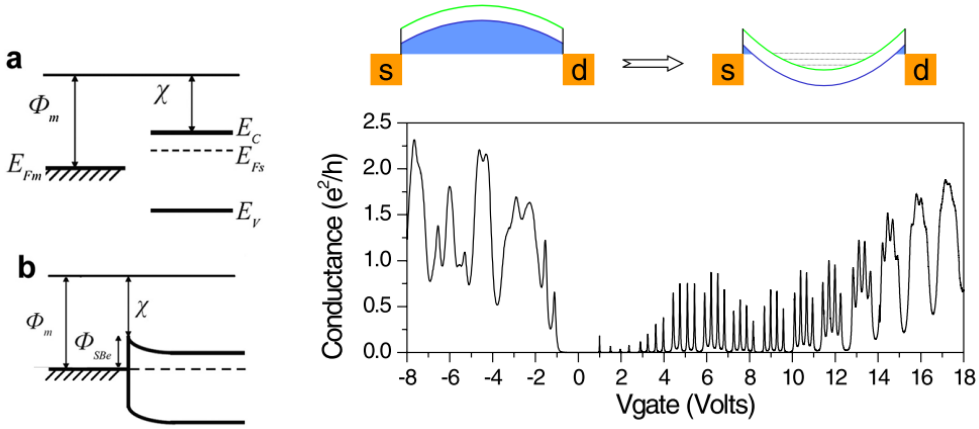


FIGURE 2.10 – Left : (a) Energy band structure before contact between a metal and a semiconductor, and (b) after. Taken from ref. [79]. Right : Schema of the band structure of a semi-conducting carbon nanotube for both negative and positive gate voltage (corresponding respectively to p and n-doping). The resulting conductance is plotted as a function of the gate voltage. From [78].

from its high work function, that accommodates well with the one of nanotubes [80, 81]. In addition, it seems that Pd has good wetting properties concerning nanotubes, increasing the contact surface and thus the transmission. For all these reasons, that is the kind of contacts we used in this thesis.

We now review the various regimes that can be found in a carbon nanotube.

#### 2.2.1.2 Good transparency (strong coupling regime) : Fabry-Pérot regime

If the reservoirs are very well coupled to the nanotube (T=1), the conductance has the maximum value $4\frac{e^2}{h}$ for any gate voltage $V_g$.

If the nanotube is very well coupled but not perfectly, an electron arriving on a barrier can be either transmitted or reflected (see fig. 2.11). For a ballistic and coherent nanotube ($L < l_e, L_\Phi$), the situation is perfectly similar to an optical Fabry-Pérot cavity. Thus, some electrons stay in the nanotube, acquiring a phase $\delta = \frac{2\pi}{\lambda_F}L$ at each round-trip in the cavity, before being finally transmitted. Thanks to the phase coherence of the nanotube, the global transmission of the system {contacts+nanotube} (and thus its conductance) results from the interference of these electrons.

The computation of the conductance is exactly the same as the transmission of an optical Fabry-Pérot cavity : the conductance oscillates when the wavelength (or the length of the nanotube) is changed. In a nanotube, $\lambda_F$ is varied by changing the gate voltage, that modifies $E_F$. A measurement of the conductance of a nanotube in this conduction regime is shown on fig. 2.11 bottom (taken from [82]) : indeed, the conductance oscillates with the gate voltage.

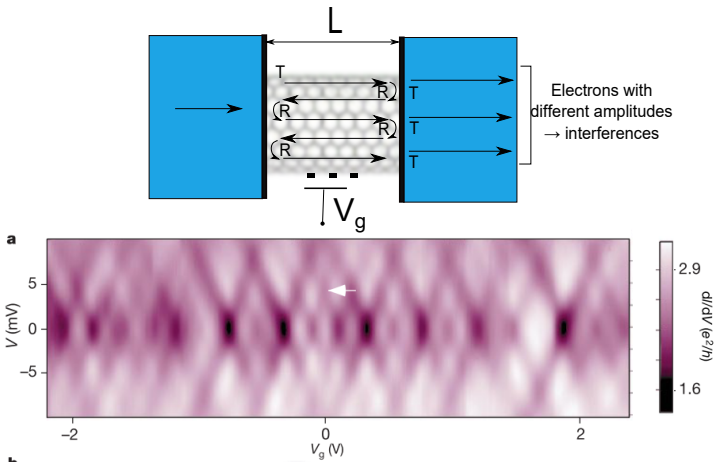


FIGURE 2.11 – Fabry-Pérot regime in a carbon nanotube. Top : schematics of Fabry-Pérot oscillations occuring in a carbon nanotube. Bottom : conductance on the Fabry-Pérot regime as a function of gate and bias voltage. From [82].

This Fabry-Pérot regime has been investigated specifically by several groups [82, 83, 84]. Actually, it is very commonly observed in CNT for large gate voltage (see for example fig. 2.10 right : Fabry-Pérot behavior is observed for $V_g < 0$ and $V_g > 15V$). Note that, if the two barriers are symmetric, the maximum conductance should reach $4\frac{e^2}{h}$. Otherwise, it means that the two contacts do not have the same transparency.

#### 2.2.1.3 Low transparency : quantum dot and Coulomb blockade regime

For low transparency contacts (*i.e.* in the weak coupling regime), because of Coulomb interactions, the conductance in a carbon nanotube has a completely different behavior.

The first consequence of a weak coupling is the confinement of the system : the energy is quantized in all directions, giving single particle energy levels separated by $\Delta E = \frac{hv_F}{2L}$. The carbon nanotube is now a quantum dot, the name dot referring to the 0 dimensionality of the system. We call C the capacitance of the CNT and $U = \frac{e^2}{C}$ the charging energy, energy needed to overcome Coulomb interaction to add a single electron on the dot.

If the contact resistance $R$ is of the order of the resistance quantum ($R \gg \frac{h}{e^2} \approx 25k\Omega$), one shows that the nanotube is isolated enough so that electrons are localized either in the dot or in the reservoirs [30]: the number of electrons N on the nanotube is well defined. In addition, if the temperature is low compared to the charging energy ($k_BT \ll U$), thermal fluctuations are not large enough to modify N. The quantum dot is then in the so-called Coulomb blockade regime, which corresponds on fig. 2.10 to $0 > Vg < 15V$. In this transport regime, for a given configuration of gate voltage at zero bias ($V_{sd} = 0$), the number of electrons on the dot is fixed, which prevents any current flow except on the charge degeneracy points.

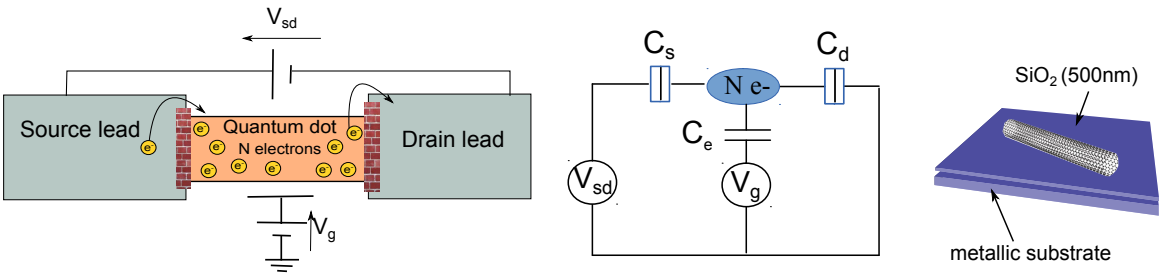


FIGURE 2.12 – Schematic representation of a quantum dot and its modelization in terms of capacitances. Right : approximation used for estimating the charging energy : the total capacitance is approximated by the capacitance between the metallic substrate (in our experiments, doped silicon, that can be used as a backgate) and the nanotube, separated by a layer of $SiO_2$.

Before describing in details these Coulomb peaks, a few words about numerical values for the charging energy. $U$ depends only on the capacitive coupling of the quantum dot (here the CNT) with its environment, namely the substrate on which it lies, the gate and the reservoirs (see fig. 2.12). As a first estimate, $C$ is the capacitance between a tube (with a known length and diameter) and a substrate (see fig. 2.12 right). It can be expressed as [57]:

$$C = \frac{2\pi\epsilon_r\epsilon_0 L}{\ln(2z/r_{tube})} \tag{2.8}$$

$L$ is the length of the CNT, $r_{tube}$ its diameter and $z$ the distance between the nanotube and the metallic substrate. This capacitance is of the order of $1.10^{-17}$ F for $L = 400$ nm, $r_{tube} = 0.5$ nm, $z = 500$ nm and $\epsilon_r = 2$ (average between SiO2 and air), giving $U \approx 6$ meV [57]. The charging energy is mainly determined by the size of the sample : the smaller it is, the larger is $U$.

### 2.2.2 Electron transport in a CNT quantum dot

#### 2.2.2.1 Coulomb oscillations and diamonds

**Coulomb peak position** To determine the number $N$ of electrons energetically favorable on the quantum dot, we have to write its energy as a function of $V_{sd}$ and $V_g$ (see fig. 2.12). It is equal to the total charge of the dot $Q$ added to the electronic energies of the N electrons [3]. $Q$ can be expressed as a function of $V_{sd}$, $V_g$ and of the capacitances $C_s$, $C_d$ and $C_g$ between the nanotube and respectively the source, the drain and the gate, giving :

$$E(N) = \frac{Q^2}{2C} + \sum_n E(n) = \frac{(e(N-N_0) - (C_gV_g + (C_s - C_d)V_{sd}/2))^2}{2C} + \sum_n E(n) \tag{2.9}$$

[3] $N_0$ represents the number of electrons at $V_g = 0$ and the bias voltage is assumed to be symmetrically applied on both contacts ($V_s = -V_d = V_{sd}/2$).

The difference of energy between the $N^{th}$ and the $(N-1)^{th}$ electronic occupancies is thus [67]:

$$\mu(N) = E(N) - E(N-1) = U\left((N-N_0) - \frac{1}{2}\right) - e\frac{C_g V_g + (C_s - C_d)V_{sd}/2}{C} + E_N \quad (2.10)$$

While $\mu(N) > k_B T$, the number of electron is determined by $V_{sd}$ and $V_g$ and no current can flow except when $\mu(N) = 0$, corresponding to the degeneracy points, where both N and N-1 electrons occupancies are allowed, giving rise to a non-zero current.

At $V_{sd} = 0$, these current peaks, also called Coulomb peaks, appear for gate voltages :

$$V_g(N)/\alpha = E_N + U\left((N-N_0) - \frac{1}{2}\right) \quad (2.11)$$

$\alpha = \frac{C_g}{eC}$ is the lever arm between the gate voltage applied and the shift in energy it induces. Coulomb peaks are therefore separated by $\Delta V_g(N) = \alpha E_{add}(N)$, where $E_{add}(N) = U + \Delta E_N$ is the energy needed to add the $N^{th}$ electron on the QD ($\Delta E_N$ being the spacing between the energy level where is the $(N-1)^{th}$ electron and the one where is the $N^{th}$).

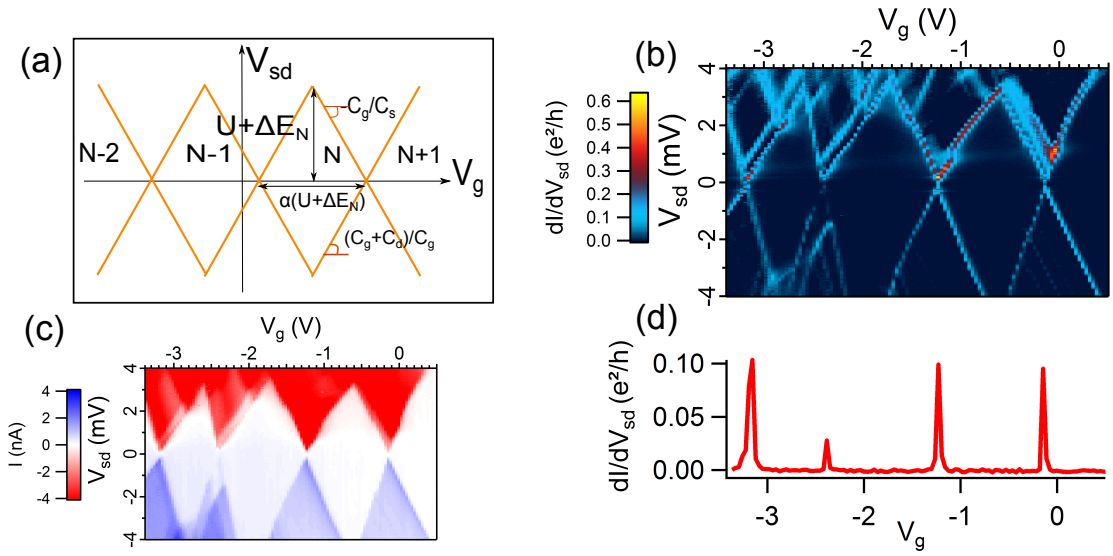


FIGURE 2.13 – (a) Typical simplified conductance map of a quantum dot (also called stability diagram). The orange lines correspond to non-zero conductance. (b) Example of the corresponding measurement of differential conductance in a carbon nanotube quantum dot contacted by 7 nm of Ti covered by 70 nm of Al, giving very high contact resistance. The lines outside from the diamonds are due to tunneling through excited states [85]. Panel (d) is an horizontal cut of (b) at zero bias, showing Coulomb peaks. (c) represents the DC current in the CNT.

Taking into account the bias voltage, that can also modify the number of electrons, one obtains the typical conductance map as a function of $V_g$ and $V_{sd}$, represented on fig. 2.13 (a). The map exhibits zero-conductance diamonds where $N$ is fixed, called Coulomb diamonds. The

width of the $N^{th}$ diamond, corresponding to an occupancy by N electrons, is $\alpha E_{add}$ and its height is $E_{add}$. Such Coulomb diamonds, measured in a CNT QD, are represented on fig. 2.13 (b-d).

From this, we can see a QD as what is represented on fig. 2.14 : a system whose states have typically a width $\Gamma$ and are separated by the charging energy $U$ added, if necessary, to the electronic level spacing $\Delta E$. These states can be shifted by the gate voltage $V_g = \alpha\epsilon_d$. The QD is coupled to the two reservoirs (typically left (L) and right (R)) with the respective coupling energy $\Gamma_L$ and $\Gamma_R$.

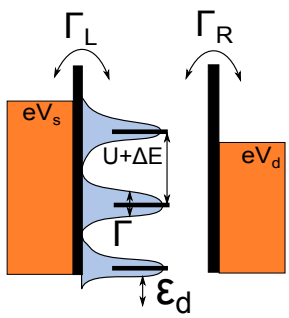


FIGURE 2.14 – Schema of a quantum dot, where the relevant quantities are represented : the charging energy $U$, the couplings with the left and right reservoirs $\Gamma_L$ and $\Gamma_R$, the total coupling $\Gamma = \Gamma_L + \Gamma_R$, $\Delta E$ the energy level spacing and $\epsilon_d$ the position of the energy levels in the dot.

**Coulomb peaks' shape** Now that we have found the position of the Coulomb peaks, we are going to detail their structure (height, shape and width) in the different regimes of temperature [67].

In the regime $\Delta E \ll k_B T \ll U$, where the temperature is large compared to the energy level spacing (but still in Coulomb blockade regime), the peak's width is linear in temperature and the maximal conductance is $G_{max} = G_\infty/2$, $G_\infty$ being the conductance at high temperature[4]. This case does not really concern CNT quantum dots, where $\Delta E$ is of the order of $U$.

In the quantum regime $k_B T \ll \Delta E \ll U$, where the energy is quantized, we have to distinguish two cases depending on the value of the coupling :

- In the low coupling regime $\Gamma \ll k_B T$, the peak's width is also linear in temperature, but the maximum depends as well on T as $G_{max} = \frac{\Delta E G_\infty}{4 k_B T}$. This is larger than the high temperature value $G_\infty$ but still smaller than $2e^2/h$. In this thesis, samples are measured at 50 mK $\leftrightarrow$ 4 $\mu$eV, and $\Gamma$ will be often larger than 100 $\mu$eV. We are very unlikely to be in this case.

[4]This kind of system can be used as a primary thermometer.

- In the intermediate coupling regime $\Gamma \gg k_B T$, the Coulomb peaks have a lorentzian shape of width linear in $\Gamma$, given by the Breit-Wigner formula [86, 67]:

$$G = \frac{2e^2}{h} \frac{4\Gamma_L \Gamma_R}{(\Gamma_L + \Gamma_R)^2} \frac{\Gamma^2}{\Gamma^2 + (\frac{2(V_g - V_g^{peak})}{\alpha})^2} \tag{2.12}$$

  The value of the maximum conductance depends strictly on the contact asymmetry $\Gamma_L/\Gamma_R$, reaching $2e^2/h$ in the symmetric case. Note that the bias dependence of the conductance has the same expression as the gate voltage one.

#### 2.2.2.2 Beyond Coulomb blockade : cotunneling processes

In the above description of Coulomb blockade, we only considered first order tunneling processes, that allow current flow only at charge degeneracy points. Any transfer of electron through the dot out of these points, that is to say without changing the occupancy, requires higher order processes. Since they involve at least two electrons that have to tunnel coherently, they are called cotunneling processes. Such kind of processes are illustrated on fig. 2.15.

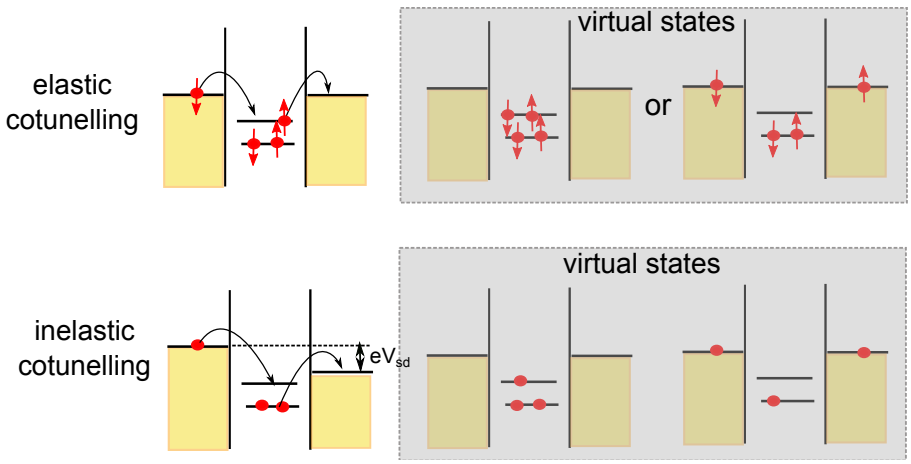


FIGURE 2.15 – Example of cotunneling processes in a quantum dot. There are of two types : eleastic and inelastic. Unlike an elastic process, an inelastic process leaves the dot in an excited state. During a short time (short compared to $\frac{\hbar}{U}$), the system lies in a virtual state with a forbidden number of electrons.

There are mainly two types of cotunneling processes : elastic and inelastic [85, 38]. Elastic processes are those which don't change the state of the dot (fig. 2.15 top). They are possible even at $V_{sd} = 0$ (since they don't change the energy of the system) and are thus dominant at low bias. Inelastic processes leave the dot in an excited state, creating an electron/hole pair (fig. 2.15 bottom), which is only possible if a bias large enough is applied across the dot (typically $|V_{sd}| > \delta E$).

To perform these processes, the system has to transit through virtual states, in which there is

a forbidden number of electron in the dot (represented on fig. 2.15). This is more likely to happen if the typical time spend in the dot $\frac{h}{\Gamma}$ is of the order of the time scale associated to the charging energy $\frac{h}{U}$, *i.e.* if $\Gamma \approx U$. Another way to understand it, in the representation of fig. 2.14, is to say that if $\Gamma \approx U$, the Coulomb peaks are broaden so that they spread all over the diamonds, allowing the current to flow [87].

The most spectacular consequence of entering this intermediate coupling regime $\Gamma <\approx U$ is the appearance of the Kondo effect, made possible by cotunneling processes. If $\Gamma$ keeps increasing, the system enters a mixed-valence regime [78, 88], that evolves toward Fabry-Pérot regime .

The Kondo effect is presented in chapter 1 in the general context of condensed matter. In the following it will be presented in the specific case of carbon nanotube QD. But before that, we discuss the consequences of the orbital degeneracy of CNT on the Coulomb blockade.

#### 2.2.2.3 Carbon nanotube : a two-level quantum dot

CNT quantum dots provide a succession of energy levels that is very specific compared to other quantum dots. The first specificity of nanotubes is the value of level spacing $\Delta E \approx \frac{hv_F}{2L}$, that is of the order of 4 meV for $L = 400$ nm, just as the charging energy $U$. It means that for a given gate voltage, only one of these level participate to transport. As a comparison, in semi-conductor quantum dots formed with gates (which are 2D QD), $\Delta E$ is of the order of $0.03 - 0.1$meV for a charging energy around 1 meV and a coupling $\Gamma \approx 0.1 - 0.5$meV [67, 43]. The second specificity is that each of these energy levels (that we will call 'shell') is four-fold degenerate, unless its orbital degeneracy is broken by the energy $\delta E$ (see section 2.1.3.2). This gives, in each shell, two two-fold quasi-degenerate levels.

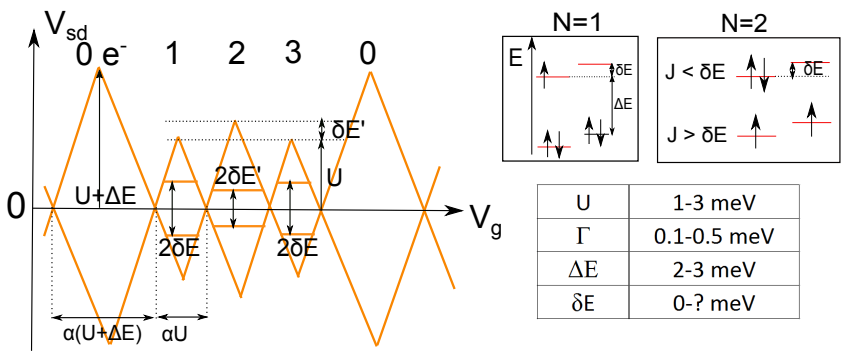


FIGURE 2.16 – Typical Coulomb diamonds of a carbon nanotube such as the one we measured. U is the charging energy, $\Delta E$ the level spacing and $\delta E$ the breaking of degeneracy such as defined in section 2.1.3.2. For N=2 occupancy, the distribution of the two electrons in the two levels depends on relative values of the exchange coupling J, that tends to maximize the spin, and the breaking of degeneracy $\delta E$.

This (quasi-)four fold degeneracy has a very clear signature on the stability diagram of the

nanotube. As stated in sec. 2.2.2.1, the height of Coulomb diamonds is equal to the addition energy $E_{add} = U + \Delta E_N$. Let's see what happens when we fill a quasi-four-fold-degenerate state, initially empty, with electrons (summarized on fig. 2.16) :

- Starting from the empty level (N=0), to add the first electron, one has to provide an energy $E_{add} = U + \Delta E$. The diamond has a size $U + \Delta E$.
- The second electron is added in the same level as the first one, thanks to the spin degeneracy. The addition energy is just $E_{add} = U$, the N=1 diamond has a height $U$.
- The addition of a third electron requires an energy $E_{add} = U + \delta E'$ to start the filling of a new level. But generally $\delta E'$ (that can be different from $\delta E$, see below and figure) remains small compared to $\Delta E$ and $U$, the $N = 2$ diamond is small compared to the $N = 0$ one.
- Finally, thanks to the spin degeneracy, the fourth electron is added for $E_{add} = U$. the $N = 3$ diamond has the same size as the $N = 1$ one.

As a summary, CNT stability diagrams present generally a periodic pattern composed by one big diamond followed by three small ones. If the degeneracy is broken, the N=2 diamond is slightly larger than the N=1 and 3 (see fig. 2.16).

In addition, if $\delta E < U$ as it is often the case in clean carbon nanotubes, the two levels are likely to participate to transport at the scale of one diamond. This is another characteristic feature of the two-level quantum dot : the presence of inelastic cotunneling current peaks for N=1 and 3 occupancies at $eV_{sd} = \pm\delta E$ (see ref. [85]).

Note that the two nearly degenerate states can be differently coupled to the reservoirs. This can be seen in the stability diagram, where the inelastic cotunneling peaks are tilted (see part 2.3.2.2 below).

**N=2 case : exchange coupling** Cotunneling peaks are also present for N=2, but their position depends strongly on the exchange coupling $J$ that favors spin alignment [89]. Depending on the relative importance of $J$ compared to $\delta E$, a triplet state ($J > \delta E$) or a singlet state ($J < \delta E$) is favored. In general, the cotunneling peaks are thus located at $V_{sd} = \pm\delta E' = |\delta E - J|$ [89]. A magnetic field can, of course, modify the situation.

We emphasize that, thanks to the orbital degeneracy, carbon nanotube are unique system for investigating two-level quantum dots. Of course, it is also possible to design two-level quantum dot using gate electrodes [90], but this is another story.

### 2.2.3 Conclusion

- The electronic transport in a carbon nanotube depends dramatically on the transmission of its contacts with the reservoirs, *i.e.* of the coupling nanotube/reservoirs. This coupling depends on the material used as electrodes and can be varied with a gate voltage.
- For low coupling, the carbon nanotube behaves as a quantum dot in the Coulomb blockade regime (at low temperature). Because of its orbital degeneracy, a quantum dot made of a carbon nanotube is a very special QD since it has, *a priori*, two (and only two) spin degenerated levels available for transport.
- For intermediate coupling regimes, cotunneling processes allow some current to flow in the coulomb blockade regime (inside the diamond) conserving the electronic occupancy in the quantum dot.

## 2.3 Kondo effects in carbon nanotube quantum dots

A carbon nanotube can *a priori* not be considered as a single-level quantum dot, that allows spin-1/2 Kondo effect (with a SU(2) symmetry), because of its orbital degeneracy. Nevertheless, since this degeneracy is generally broken with an energy splitting equal to $\delta E$, several situations are possible, that are represented on fig 2.17. The case $\delta E \gg U, \Gamma$ corresponds to the single-

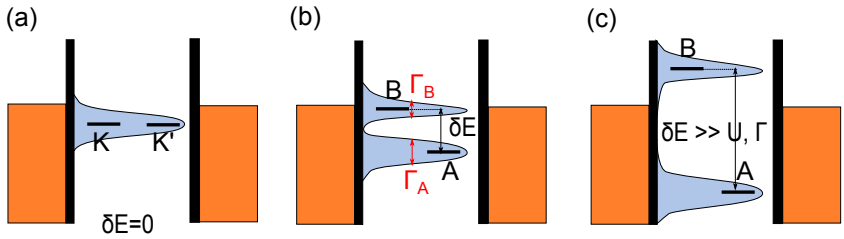


FIGURE 2.17 – Various configurations of the energy levels in a carbon nanotube quantum dot, depending on the level splitting $\delta E$.

level quantum dot (fig. 2.17 (c)), leading to standard spin-1/2 Kondo effect, and will be detailed first. Then we will address the other limit $\delta E = 0$ (or $\delta E < U, \Gamma$, fig. 2.17 (a)), where both orbital and spin degrees of freedom are degenerated, leading to Kondo SU(4). Finally, we will speak about the intermediate regime $\delta E < U$ and $\delta E > \Gamma$ (fig. 2.17 (b)), where various Kondo effects are expected, depending mainly on $\delta E$, $T_K$ and the magnetic field.

### 2.3.1 SU(2) spin Kondo effect

#### 2.3.1.1 Kondo-enhanced conductance in odd Coulomb diamonds.

We have seen that a quantum dot is a system in which one can confine electrons and control their number using an electrostatic gate. When this number of electrons is odd, there is one unpaired electron with a non-zero magnetic moment, that is localized on the QD. In this section, we assume that the breaking of the orbital degeneracy of the nanotube is large enough compared to the charging energy $U$ and the coupling $\Gamma$ so that only one level participate at a time to transport. The situation is therefore very well described by the Anderson single-impurity model (see chapter 1 section 1.2).

As emphasized in chapter 1, any oddly occupied Coulomb diamond is similar to a spin degenerate quantum impurity in a metal, likely to give rise to Kondo effect. In a quantum dot, the interaction between the reservoirs and the impurity is mediated by the elastic cotunneling processes described in section 2.2.2.2 ; the formation of the Kondo singlet is allowed by the virtual states in which the dot is either doubly occupied or empty (*i.e.* with zero effective magnetic moment). Note that the Kondo effect, creating a strongly correlated state between the dot and both reservoirs, enhances considerably these cotunneling processes, opening a well transmitted channel.

The Kondo effect is possible only if the temperature is smaller than the Kondo temperature $T_K$, whose expression is recalled (see sec. 1.2.2) :

$$k_B T_K = \sqrt{\frac{U\Gamma}{2}} e^{\frac{\pi}{2}\epsilon_d(\epsilon_d+U)/(U\Gamma)} \tag{2.13}$$

The larger is the coupling $\Gamma$, the larger is $T_K$ : at a given temperature, Kondo effect will be favored by strong coupling $\Gamma$ and we have again this idea that cotunneling processes are not possible is $\Gamma$ is too small compared to $U$. Typically, in carbon nanotube quantum dot, the Kondo temperature reaches 1.5-2K [89, 23, 91], values similar to the one obtained in InAs nanowires [45, 92]. In GaAs 2D electron gas, the $T_K$ are typically smaller, less than 1K [43, 93] [5]. Note that, on the diamonds of fig. 2.13 measured on a nanotube, there is no Kondo ridge : the coupling $\Gamma$ is probably very low, leading to a $T_K$ too low to be measured.

**Kondo resonance** The Kondo-enhancement of cotunneling gives rise to a conductance peak at zero bias that spreads all over the width of the Coulomb diamond. A characteristic stability diagram of a carbon nanotube in Kondo SU(2) regime is shown on fig. 2.18 (c) : we can see the succession of one big and three small diamonds, with Kondo ridges (bright horizontal lines at $V_{sd} = 0$) in the N=1 and N=3 diamonds.

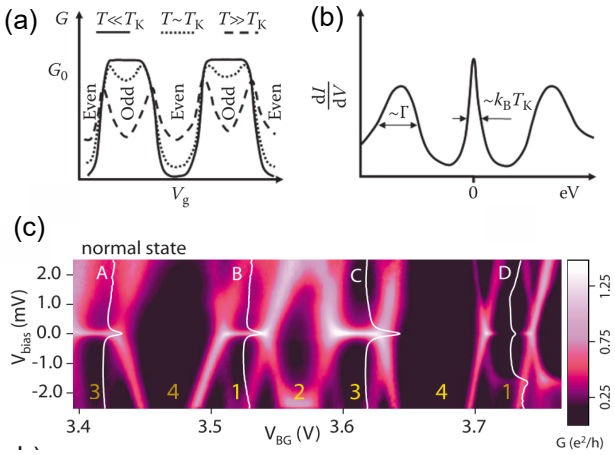


FIGURE 2.18 – (a) (b) Taken from [29]. Typical conductance measured in the Kondo regime at zero bias as a function of $V_g$ (a) and (b) at a given $V_g$ as a function of bias voltage. (c) Typical stability diagram of a carbon nanotube in the Kondo regime, such that $\delta E > U, \Gamma$. From [94].

This zero-bias anomaly is directly related to the Kondo resonance in the density of state since it is roughly proportional to the spectral density, if we neglect decoherence that can modify the shape of the conductance resonance [47]. An estimation of the Kondo temperature is then given by its half width at half maximum (HWHM).

[5] Note that the Kondo temperature can be very different from one experiment to the other, since it will depend at least on the size of the QD, the quality of the contacts, the gate voltage.

The height of the conductance peak gives also very interesting informations since it is equal, *at zero temperature and at half filling* ($\epsilon_d = -U/2$, electron-hole symmetry), to [38, 27, 29]:

$$G_0 = \frac{2e^2}{h} \frac{4\Gamma_L \Gamma_R}{(\Gamma_L + \Gamma_R)^2} \sum_n \frac{\sin^2 \delta_n}{2} \tag{2.14}$$

where $\delta_n$ is the scattering phase shift of each channel participating to transport (including spin channels), already defined in chapter 1 section 1.2.3. According to the Friedel sum rule, $\delta_n = \pi N_n$ with $N_n$ the average occupation of the state $n$.

In the case of spin-1/2 SU(2) Kondo effect, $N_\uparrow = N_\downarrow = 1/2$ [6] :

$$G_0 = \frac{2e^2}{h} \frac{4\Gamma_L \Gamma_R}{(\Gamma_L + \Gamma_R)^2} \tag{2.15}$$

The maximum conductance for a spin-1/2 Kondo peak is $2e^2/h$, reached for symmetric contacts independently of the coupling $\Gamma$ itself (provided that $T < T_K$). $\sin^2 \delta_n/2$ can also be seen as the transmission of the canal n : spin-1/2 Kondo effect with symmetric contacts leads to the opening of one spin degenerate perfectly transmitted channel.

Let's see now how this maximum is affected by the temperature.

#### 2.3.1.2 Temperature dependence

Exciting electrons around the Fermi energy, a finite temperature of the order of $T_K$ prevents electrons from participating to the Kondo singlet, and thus alters the Kondo resonance. This manifests as a reduction of the conductance, as represented on fig. 2.19 (b) and (c).

The temperature dependence of the conductance can be described by the phenomenological expression

$$\frac{dI}{dV}(T) = \frac{G_0}{(1 + (2^{1/s} - 1)(\frac{T}{T_K})^2)^s} \tag{2.16}$$

and NRG calculations have shown that spin-1/2 Kondo effect was best represented by $s = 0.22$ [33, 92]. Fitting the conductance at zero-bias as a function of temperature (*e.g.* fig. 2.19 (d)) is an equilibrium measurement, it is thus a reliable way of determining $T_K$, more trustful than its extraction from the width of the Kondo resonance [7].

[6] This formula will be very useful in the following to determine the conductance expected for more exotic Kondo effect

[7] Indeed, its shape can be modified by out-of-equilibrium decoherence (especially for symmetric couplings) and by conductance background (see fig. 2.19 (c)).

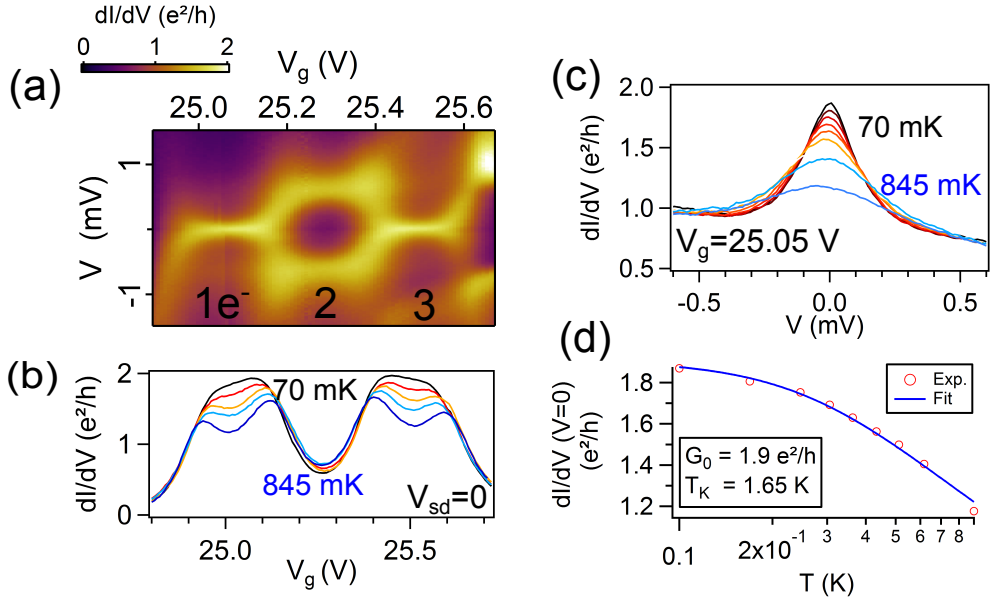


FIGURE 2.19 – Temperature dependence of a spin-1/2 Kondo resonance in a carbon nanotube quantum dot contacted with Pd contacts. (a) Stability diagram (differential conductance as a function of V and $V_g$) of the nanotube, exhibiting Kondo ridges for occupancies 1 and 3 (number of electrons in the last occupied shell). For N=2, inelastic cotunneling peaks are visible. (b) Conductance at zero bias as a function of $V_g$ for various temperatures from 70 mK to 0.85 K. At the lowest temperature, the conductance almost reaches the maximum value of $2e^2/h$, meaning that the contacts are almost symmetric. (c) Temperature dependence of the Kondo peak at the center of the N=1 diamond. (d) Fit of the conductance to extract the Kondo temperature (see text). Higher temperatures are difficult to access in our dilution fridge.

#### 2.3.1.3 Magnetic field dependence

The application of a magnetic field B has two consequences on the Kondo resonance. First, since the Kondo resonance is related to the formation of a Kondo singlet, it is naturally strongly affected by a magnetic field : the height of the resonance decreases. Then, the Zeeman field splits the QD's level into two levels located at $V = \pm 2\mu_B B$, corresponding to spin $\uparrow$ and spin $\downarrow$ [95, 96]. As B increases, the Kondo resonance is changed into two inelastic cotunneling peaks, that are still Kondo enhanced (but, at the same time, weakened by the magnetic field). An example of such a magnetic field evolution is shown on fig. 2.20 .

The magnetic field dependence, that is quite simple in the spin 1/2 Kondo effect, becomes more complicated and richer if we consider the orbital levels described in section 2.1.3.

#### 2.3.1.4 Asymmetry N=1/N=3

On fig. 2.19, the Kondo effect in the N=1 and 3 diamonds are very similar, meaning that both orbital levels, despite the breaking of degeneracy, are similarly coupled to the leads. But *a*

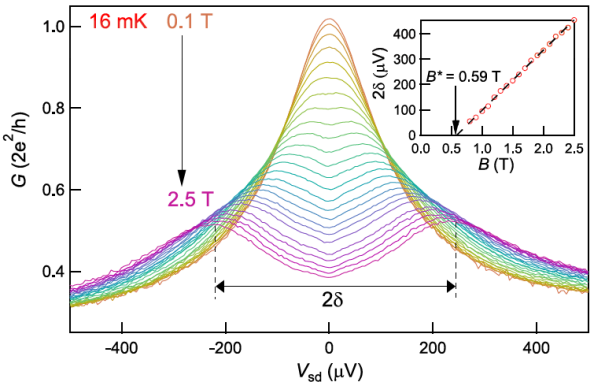


FIGURE 2.20 – Magnetic field dependence of a spin-1/2 Kondo resonance from 0.1 to 2.5 T : for low field, only the height of the resonance is affected while, for higher fields, two peaks are present. Taken from [97].

*priori*, the levels called A and B on fig. 2.21 have different couplings to the reservoirs $\Gamma_A$ and $\Gamma_B$. As shown by Holm *et al.*, this manifests in the stability diagram as a tilt of the inelastic cotunneling peaks, with a slope proportional to $\frac{d\delta E}{d\epsilon_d} = -(\Gamma_A - \Gamma_B)/(\pi U)$ [98], as it can be clearly seen on fig. 2.21 right for the two lowest panels.

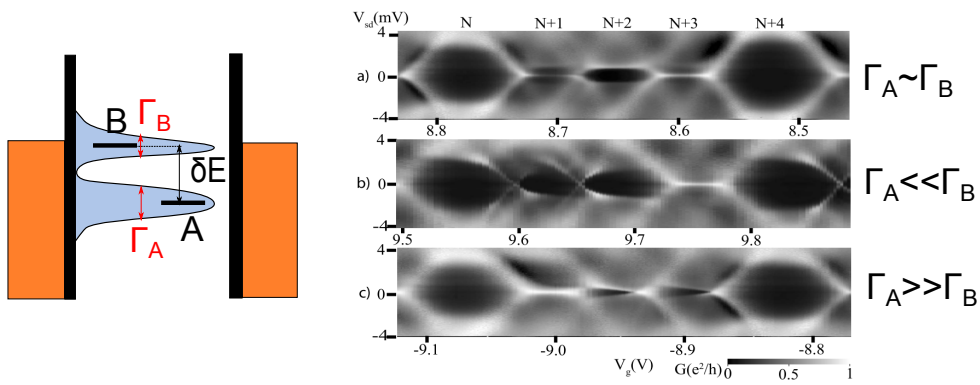


FIGURE 2.21 – Left : schematic representation of the energy levels A and B in the dot, separated by the energy $\delta E$, and coupled to the reservoirs respectively by $\Gamma_A$ and $\Gamma_B$. Right : Stability diagram measured in a carbon nanotube by Holm *et al.* [98] for three different shells. The first one, $\Gamma_A \approx \Gamma_B$, exhibits Kondo effects for both N=1 and N=3, the cotunneling peaks does not depend on the gate voltage. For the second one, the tilting of the cotunneling peaks show that $\Gamma_A \ll \Gamma_B$. Indeed, for N=1 (involving the level A), there is no Kondo effect while there is for N=3 (involving level B). In the third shell, the tilting of cotunneling peaks is inversed, as well as the observation of the Kondo effect.

Because of this asymmetry, the Kondo temperature can be different for $N = 1$ and $N = 3$ fillings of the dot such that Kondo effect can be observed in one oddly occupied diamond of the shell and not in the other (fig. 2.21 right, for $\Gamma_A \ll \Gamma_B$ (Kondo at $N = 3$ and not at $N = 1$) and $\Gamma_A \gg \Gamma_B$ (Kondo at $N = 1$ and not at $N = 3$)).

### 2.3.2 Two-level Kondo effects

We are now considering a CNT QD in which the orbital degeneracy is only slightly broken, corresponding to the panels (a) and (b) of fig. 2.17. We start by the case $\delta E = 0$

#### 2.3.2.1 SU(4) Kondo effect

SU(4) Kondo effect[8] is an effect observed when a localized impurity, of quantum degeneracy four, interacts with delocalized electron. It results as well in the screening of the degrees of freedom involved.

This SU(4) symmetry is possible *a priori* in a carbon nanotube quantum dot, if the energy levels are four-fold degenerate ($\delta E \ll \Gamma$). The other crucial condition for the correlated state to form is the conservation of all the degrees of freedom during the tunneling from the dot to the reservoirs[99]. This is naturally the case for the spin, but not for the orbital degree of freedom, that is not defined *a priori* in a metallic electrode. There are two hypothesis to explain why this is possible for carbon nanotubes : the first one is that the tail of the nanotube that is covered by the metal plays the role of a reservoir, where speaking about orbital degree of freedom is relevant [99]. In the other hypothesis, because of band-bending, the quantum dot is formed within the nanotube such that the leads are formed by the CNT itself [100].

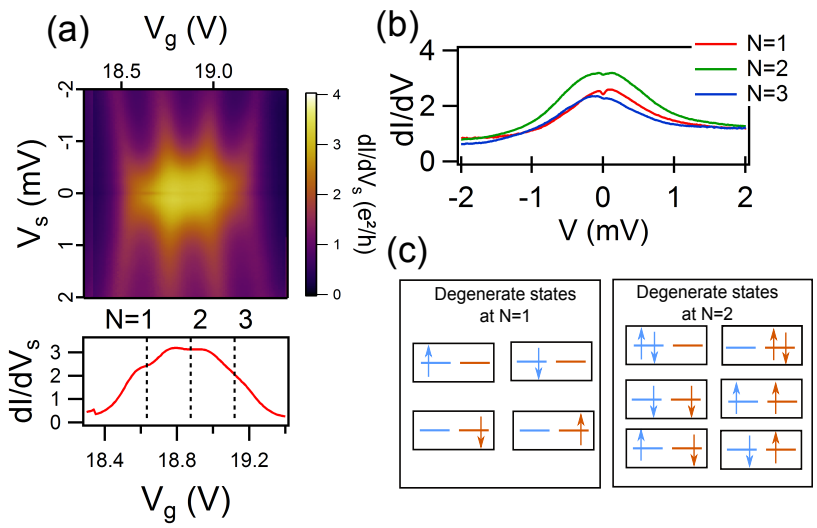


FIGURE 2.22 – Differential conductance in the Kondo SU(4) regime, measured on the same nanotube than fig 2.19 but at higher gate voltage. On the color plots, we can see that the Kondo resonance spreads all over the three diamonds N=1, 2 and 3. Below is represented a horizontal cut at $V_s = 0$, showing that the conductance goes up to 3.1 $e^2/h$ at N=2. (b) Kondo resonance for the three occupancies. (c) Degenerate states leading to Kondo SU(4) for N=1 and 2 occupancies respectively [100].

[8]SU(N) means Special Unitary group of degree N. The hamiltonian that governs SU(N) Kondo effect belongs to this symmetry group.

If we apply the formula of the conductance as a function of the phase shift 2.14 to the SU(4) Kondo effect, we have to distinguish three cases :

- For N=1 occupancy, there is one electron in four quantum states, the average occupation of one level is $N_n = 1/4$. The associated phase shift is $\delta_{N=1} = \pi/4$. The expected conductance is $2e^2/h$, coming from two spin-degenerate channels that have a 1/2 transmission.
- For N=2 occupancy (half-filling), there are two electrons in four states. The average occupation is $N_n = 1/2$, the phase shift is $\delta_{N=2} = \pi/2$. We expect the conductance $4e^2/h$ for symmetric contacts, provided by two channels perfectly transmitted. Due to the double occupancy, there are six degenerated states, represented on fig. 2.22 (c).
- For N=3 occupancy, three electrons share four levels, $N_n = 3/4$, that is equivalent to $N_n = 1/4$ and N=1 occupancy. In other words, N=1 and 3 are equivalent due to electron-hole symmetry.

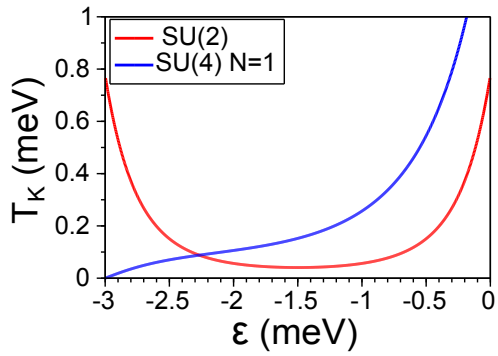


FIGURE 2.23 – Example of Kondo temperature as a function of the energy level $\epsilon_d$ for $U = 3$ meV and $\Gamma = 0.4$ meV for both Kondo SU(2) and SU(4) (N=1). $T_K^{SU(2)}$ is calculated from formula 2.13, $T_K^{SU(4)}$ from [101]. $\epsilon_d$ is chosen such that the center of the Coulomb diamond is at $\epsilon_d = -U/2$.

An example of stability diagram in a SU(4) Kondo region is represented on fig. 2.22 (a). The lines let us see the Coulomb diamonds, hidden by the Kondo ridge that is very large and spreads all over the three diamonds N=1, 2 and 3. Note that the Kondo peak is larger at $N = 2$ ($\approx 1.3$ meV) than at N=1 and 3 ($\approx 1$ meV). Even though the shape of the Kondo SU(4) resonance has been calculated in a slave-boson mean field theory (and compared to experiment) by Delattre *et al.* [102], in a first approximation, we can roughly estimate the Kondo temperature from the half-width of the Kondo peak : 7K for N=2 and 6K for N=1 or 3, values comparable to ref. [7]. These values of Kondo temperature are very large compared to the one typically obtained in a nanotube for SU(2) Kondo effect (around 1 or 2K). This enhancement is indeed predicted by theory since the equivalent of formula 1.2 for SU(N) Kondo effect is $k_B T_K \propto e^{-\frac{1}{N_0 N |J_K|}}$ [37]. On fig. 2.23 is represented the gate dependence of the

Kondo temperature in two situations, calculated from the same parameters $U$ and $\Gamma$ : in a Kondo SU(2) diamond, and in Kondo SU(4) diamond with a filling $N = 1$. Note that both are symmetric compared to the half-filling, but the position of this half-filling depends on the number of levels implied : at the center of the Coulomb diamond for one level, at the center of the $N = 2$ diamond for two-levels (not shown).

#### 2.3.2.2 Breaking of the SU(4) symmetry

This SU(4) Kondo effect survives while the Kondo temperature is larger than the zero-field splitting, either due to spin-orbit or valley-mixing ($T_K \gg \Delta_{SO}, \Delta_{KK'}$). Otherwise, if $T_K \ll \Delta_{SO}, \Delta_{KK'}$, the four states cannot be considered as degenerate, SU(4) Kondo effect is not possible anymore. But there are still states that are doubly degenerated, able to induce the SU(2) Kondo effect described above.

For N=1 or 3 electronic occupancies, the nature of this degeneracy depends on the origin of the zero-field splitting :

- If $\Delta_{SO} \neq 0$ and $\Delta_{KK'} = 0$, the levels are separated in Kramers doublets (K↑, K'↓) and (K↓, K'↑), as represented on fig. 2.24 (a) (see part 2.1.3). This two-fold degeneracy, neither spin nor orbital, is called Kramers degeneracy [59] and can give rise to SU(2) Kondo effect.
- If $\Delta_{SO} = 0$ and $\Delta_{KK'} \neq 0$, the split levels are spin degenerate, standard spin 1/2 SU(2) Kondo effect is possible (fig. 2.24 (b)).

Fig. 2.24 bottom, taken from the work of Cleuziou *et al.* [7] illustrates the interplay between Kondo effect and spin-orbit interactions in a carbon nanotube. For low $|V_g|$, the coupling is weak, leading to low $T_K$ : the SO interactions prevents SU(4) Kondo effect, there is only SU(2) Kondo effect in odd occupancies. For high $|V_g|$, the coupling is strong, $T_K$ is large, Kondo SU(4) is possible (see ref. [103] for the theory).

Note that, if $\Delta_{KK'}$ is just slightly larger than $T_K$, both A and B levels can participate to the SU(2) Kondo effect, leading to what is called two-level (2L) spin SU(2) Kondo effect. Then, as for SU(4) one, the Kondo effect is enhanced. The only way to distinguish between 2L SU(2) and SU(4) at N=1 is the magnetic field dependence of the Kondo resonance [104, 100]: applying a parallel magnetic field, a SU(4) Kondo peak is split in four peaks [31] while a 2L-SU(2) Kondo peak exhibits only a standard double splitting.

#### 2.3.2.3 Others Kondo effects

**N=1 occupancy : orbital SU(2) Kondo effect** When $\Delta_{SO} \neq 0$ and $\Delta_{KK'} = 0$, depending on the value of $T_K$ compared to $\Delta_{SO}$, one observes SU(2) or SU(4) Kondo effect.

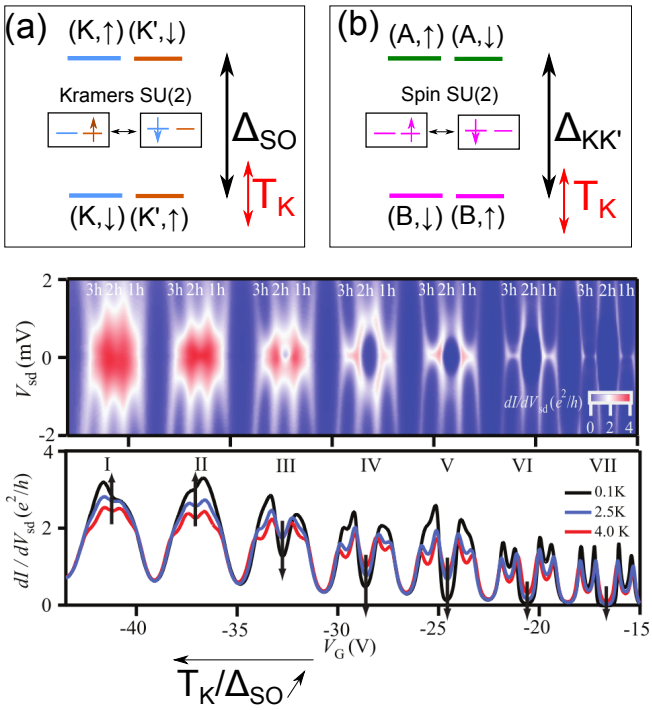


FIGURE 2.24 – Top : Breaking of the four fold degeneracy in two different cases : (a) $\Delta_{SO} \neq 0$ and $\Delta_{KK'} = 0$ and (b) $\Delta_{SO} = 0$ and $\Delta_{KK'} \neq 0$. In each case, the degenerated states leading to SU(2) Kondo effect are represented. Bottom : Interplay between Kondo effect and spin-orbit interactions in a carbon nanotube, as measured by Cleuziou *et al.* [7]. For low $|V_g|$, the coupling is weak, leading to low $T_K$ : the SO interactions prevents SU(4) Kondo effect. For high $|V_g|$, the coupling is strong, $T_K$ is large, Kondo SU(4) is possible.

But when a parallel magnetic field is applied, it breaks the orbital and spin degeneracy (see fig. 2.25), suppressing the Kondo resonance. However the orbital degree of freedom is still preserved and the states (K,↑) and (K',↑) (see fig. 2.25) cross at a magnetic field $B_0$. Then, the orbital degree of freedom is degenerated, leading to the reappearance of a Kondo resonance due to pure orbital SU(2) Kondo effect, as shown by Jarrillo-Herrero *et al.* [31].

**N=2 occupancy : Singlet-triplet Kondo effect** When the last occupied shell of a nearly degenerated carbon nanotube is occupied by two electrons, it can be energetically favorable for the system to maximize the spin, giving a spin 1, a triplet state instead of the singlet state expected (see fig. 2.26 (a)). This is equivalent to the Hund rule in atoms and is possible if the exchange interaction between parallel spins is large enough compared to the level spacing. The application of a magnetic field perpendicular to the axis (so that the orbital levels are not affected) can favor this spin alignment.

As shown on fig. 2.26 (b), there exists a magnetic field $B_C$ at which the singlet and the lowest triplet states cross : they are degenerate. This degeneracy leads to a new kind of SU(2) Kondo

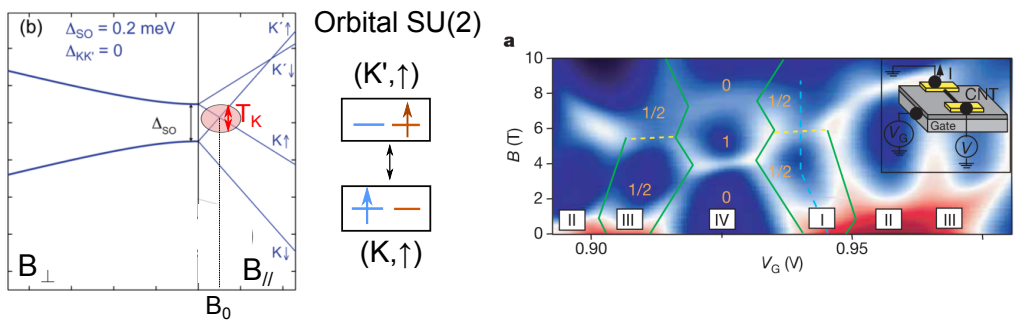


FIGURE 2.25 – Left : magnetic field dependence of the position of the energy levels. Applying a magnetic field, the energy states (K↑) and (K'↑) have the same energy at $B_{//} = B_C$, the orbital degree of freedom is degenerated, allowing orbital SU(2) Kondo effect. Adapted from [59]. Right : experimental measurement by Jarrillo-Herrero *et al.* [31]: The conductance at zero bias is represented as a function of the gate voltage and the magnetic field. For occupancies I or III, the zero bias peaks (indicating Kondo effect) present at $B = 0$ are suppressed by the magnetic field, but appear again around $B_0 \approx 5 - 6$ T due to orbital Kondo effect.

effect as measured by Nygard *et al.* [44] (fig. 2.26 (c)).

Note that this singlet-triplet transition and thus singlet-triplet Kondo effect can also be induced by a the gate voltage, leading to a quantum phase transition [105, 106].

**And all the others...** There are a lot of multi-level Kondo effects, and an infinity of crossovers between them. Presenting an exhaustive description of the situation is beyond the scope of this thesis.

Here are some bibliographic references on other Kondo effects :

- Two-stage Kondo effect for N=2 occupancy [107, 108]. In this situation, each level has its own Kondo effect with its own Kondo temperature. This leads to a large Kondo peak, with a small dip at zero bias. This can also be seen for even electronic occupancies provided that there is a Kondo box near the nanotube(*i.e.* an impurity coupled to the QD) (see ref. [109]).

- Non-equilibrium Kondo effect, by Paaske *et al.* [110], where cotunneling peaks are enhanced by Kondo effect.

### 2.3.3 Conclusion

- In a carbon nanotube quantum dot, depending on the splitting $\delta E$ of the orbital levels, various Kondo effects are possible.

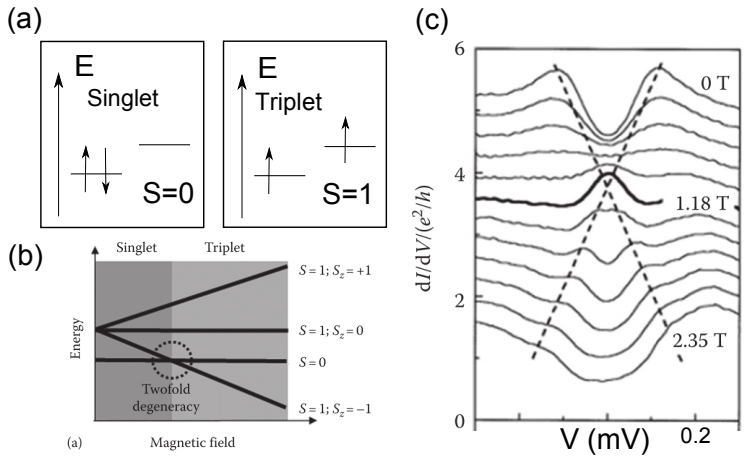


FIGURE 2.26 – (a) Singlet or triplet state for an even occupation of a nearly degenerated carbon nanotube. (b) Magnetic field dependence of the singlet and the triplet states. From [29]. (c) Observation of singlet-triplet Kondo effect by Nygard *et al.* [44].

- If $\delta E \gg U, \Gamma$, then only one level participate to transport, one observes spin 1/2 SU(2) Kondo effect.
- If $\delta E \ll U, \Gamma$, both spin and orbital degree of freedom are degenerated, one observes SU(4) Kondo effect. It spreads over the N=1, 2 and 3 occupations and enhances the Kondo temperature.
- If $\delta E \approx U, \Gamma$, a large range of Kondo effects are possible, depending on the various characteristic energy of the system.
- Applying a magnetic field, parallel or perpendicular to the axis of the nanotube, one can change the level positions and induce other kinds of Kondo effects (of SU(2) symmetry) [59].

# 3 Experimental techniques

Now that the investigated system has been described as well as the physics involved, I present in this chapter the various experimental techniques that we used to fabricate, cool down and measure the samples.

## 3.1 Making samples

Samples of nanoscopic size require specific fabrication techniques. I describe in this section the different processes we went through to make carbon nanotube samples, for current-phase relation and high frequency noise measurements.

### 3.1.1 Fabrication of metallic contacts : electronic lithography technique

#### 3.1.1.1 Lithography technique

The most basic operation of nano-fabrication is the deposition of a patterned layer of metal (or something else) on a substrate. To do so, we use the following e-beam lithography technique (also described on fig. 3.1) :

1. We deposit a layer of resist on the substrate, typically a wafer of silicon covered by a thin layer of $Si0_2$ of 500 nm. The resist used is typically PMMA (Poly(methyl methacrylate)) that is spin-coated on the substrate. In this work, we used a bi-layer MMA/PMMA :
   - MMA EL10 (the copolymere of PMMA, EL means ethyl lactate) is spin coated [1] during 60s at 2000 rpm (thickness $\approx$ 550 nm).
   - The sample is heated on a hot plate during 2 min at 180°C.
   - PMMA 950k A3 is spin coated during 60s at 4000 rpm (thickness $\approx$ 100 nm).

[1] Spin-coating is a technique which consists in applying a small amount of resist at the center of a wafer. Then it is rotated at high speed in order to spread the resist homogeneously on the surface.

- Heating of the sample 2 min at 180°C.

2. Using a scanning electron microscope Zeiss Supra55VP controlled by the NPGS (Nano-Pattern Generation Software) software, the resist is irradiated by electrons accelerated by a voltage of 30kV with a dose corresponding to 320 $\mu$C/cm$^2$. This irradiation follows a pattern designed previously using DesignCad associated to NPGS. Two diaphragms are used : a small one of diameter 7.5 $\mu$m, for the precise patterns, and a bigger one, 120 $\mu$m for coarse patterns. The typical currents are respectively 25 pA and 10 nA.

3. The resist has been damaged by the electronic irradiation, so that it can be eliminated by a proper development. This is done making the sample soak during 50s in a solution of MIBK (methyl buthyl ketone) diluted at 1 :3 with isopropanol.

4. If the lithography is successful, we can deposit the desired metal on top of the resist mask. To do so we use a multi-chamber evaporator containing a Plassys e-beam evaporator. A target of the wanted metal is heated with accelerated electrons (9.56 kV), so that the metal is evaporated toward the sample. Controlling the speed and duration of deposition, we obtain a metallic layer with a known thickness.

5. At last, we remove all the resist by dissolving it in hot acetone (around 60°C), so that only the metallic layer of the pattern remains (see fig. 3.1).

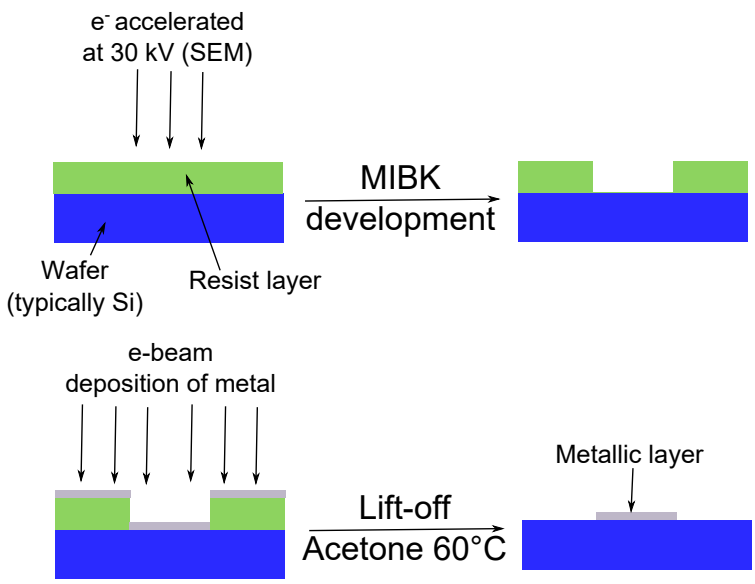


FIGURE 3.1 – Schematic description of all the steps to make metallic patterns on a substrate, as described in text.

#### 3.1.1.2 Metallic deposition : list of metals

Here is a list of the metals we can deposit with the gun (e-beam evaporation), associated with typical deposition conditions :

- Aluminum, at a rate of 1 nm/s in a vacuum of the order of $2 \times 10^{-7}$mbar. Aluminum is quite robust, its quality remains correct (in particular regarding superconductivity) even though the vacuum is not optimal.
- Niobium, at a rate of 0.2 nm/s in a vacuum of the order of $1 \times 10^{-7}$mbar. Unlike Al, the quality of niobium, in particular as a superconductor, is strongly dependent on the quality of the vacuum. It can be useful to do pre-evaporations, in order to "clean" the target. Moreover, because of its high melting point, one needs to heat at a high temperature in order to deposit Nb. It is reasonable not to deposit too much Nb at the same time (no more than 20 nm) so that the sample and the resist are not heated too much. Note that, for this reason, Niobium is generally deposited by sputtering. But since this kind of deposition is not directional, it is not suitable here, in particular for the tunnel junctions (see below).
- Gold, at a rate of 0.8 nm/s in a vacuum of the order of $4 \times 10^{-7}$mbar. Gold is mischievous : it has a very high diffusion mobility such that some Au atoms can short-circuit tunnel junctions nearby.
- Palladium, at a rate of 0.25 nm/s in a vacuum of the order of $2 \times 10^{-7}$mbar. When Pd is heated too much, there are projections that deteriorate the target and soil the chamber. We thus limit the speed of deposition.
- Titanium, at a rate of 0.25 nm/s in a vacuum of the order of $1 \times 10^{-7}$mbar. Ti is often used as a sticking layer (for example under gold). Moreover, it has the property of having getter effect[2], that is why we sometimes flash it to improve the vacuum in the chamber.

### 3.1.2 Carbon nanotubes samples (CNT)

#### 3.1.2.1 Nanotubes synthesis

In our processes, the growth of the carbon nanotubes is the first step to make any nanotube sample. We use a method called Chemical Vapor Deposition (CVD) : the substrate, where are disposed catalyst particles, is heated at a temperature around 900 °C. Then it is brought together with a gas of carbonated molecules : the carbon molecule is cracked when it touches the catalyst, the carbon atoms move toward the edges of the catalyst particles where the growth of the CNT is initiated. The process we used has been developed by Alik Kasumov [60] and is described below :

[2]The word "getter" comes from "get" : Titanium gets the dirty stuff which are in the chamber.

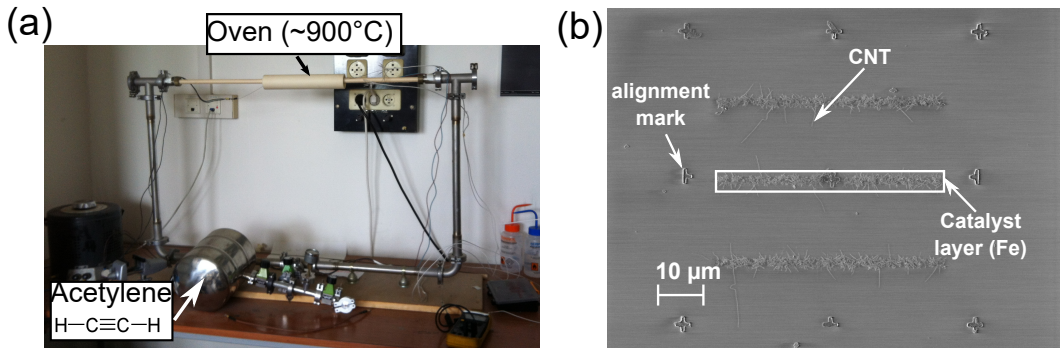


FIGURE 3.2 – (a) Optical picture of the oven used to make the nanotube CVD synthesis. A temperature around 900˚C is obtained making a current pass through a metallic wire around an alumine tube. It is controlled with a thermocouple connected to a voltmeter. (b) SEM image (inlens captor, see text) showing a typical sample after the CVD growth. One can see the alignement marks, the three lines of iron catalyst, as well as the nanotubes.

1. We start depositing, by the lithography technique, alignment marks on the substrate. Usually, one uses a metal with a good contrast in microscopy such as a bilayer of titanium and gold. But here, we have to chose a metal that will not melt during the CVD (around 900˚C), it will be niobium ($T_{melt} = 2500^{\circ}C$).

2. After alignment on these marks, still by the lithography technique, very thin (around a few nm of thickness) lines of iron catalyst are deposited at the center of the sample (see fig. 3.2 (b)).

3. The substrate with catalyst is then introduced in the oven whose picture is shown on fig. 3.2 (a). The chamber is closed and pumped until a vacuum around $10^{-5}$ mbar is reached, and heated progressively until a temperature around 900˚C. Then, a small quantity of acetylene is introduced in the oven (a few mbar) during 9s. Then it is removed, and the heating is switched off. The synthesis is over.

4. Once the sample is at room temperature, we can observe the result of the synthesis with the SEM in Inlens mode, a detector that is sensitive to charging effects, and at low voltage acceleration. What is seen on the SEM picture (such as fig. 3.2 (b)) is the charge due to the nanotube, not the nanotube itself (that is very thin, around 2 nm of diameter).

Note that this setup does not allow a perfect control of the experimental conditions, in consequence the quality of the synthesis was really dependent on the run of CVD. It seems that, in particular, the number and the length of the tubes depends on the humidity of the air the day of the synthesis. It seems to me that the more humid is the air, the more efficient is the synthesis. But without being a chemist and having time for a more involved study of the parameter "humidity" on the synthesis, this remains very speculative.

#### 3.1.2.2 Contacting the nanotubes

One then needs to connect the nanotubes. As mentioned in chapter 2, this step is crucial for the transport properties of the CNT at low temperature. The process relies on the lithography technique : the contacts are patterned on DesignCad and aligned on the tubes thanks to a SEM image such as fig. 3.2 (b). Typically, the contacts are separated by 400 nm and have a width of the order of a few $\mu m$.

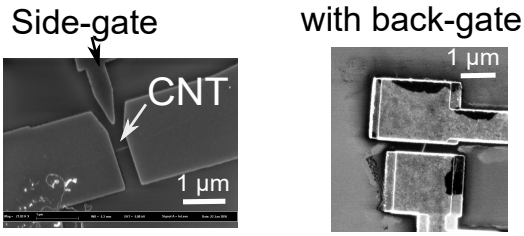


FIGURE 3.3 – Two examples of CNT contacts, one with a side-gate (left), the other with a backgate (right). SEM images, using Inlens detector.

The question is which metal to use ? As stated in chapter 2, the question is theoretically tricky. Experimentally, CNT/Palladium contacts are generally quite good (that is to say the contacts and the CNT are well coupled). If one wants superconducting contacts, Aluminum (or any other superconductor) can be deposited on top of a 6 to 8 nm layer of Pd [3]. Since Pd is not superconducting and is sometimes magnetic, it strongly reduces the total gap seen by the CNT : that's why the thickness of the Pd layer should not be too high compared to the one of Al. Some groups obtain as well good contacts using titanium [83], which less reduces the gap of aluminum. But when we tried it, the contact resistance increased rapidly in contact with atmosphere, giving very poorly coupled QD.

There are two ways of making the electrostatic gate nearby the nanotube (to tune the energy level in the quantum dot). The easiest one is to use a wafer of doped silicon, covered by a thin layer of $SiO_2$ (500 nm), that plays the role of back-gate. However, if one doesn't want to use such a back-gate (for example to control independently several QD on the same chip or to prevent energy losses at high frequency), it is possible to design a side-gate close to the nanotube (see fig. 3.3). Both can be made at the same time, in order to improve the tunability, but the side-gate is strongly screened by the back one.

Note that making good contacts on nanotubes (able to provide Kondo effect and a supercurrent for example) is not always easy. To maximize the chances of success, one should reduce at minimum the number of steps after the CNT growth. For example, an isopropanol washing of the sample before contacting the CNT seems to reduce the chances of good contact instead of increasing it.

[3] Note that if the thickness of Pd is too thin compared to the CNT diameter, the contacts are very bad.

### 3.1.3 Making tunnel junctions

In this PhD work, for the two kinds of experiments presented (current-phase relation and high frequency noise measurements), we need to make superconducting tunnel junctions, constituted of an insulator sandwiched between two superconductors.

The easiest way to do that is to use aluminum as the superconductor and aluminum oxide AlOx as the insulator. The process we used is based on the lithography technique associated with angle depositions, described on fig. 3.4.

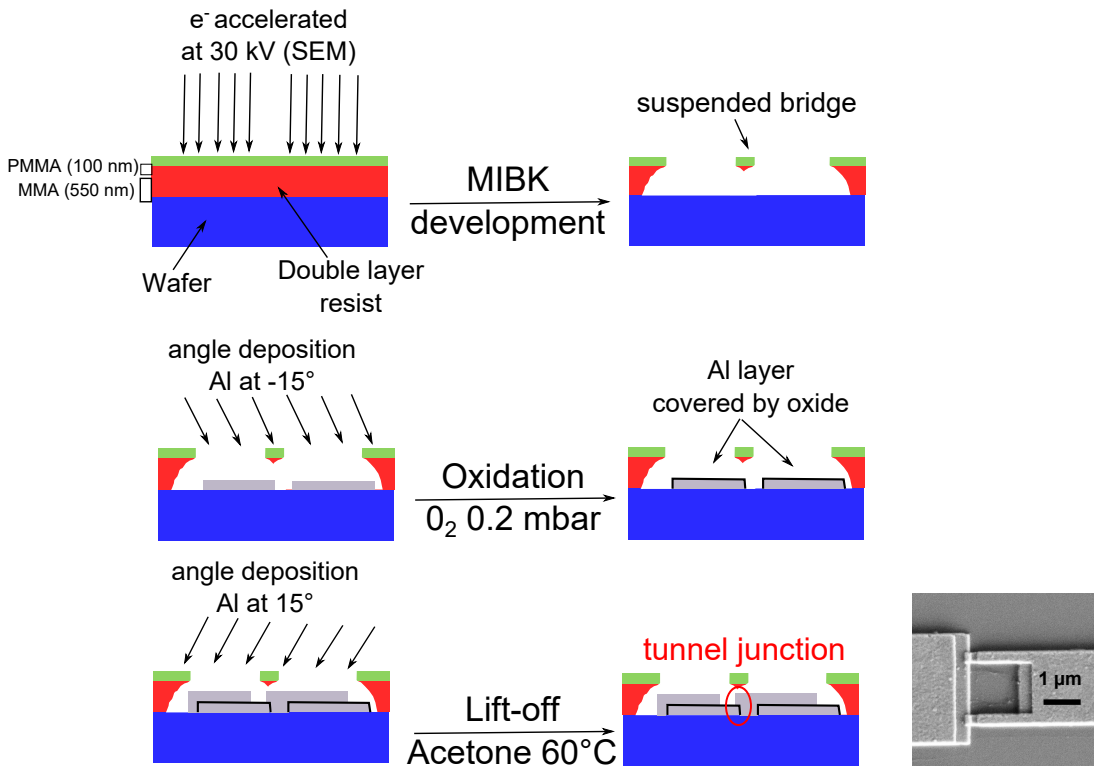


FIGURE 3.4 – Description of the process used to make Al/AlOx/Al junctions by lithography technique associated with angle deposition (see text).

For this process, it is necessary to use the bilayer of resist MMA/PMMA described previously. The PMMA, on top of the structure, is damaged locally, at the precise location of exposure. Things are different for MMA, which is more sensitive to e-beam exposure so that, combining both, it is possible to obtain a suspended resist bridge (see fig. 3.4). The first layer of aluminum is deposited on top of this structure with an angle (typically -15° measured from the vertical), so that there is no metal in the shadow of the resist bridge. It is then exposed to 0.2 mbar of oxygen during 10 to 20 minutes [4], forming a layer of aluminum oxides AlOx of the order of

[4] These oxidation condition are actually strongly dependent on the flux of oxygen, which depends on the quality of the pumping. If the replacement of oxygen is too slow, the oxide quality is very bad, giving very fragile junctions.

the nanometer. At last, a second layer of aluminum (or another metal) is deposited with an angle of 15° on top of the oxide, forming the tunnel junction.

The obtained junctions have typically a surface of 250 nm $\times$ $W$ with $W$ the patterned width of the junction. The resistances obtained are of the order of 70 k$\Omega/\mu$m$^2$ but can vary by a factor two from one oxidation to the other (the oxidation conditions are thus not very well controlled).

Aluminum is chosen for oxidation because of the good properties of AlOx as a covering insulating layer. Nevertheless, this layer is very fragile and can break if any over-voltage is applied on the junction : one needs to be very careful during the manipulations. In practice, it means wearing an anti-static bracelet and carefully grounding any equipment used. During very dry days, it may be useful to moisten air with a water spray.

## 3.2 Measuring samples

### 3.2.1 Cryogenic cooling

All the experiments described in this thesis are realized at very low temperature, below 50 mK. This temperature is lower than the one of liquid nitrogen (77 K), liquid Helium (4.2 K) and pumped liquid helium ($\approx 1K$). It can be obtained using what is called a dilution fridge, in which a mixing of two isotopes of helium (He3 and He4) undergoes a cycle of thermodynamic operations which produce low temperatures.

We describe here this thermodynamic cycle, in the permanent regime. Note that, to enter this permanent regime, the dilution fridge must be initially cooled down at a few kelvin either by a liquid Helium bath (wet dilution fridges) or by a pulse tube (dry dilution fridges).

The most important part of a dilution fridge (*i.e.* the coldest and the one that cools the samples) is the mixing chamber. It relies on the fact that, when the temperature is low enough (typically below 1K), the homogeneous phase of He3/He4 is not stable anymore and the binary phase diagram of fig. 3.5 (c) predicts an equilibrium between two separated phases : a phase of He3 diluted in He4 and a phase of nearly pure He3. The lowest temperature is obtained for a composition of the dilute phase of 93.6% of He4 and 6.4% of He3 (red circle on the phase diagram). Note that the pure He3 phase, lighter, is on top of the phase richer in He4 (see fig. 3.5 where the mixing chamber is represented).

A distillation column makes the connection between the bottom of the mixing chamber (where is the dilute phase, see fig. 3.5 (b)) and the still. The composition of the mixed phase in the still is settled by an equilibrium between osmotic pressure, the fountain pressure (due to the superfluidic properties of helium) and hydrostatic pressure, giving a proportion of 1% of He3.

This phase is then pumped. Since the He3 has a larger vapor pressure than He4, it is pumped

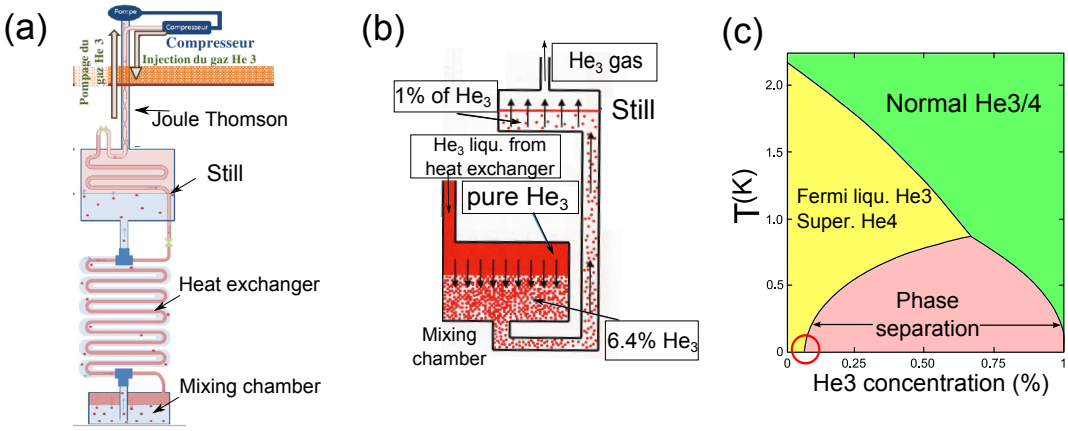


FIGURE 3.5 – (a) Schematic of a dilution fridge. (b) Simplified drawing of the mixing chamber and the still. The composition of the mixture in the still is determined by a hydrostatic equilibrium between osmotic pressure, "funtain pressure" (related to the superfluidity of Helium) and the gravity pressure. (c) Binary phase diagram for the mixture He3/He4. For temperatures low enough (typically below 1K) the mixture is not homogeneous anymore and is separated in two phases : one composed mainly of He3 and one with mainly He4. At $T = 0$, the equilibrium composition of the system is one phase of pure He3 and one composed by 93.6% of He4 and 6.4% of He3.

as a gas outside from the cold part (see fig. 3.5 (a)). Then, using a compressor, it is reinjected in the circuit where it undergoes Joule Thomson expansions and starts to be cooled down again. On the way through heat exchangers, in addition to the expansions, this "hot" He3 is cooled by the cold phase. After again some expansions through impedances, at last, He3 is liquid and arrives on the top of the mixing chamber. There, it is used to maintain the equilibrium between the dilute phase and pure He3, replacing He3 that is pumped in the still. At this stage, one can say that the He3 is diluted in He4 ; this process is endothermic and then cools the system. And the cycle can restart.

Note that the bare temperature and the cooling power of such a fridge are strongly dependent on the composition of the mixture of He3 and He4, as well as the quality of the impedances which make Joule Thomson expansions possible. If anything modifies these impedances, for example if one of them is blocked, the equilibrium is lost. Then the system is warmed up and the pressure increases in the circuit. The only solution is to bring back the mixture of heliums and to clean the impedances.

### 3.2.2 Wiring and filtering

The sample to measure is thermally connected to the coolest part of the dilution fridge : the mixing chamber. From the electronic point of view, the sample is connected to the top of the dilution fridge only by DC lines. These lines are made of manganin wires, an alloy of Cooper, manganese and nickel which is chosen because its resistivity depends very weakly on

temperature. In addition to that, it minimizes heat transfers between the sample and outside. Note that the total resistance of these wires is about 30 Ω (from the sample to the BNC connector on top of the dilution fridge).

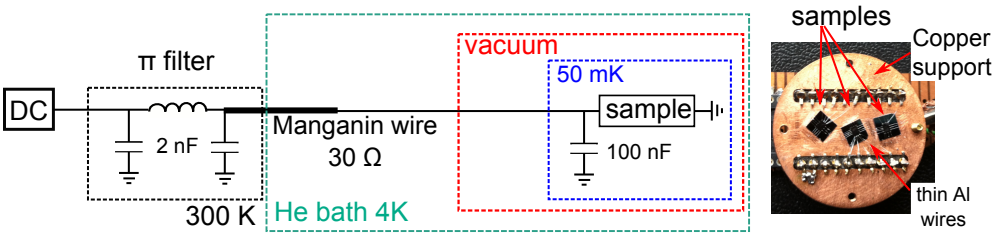


FIGURE 3.6 – Schema of the DC wiring and filtering of the dilution fridge we used. The sample is thermally connected to the mixing chamber of the dilution fridge and electrically connected to the top of the dilution fridge by manganin wires. The filtering consists in a $\pi$-filter at room temperature as well as a capacitance of 100 nF placed close to the sample.

The DC filtering is achieved by two filters (see fig. 3.6) : a $\pi$-filter on the top of the fridge at room temperature which filters frequencies above 10 kHz if the sample resistance is about 5 kΩ and a 100 nF capacitance placed close to the sample.

Note that when placed in the cryostat, the sample is located at the center of a superconducting magnet, providing a magnetic field going from 0 to 1 T (a 5T coil was also available).

### 3.2.3 Electronic measurements

Once the sample is connected and cooled down, it can be measured. I present here an example of such a measurement, namely a measurement of differential conductance as a function of the voltage bias. The setup is represented on fig. 3.7 in two different situations : (a) the sample is not electronically connected to the cryostat, it is possible to measure the current with a current-voltage converter. (b) the sample is grounded in the cryostat, we deduce the current from the voltage across a resistance. In both cases, the sample is biased with a DC bias added to an oscillating one, at a frequency of the order of 100 Hz (chosen such that there is no interference in the circuit). The differential conductance is measured directly with a lock-in amplifier. The DC current is measured as well with a voltmeter.

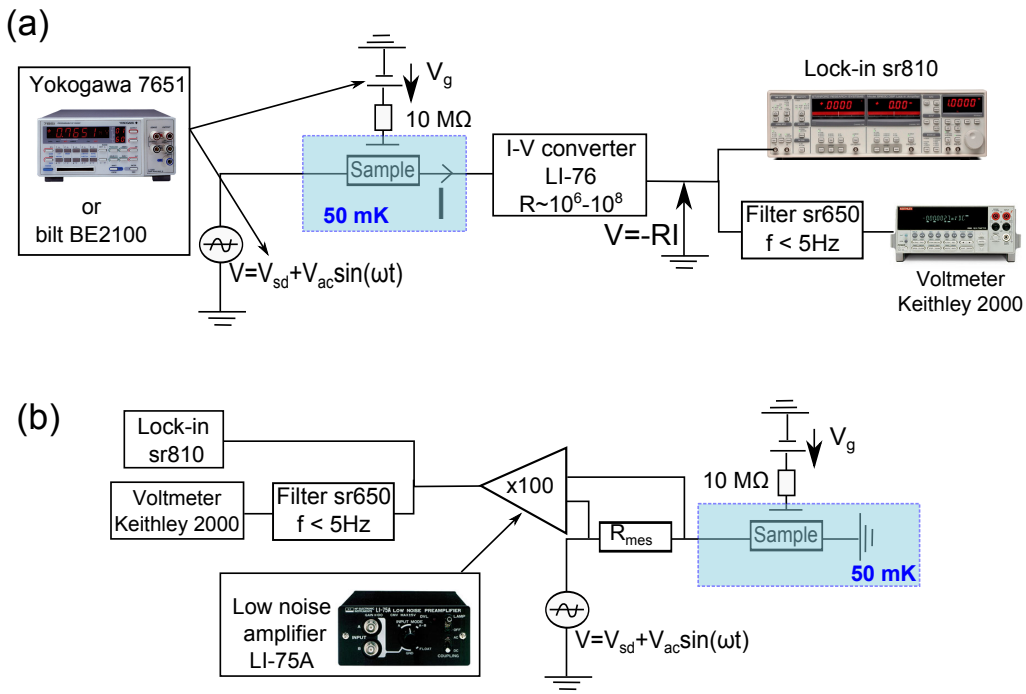


FIGURE 3.7 – Description of the electrical setup used to measure the differential conductance of a sample (typically a carbon nanotube with a gate) in two situations. (a) the sample is floating, one can use a current to voltage converter. (b) One of the sample contacts is grounded to the fridge, we deduce the current from the voltage across the resistance $R_{mes}$.

# Part II

# Josephson effect in a carbon nanotube

# 4 Josephson effect in a carbon nanotube QD : state of the art

The aim of this chapter is to introduce the physics of proximity induced superconductivity in quantum dots, while the experiment will be presented in the next chapter. After briefly recalling the basics of superconductivity and how the superconducting correlations can be induced in a normal metal, I will review the influence of Coulomb interactions and the Kondo effect on the physics of Andreev bound states.

## 4.1 Superconducting proximity effect

### 4.1.1 Superconductivity : important notions

Here are summarized the main notions that will be useful in the following to understand superconductivity. For a more complete description of conventional superconductors, see the textbooks by Laurent Lévy [54] or Michael Tinkham [111].

#### 4.1.1.1 Phenomenological description

The resistivity of a metal is generally expected to decrease with temperature, as electron-phonon and electron-electron scattering are reduced. But even at the lowest temperature, the resistivity should be non-zero because of elastic scattering due to disorder.

It has been shown 100 years ago that, actually, there exists some metals, called superconductors, whose resistivity completely vanishes below a temperature called the critical temperature $T_c$ (which depends on the material). This vanishing of resistivity is associated to another property : a perfect diamagnetism, that expels any magnetic field away from the superconductor (except on a length $\lambda$, called the penetration length). Since expelling a magnetic field requires some energy, there exists a maximum field above which superconductivity is destroyed : this is called the critical field $B_c$. As a direct consequence, there is also a maximum current which can be sustained by a superconductor, called the critical current $I_c$.

Specific heat measurements show that, around the Fermi level and on an energy scale of the order of $T_c$, there is no thermal conduction [54]. This suggests the presence of an energy gap in the density of states, where there is no quasi-particle state. We call $\Delta$ this superconducting gap, which is associated to the pairing energy of electrons of opposite spins, called Cooper pairs. Like bosonic helium atoms which form a Bose-Einstein condensate and flow without dissipation (this is called superfluidity), spin-0 Cooper pairs form a coherent macroscopic state which carries a non-dissipative current. In this description, one needs to provide the energy $2\Delta$ to break a Cooper pair. Their spatial extension, corresponding as well to its phase coherence, is of the order of $\xi_0 = \frac{\hbar v_F}{\pi\Delta}$.

#### 4.1.1.2 Ginzburg-Landau theory, order parameter and superconducting phase

This superconducting state is thus really a phase different from what we will call the "normal" state. The transition from one state to the other is shown to be a second order phase transition, at which can be associated an order parameter in a Ginzburg-Landau description, *a priori* complex :

$$\psi(\mathbf{r}) = \psi_0 e^{i\varphi(\mathbf{r})} \tag{4.1}$$

This order parameter corresponds to a kind of averaged wave-function of the Cooper pairs. $|\psi_0|^2$ represents the density of Cooper pairs $n_s$ such that $\psi = 0$ in the normal state. The phase $\varphi$ of the superconducting order parameter is called the superconducting phase.

In the framework of Ginzburg-Landau theory, it is shown that the current in the superconductor can be written as a function of the potential vector $\vec{A}$, of the flux quantum $\Phi_0 = \frac{h}{2e}$ and the order parameter $\psi$ [111]:

$$I = \psi_0^2 \frac{\hbar}{m^*} \left( \vec{\nabla}\varphi - \frac{2\pi}{\Phi_0}\vec{A} \right) \tag{4.2}$$

This relation emphasizes that a dissipation-less current is not induced by a voltage bias but by a bias of the superconducting phase $\varphi$. That is why this quantity will be crucial in the following for the investigation of the supercurrent.

#### 4.1.1.3 Microscopic origin : BCS theory

The microscopic mechanism leading to conventional superconductivity is understood through the BCS theory (from the name of its finders : Bardeen, Cooper and Shrieffer). The starting point is to say that the formation of Cooper pairs originates from attracting interactions through the lattice, involving phonons. The hamiltonian is then diagonalized thanks to a Bogoliubov transformation and provides a complete description of conventional superconductivity. Here are some results that will be useful for us [54, 111]:

- The ground state of the system is described by the so-called BCS wave-function :

$$|\psi_{BCS}\rangle = \prod_k \left(|u_k| + |v_k| e^{i\varphi}\, c^\dagger_{k,\uparrow} c^\dagger_{-k,\downarrow}\right) |0\rangle \tag{4.3}$$

  The superconducting BCS state is formed by Cooper pairs of opposite momentum and spins. $|v_k|^2$ is the probability for a Cooper pair state to be occupied, $|u_k|^2$ the probability to be empty. Note that when a pair is occupied, its phase is the macroscopic superconducting phase $\varphi$.

- The excitations of the system originate from the breaking of a Cooper pair, and are thus a linear combination of an electron and its time reversed hole ($\vec{k} \leftrightarrow -\vec{k}$, $\uparrow\leftrightarrow\downarrow$).

  - The energy of these excitations is given by $E_k = \sqrt{\xi_k^2 + \Delta^2}$, with $\xi_k$ the energy that would have an electron of momentum $\hbar k$ in the normal state (fig. 4.1 (a)).
  - Their density of states follows the expression, plotted on fig. 4.1 (b) ($n_n$ being the density of states in the normal state) :

$$n_{supra}(E) = \begin{cases} n_n(E_F) \frac{|E-E_F|}{\sqrt{(E-E_F)^2-\Delta^2}} & \text{if } |E-E_F| > \Delta \\ 0 \text{ otherwise} \end{cases} \tag{4.4}$$

  where we see that, indeed, there is no state available around the Fermi energy. The value of the superconducting gap is shown to be proportional to $T_c$ : $\Delta(T=0) = 1.76\, k_B T_c$.

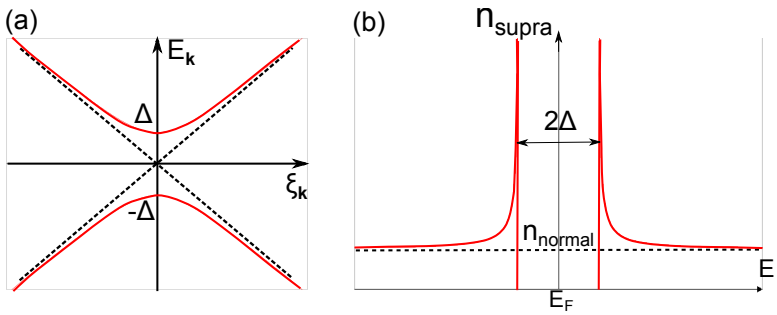


FIGURE 4.1 – (a) Energy of the excitations in the superconductor as a function of $\xi_k$ the energy that would have an electron of momentum $\hbar k$ in the normal state. The created excitations are linear combinations of electrons and holes. (b) Density of states of a superconductor at $T = 0$. The divergence at $E = \pm\Delta$ is smoothed at finite temperature.

- The order parameter introduced in the context of Ginzburg-Landau theory can be associated, under certain conditions, to the superconducting gap $\psi(\mathbf{r}) = \Delta e^{i\varphi}$.

### 4.1.2 Superconducting proximity effect

The peculiar electronic properties resulting from the pairing of electrons in Cooper pairs, are not limited to superconductors. It has been shown fifty years ago that these superconducting correlations can survive in a non-superconducting material (an insulator or a normal metal) close to a superconductor.

First the basic phenomenon, called Josephson effect, is introduced before describing the physics occurring in the normal part.

#### 4.1.2.1 Josephson effect

We consider a situation of a non-superconducting material sandwiched between two superconductors, called an SIS junction in the case of an insulator, SNS junction if the normal part is a normal metal. The two superconductors (called $S_1$ and $S_2$) are identical, in the sense that they have the same gap. In the non-superconducting part, there is *a priori* no superconducting correlation. However, at the interface with the superconductor, some Cooper pairs can penetrate in the normal part. If the length of the junction is small enough such that the coherence of the pair is conserved during the crossing of the junction, both superconductors are coupled and a supercurrent may be able to pass. We can distinguish two regimes, with respects to the coherence length $\xi_0$ : $L < \xi_0$ corresponds to the short junction regime, $L_\phi > L > \xi_0$ to the long junction regime.

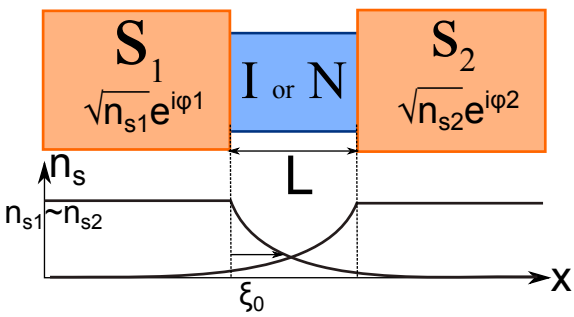


FIGURE 4.2 – Schema of a junction composed by two superconductors separated by a non-superconducting part : typically an insulator or a normal metal. The two superconductors have different superconducting phases, such that there is a phase difference $\varphi = \varphi_2 - \varphi_1$ across the junction. The case of the short junction regime is represented here, where the length of the normal part is smaller than the superconducting coherence length $\xi_0$.

Even though the two superconductors are the same, the superconducting phase (or, in other words, the phase of the superconducting order parameter) can be different, such that there is a difference of phase $\varphi = \varphi_2 - \varphi_1$ across the junction (see fig. 4.2).

In 1962, Brian Josephson predicted that, in a SIS junction, there should be a supercurrent

equal to [112]:

$$I(\varphi) = I_c \sin(\varphi) \tag{4.5}$$

with $I_c$ the critical current, the maximal supercurrent that can flow in the junction. If the junction is biased by the voltage $V$, then the phase evolves according to :

$$\frac{d\varphi}{dt} = \frac{2eV}{\hbar} \tag{4.6}$$

The first relation is called DC Josephson effect. Combined with the second one, we get that $I = I_c \sin(\frac{2eV}{\hbar}t)$, $\nu_J = \frac{2eV}{\hbar}$ being called the Josephson frequency. A bias voltage induces a AC current in the junction : this is the so-called AC Josephson effect (and will be addressed in chapter 8).

Josephson derived these relations introducing a perturbative tunnel coupling between the two superconductors in the Hamiltonian. Feynman proposed an even simpler method, where the result is found by introducing in the Hamiltonian a proportional coupling between the wave-functions of both superconductors [113]. This result, a supercurrent which evolves periodically with the superconducting phase, is a robust property of such SNS/SIS junctions, independently of the exact configuration of the system. Note that it is also valid in the case of any weak link, where the two superconducting reservoirs are separated by a weaker one (for example a constriction).

However, the exact relation between the supercurrent and the superconducting phase, called the current-phase relation, depends strongly on the strength and of the nature of the coupling between the two superconducting reservoirs. We now address this point through the Andreev reflections and bound states, describing what happens to a Cooper pair in the normal part.

#### 4.1.2.2 NS interface : Andreev reflection

Let's consider an interface between a normal and a superconducting metal, whose superconducting phase is $\varphi$ (fig. 4.3 (a)). What happens to an electron, arriving from the normal part on the interface at an energy $E_F + \epsilon$ ? If $\epsilon > \Delta$, it is converted into a quasi-particle at the same energy. But if $\epsilon < \Delta$, there is no single-particle state available. However, if the electron is reflected as an hole, then a charge $2e$ is transferred in the superconductor via a Cooper pair (see fig. 4.3 (a)) which induces a current : this is an Andreev reflection. Since the total momentum of a Cooper pair is equal to $2k_F$, the momentum of the reflected hole must verify $\vec{k_h} + \vec{k_e} = 2\vec{k_F}$ : the hole has an energy $-\epsilon$, and propagates in the opposite direction of the electron.

This intuitive statement can be rigorously derived from the Bogoliubov-de Gennes (BdG) equation, which describes non-homogenous superconductivity [114, 115], where $\hat{H}_0$ is the

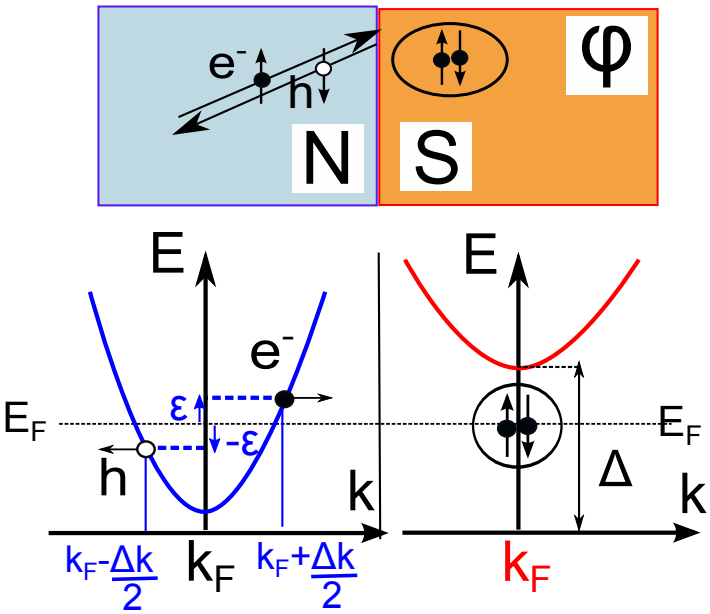


FIGURE 4.3 – Principle of an Andreev reflection : an electron at energy $\epsilon$ above $E_F$ arriving on an NS interface is reflected as a hole at energy $-\epsilon$. A charge $2e$ is transferred into the superconductor, forming a Cooper pair.

Hamiltonian in absence of superconductivity :

$$\begin{pmatrix} \hat{H}_0 - E_F & \Delta e^{i\varphi} \\ \Delta e^{-i\varphi} & -\hat{H}_0^{\ *} + E_F \end{pmatrix} \begin{pmatrix} \psi_e(\mathbf{r}) \\ \psi_h(\mathbf{r}) \end{pmatrix} = E \begin{pmatrix} \psi_e(\mathbf{r}) \\ \psi_h(\mathbf{r}) \end{pmatrix} \tag{4.7}$$

The resolution of this equation with the proper form of wave-functions and imposing the boundary condition at the interface gives that the phase acquired by the hole compared to the one of the electron after the reflection is :

$$\phi_h - \phi_e = \varphi \pm \arccos\left(\frac{\epsilon}{\Delta}\right) \tag{4.8}$$

The plus sign corresponds to the case described on fig. 4.3, the minus sign to the reflection of an incoming hole into an outgoing electron.

If we summarize the Andreev reflection process :

- If an electron at the energy $\epsilon < \Delta$ above the Fermi energy arrives on a NS interface, it is retro-reflected as a hole of energy $-\epsilon$ (below the Fermi energy). A charge of $2e$ is transferred in the superconductor at the Fermi energy, forming a Cooper pair.

- The phase shift between the outgoing hole and the incoming electron is equal to $\phi_{e\to h} = \varphi + \arccos\left(\frac{\epsilon}{\Delta}\right)$, with $\varphi$ the superconducting phase in the superconductor.

#### 4.1.2.3 SNS junction : Andreev Bound States

**Boundary conditions and Andreev Bound States** With Andreev reflections, we see that it is possible to convert an electron in a Cooper pair at an NS interface provided that a hole with opposite is reflected back. The inverse process is also possible : a Cooper pair arriving on a SN interface is converted into an electron and a counter-propagating hole of opposite spins. While its phase coherence is conserved, this so-called "Andreev pair" contains information about the former Cooper pair. Let's see what happens if we enclose the normal part between two superconductors as represented on fig. 4.4 (the SN interfaces are assumed to be perfect) :

1. At the SN interface (called left interface, L), any Cooper pair is split into an electron at energy $\epsilon$ above $E_F$ and a counter-propagating hole of opposite spin at energy $-\epsilon$. The phase of the electron at this interface is, compared to that of the hole, $\phi_{e,L} = \phi_{h,L} - \varphi_L + \arccos\left(\frac{\epsilon}{\Delta}\right)$.
2. The electron propagates in the normal part, where it acquires a phase $k_e L = (k_F + \frac{\epsilon}{\hbar v_F})L$ [1], such that its phase at the right interface is $\phi_{e,R} = \phi_{e,L} + k_e L$.
3. At the right NS interface R, it is reflected as a hole of phase $\phi_{h,R} = \phi_{e,R} + \varphi_R + \arccos\left(\frac{\epsilon}{\Delta}\right)$ at energy $-\epsilon$. A Cooper pair is created in the right superconductor.
4. This hole propagates to the left interface, acquiring a phase $k_h L = -(k_F - \frac{\epsilon}{\hbar v_F})$.
5. The hole is reflected as an electron, helped by a Cooper pair of the left superconductor. This is equivalent to the step 1, the loop is closed.

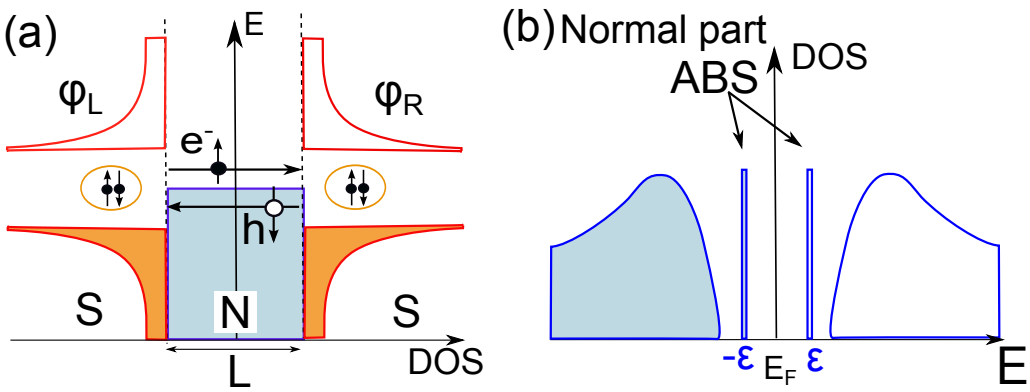


FIGURE 4.4 – Andreev Bound States. (a) Andreev reflections in a SNS junction, leading to the formation of Andreev bound states (ABS) in the normal part (see text). (b) Density of states in the normal part : the lines in the gap represent the Andreev Bound states. Inspired by ref. [116].

The succession of reflections of the electrons and holes in the normal part leads to the transfer of Cooper pairs from one superconductor to the other, and thus to the supercurrent predicted

[1] assuming that $\epsilon \ll E_F$

by Josephson. Note that this propagating vision, rather than giving an exact idea of what happens in the normal part (in particular it is strongly questionable in the short junction limit), show that only some discrete energies are allowed above the gap : the ones which make possible constructive interferences between electrons and holes after one or several round-trip in the junction. We obtain thus the relation between the energy and the superconducting phase $\varphi = \varphi_L - \varphi_R$ :

$$2\pi n = \varphi + 2\arccos\left(\frac{\epsilon}{\Delta}\right) + \frac{2\epsilon}{\hbar v_F} L \tag{4.9}$$

In other words, the boundary conditions given by the superconducting phase difference $\varphi$ impose the energy of the Andreev pair in the normal part as well as its phase dependence. The corresponding state is called Andreev Bound State (ABS).

**Andreev Bound States energy** If we limit our investigation to short junctions, where the term due to propagation vanishes[2], we obtain the energy of the ABS :

$$\epsilon = \pm\Delta\cos(\frac{\varphi}{2}) \tag{4.10}$$

$\epsilon$ can also be rigorously derived from the BdG hamiltonian 4.7, showing that an ABS can be seen as the stationary superposition of an electron and its time-reversed hole, as was expected from the Andreev reflection mechanism. This ABS is *a priori* degenerate, since (e↑, h↓) and (e↓, h↑) are equivalent.

The density of states in the normal part is represented on fig. 4.4 (b) (to be compared with the one of a superconductor of fig. 4.1) : a gap is induced in the continuum by the superconductors nearby, but discrete Andreev Bound States stand below the gap (with a phase-dependent position) at energies $\pm\epsilon$ around $E_F$. Note that in this representation, the ground state is obtained by filling the states below the Fermi energy : the occupied ABS is the one at $-\epsilon$ (with $\epsilon > 0$).

**Case of non-perfect NS interface** Until now, we only considered a single channel, and assumed that the NS interfaces were perfect (transmission $T = 1$). The energy of the ABS can be derived in a more general case of the short SNS junction, with $N$ transport channels of transmissions $T_n$ (as defined in the scattering matrix formalism [114]). Thus, a channel of transmission $T_n$ gives an ABS at the energy : $\epsilon_n = \pm\Delta\sqrt{1 - T_n \sin^2(\varphi/2)}$ (see fig. 4.5 (a)).

[2]This assumption is completely relevant in the case of carbon nanotube junctions we are interested in, where $\frac{2\Delta L}{\hbar v_F} \ll 1$. Note that this condition is equivalent to $L < \xi_0$ stated above.

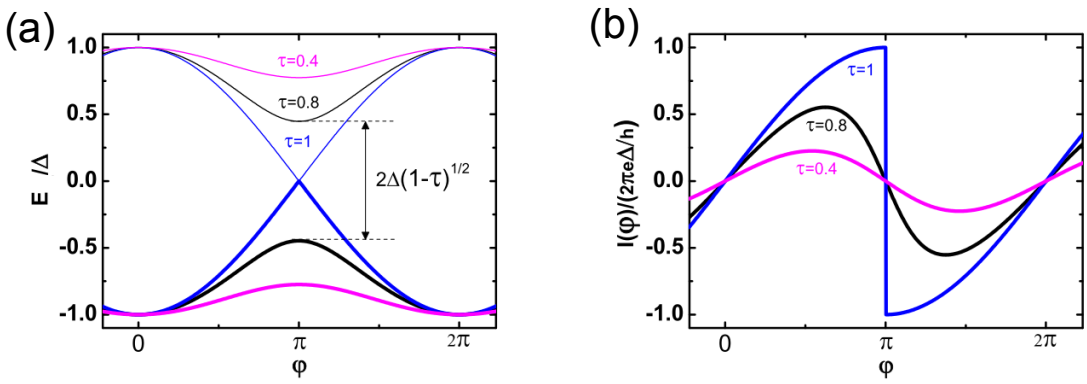


FIGURE 4.5 – (a) Phase dependence of the energy of the Andreev Bound States for one channel in a SNS junction in the short junction limit, for various transmissions $\tau$ (called T in the text). Corresponding current-phase relation, obtained from the derivative of the ABS. Taken from [117].

#### 4.1.2.4 Current-phase relation in an SNS junction

Before giving the phase-dependence of the supercurrent in the short SNS junction, we can make two general statements about current-phase relations [118]:

- If the phase $\varphi$ changes by $2\pi$ in a superconducting reservoir, it doesn't change the physical state of the system : the supercurrent is a periodic function of the superconducting phase
- Generally, the current-phase relation is an odd function of $\varphi$. Indeed, according to eq 4.2, we expect the sign of the supercurrent to change with the sign of the phase. This is a very important constraint on the supercurrent, that can only be overcome by a breaking of the time reversal symmetry.

The exact supercurrent in the junction is given by the derivative of the free energy $F = -k_B T \ln(Z)$ with respect to $\varphi$ ($Z$ being the partition function) [118, 119]. It can be divided in two components : the current carried by the ABS, added to a current involving the continuum above the gap (if the continuum states are phase-dependent). It appears that, in various systems, the dominant contribution is given by the ABS [120, 119], they are sufficient to give a good qualitative idea (and are easier to calculate). Thus, at zero temperature, each of these bound state carries a current $i_n = \frac{2e}{\hbar}\frac{\partial \epsilon_n}{\partial \varphi}$ such that the total Josephson current is :

$$I = -\frac{2e}{\hbar}\sum_n \frac{\partial \epsilon_n}{\partial \varphi} = \frac{e\Delta}{2\hbar}\sum_n \frac{T_n \sin(\varphi)}{\sqrt{1 - T_n \sin^2(\varphi/2)}} \tag{4.11}$$

Obviously, this current-phase relation (called CPR in the following) is more complex than the simple sinus first predicted by Josephson. However, in the limit of weakly transmitted channels $T_n \ll 1$, the expression $I = I_c \sin(\varphi)$ is recovered, with $R_n I_c = \frac{\pi\Delta}{2e}$ ($R_n$ being the

resistance in the normal state $R_n = \frac{h}{2e^2T}$). For an arbitrary transmission, the current-phase relation contains harmonics, the extreme limit being $T \approx 1$ (represented on fig. 4.5 (a) in blue), yielding a singularity at $\varphi = \pi$ : the current-phase relation is then strongly anharmonic, close to a saw-tooth (see fig. 4.5 (b)). However, as soon as there is a finite temperature, the highest harmonics are suppressed first, such that the current-phase relation tends to be sinusoidal [118].

Note that the ground state of the system corresponds to the occupation of the states below the Fermi energy which yields, in this system, to current-phase relations in $\sin(\varphi)$ (or harmonics). If the system is excited, such that there is a non-thermal distribution, the ABS above the $E_F$ participates as well to the supercurrent, giving a contribution in $-\sin(\varphi) = \sin(\varphi + \pi)$ : the amplitude of the supercurrent can be controlled [121] or even reversed [122]. Such a reversal of the sign of the supercurrent is an example of what is called a 0-$\pi$ transition.

#### 4.1.2.5 Multiple Andreev reflections

Until now, we have only considered SNS junctions at equilibrium, without any bias voltage, as needed to see the supercurrent. Because of the gap in the density of states, there should be *a priori* no current in the junction for a bias below the superconducting gap ($V < 2\Delta$). But experimentally, one observes a non-zero conductance, with peaks at biases $V_n = 2\Delta/(ne)$ (see fig. 4.6 (b)).

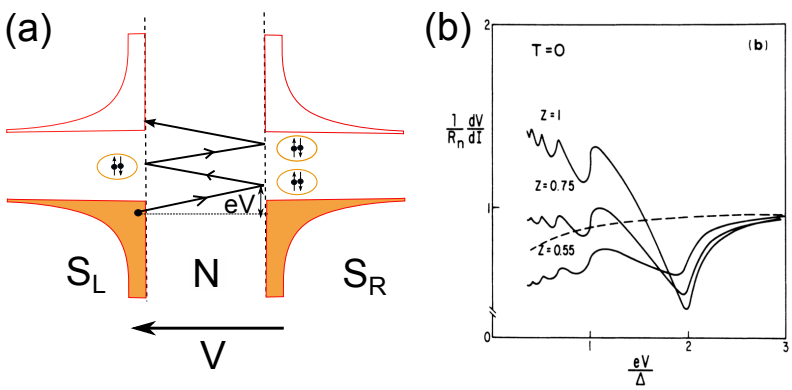


FIGURE 4.6 – (a) Multiple Andreev reflections in an SNS junction biased by a voltage V. If $eV = 2\Delta/n$, an electrons is reflected (n-1) times on a NS interface, each time transferring a Cooper pair. The transfer of charge from one side to the other is equal to n. (b) Calculated subgap resistance for various strengths of barriers z : the larger is z, the smaller is the transmission of the barrier. From ref. [123].

Klapwijk *et al.* [124] proposed that this was due to multiple Andreev reflections (MAR). Let's consider a junction biased with a voltage V, as represented on fig. 4.6 (a), where an electron is injected at $S_LN$ interface. During the propagation in the junction, the electron acquires an energy $eV$ because of the voltage bias. Then, on the interface $NS_R$, it is reflected as a hole. This hole acquires again an energy $eV$ during its propagation toward the $NS_L$ interface. After

$n$ reflections, the Andreev pair has acquired an energy $neV$ : if $neV = 2\Delta$, the electron can leave the normal part as a quasi-particle in the superconductor : there is a non-zero current.

Note that the exact structure of the sub-gap conductance depends strongly on various parameters. In particular of the transmission of the junction : while when $T \approx 1$, the peaks are mixed [125], the signal is weaken when $T \ll 1$. The symmetry of the barriers is also very important.

## 4.2 Josephson effect in a carbon nanotube quantum dot

We now focus on the normal material we are interested in : carbon nanotube quantum dots.

### 4.2.1 Qualitative description

#### 4.2.1.1 Description of the system

The aim of this work is to investigate the Josephson effect in a carbon nanotube. A CNT is generally not intrinsically superconducting [3], except maybe at Van Hove singularities [127]. But it has been shown in 1999 that it was however able to sustain a supercurrent by proximity effect [128].

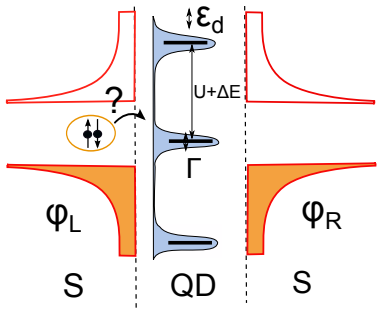


FIGURE 4.7 – Schema of a quantum dot sandwiched between two superconductors. The superconducting reservoirs are supposed identical except that there is a difference of superconducting phase $\varphi = \varphi_R - \varphi_L$ between them. The energy levels in the quantum dot are represented with their characteristic energy scales : the charging energy U, the energy level spacing $\Delta E$, the width $\Gamma$ of the levels (also the coupling between the dot and the reservoirs) and $\epsilon_d$ the shift of the energy levels, controlled by a gate voltage.

As shown in chapter 2, a contacted carbon nanotube with barriers at the interface with reservoirs should be seen as a quantum dot, with quantized energy levels and in the Coulomb blockade regime if the temperature is low enough. I recall on fig. 4.7 the energy scales of the system : the charging energy U needed to add an electron on the dot, the energy level spacing $\Delta E$ and the width $\Gamma$ of the levels (also the coupling between the dot and the reservoirs). The position of the energy levels can be shifted by $\epsilon_d$, controlled by a gate voltage.

#### 4.2.1.2 Different regimes

Concerning the proximity effect, the situation is strongly dependent on the relative values of the parameters of the dot :

If $\Gamma \gg U, \Delta$, in the strong coupling regime, the energy levels in the dot are so broad that

[3] Individual nanotubes are not superconducting, but ropes can be [126]. We work here only with individuals tubes.

they overlap. The density of states in the dot is only thinly modified by the gate voltage, the physics of the system is similar to the one of a SNS junction, generally in the short-junction limit : the supercurrent is typically proportional to the conductance in the normal state.

On the contrary, if $\Gamma \ll U, \Delta$, the coupling is low and the system is in a strong Coulomb blockade regime : out of the charge degeneracy points, it is not possible to add or remove an electron on the dot. In the normal state, it manifests as a zero conductance equal to zero, and thus no supercurrent in the superconducting state. However, on the charge degeneracy points (*i.e.* on the Coulomb peaks) a supercurrent is possible, as calculated by Beenakker *et al.* [129]. Interestingly, if $\Gamma < \Delta$, the relation $R_n I_c \propto \Delta$ is not valid anymore and is replaced by $R_n I_c \propto \Gamma$. This makes thinks about another situation where $R_n I_c$ no longer follow the gap : in the long junction regime, where it is proportional to the Thouless energy, the inverse of the time spent by an electron in the junction [130]. In the quantum dot, the coupling $\Gamma$ represents as well the inverse of the time spent in the dot which, if $\Gamma < \Delta$, can be seen as an effective long junction from the $R_n I_c$ product point of view.

The most interesting case is the intermediate regime $\Gamma \approx U \approx \Delta$. In this limit, U is high enough to give rise to Coulomb blockade while $\Gamma$ is sufficiently large to allow the cotunneling processes described in section 2.2.2.2 of chapter 2. In the normal state, these cotunneling processes allows an electron to enter the dot (and thus to change the electronic occupancy) provided that another one goes out during a time shorter than $\hbar/U$ (the typical tunneling time being $\hbar/\Gamma$). In the superconducting state the situation is more complicated since, instead of a single electron, one needs to make the two electrons of a Cooper pair tunnel through the dot coherently in order to observe a supercurrent. Because of the exclusion principle, the situation will be strongly dependent on the parity of the number of electrons in the dot.

In the next section, we give a qualitative image of what happens in this intermediate regime, before giving a more quantitative understanding.

#### 4.2.1.3 Parity induced 0-$\pi$ transition

To transfer a Cooper pair through a quantum dot by cotunneling processes, one needs to break the pair (which is possible during a time $\hbar/\Delta$) and make the electron co-tunnel one by one (during typically the time $\hbar/\Gamma$) : this is possible only if $\Delta < \Gamma$. Depending on the parity of the number of electrons in the dot, different processes are possible (see ref. [131, 3]).

For an even number of electrons, the highest occupied energy levels is filled, as represented on fig. 4.8 (note that the electronic energy levels are represented, instead of the addition spectrum, because the occupancy is not affected by cotunneling), the system is in a singlet state. We want to transfer a Cooper pair from the left to the right reservoir. In a first step, one electron from the dot tunnel to the right electrode (1) and is replaced by the electron of the Cooper pair with the same spin (2). In a second step, the electron on the dot with the opposite spin tunnel to the right and is replaced by the second electron of the Cooper pair.

At the end, the ordering of the Cooper pair is unchanged.

For an odd number of electrons, the system is in a doublet state. Things are different since there is only one electron, spin up or down, in the highest occupied state. If, in the first step, we inter-exchange electrons of same spin, it will not be possible to reform a zero-spin Cooper pair in the right electrode. We thus have to invert the spins : in the first step a spin down (for example) of the Cooper pair replaces a spin up in the dot. In the second step, spin up of the Cooper pair replaces a down in the dot (see fig. 4.8). At the end, the spin ordering of the Cooper pair formed in the right contact has been inverted.

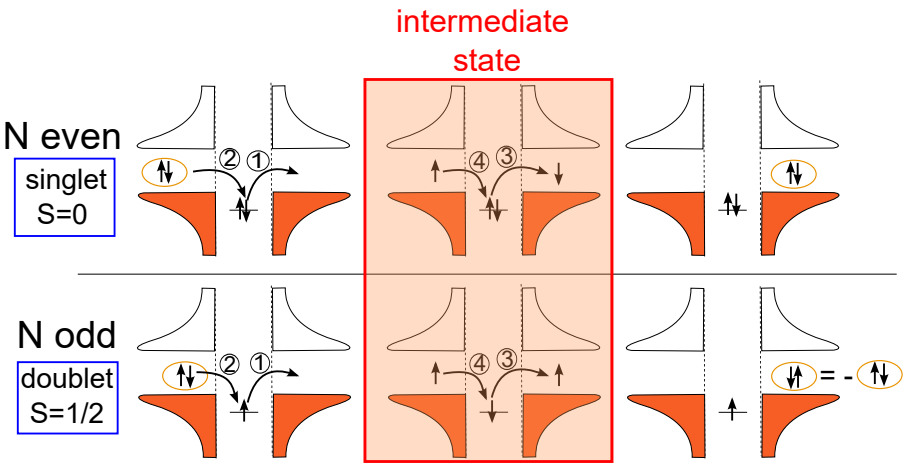


FIGURE 4.8 – Qualitative explanation for the parity induced 0-$\pi$ transition. Depending on the even or odd parity, the co-tunneling processes are different (see text).

These spin-flip processes strongly affect the supercurrent, as it has been first pointed out by Kulik in 1966 [132]. These processes are of fourth order and, in the doublet state, are the first one leading to a non-zero current. Consequently, the supercurrent is weaken[133] and the current-phase relation is dephased by $\pi$ ($I = I_c \sin(\varphi + \pi) = -I_c \sin(\varphi)$) : this is a $\pi$-junction [134, 131, 3]. This name is given by opposition to the singlet case, where the current-phase relation is a standard one : $I = I_c \sin(\varphi)$.

The transition from a 0 to a $\pi$ junction is achieved by tuning the dot's occupancy with a gate voltage, this is called a gate-controlled 0-$\pi$ transition. It has been experimentally observed in 2006 by Van Dam *et al.* [4] in an InAs nanowire QD and Cleuziou *et al.* [135] in a CNT. In both experiments, the QD is inserted in a superconducting loop so that the phase is controlled by a magnetic field, allowing the measurement of the current-phase relation (we will come back on this kind of measurement in the following). Jorgensen *et al.* [136] measured as well this gate-controlled 0-$\pi$ transition in 2007, also in a CNT but without control of the phase (the sign reversal of the supercurrent is deduced from a diminution of the critical current, see fig. 4.9).

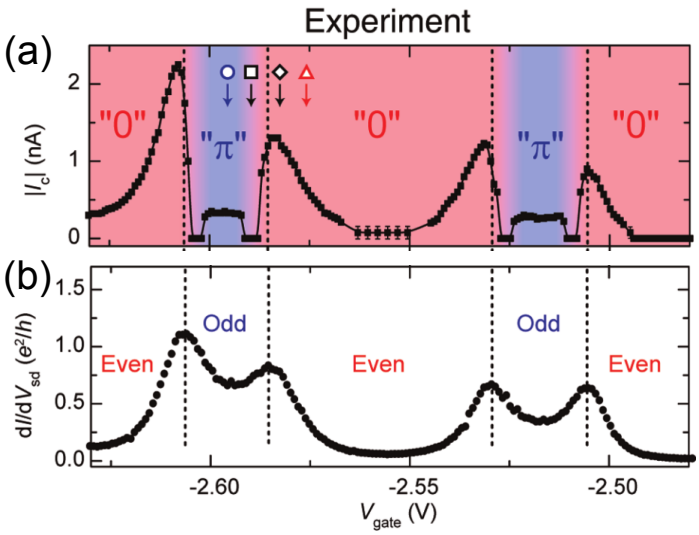


FIGURE 4.9 – Sign reversal of the supercurrent in a carbon nanotube quantum dot contacted with superconducting electrodes, when the gate voltage is tuned. From [136].

#### 4.2.1.4 Competition between Kondo effect and superconductivity

We now focus on Coulomb diamonds corresponding to an odd number of electrons. We should take into account something that we have completely neglected until now : the Kondo effect. As developed in chapter 1, in the normal state, the Kondo effect manifests itself as enhanced cotunneling processes which overcome Coulomb blockade. This gives rise to a resonance in the density of states at the Fermi level, *i.e.* as a conductance resonance at zero bias, as well as a screening of the local magnetic moment of the dot. In other words, the Kondo effect transforms a doublet state in a Kondo singlet state.

When the electrodes of a Kondo quantum dot turn superconducting, the situation becomes quite complex and requires a serious theoretical treatment (we will come back to this later). We can however try to guess qualitatively what is going to happen [3]:

- If $\Delta \gg T_K$, there is no electron around the Fermi level in a range of energy $T_K$ that is able to participate to the Kondo screening. The situation is not modified compared to the case described above : this is a $\pi$-junction.
- In the $\Delta \ll T_K$ case, the Kondo correlations exist in the system. The cotunneling processes are enhanced, making the transfer of Cooper pairs easier, and favoring the formation of a Kondo/BCS singlet state. Both Kondo effect and superconductivity cooperate so that a 0-junction is recovered, with possibly a very high supercurrent.
- Intermediate regime $\Delta \approx T_K$ : how does the system transit from 0 to $\pi$-junction in this regime of strongest competition ? We will see that in this regime, the superconducting phase plays a role in the transition, as predicted first by Rozhkov *et al.* [137] in 1999 and

Clerk *et al.* in 2000 [138]. Measuring the CPR in this regime was our first motivation for measuring the CPR in a CNT QD.

This 0-$\pi$ transition driven by the ratio $\Delta/T_K$ was predicted some time ago by Glazman and Matveev, in 1989 [134]. The first occurrence of this interplay came in 2002 by Buitelaar *et al.* [51], who proved that the conductance at zero bias in the superconducting state is suppressed if $\Delta > T_K$ and enhanced otherwise. Then, in 2009, this result has been supported by critical current measurements in a carbon nanotube by Eichler *et al.* [94] (only the critical current was measured, not the current-phase relation).

Note that the problem has also be tackled through the spectroscopy of the Andreev bound states, as for example in ref. [116, 139, 140, 141, 142]. These experiments enable in particular to visualize the crossing of the Andreev levels as a function of the different parameters.

### 4.2.2 Proximity effect and single-impurity Anderson model

We try here to give an idea of the theoretical treatment of the transport in a quantum dot with superconducting electrodes, with the objective of making the connection between the Andreev states described above in the case of the SNS junction and the qualitative arguments given in the case of the quantum dot.

#### 4.2.2.1 Superconducting Anderson Hamiltonian

We want to solve the Anderson Hamiltonian 1.3 with superconducting electrodes [143, 119], written as :

$$H = \sum_{i=L,R} H_i + H_{at} + \sum_{i=L,R} H_{Ti} \tag{4.12}$$

With the following terms :

- $H_i = \sum_{\vec{k},\sigma} \epsilon_{\vec{k}} a^\dagger_{\vec{k},\sigma,i} a_{\vec{k},\sigma,i} - \sum_{\vec{k}} (\Delta_i a^\dagger_{\vec{k},\uparrow,i} a^\dagger_{-\vec{k},\downarrow,i} + H.c.)$ is the BCS hamiltonian for each lead, with superconducting gaps $\Delta_i = \Delta e^{i\varphi_i}$.

- $H_{at} = \epsilon_d \sum_\sigma d^\dagger_\sigma d_\sigma + U n_\uparrow n_\downarrow$ is the energy associated with the isolated dot ($U$ is the charging energy).

- $H_{T,i} = \sum_{\vec{k},\sigma} (t d^\dagger_\sigma a_{\vec{k},\sigma,i} + H.c.)$ is the tunneling coupling between the dot and the electrodes. $t$ is assumed to be symmetric between L and R and is related to the coupling $\Gamma$ by $\Gamma = \pi t^2 \rho_0$.

#### 4.2.2.2 Superconducting atomic limit : competition between superconducting correlations and Coulomb blockade

To understand the physics of such a system, we start by considering the superconducting atomic limit, which consists in taking a large gap $\Delta \to \infty$ so that the quasi-particles does not participate to transport. It means that the dot is disconnected from the superconducting reservoirs regarding the quasi-particles. However, thanks to a proper treatment of the approximation [4], the dot is still coupled to the Cooper pairs, so that there is a non zero supercurrent [119]. It means in particular that there is no Kondo correlations ($\Delta \gg T_K$). After a Green functions calculation, it can be shown that the system is equivalently described by the effective Hamiltonian [143, 119]:

$$H_{eff} = \sum_\sigma \xi_d d_\sigma^\dagger d_\sigma - \tilde{\Delta}_\varphi (d_\uparrow^\dagger d_\downarrow^\dagger + H.c) + \frac{U}{2}\left(\sum_\sigma d_\sigma^\dagger d_\sigma - 1\right)^2 \tag{4.13}$$

where $\xi_d = \epsilon_d + U/2$ is the energy level of the dot shifted so that $\xi_d = 0$ corresponds to particle/hole symmetry (the center of the Coulomb diamond). In this atomic limit, we are in the regime $\Gamma \ll \Delta$ which was found in the section 4.2.1.2 to correspond to an effective long-junction. That's why the local pairing amplitude induced in the dot by the superconducting reservoirs is no longer the superconducting gap but a quantity related to the time spent in the dot $1/\Gamma$ : $\tilde{\Delta}_\varphi = \Gamma/2\cos(\varphi/2)$. It is interesting to note that $\tilde{\Delta}_\varphi$ is also modulated by the superconducting phase : the pairing interactions are the strongest around $\varphi = 0$ or $2\pi$ and vanish at $\varphi = \pi$. The question is : are these interactions large enough to overcome the Coulomb repulsion and form a BCS-like singlet state ? To answer this question, one has to compare the four eigenstates of the effective Hamiltonian, obtained thanks to a Bogoliubov transformation [144, 119].

Two of them are the doublet states $|\uparrow\rangle$ and $|\downarrow\rangle$, of energy $E_\uparrow = E_\downarrow = E_\sigma = \xi_d$. They correspond to the state of the system without superconducting coupling, and lead to a $\pi$-junction.

The two other ones are BCS-like state, linear combinations of the empty state $|0\rangle$ and the doubly occupied dot $|\uparrow\downarrow\rangle$ :

$$|+\rangle = u\,|\uparrow\downarrow\rangle + v^*\,|0\rangle\,, \quad E_+ = \tfrac{U}{2} + \xi_d + \sqrt{\xi_d^2 + \tilde{\Delta}_\varphi^2} \tag{4.14}$$

$$|-\rangle = -v^*\,|\uparrow\downarrow\rangle + u\,|0\rangle\,, \quad E_- = \tfrac{U}{2} + \xi_d - \sqrt{\xi_d^2 + \tilde{\Delta}_\varphi^2} \tag{4.15}$$

where u and v are real coefficients. These are singlet states which can be seen as superpositions of electron and holes : they correspond to the Andreev bound states found in the SNS junction and give rise to a 0-junction. Note the term $U/2$ that shifts the energies $E_{+,-}$, due to the Coulomb repulsion and is opposed to the formation of the singlet.

[4] The electronic bandwidth D must be taken infinite as well, before $\Delta \to \infty$

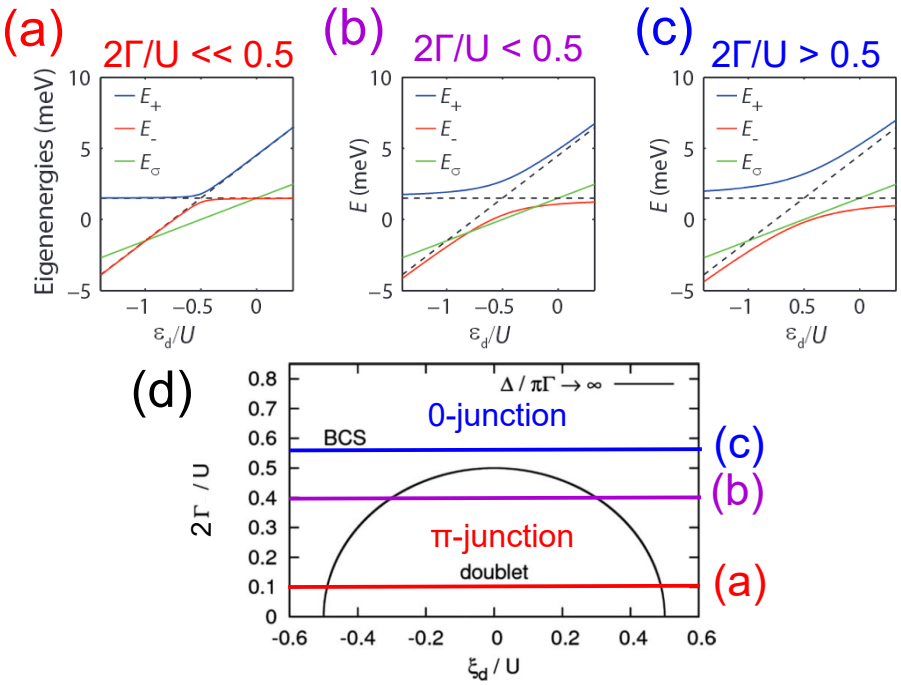


FIGURE 4.10 – (a), (b) and (c) Energy of the eigenstates of the system as a function of the energy level of the dot $\epsilon_d$, for three different ratio of $\Gamma/U$. In blue an red are represented the energy of the BCS-like states, in green the doublet energy. Taken from [145]. (d) Corresponding phase diagram, giving the ground state of the system as a function of the various parameters (remember that $\xi_d = \epsilon_d + U/2$). Taken from [119].

For a given set of parameters ($U$, $\Gamma$) and position of the energy level of the dot $\xi_d$, the ground state may be a doublet ($|\uparrow\rangle$ or $|\downarrow\rangle$, they are degenerated) or the BCS singlet ($|-\rangle$, whose energy is always lower than that of $|+\rangle$). The relative positions of these eigenenergies are given on fig. 4.10 for three ratios $\Gamma/U$. The first case (a) is a regime of strong Coulomb repulsion U compared to the coupling/pairing $\Gamma$ : the magnetic state of the system is almost non-perturbed by superconductivity, the ground state is a doublet in the region of odd number of electron ($-1 < \epsilon_d/U < 0$) and a singlet otherwise. The second case (b) corresponds to $\Gamma \approx U/2$, where the stability domain of the doublet state over $\epsilon_d$ is reduced. The last one is $\Gamma > U/2$, where the Coulomb interaction is not strong enough to stabilize the doublet for any value of $\epsilon_d$.

Generally, in the literature, what are called "Andreev Bound States" are the transition energies from the doublet to the singlet states :

$$\epsilon_- = E_- - E_\sigma = \frac{U}{2} - \sqrt{\xi_d^2 + \tilde{\Delta}_\varphi^2} \tag{4.16}$$

$$\epsilon_+ = E_+ - E_\sigma = \frac{U}{2} + \sqrt{\xi_d^2 + \tilde{\Delta}_\varphi^2} \tag{4.17}$$

In some sense, they correspond to the excitation energies of the BCS theory which, by the way, have very similar expressions ($E_k = \sqrt{\xi_k^2 + \Delta^2}$) except that the Coulomb interaction is added. Note that, in the SNS junction, for one channel, we had only one ABS (added to its excited counterpart), spin-degenerate. In the single-level QD the Coulomb interaction breaks this degeneracy, since adding a second electron costs energy : we have two non-degenerate ABS added to their excited counterpart.

#### 4.2.2.3 Finite gap : influence of the Kondo effect

In our experiment, $\Delta \approx 0.2$ meV (for aluminum based contacts), $U \approx 3$ meV and $\Gamma \approx 0.5$ meV (see chapter 2) : the atomic limit cannot give quantitative results, we have to take into account the Kondo correlations.

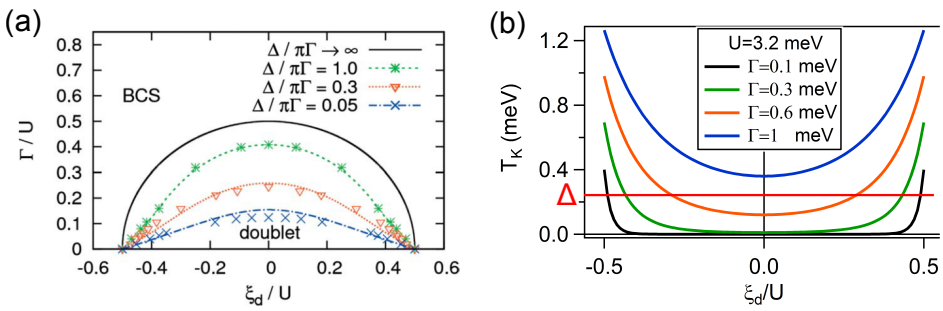


FIGURE 4.11 – (a)Phase diagram of the system for various values of the superconducting gap. In black is the atomic limit, in colors the finite gap limit, with the values of $\Delta/\Gamma$ indicated on the top right. The symbols represent NRG data from [144], the dashed lines the perturbative calculation of ref. [119]. Taken from ref. [119]. (b) Kondo temperature plotted from formula 1.5 for $U = 3.2$ meV and various values of $\Gamma$ as a function of $\xi_d/U$. An example of superconducting gap $\Delta$ is plotted, in order to understand qualitatively the evolution of the phase diagram (a) as a function of the ratio $\Delta/\Gamma$.

This can be done by NRG calculations [144] or by a perturbative calculation around the effective Hamiltonian [119] and gives the phase diagram represented on fig. 4.11 (a). As expected, the Kondo correlations favor the formation of a singlet state : as $\Gamma$ increases (meaning an increase of $T_K$ according to formula 1.5), the doublet region is reduced compared to the singlet one. The nature of the singlet is also modified : in the $\Delta \to \infty$ limit it is purely BCS, if $\Delta \to 0$ it is purely Kondo, in between it is BCS/Kondo-like.

The singlet/doublet transition can then be seen as driven by the relative strengths of the Kondo effect and superconducting correlations : the larger is the ratio $T_K/\Delta$, the more stable is the Kondo-singlet. Like in the atomic limit, the doublet state is more likely to appear at the center of the Coulomb diamond ($\xi_d = 0$) than on the edge. While in the atomic limit this can be understood as the appearance of a mixed valence regime on the edges of the diamond which favors a singlet state, in presence of Kondo effect this is compatible with the $\xi_d$ dependence of the $T_K$ (which is minimum at the center of the diamond, as represented on fig. 4.11). In reality, we are facing a complex interplay between the superconducting correlations, the Coulomb

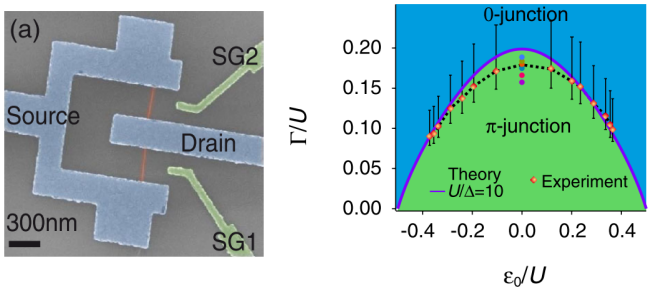


FIGURE 4.12 – Investigation of the singlet-doublet transition by R. Maurand et al. [91], realized in a carbon nanotube QD where $\epsilon_d$ and $\Gamma$ can be tuned independently thanks to a side-gate and a back-gate. Left : picture of the sample. Right : phase diagram of the 0-$\pi$ transition.

interactions and the Kondo effect.

The phase diagram of the singlet-doublet transition has been investigated theoretically and experimentally in details by Maurand *et al.* [91], in a carbon nanotube QD where $\epsilon_d$ and $\Gamma$ can be tuned independently thanks to a side-gate and a back-gate (see fig. 4.12 left). The CNT is inserted in a SQUID such that its current-phase relation can be measured as a function of $\Gamma$ and $\epsilon_d$, giving the phase diagram of fig. 4.12, panel right.

#### 4.2.2.4 Phase dependence of the ABS, current-phase relation and phase-driven 0-$\pi$ transition.

Let's now focus on the phase dependence of the ABS, giving rise to the current-phase relation. In the superconducting atomic limit, the energy levels are given by equation 4.16. They can also be calculated in the general case taking into account the Kondo correlations, as for example in ref. [119], showing that the physics of the singlet/doublet transition is qualitatively the same in both regimes. On fig. 4.13 are represented the phase-dependence of the Andreev Bound States calculated in a mean-field approximation [146] in three different regimes, as well as the derivative as a function of the phase of the ones below the Fermi energy, giving the dominant contribution to the supercurrent at zero temperature.

- The singlet state corresponds to the blue part on the phase diagram, where $T_K > \Delta$ such that the Kondo effect cooperates with the superconductivity to form the singlet-state. The most striking difference with a standard SNS junction is that the degeneracy of the ABS is broken : each ABS is split in two because of the Coulomb interaction. Moreover, as in the atomic limit, the ABS are detached from the continuous spectrum above the gap $\Delta$. However, the sign of the current is the same as in a standard junction : this is a 0-junction.
- The doublet state, where $T_K < \Delta$ such that the Kondo effect does not survive to superconductivity, corresponds to the red region. Then the inner bound states (those

which have the strongest phase dependence) have been exchanged : the sign of the supercurrent is reversed, this is a $\pi$-junction.

- The third case is the most intriguing, corresponding to the purple line on the phase diagram, where the Kondo effect and superconductivity are of the same order of magnitude ($T_K \approx \Delta$). There, the inner ABS cross at the Fermi energy for some values of superconducting phase (see fig. 4.13 (b)) such that the ground state around $\varphi = \pi$ is a doublet and the ground state around $\varphi = 0$ is a singlet. The consequence on the CPR is spectacular : it looks like a $\pi$-junction around $\varphi = \pi$ and to a 0-junction around $\varphi = 0$. Since the system transits from a doublet to a Kondo singlet varying the superconducting phase, we can see the situation as a phase-dependent Kondo screening.

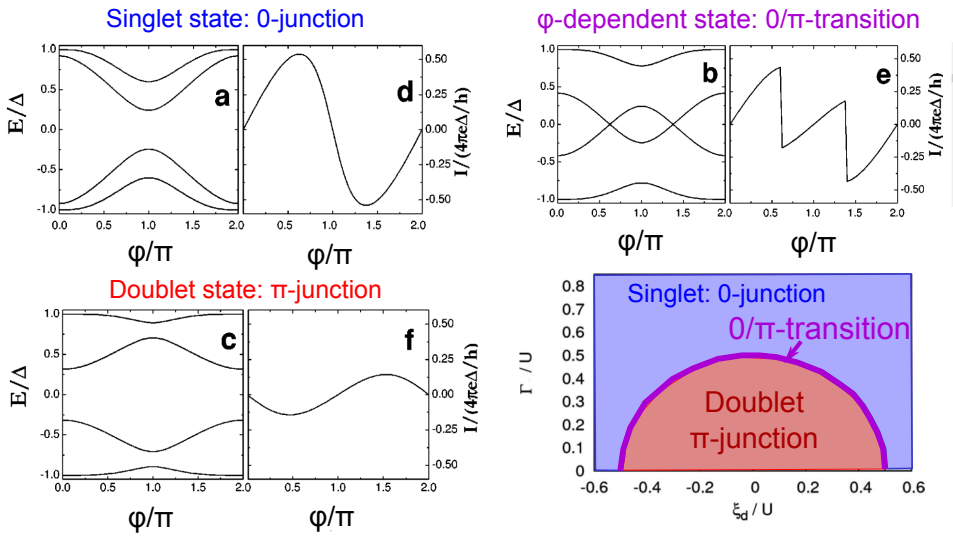


FIGURE 4.13 – Andreev Bound States and corresponding current-phase relation in the three regions of the phase diagram : the singlet state (in blue), doublet state (red), and at the transition (purple line). Adapted from ref. [146]. Note that these curves have been obtained from a mean field approximation, where the Kondo correlations are not taken into account (but are qualitatively similar).

This simple mean-field approach is not the only one to predict such a phase-dependent 0-$\pi$ transition. This doublet to singlet transition driven by the phase can also be shown using renormalization group theories [143, 147] and Quantum Monte Carlo [148, 10] (see fig. 4.14 for two examples).

But, until now, this kind of current-phase relation had not been measured. The CPR measured by Maurand *et al.* [91] at the 0-$\pi$ transition, represented on fig. 4.14 (c), exhibit some anharmonicities which may be related to this phenomenon, but the symmetry of these curves is problematic : they are not odd functions of the superconducting phase as they should be in absence of any breaking of the time reversal symmetry.

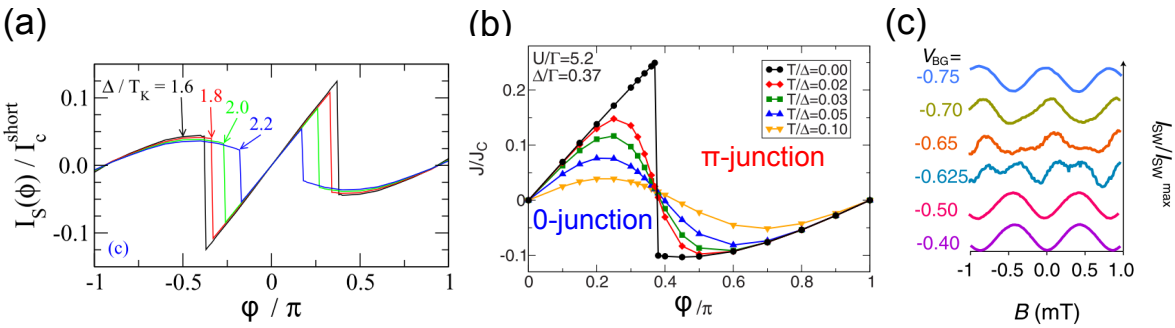


FIGURE 4.14 – Current-phase relation predicted at the 0-$\pi$ transition. (a) From ref. [147], at T=0 for various ratio $\Delta/T_K$. (b) From ref. [143], for finite temperatures. We see that the transition is quickly smoothed as T increases. (c) Current-phase relations measurements around the 0-$\pi$ transition (the magnetic field B is proportional to the superconducting phase) as measured by Maurand *et al.*. Note that the CPR at the transition are not odd functions of the phase (see text).

The aim of this work is to measure accurately and systematically the current-phase relation at this 0-$\pi$ transition and confront it to theoretical predictions in order to demonstrate the driving of the 0-$\pi$ transition by the superconducting phase.

### 4.2.3 Josephson effect in a two-level quantum dot

#### 4.2.3.1 Why is it different in a multi-level QD ?

Until now, we have considered a single-level (SL) quantum dot, where the measurement of the CPR (0 or $\pi$-junction) tells about the state of the system (singlet or doublet). But, as demonstrated in chapter 2, a carbon nanotube is generally a two-level (2L) QD, in which the Josephson effect is dramatically affected.

The situation is summarized on fig. 4.15 (a). We want to induce a supercurrent in a QD where the gate voltage is chosen such that two levels may participate to the transport of Cooper pairs : these two levels are called A and B and are separated by an energy $\delta E$ (which represents the breaking of the orbital degeneracy). They may be differently coupled to the reservoirs and we call respectively $\Gamma_A$ and $\Gamma_B$ these couplings (they may be different for left and right reservoirs, but we will neglect this point in the following).

As stated above, the $\pi$-junction in a SL-QD with an odd number of electrons is possible since the Cooper pair cannot be transfered without spin-flip during the cotunneling. But if other levels (empty or full) are available, this is not true anymore. This has been experimentally pointed out in 2006 by Van Dam *et al.* [4]. In this experiment, the Josephson effect has been measured in an InAs nanowire where the Kondo effect was negligible and several levels participate to transport. When they measured the supercurrent at a fixed phase $\varphi = \pi/2$ as a function of the gate voltage (this quantity can roughly be seen as the critical current,

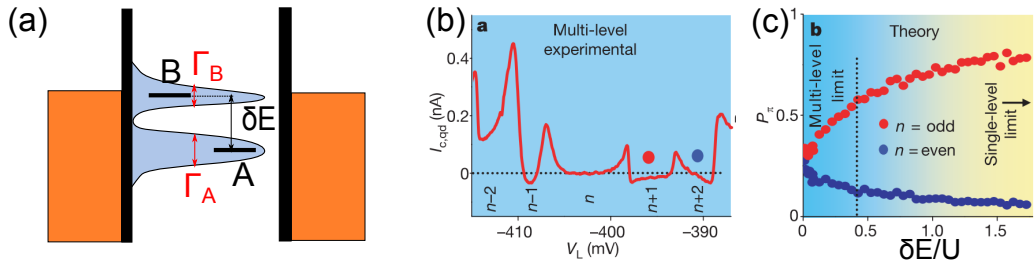


FIGURE 4.15 – (a) Schema of a two-level quantum dot such as the one we are interested in. The two energy levels, called A and B, are separated by an energy $\delta E$. They may be differently coupled to the reservoirs. (b) Supercurrent measured at a fixed phase as a function of the gate voltage in an InAs QD in the multi-level regime. From the work of Van Dam *et al.* [4]. (c) From the same paper, the theoretical probability of observing a 0 or $\pi$ junction for even or odd occupation in a QD depending on its mean level spacing divided by the charging energy. This has been obtained considering a random distribution of levels and couplings in the dot.

with a positive sign for 0-junctions and negative for $\pi$-junctions), they obtained the curve represented on fig. 4.11 (b). The supercurrent in the "n+2" diamond is quite surprising : it becomes negative for an even number of electrons. In addition to that, the supercurrent is not symmetric compared to the center of the diamond. Such a behavior was actually predicted in 1998 by Shimizu *et al.* [149] and is due to the participation of several levels to transport. In this work the authors have shown that in a multi-level regime, using a random distribution of energy levels with different couplings, both 0 and $\pi$-junctions are possible for both odd and even occupancies (fig. 4.15 (c)).

To our knowledge, there is no other measurement of Josephson effect in a multi-level QD (except ref. [150], but this question is not raised explicitly). It seems that all the previous measurements of supercurrent realized in CNT were in the SL regime ($\delta E \gg U, \Gamma$). Let's see now what is exactly expected when only two levels are considered.

#### 4.2.3.2 Two-level regime predictions without Kondo effect

The supercurrent in a two-level quantum dot has been calculated by Shimizu *et al.* using an Anderson-like Hamiltonian [149]. For each co-tunneling event, there are *a priori* $24 = 4!$ sequences possible to transfer a Cooper pair through the QD. The sign of the contribution to the current of each sequence is given by the number of electron permutations (*i.e.* the number of processes with spin-flip) and the sign of the wave-function (see ref. [149] and supp. informations of ref. [4]).

In the single level regime, when there is one electron in the dot, only six of them are available, and they contribute negatively to the current. When there are two electrons in the dot, only some processes giving positive contributions to the currents are allowed. In a two-level QD, a second path is available, such that the twenty-four processes are *a priori* possible for both

even and odd occupancies. That is why a $\pi$-junction is not necessary related to a doublet state. Note that the Kondo correlations are not considered here.

The result of the calculation is shown on fig. 4.16 where is represented the supercurrent at the fixed phase $\varphi = \pi/2$ for one (a), two (b) and three levels (c).

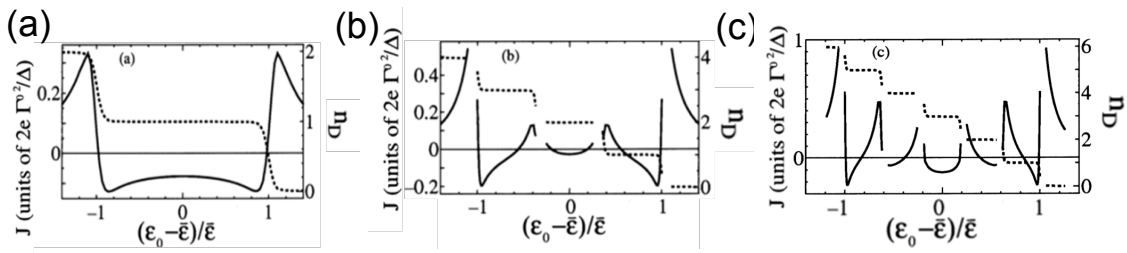


FIGURE 4.16 – Continuous line : supercurrent at $\varphi = \pi/2$ versus the energy level in the dot (proportional to the gate voltage) for (a)a one level QD, (b) two-level and (c) three-level [149]. The dotted lines (right axis) represent the electronic occupancy of the dot.

A first striking point is that these three curves are symmetric with $\bar{\epsilon}$. $\bar{\epsilon}$ is energy at half-filling, corresponding to an occupation of the dot of $n_d = 1$ for a single-level, $n_d = 2$ for a two-level and $n_d = 3$ for a three-level. This is why the supercurrent is not anymore symmetric compared to the center of the Coulomb diamonds at $n_d = 1$ or 3. Note as well the $\pi$-junctions at $n_d = 2$ and the 0-$\pi$ transitions inside the $n_d = 1$ or $n_d = 3$ diamonds and not at the edges, as in the SL regime.

Still without considering the Kondo effect, Yu *et al.* focused on the carbon nanotube case, with two spin-degenerate levels [151]. Two parameters, specific to CNT, are taken into account : the small energy $\delta E$ between the two levels, and a new parameter, $T_2$, which quantifies how much the orbital degree of freedom is conserved during tunneling : $T_2 = 0$ if it is conserved, non-zero otherwise. The results are presented on fig. 4.17. The influence of $\delta E/\Delta$ is shown on panel (a) : its main effect is to increase the size of the N=2 diamond (as expected, see chapter 2). The influence of orbital mixing ($T_2 \neq 0$) is more interesting : it suppresses the $\pi$ behavior at $N = 2$. In panel (c), both effects are taken into account.

Note that Droste *et al.* [152] and Karrash *et al.* [153] have also calculated the supercurrent in double dots in series, a system *a priori* different from a CNT where both levels are connected to both reservoirs. The results are thus not directly transposable.

Note as well that, in all these articles, no current-phase relations are presented in the ML-regime. Current-phase relations are however presented in the article by Lee *et al.*, but it concerns only the 2L-QD occupied by two electrons.

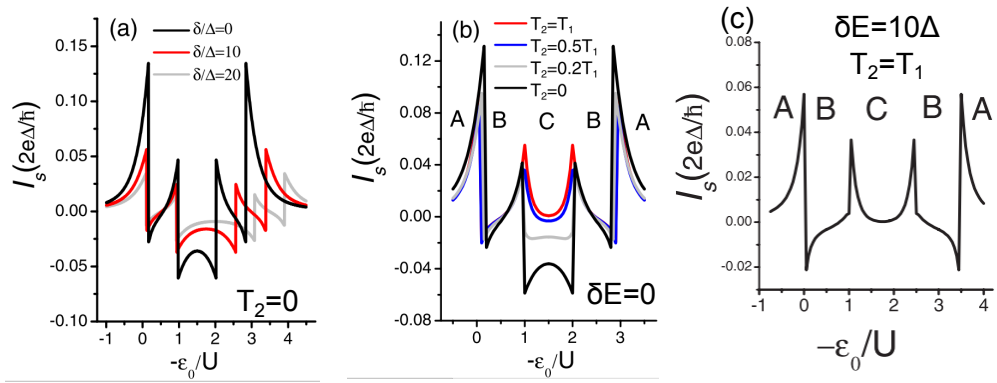


FIGURE 4.17 – Supercurrent in a CNT QD in absence of Kondo effect versus the energy level in the dot (proportional to gate voltage), as a function of two parameters : (a) the small level spacing $\delta E$ (written $\delta$ in the legend), without orbital mixing and (b) $T_2$, a parameter which quantifies how much the orbital degree of freedom is conserved, with $\delta E = 0$ ($T_2 = 0$ if there is conservation, $T_2 = T_1$ correponds to a high mixing of orbitals). (c) Both parameters are taken non-zero : $\delta E = 10\delta$ and $T_2 = T_1$. Figures taken from Yu *et al.* [151].

#### 4.2.3.3 What about the Kondo effect ?

When the Kondo correlations are taken into account, the situation becomes much more complex. It has for example been taken into account in an article by Lee *et al.* [12], but only in the case of a double occupancy of the 2L-QD.

Zazunov *et al.* [154] have tackled more specifically the case of the SU(4) Kondo effect (for N=1 occupancy), Lim *et al.*[155] did it in presence of spin-orbit coupling. The calculations provide also a rich phase diagram.

### 4.2.4 0-$\pi$ transitions

In the single-level regime, we have presented a transition from a 0 to a $\pi$-junction, originating from a crossing of Andreev levels, induced by an interplay between Coulomb interactions and the superconducting correlations, helped by the Kondo effect. There are some other effects leading to 0-$\pi$ transitions. Let's take a few moment to learn more about them.

#### 4.2.4.1 Back to the $\pi$-junctions

In order to generalize the notion of $\pi$-junction, we can consider the free energy F of the junction, from which the Josephson current is calculated by $I = -\frac{2e}{\hbar}\frac{\partial F}{\partial \varphi}$ [118].

If the current-phase relation is $I = I_c \sin(\varphi)$ (+ harmonics), the minimum of $F$ is at $\varphi = 0$ : this is why we call it a 0-junction (see fig. 4.18 (a)). On the other hand, for a CPR $I = I_c \sin(\varphi + \pi)$ (+ harmonics) the minimum energy is at $\varphi = \pi$ : this is a $\pi$- junction (fig. 4.18 (d)) [118]. What

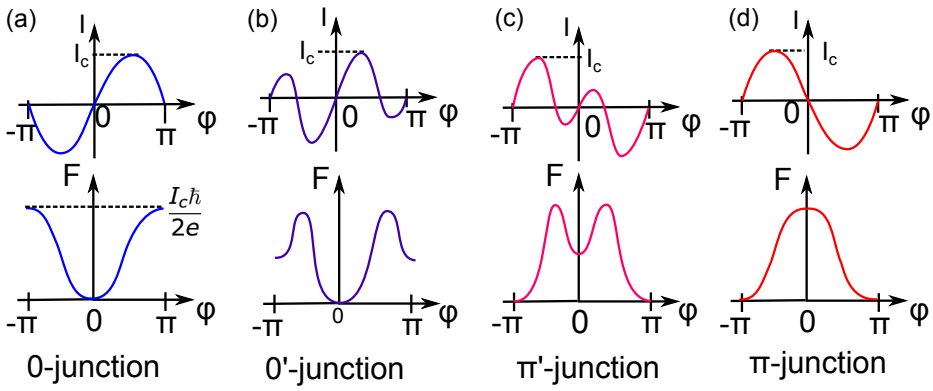


FIGURE 4.18 – Current-phase relation and free energy F (see text) for four different kinds of Josephson junctions.

about the CPRs predicted at the single-level 0-$\pi$ transition, as represented on fig. 4.14 ? We argued that the CPR has a 0 or a $\pi$ behavior depending on the value of the superconducting phase, this is neither 0 nor $\pi$ state. The situation is depicted on fig. 4.18 (b) and (c) : depending on the proportion of 0 and $\pi$ behaviors, the global minimum of the free energy is at $\varphi = 0$ or $\pi$. But there is as well a local minimum at respectively $\varphi = \pi$ and 0 : this is called a $0'$ or $\pi'$ junction [148].

In the SL 0-$\pi$ transition, the system thus transits from 0 to $\pi$ through 0' and $\pi'$ states. Is it general to all 0-$\pi$ transitions ? Does it depend on their physical origin ? What are the different kinds of 0-$\pi$ transitions ? That's the questions we are trying to address now.

Before that, note that non-0 junctions, beyond their fundamental interest, are of potential importance in the qubit community. Indeed, to fabricate a phase qubit, one needs a junction with two equivalent minima in the free energy, so that it constitutes a two-states system. This kind of device can be designed for example from loops containing both 0 and $\pi$-junctions [156]. $\pi$-junctions can also be used instead of 0-junctions to reduce the size of some quantum electronic devices [157].

#### 4.2.4.2 Various 0-$\pi$ transitions

**Single level Quantum Dot 0-$\pi$ transition** As stated above, this 0-$\pi$ transition is the consequence of a transition from a doublet to a Kondo/BCS singlet, driven by the ratio $\Delta/T_K$. In this context, it worth noting that the critical current is expected not to be non-zero at the transition, since the system transits through 0' and $\pi'$ states.

**Two-level Quantum Dot 0-$\pi$ transition** In a two-level QD, transitions from $\pi$ to 0-junctions may happen when the contributions of the various processes (those leading to

positive and negative current) vary with the gate voltage. How is the CPR at the transition ? Lee *et al.* answer this question in the case of a double occupancy of the 2L QD. When the $0/\pi$ transition corresponds to a transition between two different ground states (singlet/triplet transitions), it goes through intermediate 0' and $\pi'$ states (with the corresponding anharmonic CPR). However, when the 0-$\pi$ transition does not involve any change of magnetic state, the amplitude of the supercurrent simply goes to zero. To our knowledge, there is no generalization of this work for single occupancy of the 2L QD.

**SFS $\pi$-junctions/Zeeman $\pi$-junctions** The most famous way of fabricating a $\pi$-junction is to make a ferromagnetic Josephson junction, a thin ferromagnetic layer sandwiched between two superconductors (SFS). In this context, this is equivalent to applying a Zeeman magnetic field. In a ferromagnetic material or in presence of a Zeeman field, it exists an exchange energy $E_{ex}$ between the spins up and down (see fig. 4.19 (a) and [158, 159] for SFS junctions or [160] for Zeeman field $\pi$-junctions). This exchange energy induces a phase shift between the electron and the hole of the Andreev pair after propagation in the junction of length $d_f$ : $\Delta\phi = 2E_{ex}d_f/(\hbar v_F)$. It follows an oscillation of the superconducting order parameter, leading to a $\pi$-junction when $\Delta\phi \in [\pi/2, 3\pi/2]$ [161].

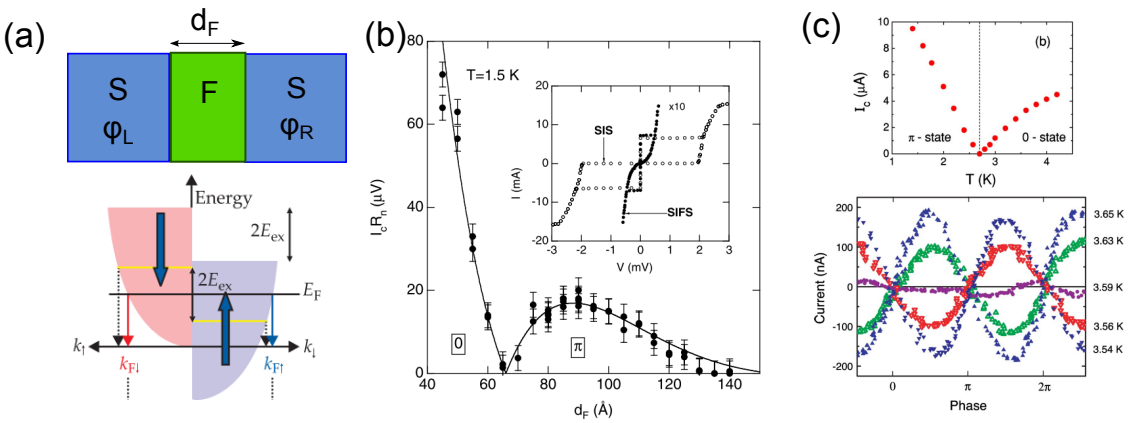


FIGURE 4.19 – (a) Schema of a SFS junction of size $d_F$ and of the electronic band structure in the F part. The density of states of spins up and down are shifted, so that, at the same energy, $k_\uparrow \neq k_\downarrow$. (b) Thickness driven 0-$\pi$ transition measured by Kontos et al. [161]. (c) Temperature driven 0-$\pi$ transition measured by Frolov et al. [162]. At the transition, the amplitude of the CPR (*i.e* the critical current) becomes too small to be measured.

Another way to see the phenomenon is to remark that the spin-degeneracy of the ABS is lifted by the exchange/Zeeman field [160]. Depending on its amplitude, the position of the ABS is modified, potentially leading to $\pi$-junctions or 0'/$\pi'$-junctions in the case of ABS crossings.

At the time I write these lines, it seems that nobody published measurements of Zeeman $\pi$-junctions (mainly because measuring a CPR with a high magnetic field is not that easy). However, in SFS junctions, the phenomenon has been largely investigated and is still an

intense subject of research, in relation with superconducting spintronics. The 0-$\pi$ transition in SFS junctions, driven by the thickness of the F layer, has been observed by Kontos *et al.* in 2002 [161], through critical current measurements (see fig. 4.19), followed in 2003 by the phase dependence [163]. If the temperature T is of the order of the exchange energy, the 0-$\pi$ transition can also be driven by the temperature [164]. The current-phase relation has been measured at this T-driven 0-$\pi$ transition by Frolov *et al.* [162], giving an interesting result : at the transition, the amplitude of the CPR (*i.e* the critical current) vanishes, or at least becomes too small to be measured (fig. 4.19 (c)). This result is in conflict with most theories predicting that, even though the first harmonic vanishes at the transition, it should remain a least a double harmonic contribution, so that the critical current is non-zero at the transition [165]. This second harmonic has been indeed detected by Shapiro steps measurements done in 2004 [166]. If we consider the transition as originating from a crossing of ABS, there should obviously be higher harmonics in the CPR at the transition, but they may be difficult to measure at the temperatures at which the transition happens (of the order of 3K).

Lim *et al.* present a variant of the Zeeman induced 0-$\pi$ transition, in the specific case of CNT and in presence of spin-orbit coupling[155]. In this case, because of the second conduction channel, there are two times more Andreev levels, split by spin-orbit coupling and magnetic field. 0-$\pi$ transitions are again induced by crossing of Andreev levels.

**Controllable Josephson junctions** If an SNS junction is thermally excited, the ABS above the Fermi energy can be populated. Then, they participate as well to the supercurrent giving a negative contribution : the amplitude of the supercurrent can be controlled [121] or even reversed [122]. Because of the phase-dependence of the ABS (like on fig. 4.5, the ABS are closer around $\varphi = \pi$ than 0), it is easier to populate the excited levels for superconducting phases around $\varphi = \pi$. That is why 0' and/or $\pi'$ phase are predicted and measured [167]. It is interesting to note that the measured current-phase relations at the transition have the same unexpected even symmetry as the one measured by Maurand *et al.* (see fig. 4.12).

#### 4.2.4.3 Quantum phase transitions ?

We have presented a number of 0-$\pi$ transitions, whose common characteristic is a sign reversal of the supercurrent. These sign reversals have a wide variety of origins : singlet-doublet transition, thermal excitation or a Zeeman/exchange splitting of the ABS, two-level regime in QDs.

Is it possible to classify these transitions among the (quantum) phase transitions ?

A quantum phase transition (QPT) is a phase transition happening at zero temperature, induced by the variations of a parameter different from temperature [168]. As any phase transition, it results from the competition between different ground states of the system, leading to different macroscopic phases. In this respect, the 0-$\pi$ transition induced by thermal

excitation by Baselmans *et al.* [167] is not a QPT.

Just like classical phase transitions, QPTs can be classified in first order transitions and second (or higher) order transitions. First order ones result from a level crossing, such that the two states coexist during the transition. In a second order QPT, the transition is continuous and driven by quantum fluctuations instead of thermal ones [169]: there exists a quantum critical region which is described by critical exponents, providing a very rich physics.

Speaking of quantum phase transition in a quantum dot is questionable. Is the reversing of the sign of the supercurrent a change of phase ? However, if it is the manifestation of a transition from a doublet to a singlet ground state, then this terminology is clearly suitable provided that this ground state is a collective one, not just a local one.

Some quantum phase transitions have been investigated in quantum dots. Mebrahtu *et al.* [170] studied resonant tunneling in a Luttinger liquid formed in a CNT between two barriers, where a second order QPT occurs varying the symmetry of these barriers. Roch *et al.* [106] have measured an infinite order QPT (Kosterlitz-Thouless transition) in a single molecule QD, where the system transits from a singlet to a triplet ground state varying the gate voltage. In both cases (singlet and triplet), the Kondo effect is involved, inducing a correlated state between the dot and the leads : it is appropriate to speak of QPT. Another example of QPT of second order is given by the investigation of the crossover between one and two-channel Kondo effect by Iftikhar *et al.* [41].

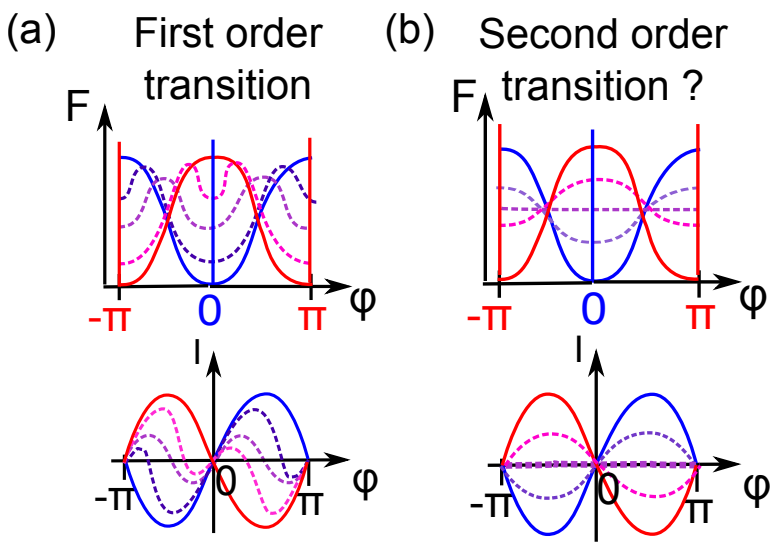


FIGURE 4.20 – Qualitative representation of free energy and the current-phase relation expected for two kinds of 0-$\pi$ transitions : (a) first order transition, as predicted for the 0-$\pi$ transitions due to level-crossing and (b) an hypothetic second order transition. In the first order case, at the transition, both 0 and $\pi$ states coexist at different $\varphi$, the critical current never vanishes and the CPR is anharmonic. In the second order case, the amplitude of the CPR decreases until 0, where the sign change occurs, and increases again in the other state.

In the case of the $0/\pi$ transition in a single-level QD, the use of the term quantum phase transition is reasonable. It is clearly due to a crossing of Andreev levels, and is thus a first-order QPT [91]. Typical free energies F and the corresponding CPRs are represented on fig. 4.20 (a) : at the transition, F has two minima, one at 0 and the other at $\pi$ (one of these minima can be local and the other global). That is why the CPR is strongly non-harmonic and its critical current never vanishes. The transition is discontinuous since, between the 0 and $\pi$ states, one can find mix states (0' and $\pi'$). Note that there is no quantum criticality associated to this transition.

0-$\pi$ transitions in SFS junctions and induced by a Zeeman field are also due to a level-crossing, the CPR at the transition should be similar to fig. 4.20 (a).

The situation is more complex in two-level quantum dots. According to Lee *et al.* who calculated the case of double occupation, while 0-$\pi$ transitions are the consequence of a transition from a magnetic state to the other (singlet, doublet, triplet), the system transits through the intermediate states 0' and $\pi'$. But as soon as the 0-$\pi$ transition does not involve a change of ground state of the system itself, there is no intermediate CPR and the critical current vanishes at the transition, as represented on fig. 4.20 (b). In this case, the amplitude of the CPR decreases until vanishing at the transition, and increases again but with a sign reversal. In this case, there is no intermediate state 0' or $\pi'$, it is the kind of transition that would be expected for a second order phase transition. Does it mean that these transitions without change of magnetic state are second order transitions or simply that they are not anymore quantum phase transitions ? Is it possible to extend this result to single occupancies ? For us, these questions are open.

## 4.3 Conclusion

- Superconducting correlations result from the attractive interactions between electrons in a metal, forming Cooper pairs. It results in a non-dissipative current induced by the superconducting phase $\varphi$, a macroscopic quantum parameter of the superconductor.

- These superconducting correlations can be induced in a non-superconducting material placed nearby superconductors, forming SNS junctions. This gives rise to a supercurrent in the junction, which is a periodic function of $\varphi$. The exact relation between the current and the phase, called the current-phase relation (CPR), gives insight into the physics of the normal part.

- It is possible to induce such a supercurrent in a CNT QD. Because of the Coulomb blockade and exclusion principle, if only one energy level participate to transport, the CPR is strongly dependent on the parity of the number of electrons on the QD : for odd occupancies, the supercurrent undergoes a sign reversal : this is a $\pi$-junction.

- However, if the Kondo effect is strong enough compared to superconductivity ($T_K \gg \Delta$),

it can help the formation of a BCS-Kondo singlet and restore a 0-junction. If $T_K \approx \Delta$, the system undergoes a 0-$\pi$ transition : the CPR is predicted to be very anharmonic since the transition from one ground state to the other (singlet to doublet state) is expected to be driven by $\varphi$. This is this CPR that we would like to measure.

- If two levels participate to the transport of Cooper pairs, the 0 or $\pi$ character of the CPR is no longer a good indicator of the ground state of the system since a second path for the electrons enables to overcome the exclusion principle. This regime is very poorly known experimentally, that's why we would like to use a CNT QD, which can be a perfect two-level system, to understand it better.

# 5 Current-phase relation measurement in a carbon nanotube quantum dot

We present in this chapter our measurements of current-phase relation in a carbon nanotube quantum dot. In a first part I describe the principle of the measurement, as well as the specific experimental setup used in this work. Then, the experimental results are presented. This work as been published in refs. [8] and [9].

## 5.1 Current-phase relation : experimental setup

### 5.1.1 Principle of measurement

Let's consider a Josephson junction[1], with a current-phase relation (CPR) equal to :

$$I(\varphi) = I_c f(\varphi) \tag{5.1}$$

with $I_c$ the critical current (*i.e.* the maximum of the CPR), and $f$ a periodic function of the superconducting phase. Our goal is to measure this CPR.

In this section, we first briefly introduce the problematic of the dynamics of Josephson junctions in order to understand which quantities are measurable. Then we present switching current measurements and, finally, we will see how to phase bias a junction and how the current-phase relation can be measured using a Superconducting Quantum Interference Device (SQUID). We will also discuss the setup we used to improve this detection.

#### 5.1.1.1 RCSJ model : switching current and hysteresis [111]

At finite temperature, even in absence of voltage bias, it is no longer possible to consider the phase as absolutely fixed : it undergoes fluctuations. To take into account this phase dynamics,

[1] I use this term in a generic way, referring to any non-superconducting material sandwiched between two superconductors.

we can use the resistively and capacitively shunted junction (RCSJ) model [2]. It consists in modeling the Josephson junction as a perfect Josephson element, such that $I = I_c \sin(\varphi)$ (we consider here the simplest case of a tunnel junction), in parallel with a resistance and a capacitor (see fig. 5.1 (a)). The whole system is biased by a current $I$ and $V$ is the voltage across it. This section will be based on M. Tinkham's book [111], the reader can refer to it for more details.

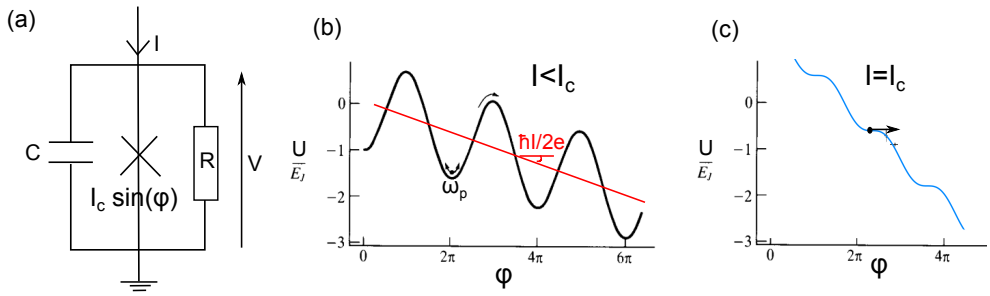


FIGURE 5.1 – (a) RCSJ modelisation of a real Josephson junction : the pure Josephson component ($I = I_c \sin(\varphi)$) is in parallel with a resistance $R$ and a capacitor $C$. (b) The phase dynamics is equivalent to the movement of a particle in the effective potential U, and submitted to a frictional force (see text). In the case of a superconducting tunnel junction, this potential is a cosine, tilted proportionally to the current I. (c) When $I = I_c$, there is no barrier preventing the particle from moving along $\varphi$, leading to the appearance of a voltage $V = \frac{\hbar}{2e}\frac{d\varphi}{dt}$.

**Tilted-washboard potential** Remembering the Josephson relation $\frac{d\varphi}{dt} = \frac{2eV}{\hbar}$ and Kirchhoff's current law, we can write [111]:

$$\frac{d^2\varphi}{dt^2} = -\omega_p^2 \sin(\varphi) + \omega_p^2 \frac{I}{I_c} - \frac{\omega_p}{Q}\frac{d\varphi}{dt} \tag{5.2}$$

with $\omega_p = \sqrt{2eI_c/\hbar C}$ and $Q = \omega_p RC$. This is formally similar to the equation of the motion of a particle, whose position is given by $\varphi$, in an effective potential

$$U(\varphi) = -E_J \cos(\varphi) - \frac{\hbar I}{2e}\varphi \tag{5.3}$$

and subjected to a frictional force $\frac{\hbar}{2e}^2 \frac{1}{R}\frac{d\varphi}{dt}$, with $E_J = -\frac{\hbar}{2e} I_c$. The potential 5.3 looks typically like fig. 5.1 (b) : it is a cosine tilted proportionally to the current $I$, informally called tilted washboard potential.

**Switching current** At zero temperature $T = 0$, while $I < I_c$, the phase is trapped in a local minimum of potential, where it can oscillate at pulsation $\omega_p$, but does not change

[2] Note that even at zero temperature, the phase can have a dynamics, due macroscopic quantum tunneling[171]. This effect will be neglected in the following.

dramatically. We still have $< V >= 0$, and the supercurrent is equal to $I = I_c \sin(\varphi)$. When the current is increased to $I = I_c$ (fig. 5.1 (c)), there is no barrier preventing the phase from increasing leading to a rapid onset of voltage $V = \frac{\hbar}{2e}\frac{d\varphi}{dt}$ across the junction. The current becomes dissipative.

This has important consequences for the critical current at non-zero temperature. Then, by thermal activation, it is possible for the fictitious particle to leave its local potential minimum for $I < I_c$. This current at which the particle tunnel the barrier during an increase of I, leading to the appearance of $V \neq 0$, is called the switching current $I_s$, and is always lower than the critical current. The larger is the temperature, the lower is the switching current.

**Retrapping current and hysteresis** We consider now the situation of a junction biased by a current $I > I_s$, in the normal state. We want to decrease the current in order to come back in a superconducting state (*i.e* we want to trap the particle in a local minimum). If the effective frictional force undergone by the particle is strong (we then say that the junction is overdamped), the particle is trapped as soon as $I < I_s$. But if this frictional force is weak (underdamped junction), then the particle will be retrapped only for a current lower than $I_s$ : this is the retrapping current $I_r < I_s$. Then the $V(I)$ characteristic of the junction is hysteretic (see fig. 5.2 (a) and (b)).

The dynamics of Josephson junctions in the general case is much more richer than what is presented here, but an exhaustive description is far beyond the scope of this manuscript. See for example the PhD thesis of I. Petkovic [172] for a detailed investigation in the specific case of ferromagnetic Josephson junctions.

#### 5.1.1.2 Critical current measurement

In absence of phase biasing, the phase across the Josephson junction is completely uncontrolled and the phase dependence of $I$ is *a priori* not experimentally accessible. However, the critical current can be simply obtained from a measurement of the $V(I)$ characteristic of the junction : it is the biasing current at which the junction turns non-superconducting, *i.e* the current at which a finite voltage appears across the junction (see fig. 5.2 (a) and (b)). As developed in the previous section, at finite temperature what is measured actually is not the critical current but a switching current, lower than the critical one.

Measuring only one $V(I)$ characteristic and reading $I_s$ on the curve is imprecise since the switching current originates from a thermal escape, and thus fluctuates around a mean value. A correct $I_s$ measurement must be averaged. To do so, we use the experimental setup described on fig. 5.2 (c). The sample is biased with a linearly increasing current (a "ramp of current" properly chosen, see figure), at a frequency which was typically $f = 273$ Hz. Then the voltage across the junction is monitored by a frequency counter, which is also synchronized on the incoming ramp of current. This voltage signal is schematically represented in red on fig. 5.2.

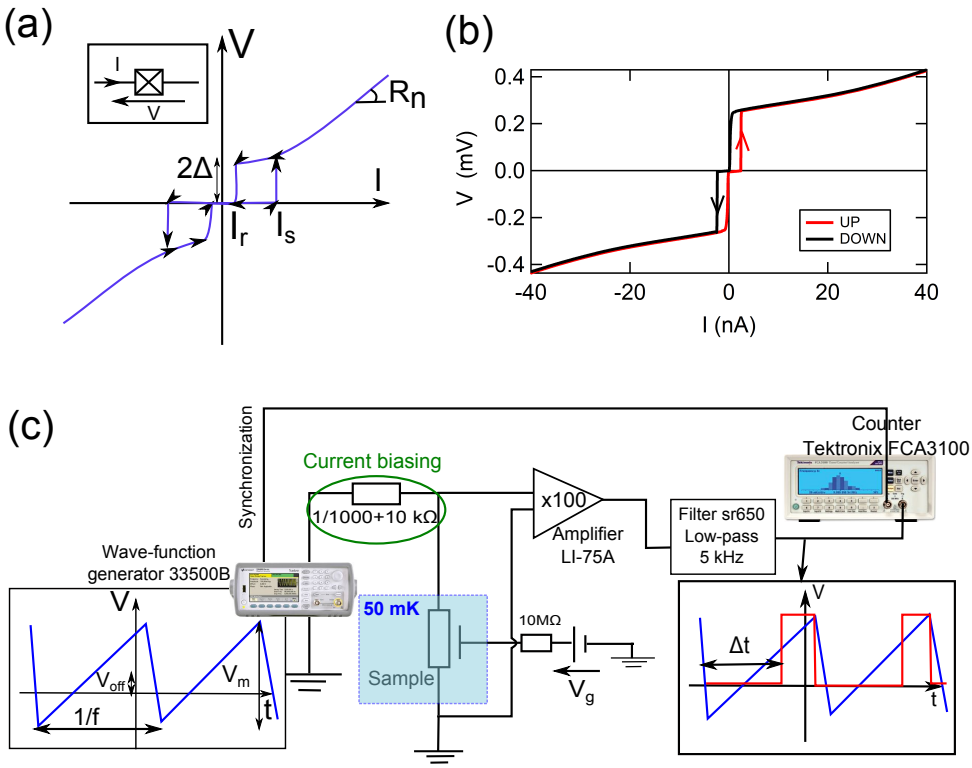


FIGURE 5.2 – (a) Typical characteristic of an underdamped junction, with an hysteretic behavior. $I_s$ and $I_r$ are respectively the switching and the retrapping currents. (b) Experimental measurement in a typical Josephson tunnel junction of normal resistance around $R_n = 8$ kΩ. (c) Electronic circuit used to measure the critical current of a Josephson junction (see text). In blue is represented the voltage ramp, used to make a current biasing with a resistance. In red is schematically represented the voltage across the junction.

While $I < I_s$, the junction is in the superconducting state with $V = 0$. As soon as $I = I_s$, $V$ becomes finite. The time $\Delta t$, measured from the beginning of the ramp, at which this sudden increase of voltage happens, is monitored by a frequency counter and averaged (typically 500 or 1000 times). The switching current is then deduced from the average time.

#### 5.1.1.3 Current-phase relation measurement : Superconducting Quantum Interference Device

**Phase biasing** To measure the current-phase relation, we need first to control the superconducting phase across the junction. To do so, we insert it in a superconducting loop where a perpendicular magnetic field imposes a flux $\Phi = B \times S$, $S$ being the area of the loop (see fig. 5.3 (a)).

In a superconductor, the current flows only in a thin layer close to the surface. If the loop is large enough, one can find a contour where the current is equal to zero [54]. Then, integrating

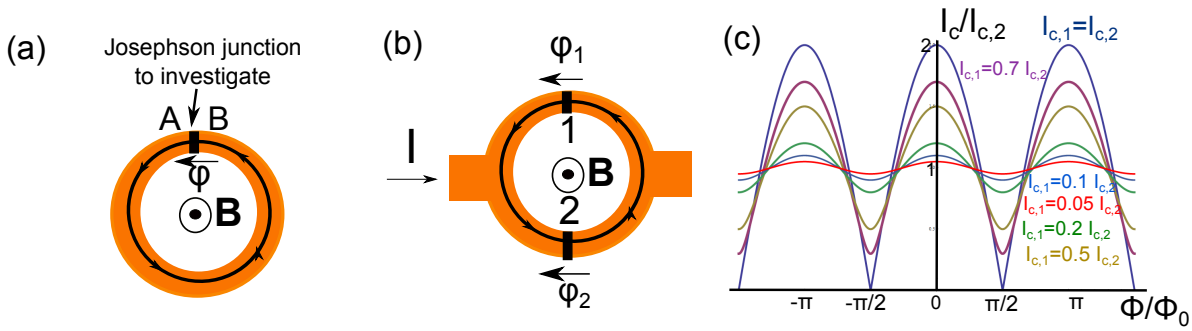


FIGURE 5.3 – (a) AC SQUID, containing a Josephson junction. A magnetic field $\vec{B}$ is applied perpendicularly to the device in order to control the phase $\varphi$ across the junction. (b) DC SQUID, a superconducting loop where two junctions have been inserted. (c) Critical current of the DC SQUID $I_c$ as a function of the magnetic flux enclosed by the loop for various ratios of the critical currents of the two junctions ($I_{c,1}/I_{c,2}$).

the formula 4.2 on this contour (the black circle on fig. 5.3 (a)), one finds that the vector potential is proportional to the phase gradient : $\vec{A} = \frac{2\pi}{\Phi_0}\vec{\nabla}\varphi$. On the other hand, the periodic boundary conditions in the loop gives that $\oint \vec{\nabla}\varphi.\vec{dl} = 2\pi n$ with $n$ an integer [111] (this is called the fluxoid quantization). In our loop, it gives the relation between the phase $\varphi$ across the junction and the flux $\Phi$ :

$$2\pi n = \frac{2\pi}{\Phi_0}\oint \vec{A}.\vec{dl} + \varphi = \frac{2\pi\Phi}{\Phi_0} + \varphi \tag{5.4}$$

Varying the flux $\Phi$ using a magnetic field, we can control the superconducting phase.

**Two junctions in the loop : DC SQUID** We consider now the situation represented on fig. 5.3 (b), where a second junction is inserted in the loop. This kind of device is called a SQUID, for Superconducting QUantum Interference Device. Then the fluxoid quantization gives :

$$\varphi_1 = \varphi_2 + \frac{2\pi\Phi}{\Phi_0} + 2\pi n \tag{5.5}$$

On the other hand, we can write the total current in the SQUID as the sum of the ones in each junction which yields :

$$I(\varphi_1, \varphi_2) = I_{c,1}f_1(\varphi_1) + I_{c,2}f_2(\varphi_2) = I_{c,1}f_1\left(\varphi_2 + \frac{2\pi\Phi}{\Phi_0}\right) + I_{c,2}f_2(\varphi_2) \tag{5.6}$$

The CPR of the whole SQUID is *a priori* quite complicated. But the measurable quantity is its critical current, *i.e.* the maximum of the $I$ as a function of $\varphi_2$. In the case of sinusoidal

CPRs, it is shown to be equal to [54]:

$$I_c = \sqrt{(I_{c,1} - I_{c,2})^2 + 4I_{c,1}I_{c,2}\cos^2\left(\frac{\pi\Phi}{\Phi_0}\right)} \tag{5.7}$$

Note that the maximum of the supercurrent of the SQUID is itself modulated by the magnetic field. In the case of a symmetric SQUID, with $I_{c,1} = I_{c,2} = I_0$, we get $I_c = 2I_0\left|\cos\frac{\pi\Phi}{\Phi_0}\right|$ : this is a very anharmonic function (see fig. 5.3 (c)), but still periodic in $\Phi$ : this can be used to measure small magnetic fields.

**Asymmetric SQUID : CPR measurement** In the case of a very asymmetric SQUID, the critical current of one of the junctions is very small compared to the other one : $I_{c,1} \ll I_{c,2}$. Then, it can be shown that for any CPR of the "small" junction $I_1 = I_{c,1}f(\varphi_1)$ and for a sinusoidal CPR of the "big" junction $I_2 = I_{c,2}\sin(\varphi_2)$ :

$$I_c = I_{c,2} + I_{c,1}f\left(\pi/2 - 2\pi\frac{\Phi}{\Phi_0}\right) \tag{5.8}$$

The critical current of the whole SQUID is equal to the critical current of the big junction (the one with a high supercurrent) modulated by the current-phase relation of the small junction (the one with a small critical current), dephased by $\pi/2$ (see fig. 5.3 (c)). In other words, when one junction has a big supercurrent compared to the other one, the phase across it is fixed at $\pi/2$ and all the variation of the phase by the magnetic field is applied across the small one.

An asymmetric SQUID is a very convenient device to measure the current-phase relation. This has been first done by Della Roca *et al.* [5], who measured the CPR of superconducting atomic contacts embedded in a SQUID, together with a reference tunnel Josephson junction of higher critical current such that the device is indeed asymmetric. In this work, the authors checked that, even at finite temperature, the measurement of the switching current as a function of the magnetic field is proportional to the CPR. This is true mainly because of the SQUID asymmetry : indeed, the overall effective potential felt by the phase, which determines the thermal escape, is dominated by the contribution of the big reference junction. Since the phase across this junction is pinned to $\pi/2$ at the switching, this contribution is constant[3]. It is the contribution of the small junction that evolves with the parameters of the experiment (mainly the gate voltage in our case), but thanks to the approximation $I_{c,1} \ll I_{c,2}$, it does not affect so much the thermal escape.

This kind of setup has also been used in Grenoble [135, 91] to measure the CPR in a CNT QD. In these experiments, the Josephson junction which plays the role of the big one is a CNT tuned with a gate in a highly conducting zone.

[3]This contribution can vary with the magnetic field if the critical current of the junction depends itself on the magnetic field. This can be neglected at the small scale of field needed to measure the CPR (a few Gauss).

### 5.1.2 Experimental setup

#### 5.1.2.1 Principle : three junctions SQUID

Our experimental setup is based on an asymmetric SQUID as described above : the Josephson junction of interest, here a CNT QD Josephson junction, is embedded in a superconducting loop. In the other branch of the loop is inserted a reference superconducting tunnel junction. We have however slightly modified this setup by adding a second identical reference junction as well as a third contact between them, as represented on fig. 5.4 (a). The principle of the current-phase relation remains strictly identical. Assuming that the two reference junctions have the same critical current $I_0$, the critical current of the SQUID is :

$$I_c = I_0 + I_{CNT} f\left(\pi - 2\pi \frac{\Phi}{\Phi_0}\right) \tag{5.9}$$

Now, there is a $\pi/2$ phase across each big junction, dephasing the CPR by $\pi$ instead of $\pi/2$.

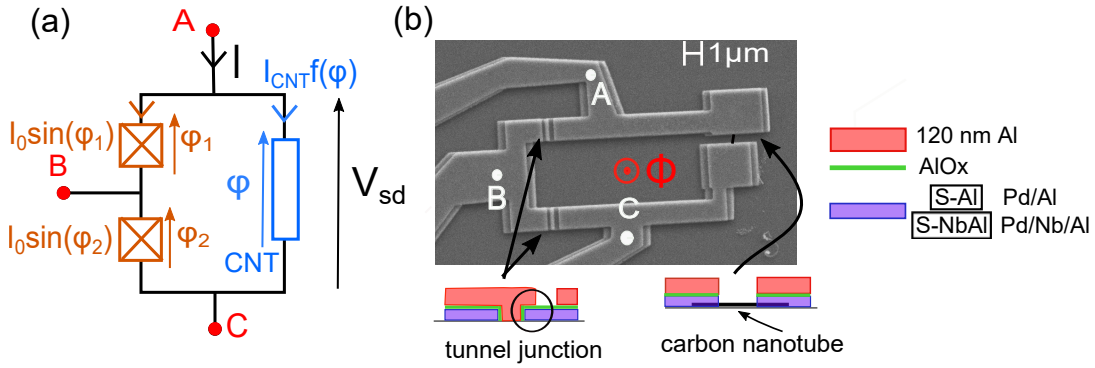


FIGURE 5.4 – (a) Schema of the measured asymmetric SQUID, containing two reference JJs in parallel with a CNT based Josephson junction. To phase bias the CNT junction, a magnetic flux $\Phi$ is applied with a magnetic field perpendicular to the SQUID. (b) Scanning electron microscopy image of the sample, with the layers constituting the tunnel junctions and the contacts of the CNT. The first layer of sample S-Al is made of Pd(7 nm)/Al(70 nm). The first one of S-NbAl is made of Pd(7 nm)/Nb(20 nm)/Al(40 nm).

The main advantage of this setup is that, taking benefit from the third contact, one can access the conductance of each of the three components : the two junctions and the CNT (in a simple SQUID, this is impossible without opening the loop). This is for example very interesting to test the CNT and determine its room temperature resistance. This allows as well to measure the differential conductance of the CNT in the superconducting state.

#### 5.1.2.2 Test of the setup

In order to be sure that this modified SQUID enables the measurement of the current-phase relation, it has been tested with Josephson junctions whose CPR was known. The verification

was needed in order to check that the dynamics of the system was not modified by the third junction.

This verification is related in ref. [6], where a model is proposed to understand the phase dynamics of the three junctions SQUID. This model is compared to the CPR measurement of a Josephson tunnel junction with a small critical current instead of the CNT. As expected, the measured CPR is sinusoidal. A CPR measurement has also been performed on a CNT in a high conducting regime, where the channel transmission has been extracted from the normal conductance at zero bias : the CPR has the shape expected from formula 4.11 after being renormalized by a factor which depends on the sample but not on the gate voltage.

From this, we can say that we can reliably measure current-phase relations with this setup. Note however that the proportionality factor between the measured switching current and the critical current is not known (but constant for a given sample).

#### 5.1.2.3 Sample fabrication

The CNT are first grown by chemical vapor deposition (see chapter 3) on a silicon wafer covered by an oxide layer. We chose to use a doped silicon wafer so that it can play the role of a back-gate for the nanotube.

The nanotube contacts and the tunnel junctions are made during one unique lithography step. A first aluminum-based multi-layers is deposited with an angle of 15°, is oxidized under oxygen and is covered by a second layer of aluminum (120 nm) (fig. 5.4) (read chapter 3 for details about making tunnel junctions and lithography techniques). The contacts of the nanotube are separated by a distance $L = 400$ nm. Two samples have been measured, with two different contacts on the nanotubes (the first layer mentioned above, in purple on fig. 5.4). The first sample, called S-Al, is contacted with a Pd(7 nm)/Al(70 nm) bilayer, whose superconducting gap is $\Delta_{PdAl} = 65 \pm 5$ $\mu$eV. The superconducting gap of pure aluminum is about $\Delta_{Al} \approx 200$ $\mu$eV but, here, it is strongly reduced by the palladium layer, which is essential for good contacts on CNT. For the second sample, called S-NbAl, we added a niobium layer between palladium and aluminum, in order to increase the gap to $\Delta_{PdNbAl} = 170 \pm 5$ $\mu eV$ [4] : Pd(7 nm)/Nb(20 nm)/Al(40 nm). The sample measured are similar to the one represented on fig. 5.4 (b).

For sample S-Al, the two Josephson junctions have normal resistances $R_{n,1} = 9$ k$\Omega$ and $R_{n,2} = 9.5$ k$\Omega$, corresponding to theoretical critical currents around 20 nA (obtained thanks to multi-gap Ambegaokar formula [173]). For sample S-NbAl, we measure $R_{n,1} = 1.6$ k$\Omega$ and $R_{n,2} = 1.9$ k$\Omega$, corresponding to 260 and 300 nA.

The sample is then cooled down in a dilution refrigerator of base temperature 50 mK as

[4] This value of the superconducting gap felt by the CNT has been extracted from differential conductance measurement in the superconducting state.

detailed in chapter 3. The phase difference across the CNT-junction $\varphi$ is controlled applying a magnetic field $B$ perpendicularly to the sample. The magnetic flux enclosed by the loop is $\Phi = B \times S$, with $S \approx 40\ \mu\text{m}^2$ the loop area.

## 5.2 Characterization of the sample in the normal state

Before presenting the current-phase relation measurements in the samples, we detail here their characterization in the normal state, in order to determine the parameters of the CNT quantum dots.

### 5.2.1 Differential conductance in the normal state

As detailed in chapter 2, a CNT QD can sustain different regimes, depending on the values of the coupling $\Gamma$ between the dot and the reservoirs and the charging energy $U$ : as $\Gamma$ increases compared to $U$, the transport regime goes from pure Coulomb blockade to Kondo effect, and finally Fabry-Pérot regime. To characterize the system, we need to establish the stability diagram of the system (such as what is represented on fig. 2.13). To do so, we measure the differential conductance $dI/dV_{sd}$ of the sample as a function of the bias voltage $V_{sd}$ and the gate voltage $V_g$ in the normal state. This is done using the lock-in-amplifier technique described on fig. 3.7 (with a modulation of 20 $\mu$V) and applying a magnetic field large enough to suppress the superconductivity in the contacts. Note that we measure the contribution of both the nanotube and the reference Josephson junctions. In the normal state, the contribution of the tunnel junctions is constant and it can be subtracted to obtain the conductance of the nanotube alone.

For sample S-Al, contacted with palladium and aluminum, a magnetic field $B = 0.13$ T is enough to suppress superconductivity. However, for the sample S-NbAl contacted using niobium, we needed to apply a much higher magnetic field to affect the superconductivity. We choose to apply a magnetic field of $B = 1$ T, mainly to preserve the Kondo effect. The resulting stability diagrams of both samples are represented on fig.5.5 and 5.6.

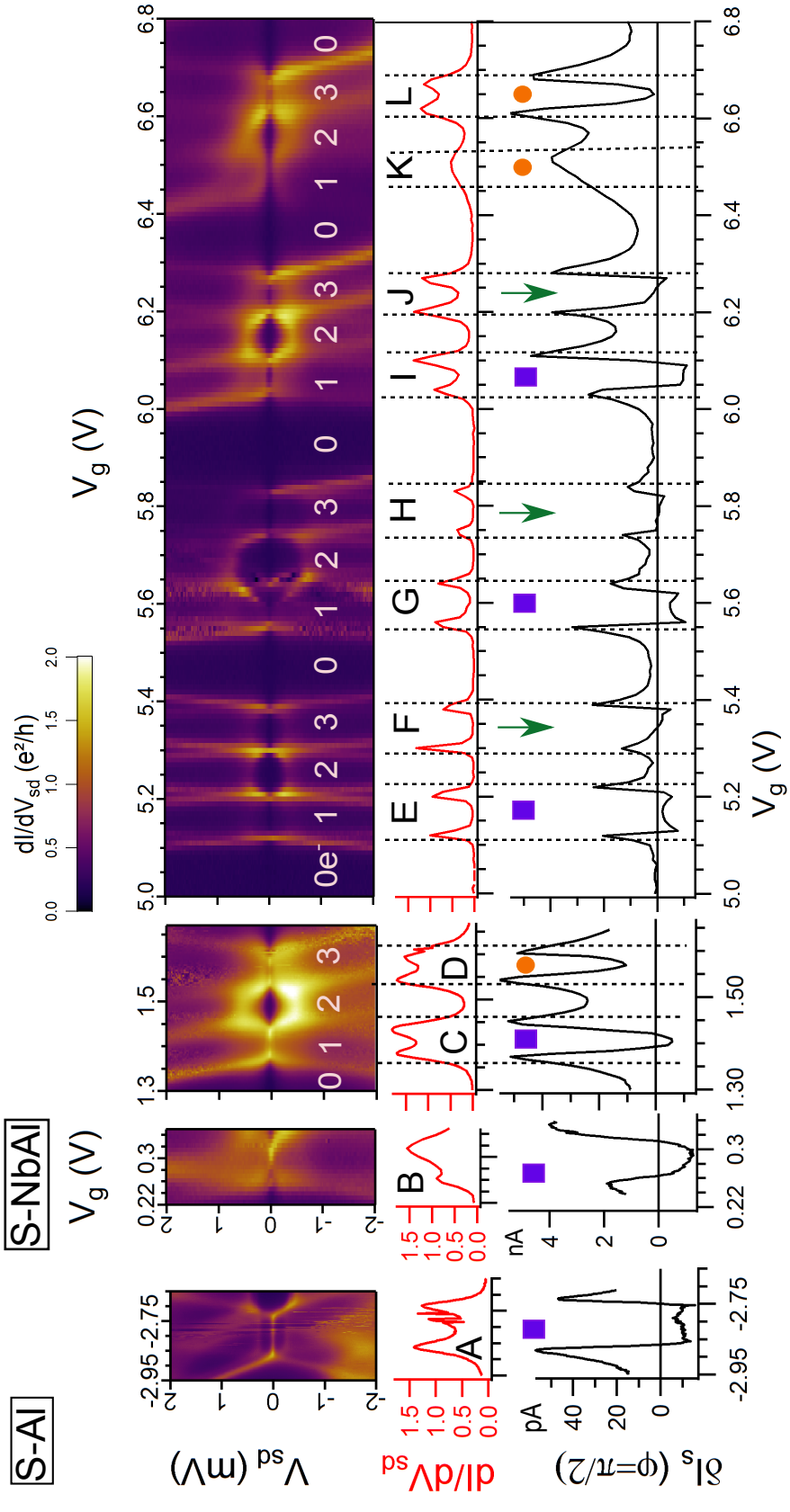


FIGURE 5.5 – Colorplot : Differential conductance $dI/dV_{sd}$ as a function of bias voltage $V_{sd}$ and gate voltage $V_g$ for both samples S-Al and S-NbAl in the normal state, applying $B = 0.13$ T for S-Al (diamond A) and $B = 1$ T for S-NbAl (diamonds B to L). In white is written the number of electrons in the last occupied shell. Red graphs : horizontal cuts showing $dI/dV_{sd}$ at zero bias versus gate voltage $V_g$ in the normal state. Black graphs : supercurrent $\delta I_s(V_g)$ for a superconducting phase difference of $\varphi = \pi/2$. Orange circles indicate Kondo induced 0-junction, for odd occupancies. Purple squares show $\pi$-junctions with a single-level behavior. The green arrows indicate two-level 0-$\pi$-junctions. The consequences of two-level physics are more spectacular for F and J than for H, where $\delta E$ is larger than in F and J (see table 5.1).

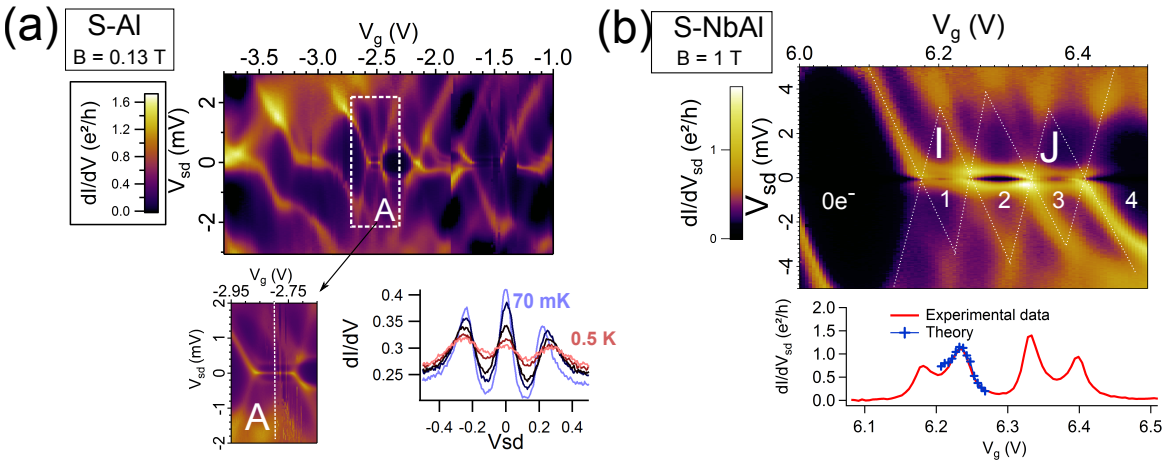


FIGURE 5.6 – (a) Differential conductance ($\mathrm{d}I/\mathrm{d}V_{sd}$) in the normal state of the CNT junction versus gate voltage $V_g$ and bias voltage $V_{sd}$ for a large range of $V_g$ for sample S-Al. We focus on the diamond presenting Kondo effect : diamond A. A 0.13T magnetic field is applied to destroy superconductivity in the contacts. The temperature dependence of the conductance at the center of the Kondo ridge A is also presented. (b) Same quantity, in sample S-NbAl, on a range of gate voltage including diamonds I and J. A 1T magnetic field is applied to suppress superconductivity in the contacts. The number of electrons in the last occupied energy levels is indicated in white. Below, $\mathrm{d}I/\mathrm{d}V_{sd}(V_{sd})$ at zero bias is plotted. The blue symbols superimposed with the curve correspond to the theoretical fit of the conductance (see text).

### 5.2.2 Determination of the QD's parameters

#### 5.2.2.1 Determination of the charging energy and the energy level spacings

The sample S-Al exhibits Coulomb diamonds (fig. 5.6 (a)). We focus on the diamond called A, where there is a maximum of conductance at zero bias, indicating Kondo effect. Two satellite peaks at finite $V_{sd}$ indicate inelastic cotunneling.

In the sample S-NbAl, Coulomb diamonds are present on a large range of gate voltage (diamonds B to L and more, not shown) with a four-fold degeneracy. These features are typical of a CNT, where each energy level is nearly orbitally degenerated in addition to the spin degeneracy. This enables the determination of the electronic occupancy of the highest occupied shells : N=0, 1, 2 or 3 electrons (white numbers on fig. 5.5). The presence of cotunneling peaks at finite energy indicates that the orbital degeneracy is lifted, either due to spin-orbit interactions, boundary conditions or defects in the nanotube [72, 13, 75]. In most oddly-occupied diamonds, the conductance is non-zero at zero-bias, suggesting the presence of Kondo effect (diamonds B-D and I-L).

The relevant energies of the system can be determined from these stability diagrams (fig. 2.16) : $\Delta E$ the spacing between two successive energy levels in the CNT, $U$ the charging energy and $\delta E < \Delta E$, $U$ the lift of degeneracy [89, 98]. The procedure is the following :

first, the lever arm $\alpha$ between $V_g$ and the energy $\epsilon_d$ (see fig. 2.16) is extracted from the ratio between the height and width of a well defined diamond. Then, measuring the width of the other diamonds, we obtain $U$ and $\Delta E$. The lift of the orbital degeneracy $\delta E$ is determined from the spacing between the inelastic cotunneling peaks in the diamonds. These parameters are summarized in table 5.1 for all the diamonds with odd electronic occupancies.

#### 5.2.2.2 Determination of the Kondo temperature in sample S-Al

The Kondo temperature is evaluated from the temperature dependence of the Kondo resonance, represented on fig. 5.6 (a). See section 2.3.1.2 for a detail of this procedure. Once $T_K$ is evaluated, $\Gamma$ is obtained from the formula, recalled from chapter 2 :

$$T_K = \sqrt{\Gamma U/2}\exp(-\pi\frac{|4\epsilon^2 - U^2|}{8\Gamma U}) \tag{5.10}$$

#### 5.2.2.3 Determination of the Kondo temperature in sample S-NbAl

In sample S-NbAl, the determination of the coupling $\Gamma$ or of the Kondo temperature is more complicated because of the presence of the 1 T magnetic field.

**Choice of the magnetic field** In order to understand the choice of 1 T for the sample with niobium, the magnetic field dependence of the differential conductance is given on fig. 5.7 (c). At zero magnetic field, we recognize the superconducting gap centered around zero bias. The sub-gap current may be due to multiple Andreev reflections and, at zero bias, to the supercurrent itself. To make these features disappear, we need to apply a magnetic field of 1 T, that's why we have chosen this value. However it is very questionable since, at higher field, a dip appears again, suggesting that some other physics is involved, probably related to the (multi-level) Kondo effect.

Note that the field dependence depends on the diamonds and, even with the 1 T magnetic field, there is still a dip at zero bias for most gate voltages (see fig. 5.5 and 5.7 (a)). Moreover, the temperature dependence of the Kondo peak in diamond C is shown on fig. 5.7 (b) : the temperature affects only the top of the peak, which seems to be superimposed with a large structure, independent of temperature. This large structure is too large to be the Kondo peak, and is found all over the sample.

We can give the following reasons to account for these unusual features in the conductance :

- The 1 T magnetic field strongly affects The Kondo effect, whose $T_K$ is generally around 1K in CNT, so that the resonance can be split. This would explain the zero bias dip seen in I, J and K.

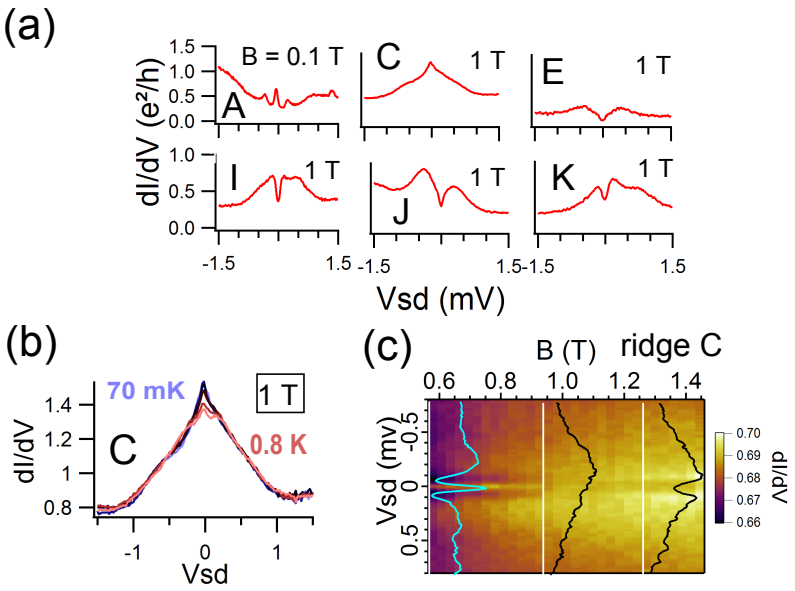


FIGURE 5.7 – (a) Differential conductance $dI/dV_{sd}$ in the normal state as a function of $V_{sd}$ at half-filling of six different diamonds : A (S-Al) and C, E, I, J and K (S-NbAl). (b) Temperature dependence of the same quantity, for ridges A (S-Al) and C (S-NbAl). To destroy the superconductivity in the contacts, a magnetic field is applied perpendicular to the sample : $B = 0.13$ T for the diamond A and $B = 1$ T for the diamonds C, E, I, J and K.

- These zero bias dip could also be due to some remaining superconductivity. We did not increase the field above 1T in order not to affect too much the Kondo effect.
- The large structures could be interpreted as the superimposition of the inelastic cotunneling peaks at $V_{sd} \approx \pm 0.3 - 0.5$ meV with the split Kondo peaks.
- This makes also think about two-stage Kondo effect [107]. This Kondo effect, involving two energy levels, is expected to occur in N=2 occupied diamonds, but it has also been observed in N=1, 3 diamonds and interpreted as due to the presence of a Kondo impurity nearby the sample [109]. However, we have no clear evidence of that.

**Determination of the coupling Γ by fitting with theory** Despite these difficulties, assuming that the unusual features at zero bias are mainly caused by the magnetic field (splitting of the Kondo resonance) and using a theory able to take it into account, we can however have an estimation of the coupling Γ.

This has been done in collaboration with David Luitz and Volker Meden, who performed a fit of our data by Quantum Monte Carlo (QMC) calculations (see our paper [8]). However, since this method was very time consuming, we only used it for the diamond I, whose differential conductance is given with more details on fig. 5.6 (b). The junction is modeled by an Anderson

impurity model with right ($R$) and left ($L$) BCS superconducting leads and superconducting order parameter $e^{\pm i\varphi/2}\Delta$, as in refs. [138, 134, 146, 147, 148, 144, 143, 119, 10, 174]. The interaction of electrons on the QD is given by a standard Hubbard term with charging energy $U$ and the coupling of the leads to the QD is described by the energy independent hybridization strength $\Gamma_{L/R}$. Our friends theoreticians solved it using the numerically exact CT-INT Monte Carlo method [10] in the normal state ($\Delta = 0$) in a magnetic field and calculated the finite temperature linear conductance for different $\Gamma_{L/R}$ as a function of the dot energy $\epsilon_d$. The amplitudes of the magnetic field and the charging energy are fixed to the experimentally determined values $B = 1\,\mathrm{T}$ and $U = 3.2\,\mathrm{meV}$ of diamond I. A comparison with the measured conductance at zero source drain voltage (i.e. in equilibrium) yields a set of parameters that fit the experiment best. The best fit is displayed in fig. 5.6 (b) (blue symbols) and corresponds to $\Gamma_R + \Gamma_L = 0.44\,\mathrm{meV}$, $\Gamma_R/\Gamma_L = 4$. We also slightly varied $T$ to estimate the electronic temperature in the sample and obtained $T = 150\,\mathrm{mK}$.

**Other diamonds** For diamonds B and C, the Kondo temperature is evaluated similarly as for sample S-Al, from the temperature dependence of the Kondo resonance (fig. 5.7 (b)). For the other oddly occupied diamonds of sample S-NbAl, the Kondo resonances are not clear enough to extract $T_K$ directly and we could not use the QMC method for all these diamonds. Following Ref. [89], we roughly estimate the coupling $\Gamma$ from the width in $V_{sd}$ of the inelastic cotunneling peaks at N=2, and assumed that $\Gamma$ does not vary within the same shell. We estimate that these approximations are correct within an uncertainty of 20%. Once $T_K$ or $\Gamma$ is evaluated, the other one is obtained from the formula 5.10.

#### 5.2.2.4 Summarize of the determination of the parameters

All the parameters are gathered in table 5.1.

For S-NbAl, $\Delta E$ is typically equal to 4-5 meV, a value reasonably consistent with the expression $\Delta E \approx \frac{hv_F}{2L}$, with $v_F \approx 8.10^5$ m/s the Fermi velocity [57] for a metallic nanotube and $L = 400$ nm. The value of $\delta E$ varies between 0.2 and 0.8 meV, which is small compared to U (around $2-3$ meV) and of the order of $\Gamma$ ($0.2-0.5$ meV), suggesting that the two-level physics associated to CNT is relevant (see section 4.2.3). Note that, for the range of gate voltage presented, there is no signature of SU(4) Kondo effect, that would be characterized by a strong Kondo effect spreading over N=1, N=2 and N=3 diamonds and a conductance that can reach $4e^2/h$ [78]. To observe this kind of exotic Kondo effect, the Kondo temperature should be very large compared to the lift of degeneracy $\delta E$ [7]. We present in section 5.4.2 a range of gate voltage where this condition is fulfilled.

| | A | B | C | D | E | F | G | H | I | J | K | L |
|---|---|---|---|---|---|---|---|---|---|---|---|---|
| Occupancy (N=) | 1 | 1 | 1 | 3 | 1 | 3 | 1 | 3 | 1 | 3 | 1 | 3 |
| U (meV) | 1.6 | 2.8 | 2.3 | 2.3 | 3.9 | 3.9 | 3.4 | 3.4 | 3.2 | 3.2 | 2.3 | 2.3 |
| $\Gamma$ (meV) | 0.25 | 0.43 | 0.5 | 0.5* | 0.35* | | 0.4* | | 0.44 | 0.45* | 0.55* | |
| $\Delta E$ (meV) | 1 | 5 | 4 | | 4 | | 5 | | 4 | | 3.5 | |
| $\delta E$ (meV) | 0.3 | 0.8 | 0.5 | 0.2 | 0.4 | 0.4 | 0.7 | 0.7 | 0.3 | 0.3 | 0.25 | 0.25 |
| $T_K$ (meV) | 0.036 | 0.06 | 0.13 | 0.13* | 0.01* | | 0.03* | | 0.048 | 0.05* | 0.15* | |
| $\Delta$ (meV) | 0.065 (Pd/Al) | 0.17 (Pd/Nb/Al) | | | | | | | | | | |

TABLE 5.1 – Quantum dot's parameters for different gate voltage regions : the charging energy U, the coupling $\Gamma$, $\Delta E$ the level-spacing, $\delta E$ the lift of orbital degeneracy, $T_K$ the Kondo temperature calculated with formula 5.10 (at $\epsilon_d = 0$) and the superconducting gap $\Delta$. The values with a * are known only with a 20% uncertainty, while the other values are given within a 10% uncertainty.

## 5.3 Superconducting state : Current-phase relation measurements

We now restore superconductivity, switching off the magnetic field, so that we can measure the current-phase relation (CPR) of the QD JJ. For this, we follow the experimental procedure described in section 5.1.1.2, with a current linearly increasing at a rate $\mathrm{d}I/\mathrm{d}t = 37\ \mu$A/s. The phase is controlled varying a magnetic field of the order of a few Gauss. To obtain the modulation $\delta I_s$ of the switching current of the SQUID versus the magnetic field, the constant contribution of the reference junctions is subtracted (this contribution represents 2 nA for sample S-Al and 90 nA for sample S-NbAl).

### 5.3.1 Superconducting state : Gate controlled 0 or $\pi$-junction and two-level physics.

We first focus on the measurement of the supercurrent at a fixed phase $\varphi = \pi/2$, represented as a function of the gate voltage on Fig. 5.5 (black curves). This quantity is proportional to the critical current of the junction in the case of sinusoidal CPRs (which represent most of the CPRs at finite temperature), with an additional information on the sign.

For the diamonds with an even electronic occupancy, this supercurrent is always positive, indicating 0-junctions. In contrast, for odd occupancies, there are two situations : for some diamonds, A, B, E, F, G, H, I and J (blue squares and green arrows on Fig. 5.5), the supercurrent is negative around the center of the diamond and has a reduced amplitude : this is the signature of a $\pi$-junction. But, for the other odd diamonds (D, K, L, orange circles

on Fig. 5.5, and diamonds at $V_g \geq 6.8$V (not shown), the supercurrent does not change sign. These odd parity 0 junctions are attributed to the Kondo effect that screens the magnetic moment of unpaired electrons (see section 4.2.2). This hypothesis is corroborated by the comparison of the ratio $\Delta/T_K$ for the different diamonds (see table 5.1). When $T_K \ll \Delta$, the Kondo correlations are suppressed by the superconducting proximity effect such that the junction turns $\pi$. But when $T_K \geq \Delta$, as for diamonds C, D, K, L and $V_g \geq 6.8$V, the supercurrent is enhanced by the cooperation of the Kondo effect and superconductivity, leading to a 0-junction.

However, some of the odd parity $\pi$-junctions (F, H and J, green arrows on Fig. 5.5), of filling factors N=3, reveal unusual features. For typical single-level $\pi$-junctions as the ones indicated by blue squares, the supercurrent is symmetric relatively to the center of the diamond [4, 174] (see fig. 4.16 (a)), which corresponds to the half-filling point in a single-level description. But for the diamonds indicated by green arrows, the supercurrent $\delta I_s$ has a completely different behavior. All over the left side of the diamond (close to the N=3 to 2 degeneracy point), the supercurrent is positive. This 0-junction in an odd-occupied diamond cannot be attributed to the Kondo effect, that is not strong enough to change the doublet in singlet as in diamonds D and L. Therefore, it can only be attributed to the participation of a second energy level to the transport of Cooper pairs [137, 12]. Close to the N=3 to 4 degeneracy point (right side of the diamond), the junction is in a $\pi$ state. The 0 to $\pi$ transition occurs around the center of the N=3 diamond, and the $\pi$-0 transition between the N=3 and N=4 diamonds.

The supercurrent is asymmetric with respect to the center of the diamond, similarly to what has been measured by Van Dam *et al.* [4] in multi-level quantum dots (fig. 4.15 (b)). This is also what was predicted, but not yet measured, in the particular case of two-level quantum dots [149] and carbon nanotubes [151] (see fig. 4.16 (a) and 4.17). The striking point of our experiment is that these two-level behaviors, are observed, for three diamonds, at N=3 occupancies instead of both N=1 and N=3 as predicted. This point will be discussed in the following (in section 5.3.3).

Our experiment thus demonstrates the existence of two kinds of gate induced 0-$\pi$ transitions : some involve only single-level physics whereas others have signature of two-level physics. In the next two sections, we detail the phase dependence of the supercurrent in each regime.

### 5.3.2 Current-phase relation in the single-level regime

In this part, we discuss the phase dependence of the supercurrent in the single-level regime (in this experiment, it means investigating the N=1 diamonds).

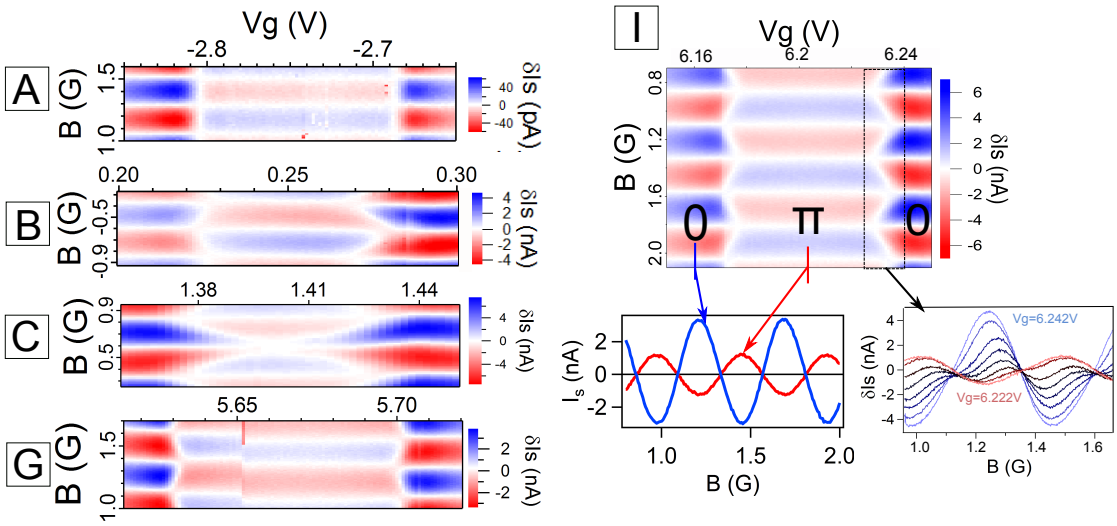


FIGURE 5.8 – Modulation of the switching current of the SQUID $\delta I_s$, proportional to the CPR, as a function of the magnetic field B and the gate voltage $V_g$, for the diamonds A, B, C, G and I. Vertical cuts at the 0-$\pi$ transition are represented for ridge I, showing the whole transition. For the diamond G, the color-plot exhibits a discontinuity, probably due to the trapping of a vortex. For the diamond I, some vertical cut of the colorplot are shown in the 0, $\pi$, and transition regions.

#### 5.3.2.1 Detailed analysis of the single-level 0-$\pi$ transition

**CPR at the 0-$\pi$ transition** In this section, we focus on oddly occupied diamonds in the single-level regime, which present in the superconducting state a $\pi$-junction centered in the middle of the diamonds and 0-junction on the edges : diamonds A, B, C, G and I. This pattern is consistent with 0-$\pi$ driven by the interplay between the Kondo effect and the superconductivity, since $T_K$ is symmetric with respect to the center of the diamond, where it is minimal, and increases on the edges (formula 2.23).

The modulation of the switching current $\delta I_s$ versus magnetic field B, proportional to the CPR, is measured for various $V_g$ and is represented on Fig.5.8 for some representative oddly-occupied ridges. Diamond A, from sample S-Al, presents a small supercurrent ($\approx$ 40 pA) and a transition from 0 to $\pi$ that extends on a very small range of $V_g$ (smaller than 100 $\mu$V), beyond the precision of our experiment. In contrast, in sample S-NbAl, due to a larger superconducting gap, the $\pi$-junction supercurrent is larger ($\approx$ 4 nA). Moreover, the width in gate voltage of the transition is larger, allowing to measure the CPR very accurately in the transition region. Noteworthy, the region C exhibits an incomplete 0-$\pi$ transition where the CPR is not completely reversed in the center of the diamond ($\pi'$ state).

On fig. 5.9 are shown CPRs extracted from the 0-$\pi$ transition of diamond I and C. On the edges of the diamonds, far from the transition (fig. 5.9 (a.1) et (b.1)), the junction behaves as a regular 0-junction, with a CPR proportional to $\sin(\varphi)$. In contrast, at the center of the diamond (Fig. 5.9.(a.6)), where $T_K$ is minimum, the CPR is $\pi$-shifted ($\delta I_s \propto \sin(\varphi + \pi)$) and

has a smaller amplitude, characteristic of a $\pi$-junction. In between, the CPR is anharmonic : a distortion appears first around $\pi$ and develops as $T_K$ decreases. The CPR is composite, with 0-junction behavior around $\varphi = 0$ and a $\pi$-junction behavior around $\varphi = \pi$. The transition from one part to the other is achieved by varying the superconducting phase. The global state of the system is called 0' or $\pi'$ depending on what is the dominant contribution (and where is the global minimum of the free energy, see section 4.2.4).

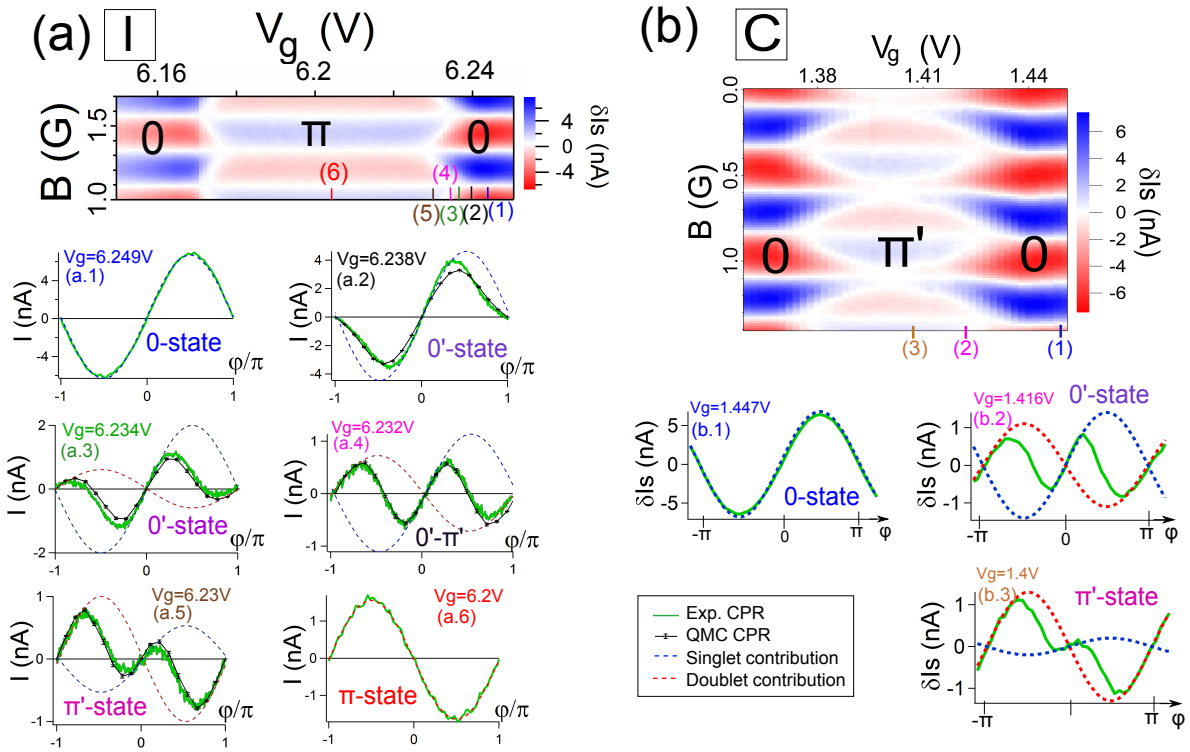


FIGURE 5.9 – (a) CPR, for diamond I, near the transition (green continuous line) versus the superconducting phase $\varphi$. The dashed lines are guides to the eyes and represent the contributions of the singlet (0-junction, in blue) and the doublet state ($\pi$-junction, in red). (b) Same type of curves for region C, which exhibits an incomplete 0-$\pi$ transition.

**Comparison with QMC calculations** For a quantitative comparison between theory and experiment, still in collaboration with D. Luitz and V. Meden, we performed a second CT-INT calculation in the superconducting state ($B = 0$) in diamond I to obtain the CPRs in the transition regime. Using the measured value of the superconducting gap $\Delta = 0.17\,\text{meV}$ and the previously determined parameters, the Josephson current has been computed as a function of the phase difference $\varphi$. The theoretical CPR are calculated at various $\epsilon_d$ (related to $V_g$ by $\epsilon_d = \alpha V_g$) and plotted as black lines in comparison to our experiments in fig. 5.9 (a.2) to (a.5). Since our setup yields a switching current that is necessarily smaller than the

critical current, the experimental CPRs were multiplied by a unique correction factor chosen to obtain the best agreement with the QMC results. The agreement for the shape of the CPR is excellent ; however a shift of the energy level $\delta\epsilon_d = 0.28$ meV of the theoretical CPRs is needed to superimpose them with the experimental ones : the QMC calculations predict a transition region centered around a smaller $\epsilon_d$ than measured experimentally (see fig. 5.10 (a)). Note however that the width of this transition is very well reproduced. Interestingly, these data have been fitted by Zonda *et al.* [175] with a perturbative theory : they argue that, with a charging energy of 3.4 meV instead of 3.2, the theory works perfectly. It seems that this discrepancy between experiment and theory would originate from a bad estimation of $U$.

The comparison of the measurements and calculations can even be refined employing Fourier decompositions $I(\varphi) = a_1 \sin(\varphi) + a_2 \sin(2\varphi) + a_3 \sin(3\varphi) + \dots$ of the $2\pi$-periodic CPRs. The first three amplitudes are sufficient to describe the experiment perfectly ; see fig. 5.10 (b) where they are shown as functions of $\epsilon_d$. The theoretical model thus exactly captures the nontrivial finite temperature phase dependence of the measured Josephson current.

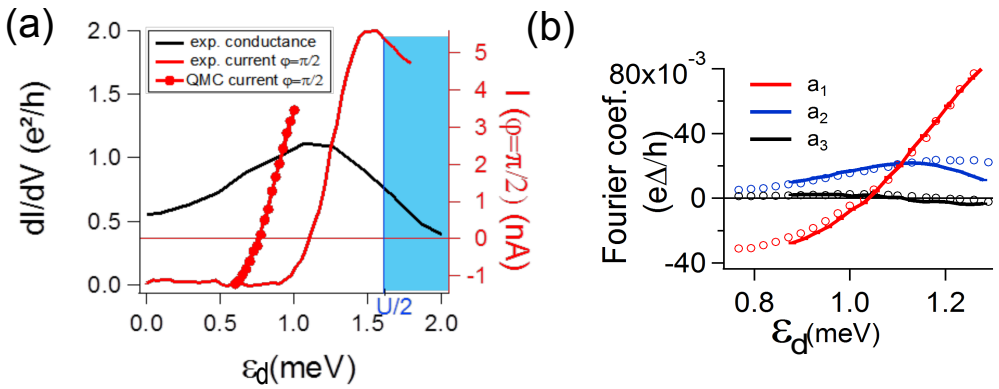


FIGURE 5.10 – (a) Supercurrent at a fixed superconducting phase difference $\varphi$ for diamond I, as a function of $\epsilon_d$ as well as the conductance in the normal state at zero bias. While the experimental data are represented with the red line, the dotted red line represents QMC data, without any adjustment. Only the positive values of $\epsilon_d$ have been plotted. Note that ref. [175] explain the shift of the calculations compared to theory by a slightly wrong estimation of the charging energy U. (b)Fourier analysis of the CPRs of diamond I near the transition for different level energies $\epsilon_d$. The circles correspond to the experimental data whereas the continuous lines correspond to the QMC calculation (red, blue and black : harmonics 1, 2 and 3).

These data are thus consistent with a phase controlled level-crossing quantum transition in a single-level QD. In other words, one can control the magnetic state of the junction, doublet or singlet, with the superconducting phase.

#### 5.3.2.2 Universal phase diagram of the first order transition

We present here a quantitative study of the level-crossing quantum transition in the single-level regime. We call $\varphi_c$ the superconducting phase at which, at a fixed gate voltage, the system

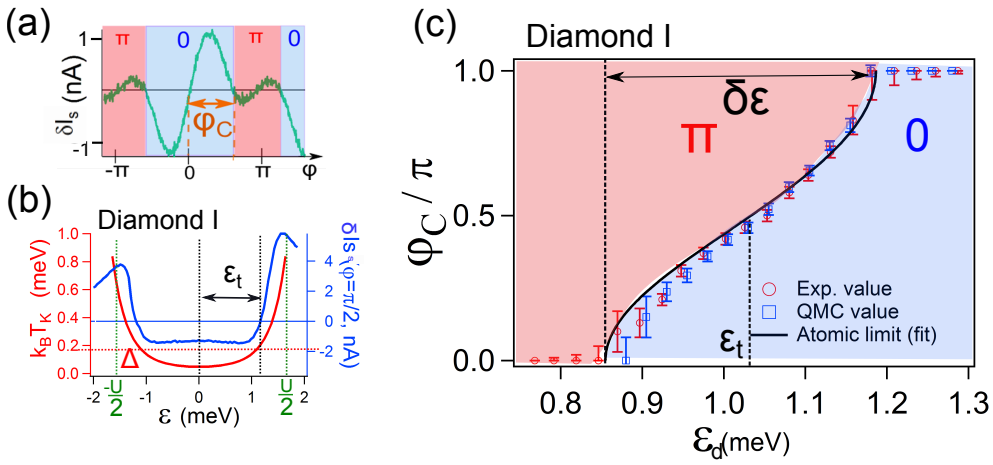


FIGURE 5.11 – Phase dependent transition : definition of the relevant quantities. (a) Definition of the critical phase $\varphi_C$ such that the CPR has 0-behavior for $\varphi \in [0, \varphi_C]$ and $\pi$-behavior for $\varphi \in [\varphi_C, \pi]$. (b) $T_K$ (red line), $\Delta$ (red dotted line) and $\delta I_S(\varphi = \pi/2)$ (blue line) for the diamond I as a function of the energy level $\epsilon_d$, defined as equal to zero at the middle of the diamond and such that $\epsilon_d \in [-U/2, U/2]$. One can notice that the sign of $\delta I_s$ changes when $T_K \approx \Delta$. $\epsilon_t$ is the value of $\epsilon$ for which the junction switches from $\pi$ to 0 at $\varphi = \pi/2$. (c) Critical phase $\varphi_c$ plotted as a function of $\epsilon_d$ for diamond I, yielding a phase diagram of the $\varphi$-controlled transition. We call $\delta\epsilon$ the width of the transition.

undergoes the transition from 0 to $\pi$. Theoretically, this critical phase $\varphi_c$ is defined at T=0, where the transition is expected as a jump in the supercurrent (see section 4.2.4.3 of the previous chapter). At finite temperature the transition is rounded but, if T is small enough, $\varphi_c$ equals the phase at which the supercurrent is zero [143, 8]. On fig. 5.11 (c), we compare $\varphi_c(\epsilon_d)$ from experiment and theory : they both display the same characteristic shape. We try as well to compare these data to an analytical formula obtained in the atomic limit of the Anderson impurity model with $\Delta \gg \Gamma$ and $T = 0$ : $\varphi_c(\epsilon) = 2 \arccos \sqrt{g - (\epsilon/h)^2}$ : a fit of our data with this formula gives a very good agreement for $g = 2.2$ and $h = 0.72$ meV. Note that since we are not at all in an atomic limit, these fit parameters do not correspond to the ones of the experiment.

Is this phase diagram specific to this diamond or is it more general, as suggested by the good agreement with the atomic limit model ? To answer this question, we have compared the phase driven 0-$\pi$ transitions in several diamonds. Each transition is characterized by two parameters : the value of $\epsilon_d$, called $\epsilon_t$, at which the junction changes from $\pi$ to 0 at $\varphi = \pi/2$, and the width $\delta\epsilon$ of the transition. These quantities are defined on Fig. 5.11 (b) and (c) and given in table 5.2 for the concerned diamonds (B, C, G and I). $\delta\epsilon$ is found to depend strongly on the parameters of the diamonds : large transition's widths correspond to ratios $T_K(\epsilon = 0)/\Delta$ close to 1 (see left inset of fig. 5.12).

To compare these eight transitions (left and right sides of four diamonds), we plot on fig. 5.12 the critical phase $\varphi_c$ as a function of $(\epsilon_d - \epsilon_t)/\delta\epsilon$. For diamonds B, G and I, the scaled data fall on the same curve, with an arccosine dependence.

| meV | B | | C | | G | | I | | J right |
|---|---|---|---|---|---|---|---|---|---|
| U | 2.8 | | 2.3 | | 3.5 | | 3.2 | | 3.2 |
| $k_B T_K$ | $\approx 0.06$ | | 0.13 | | $\approx 0.03$ | | 0.05 | | 0.05 |
| $2\delta\epsilon/U$ | 0.23 | 0.43 | 0.87 | 0.96 | 0.06 | 0.06 | 0.15 | 0.2 | 0.2 |
| $2\epsilon_t/U$ | 0.79 | 0.64 | 0 | 0 | 0.74 | 0.74 | 0.75 | 0.69 | 0.8 |

TABLE 5.2 – Values of U, $T_K$, $\delta\epsilon$ and $\epsilon_t$, given in meV for the investigated diamonds. For diamonds B, C, G and I, there are two transitions (0 to $\pi$ and $\pi$ to 0), with different parameters. In diamond J, only the right side of the diamond exhibits a phase dependence of the transition.

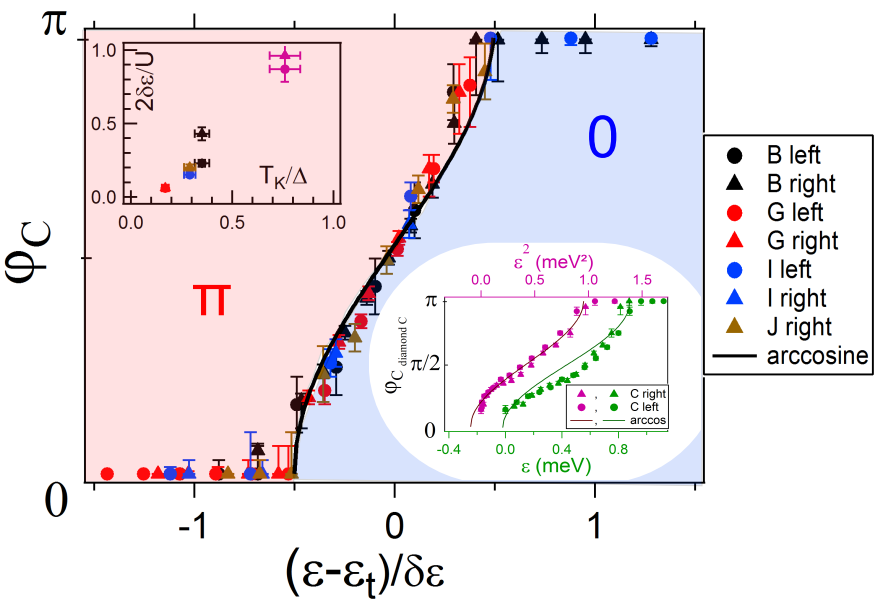


FIGURE 5.12 – Universal scaling of the phase-induced transition. Critical phase $\varphi_c$ plotted as a function of $(\epsilon - \epsilon_t)/\delta\epsilon$ for the diamonds B, G, I and J (left and right sides of the diamond) such that the various curves collapse on an arccosine curve (black line). Inset left : scaling quantity $\delta\epsilon_d$, normalized by $U/2$, as a function of the ratio $T_K/\Delta$. It shows that $2\delta E/U$ varies linearly with $T_K/\Delta$, the quantity that controls the 0-$\pi$ transition. Inset right : same quantity for the diamond C, where the 0-$\pi$ transition is incomplete. To obtain an arccosine shape, one has to plot $\varphi_c$ as a function of $\epsilon_d^2$ instead of $\epsilon_d$ (see text).

To understand qualitatively this scaling, we propose a very naive model, within the following assumptions : (i) the ABS have a cosine shape (ii) the shift of one ABS compared to the other is proportional to $T_K/\Delta$. While $\Delta$ is fixed for the whole experiment, $T_K$ varies as indicated in formula 5.10 and plotted on fig. 5.11 (b). According to (i), we write the energies of the highest occupied ABS $E^-$ and the lowest empty $E^+$ :

$$E^+ = E_0^+ + E_m^+ \cos(\varphi) \tag{5.11}$$

$$E^- = -E_0^- - E_m^- \cos(\varphi) \tag{5.12}$$

(ii) tells us that $E_0^+ + -E_0^- = k\frac{\Delta}{T_K}$ with k a constant. In this simple picture, the 0-$\pi$ transition occurs when $E^+(\varphi_c) - E^-(\varphi_c) = 0$, that is to say :

$$\varphi_C = \arccos(-k\frac{T_K}{\Delta}\frac{1}{E_m^+ + E_m^-}) \tag{5.13}$$

If $T_K(\epsilon_d) \propto \epsilon_d$, this gives the arccosine fit on fig. 5.12. However, this does not work for diamond C (inset right of Fig 5.12), where the transition takes place close to $\epsilon_d = 0$ and on a large range of $\epsilon_d$. Then, the linearization is not valid anymore and, to the lowest order in $\epsilon_d$, $T_K(\epsilon_d) \propto \epsilon_d^2$, yielding $\varphi_c \propto \arccos(\text{cste} + \epsilon_d^2)$ (inset of fig. 5.12 right).

We thus show that for all the diamonds exhibiting a complete 0-$\pi$ transition, the scaled curve $\varphi_c = f((\epsilon_d - \epsilon_t)/\delta\epsilon)$ gives a robust characteristic of the phase-mediated 0-$\pi$ transition.

#### 5.3.2.3 Sensitivity to the environment

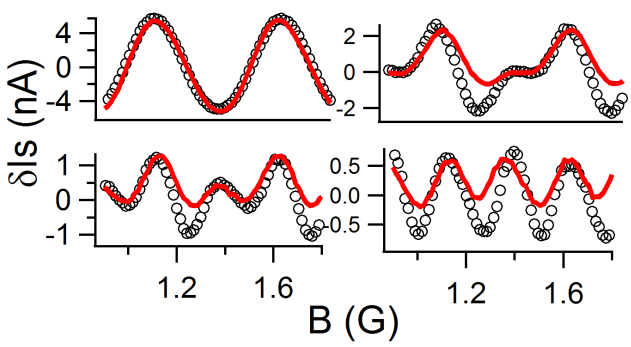


FIGURE 5.13 – Modulation of the switching current at the 0-$\pi$ transition in diamond C with optimization of the environment (in black dots) and without (in red lines). The amplitudes of the optimized curves have been readjusted in order to compare the shapes of the curves.

At the 0-$\pi$ transition we noticed that, in some situations, we measured surprising CPR with an incorrect symmetry. Indeed, a CPR should respect the time-reversal symmetry that imposes the energy to be an even function of the superconducting phase, and thus the current-phase

relation to be an odd function of $\varphi$. But the CPR represented in red on Fig.5.13 are obviously not odd functions of B, which is non-physical. Note that this kind of feature is also what has been published (but not explained) by Maurand *et al.* [91]. We fixed the problem optimizing the electromagnetic environment, namely fixing the polarization of a Josephson junction, which was fortuitous placed nearby, to maximize its impedance. We then obtain the CPR's represented in black dots on Fig. 5.13, which have the good symmetry properties.

Note that these distortions of the CPR only happen in the 0-$\pi$ transition region, where the ABS are so closed that, if the electromagnetic environment affects the phase dynamics, phenomena such as Landau-Zener transitions could also occur. However, this point is still not completely clear.

### 5.3.3 Effect of the two-level regime on the 0-$\pi$ transition

Now we focus on the two-level 0-$\pi$ transitions, and more particularly on diamond J, corresponding to a N=3 filling factor. The modulation of $I_s$ versus the magnetic field, proportional to the CPR, is represented on Fig. 5.14 (a) as a function of $V_g$. CPRs are also shown for some particular values of gate voltage (fig. 5.14 (b)).

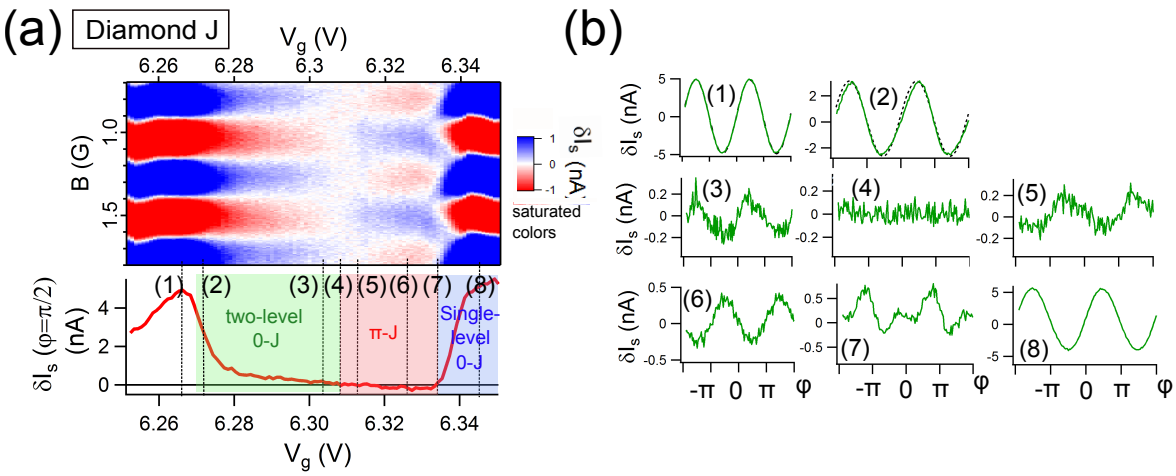


FIGURE 5.14 – (a) Modulation of the switching current of the SQUID versus the magnetic field, proportional to the CPR, as a function of the gate voltage $V_g$, for the diamond J. The supercurrent at the transition being very low, the color scale is saturated. (b) Supercurrent versus the superconducting phase $\varphi$ at some particular gate voltage, indicated by the numbers on panel (a). Note the zero amplitude of the CPR (4) and the fact that the CPR (2), in the two-level 0-junction, has a stronger anharmonicity than (8), on the degeneracy point. Dashed line on (2) : guide for the eyes representing a sinus, showing that the continuous line is not perfectly harmonic.

On the right side of the diamond, close to the $N = 3$ to 0 degeneracy point (fig. 5.14 (b) (8)), the 0-$\pi$ transition is achieved through 0' and $\pi'$ states, similarly to the one investigated in the single-level regime. In addition, $\varphi_c = f((\epsilon - \epsilon_t)/\delta\epsilon)$ collapses on the same arccosine shape as the single-level 0-$\pi$ transitions (see fig. 5.12). But on the left side of the diamond, from the

$N = 3$ to 2 degeneracy point to the center of the diamond (fig. 5.14 (b) (1) to (3)) , the CPR behaves as a 0-junction. The supercurrent's amplitude decreases with $V_g$ and evolves from 0 to $\pi$ continuously. Close to the transition, around the center of the diamond (fig. 5.14 (b) (2) to (4)), the CPR becomes slightly anharmonic. But, unlike in the other transitions, no 0' or $\pi'$ state is observed. Note as well that the current-phase relation has a larger anharmonicity in the two-level 0-junction than on the charge degeneracy points, while its amplitude is smaller (fig. 5.14 (b) (2), to compare with fig. 5.14 (b) (1) or (8)).

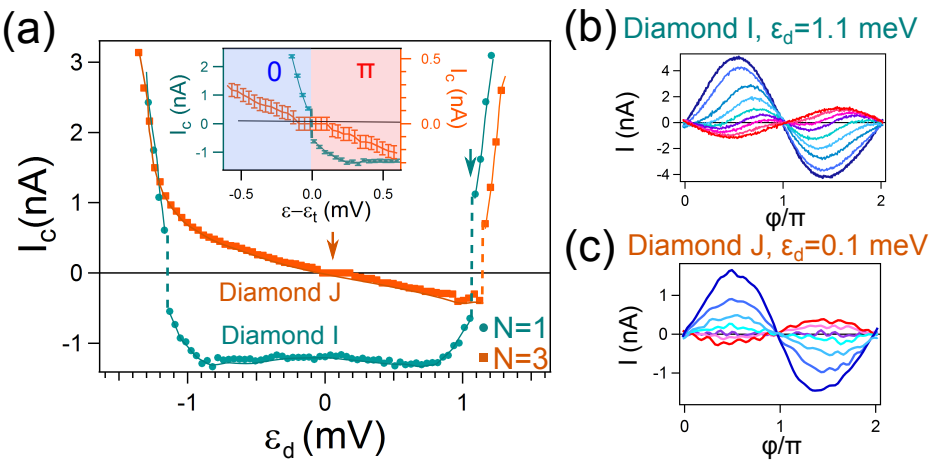


FIGURE 5.15 – (a) Critical current $I_c$, defined as the maximum amplitude of the measured switching current, as a function of the energy level $\epsilon$. $I_c$ is defined as positive for a 0-junction, and negative for a $\pi$-junction. This quantity is plotted for the two diamonds I (N=1, blue dots) and J (N=3, orange squares), respectively in the single-level and two-level regime. The dashed lines materialize discontinuities of $I_c$, specific of first order transitions. Inset : focus on two 0-$\pi$ transitions, centered around $\epsilon_t$ (see Fig. 5.11.(c) for the definition) : at $\epsilon = -1.1$ meV in diamond I, and at $\epsilon = 0.1$ meV in diamond J. (b) Current-phase relations around the 0-$\pi$ transition in diamond I, at $\epsilon_d = 1.1$ meV, indicated by a green arrow. The CPR becomes anharmonic and the critical current never vanishes. (c) Current-phase relations around the 0-$\pi$ transition in diamond J, at $\epsilon_d = 0.1$ meV, indicated by an orange arrow. The CPR is harmonic all over the transition, and the critical current vanishes at the transition.

To go further, we consider now the critical current $I_c$. This quantity is the maximum of the CPR and is extracted here as the maximum amplitude of the modulation of the switching current, positive for a 0-junction, and negative for a $\pi$-junction. It is represented as a function of $\epsilon_d$ on fig. 5.15 (a), for diamonds I and J, respectively in the single and two-level regime. In diamond I (N=1), the phase-dependence of the single-level transitions gives rise to discontinuities of $I_c$, which characterize a first order transition [91, 168]. For diamond J (N=3), the 0-$\pi$ transition at $\epsilon_d = 0.1$ meV does not exhibit this phase-dependence, yielding a vanishing critical current at the transition. This is not anymore a first order transition, contrary to the transition at the other side of the diamond J ($\epsilon_d = 1.2$ meV). According to ref. [12], this kind of 0-$\pi$ transition, without intermediate state 0' or $\pi'$, is indeed possible when there is no change of the magnetic state of the system. This emphasizes that we are facing a transition between a 0-doublet state and a $\pi$-doublet (instead of a 0-singlet and a $\pi$ doublet as in the single level regime and on

the right side of the diamond), specific to the two-level regime.

The two other diamonds indicated by green arrows on Fig. 5.5, F and H, present the same features. This breaking of the electron/hole symmetry is thus observed in the three $N = 3$ diamond where the Kondo effect is not strong enough to change the doublet in singlet.

This kind of gate dependence of the supercurrent is predicted in carbon nanotube QD (see section 4.2.3), in absence of Kondo effect. The comparison of our data with ref. [151], represented on fig. 4.17 suggests that in our experiment, the channels associated with each orbital are mixed during the transfer of Cooper pairs. This is also why we do not observe two-level induced $\pi$-junctions for even occupancies of the dot.

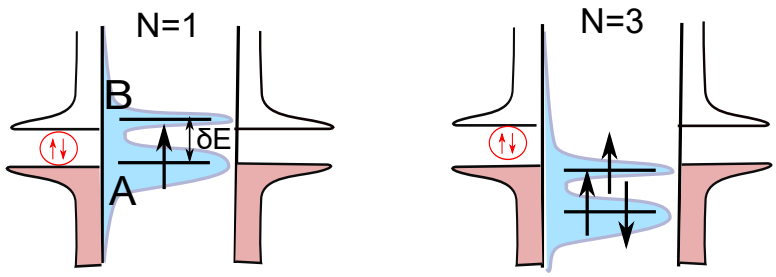


FIGURE 5.16 – Schematic explanation of the symmetry breaking observed in the supercurrent between $N = 1$ and $N = 3$ fillings. The lower energy level A is better coupled to the reservoirs than the higher one B (see text).

To explain why this two-level behavior is observed for $N = 3$ but not for $N = 1$, we propose that the two orbital levels A and B (see fig. 5.16) of the CNT are slightly differently coupled to the electrodes, as in ref. [98] and section 2.3.1.4. A detailed analysis of the gate dependence of the inelastic cotunneling peaks in the even diamond between I and J in the normal state show indeed that $\Gamma_A \geq \Gamma_B$ (fig. 5.5). Following ref. [98], we roughly evaluate $\Gamma_A - \Gamma_B \approx 0.07$ meV.

When two quasi-degenerated levels have different widths, the supercurrent is mostly carried by the broader one. We therefore expect different behaviors for N=1 and N=3, as pointed out theoretically by Droste *et al.* [152]. Here, the lower level A is more coupled to the electrodes than the higher one (B) (see Fig. 5.16). For $N = 1$, the unpaired electron occupies the level A and the level B is too poorly coupled to participate to the transfer of Cooper pairs : we are in a single-level situation, the junction is $\pi$. For $N = 3$, the unpaired electron is in the poorly-coupled-level B, which thus participates to the transport : the system is in a two-level regime. According to this interpretation, in the opposite situation of a level B better coupled than the level A, the $N = 1$ diamond would exhibit the two-level physics instead of the N=3 diamond. Interestingly, while the only signature in the normal state of this breaking of the e/h symmetry is a slight change of the position of the cotunneling peaks, the supercurrent is strongly and qualitatively modified.

There could be another reason for the electron-hole (N=1/3) symmetry to be broken in a

carbon nanotube : spin-orbit coupling [100, 103, 152]. According to Brunetti *et al.* [14], the consequence on the supercurrent could be similar to what we observe. It is however difficult to be affirmative, since we are not able to measure the value of the SO coupling in our system. It would indeed require to study the evolution of cotunneling peaks versus the magnetic field parallel to the nanotube.

Note that this N=1/3 symmetry breaking in the supercurrent can also be seen for diamonds C-D and K-L. But the Kondo effect there is much stronger than in E-F, G-H and I-J, explaining why this unusual $\pi$-junction is not observed in D and L. Therefore, at this qualitative level, we cannot say whether one or two levels participate in transport.

In conclusion, our data exhibit two-level physics, qualitatively consistent with the theoretical expectations for the gate dependence. Since the orbital levels have different width, this regime is observed only when the highest occupied level is the less coupled one. We reveal as well the phase dependence of the supercurrent in this two-level regime. While single-level 0-$\pi$ transitions (between a 0 singlet and a $\pi$ doublet) are discontinuous first order transitions, the transition between the doublet 0-junction and the doublet $\pi$-junction is continuous, indicating a different physical mechanism. The transition involving two different magnetic states originates from a level-crossing, while the transition involving only doublet states is due to a relative variation of the positive and negative contributions to the supercurrent.

### 5.3.4 Toward a $\varphi_0$-junction ?

Let's have a closer look on the CPR measured in the two-level regime, represented on fig. 5.17. It seems that, on the edges of the gate voltage region, the CPR exhibits a small continuous phase shift.

Until now, we have insisted on the fact that a current-phase relation is necessary an odd function of the phase : $I(-\varphi) = -I(\varphi)$ such that $I(\varphi = 0) = 0$. But if the time reversal symmetry (TRS) is broken in the system, it is possible to observe a non-zero current for a zero phase bias, called the anomalous current $I_a$ which can be defined like this :

$$I = I_0 \sin(\varphi) + I_a \cos(\varphi) \tag{5.14}$$

(with harmonics if the CPR is non-sinusoidal). Equivalently, we can write the supercurrent as $I = I_c \sin(\varphi + \varphi_0)$, this is why such a junction is called $\varphi_0$-junction.

To quantify the measured effect, we represent on fig. 5.17 (c) the results of fit for both $\varphi_0$ and $I_0$, $I_a$ as defined above.

Is the feature on our measurements related to a breaking of the TRS ? First, one should note that this result comes from a unique measurement, without any check. It could be due to the trapping of a vortex in the coil or whatever. However, the symmetry of the effect on both

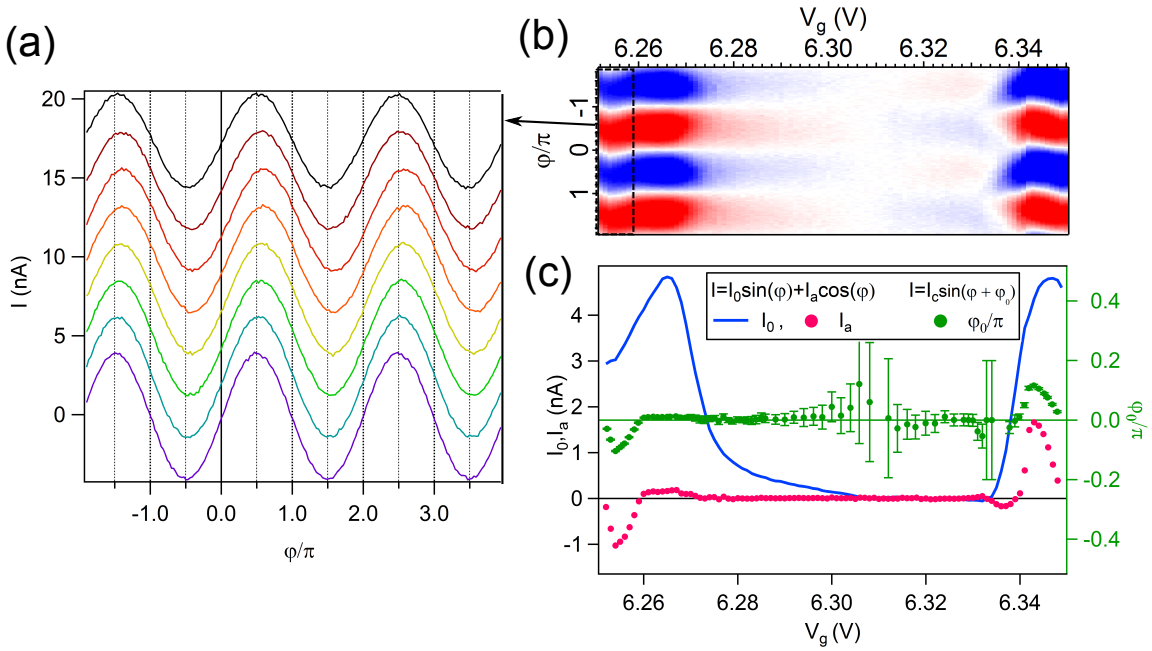


FIGURE 5.17 – (a) Current-phase relations for various values of gate voltage on the left edge of the gate voltage region (square in black on (b)). We can see that these CPRs look sinusoidal and that some of them are slightly dephased (in particular the red and orange). (c) Result of sinusoidal fits all over the diamond. In blue and pink are represented the critical current $I_0$ and the anomalous current $I_a$ from $I = I_0 \sin(\varphi) + I_a \cos(\varphi)$, in green the phase shift $\varphi_0$ from $I = I_c \sin(\varphi + \varphi_0)$. Note that the error bar diverges at the 0-$\pi$ transitions : at the center where the amplitude almost vanishes, and on the right edge where the CPRs are strongly anharmonics.

edges of the diamonds makes us think about something related to Coulomb blockade.

This could be due to the presence of spin-orbit coupling in the nanotube, as well as to a small magnetic field [5] associated to the participation of two-levels to the transport of Cooper pairs. Zazunov *et al.*[11] as well as Brunetti *et al.* [14] have shown that a substantial anomalous current could be observed in this kind of system, especially in oddly occupied diamonds, where Coulomb interactions enhance the effect. This requires further investigations, in particular measuring other samples.

## 5.4 Supplementary measurements

### 5.4.1 Spectroscopy of Andreev Bound states.

The CNT Josephson junction is embedded in a three arms SQUID. As detailed in a previous article [6], it allows the measurement of the differential conductance of the CNT in the

[5]The magnetic field applied on the sample is actually very small, of the order of a few Gauss. But there could be also a local effective magnetic field induced by exchange coupling between the electrons in the dot.

superconducting state. This is done applying to the point B (see Fig. 5.4) a voltage large enough to have a voltage-independent contribution of the Josephson junctions to the differential conductance.

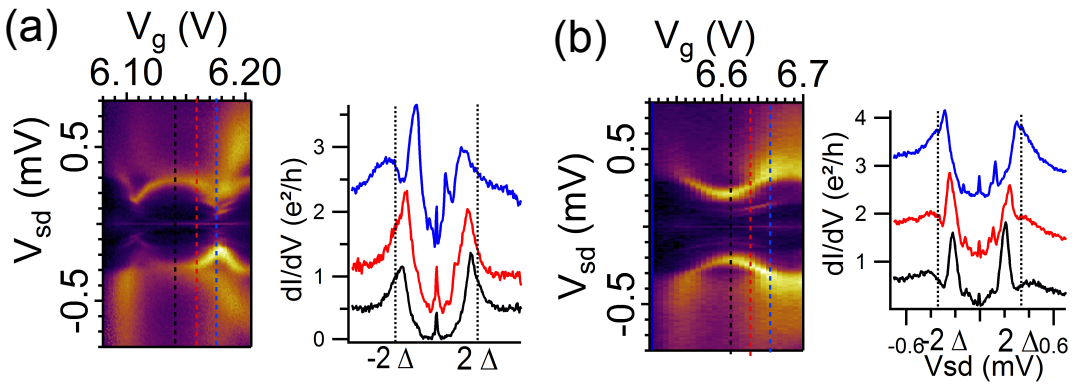


FIGURE 5.18 – Differential conductance as a function of the bias voltage ($dI/dV(V_{sd})$) in the superconducting state for two diamonds : (a) I ($\pi$-junction) and (b) K (0-junction).

In a system perfectly symmetrically coupled ($\Gamma_L = \Gamma_R$), one expects to observe multiple Andreev reflections (MAR) if the total coupling $\Gamma = \Gamma_L + \Gamma_R$ is low enough, or resonant tunneling otherwise [176]. But if one electrode is very well coupled to the QD compared to the other ($\Gamma_L/\Gamma_R \gg 1$), one expects the poorly coupled lead to probe the density of states in the quantum dot and thus make the spectroscopy of the levels, as in Ref. [116, 141]. For intermediate coupling, one observes a crossover between the two situations [177], as for example ref. [178, 179, 180, 140].

This measurement of $dI/dV(V_{sd})$ in the superconducting state (zero magnetic field) has been done for two diamonds of S-NbAl, I and K, and represented on fig. 5.18. Diamond I is a single-level $\pi$-junction while K is a single-level 0-junction. Due to the high magnetic field, the contact asymmetry cannot be directly extracted. Thanks to QMC calculations, it has been shown in Ref. [8] that the asymmetry of ridge I is equal to $\Gamma_L/\Gamma_R \approx 4$. We can expect a value slightly smaller for K, but not very different because they are very close in gate voltage. Because of this asymmetry, the system is not in a pure MAR regime and, according to Ref. [140], this asymmetry is large enough to interpret the conductance measurements as a spectroscopy of ABS.

For the two diamonds, the ABS are qualitatively different : for the ridge I, we observe a crossing of Andreev levels, characteristic of $\pi$-junctions. For the diamond K, because there is no $\pi$-junction, the Andreev-levels do not cross. Even though this kind of measurement has already been done in a similar system in Ref. [140]), where this spectroscopy of Andreev levels had been done on the same sample as the critical current measurement, here the spectroscopy is done in parallel with the current-phase relation measurement.

Note that this measurement of the conductance as a function of the bias voltage cannot give any information about the phase-dependent 0-$\pi$ transition. Indeed, as soon as the JJ is voltage biased, the superconducting phase is not controlled anymore and varies as $d\varphi/dt = 2eV/\hbar$ [111].

### 5.4.2 SU(4) Kondo effect ?

We present here measurements on sample S-NbAl in a range of gate voltage where the coupling between the carbon nanotube to the electrodes is larger. On the stability diagram represented on Fig. 5.19, we can guess diamond-like features, showing a succession of three small diamonds, one big, and again three small ones. However, contrary to fig. 5.5, the non-zero conductance at zero bias, *i.e.* the Kondo effect, spreads all over the three small diamonds ($N = 1$, 2 and 3). In addition, the zero bias conductance in the $N = 2$ diamond reaches $2.5e^2/h$.

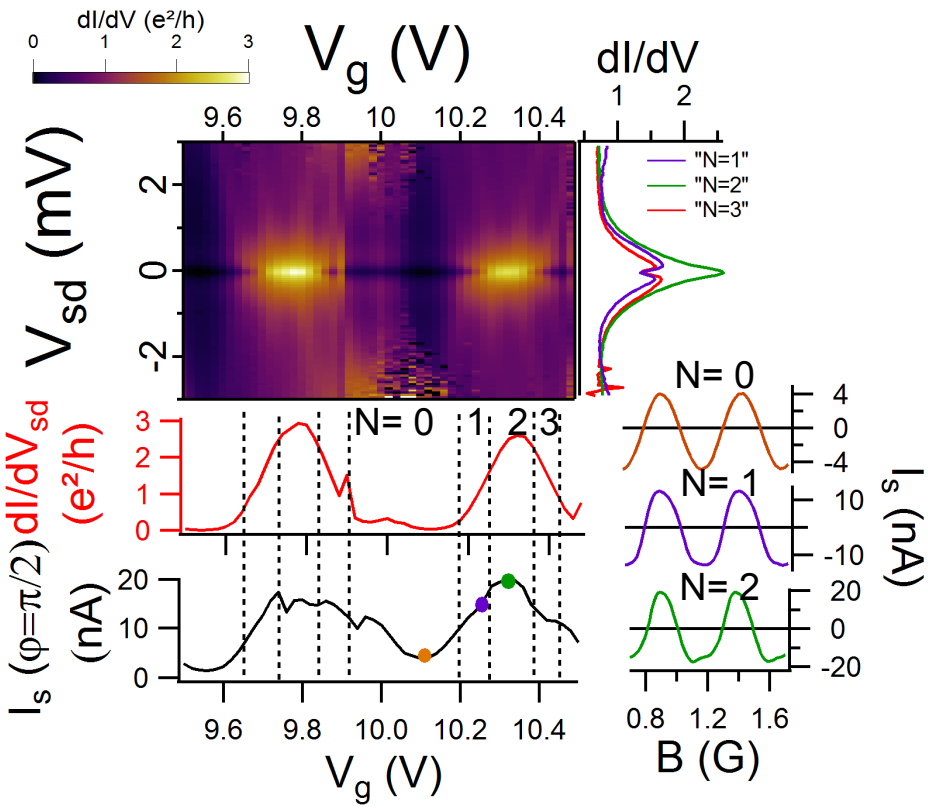


FIGURE 5.19 – Data in the normal and superconducting state in a gate zone corresponding probably to SU(4) Kondo effect. Colorplot : differential conductance as a function of $V_{sd}$ and $V_g$. A magnetic field of 1T is applied perpendicularly to the sample to suppress the superconductivity in the contacts. On the right are plotted vertical cuts of the color-plot, yielding $dI/dV_{sd}(V_{sd})$ at the middle of N=1, N=2 and N=3 diamonds. Red curve : $dI/dV_{sd}(V_g, V_{sd} = 0)$ in the normal state. Black curve : supercurrent $\delta I_s(V_g)$ for a superconducting phase difference of $\varphi = \pi/2$. On the right are plotted current-phase relations at the center of N=0, 1 and 3 diamonds.

These features seem to indicate SU(4) Kondo effect, where two independent degrees of freedom, here the spin and the orbital pseudo-spin, are involved [104, 78] (see section 2.3.2.1). We were not able to measure the conductance as a function of the magnetic field, that would confirm the presence of this effect.

Still, we measure as well the current-phase relation in this regime (fig. 5.19). First, the junction is in a 0-state for all gate voltages. We notice as well that the supercurrent is very high, reaching 20 nA in the N=2 diamond around $V_g = 10.35V$. Such an increase of the critical current compared to the Kondo SU(2) case is expected since, in Kondo SU(4) at N=2 filling, two perfectly transmitted channels are open (instead of one in Kondo SU(2)). Unfortunately, due to this high value of the supercurrent, in this regime our experimental setup cannot be considered anymore as an asymmetric SQUID. The CPR measurement is therefore not reliable, which may explain the unusual anharmonicities observed at N=2.

## 5.5 Conclusion

Here are summarized the conclusions of theses measurements of current-phase relation in a carbon nanotube QD where two orbital levels may participate to the transport of Cooper pairs.

- When the QD is filled by an even number of electron, we measure no sign reversal of the supercurrent : these are 0-junctions.
- When there is an odd number of electrons in the dot, and $T_K > \Delta$ : the Kondo effect and the superconducting correlations cooperate and lead to a Kondo-enhanced 0-junction.
- Still for odd occupancies but with $T_K < \Delta$ : the Kondo correlations cannot develop, the Josephson effect is dominated by Coulomb interactions. The system transits in a $\pi$-junction state, where the sign of the supercurrent is reversed. We can however distinguish two different cases :
  - When the unpaired electron is in the best coupled orbital level, the supercurrent is symmetric with respect to the center of the diamond : only one level participate to the transfer of Cooper pairs through the dot.
  - When the unpaired electron occupies the less coupled orbital level, this symmetry is broken and one of the 0-$\pi$ transition occurs around the center of the diamond without change of magnetic state. This is made possible by the participation of the second level to transport.

  In other words, the electron/hole symmetry can be broken if the orbital levels are nearly degenerate and differently coupled to the electrodes. Note that the Josephson effect is far more sensitive to this symmetry breaking than the normal state conductance.

- In the single-level regime, we investigate in details the 0-$\pi$ transition :
  - We prove that the critical current never vanishes at the transition and that the system transits through 0' and $\pi'$ states, where the current-phase relation is strongly anharmonic. This confirms the level-crossing nature of the transition, leading to a singlet to doublet transition driven by the superconducting phase.
  - The critical phase, at which happens the transition, is extracted for several different diamonds, giving a phase diagram of the transition. We show that it exhibits an universal behavior, independent of the values of the parameters of the quantum dot.
- Similarly, we measure the current-phase relation in the two-level regime :
  - One of the 0-$\pi$ transitions, the one between the doublet $\pi$-junction and the singlet 0-junction, presents the same phase-driven transition as in the single-level regime, with a discontinuous supercurrent.
  - The other one, between a doublet 0-junction and a doublet $\pi$-junction, is completely different : there is a complete cancellation of the critical current and no 0' or $\pi'$ states. This is thus a new kind of 0-$\pi$ transition.

# Part III

# Noise measurements in the Kondo regime

# 6 Noise in a mesoscopic system

This chapter starts by an introduction to the problematic of noise in an electric system, focusing on the current fluctuations in mesoscopic systems. Emphasis is given to out-of-equilibrium noise, also called shot noise, that is the noise measured in the following. At the end of this chapter is presented a measurement of low frequency shot noise in a carbon nanotube in the Kondo regime that was performed in Osaka, Japan. The next chapter will address the finite frequency version of the measurement, still in the Kondo regime, which is one of the main achievements of this PhD work.

## 6.1 Definition and different regimes

### 6.1.1 Definition of noise

When measuring transport in an electronic system, the interesting quantities are generally the averages values of the current or the voltage $< I >$ or $< V >$, where $< ... >$ represents the statistical average (if the system is assumed to be ergodic, this is equivalent to a time average). But in reality, the current fluctuates around $< I >$, this is what we call the current noise. These fluctuations are expressed as $\delta I(t) = I(t) - < I >$, the difference between the value of I at time t and the averaged value (see fig. 6.1).

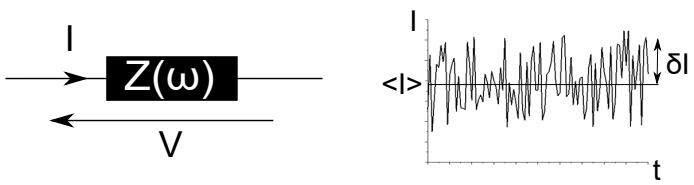


FIGURE 6.1 – Example of a fluctuating signal, the electrical current, through an impedance $Z(\omega)$ and definition of the average current $< I >$ and the fluctuation $\delta I(t)$.

These fluctuations may come from the detection setup or from an external source : then the

noise is not interesting and not desired. But if they originate from the sample itself, this noise is potentially interesting since it can provide informations about the investigated system.

Current fluctuations are characterized by their amplitude but also by their time scale : the auto-correlator $C_{I,I}(\tau) =< \delta I(t)\delta I(t+\tau) >$ tells how much the current at time $t$ is correlated to the one at time $t+\tau$. In the general case, the spectral density of noise is defined as the Fourier transform of $C_{I,I}(\tau)$ [1] [181] :

$$S_I(\nu) = \int C_{I,I}(\tau)e^{i2\pi\nu\tau}d\tau \tag{6.1}$$

### 6.1.2 Noise in a quantum system

For a quantum treatment of noise, the current has to be replaced by the current operator $\hat{I}$ in definition 6.1 [182]:

$$S_I(\nu) = \int < \delta\hat{I}(t)\delta\hat{I}(t+\tau) > e^{i2\pi\nu\tau}d\tau \tag{6.2}$$

Because of the non-commutation of $\hat{I}(t)$ and $\hat{I}(t+\tau)$, $S_I(\nu) \neq S_I(-\nu)$ a priori. This is not a problem for most experiments, which measure both $S_I(\nu)$ and $S_I(-\nu)$ at the same time, that's why sometime people prefer to calculate the so-called symmetrized noise :

$$S_I^{sym}(\nu) = S_I(\nu)+S_I(-\nu) = \int < \delta\hat{I}(t)\delta\hat{I}(t+\tau) > e^{i2\pi\nu\tau}d\tau + \int < \delta\hat{I}(t)\delta\hat{I}(t-\tau) > e^{i2\pi\nu\tau}d\tau \tag{6.3}$$

But some information are lost in the symmetrization. That's why measuring the non-symmetrized noise of formula 6.2 provides more information and is thus more interesting. In particular, as it will be shown in the following, it enables to separate the contributions of the emission and absorption processes.

### 6.1.3 Equilibrium noise

Within this quantum description, it can be shown [183, 184] that the spectral density of non-symmetrized current noise induced by a given impedance $Z(\omega)$ is, at equilibrium (*i.e.* without bias voltage) and at temperature $T$ :

$$S_I^{eq}(\nu) = \frac{h\nu}{Re(Z(\nu))}(1+\coth(\frac{h\nu}{2k_BT})) \tag{6.4}$$

[1] Note that here and all along this thesis, the spectral density of noise is per unity of frequency $\nu$ (thus expressed in $A^2/Hz$). The density of noise per unity of pulsation $\omega$ (in $A^2/(rad/s)$) is equal to the previous quantity divided by a factor $2\pi$.

We see that, indeed, the noise differs for positive and negative frequencies. To understand this asymmetry $\nu/-\nu$, it is interesting to look at this expression in two limit cases.

**Low frequency regime** $|h\nu| \ll k_B T$ Then formula 6.4 gives :

$$S_I^{eq}(\nu) = \frac{2k_B T}{Re(Z(\nu))} \tag{6.5}$$

This is the well known expression of the Johnson-Nyquist noise, or thermal noise. It expresses also the fluctuation-dissipation theorem, a very general result in statistical physics that gives the relation between the fluctuations of a system and the imaginary part of its response function (related to the dissipation) [185].

This regime is called classical since the time scale at which the noise is measured is so long that all the quantum fluctuations are washed out by the thermal ones. In this limit, the symmetrized noise does not depend on the frequency and gives the usual expression $S_I^{sym} = \frac{4k_B T}{Re(Z(\nu))}$ for the thermal noise. Note that, despite its denomination of "classical", this noise can carry signatures of quantum physics.

**High frequency** $h\nu \gg k_B T$ In this regime, formula 6.4 leads to two different expressions depending on the sign of the frequency (see fig. 6.2 (a) right for a graphical representation in the case of a sample of conductance G) :

$$\text{If } \nu < 0, \qquad S_I(\nu) = 0 \tag{6.6}$$

$$\text{If } \nu > 0, \qquad S_I(\nu) = 2\frac{h\nu}{Re(Z(\nu))} \tag{6.7}$$

In this limit, the spectral density of noise vanishes for negative frequencies and is proportional to $h\nu$ for positive ones. This can be understood by making the distinction between the noise originating from the emission of energy by the system, given by negative frequencies, and the one coming from absorption processes, represented by positive frequencies. Indeed, if the system is at equilibrium (applied voltage V=0) and at zero temperature, it cannot emit any photon at any frequency, the spectral density of emission noise is equal to zero. However, the absorption of photons is allowed by zero-point fluctuations, inducing fluctuations of current : the spectral density of noise is proportional to the photon's energy $h\nu$ (see fig. 6.2 (a)). As in the classical regime, this result is consistent with the fluctuation dissipation theorem [185]:

$$S_{abs}(|\nu|) - S_{em}(|\nu|) = 2\frac{h\nu}{Re(Z(\nu))} \tag{6.8}$$

This regime of high frequency is called the quantum regime because it is due to zero-point

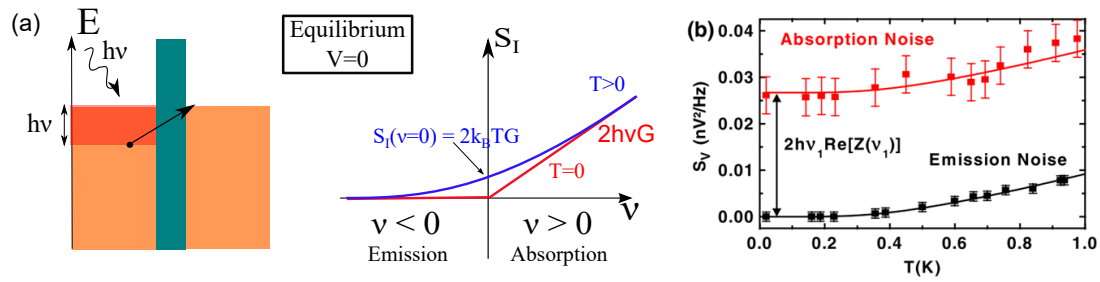


FIGURE 6.2 – (a) Example of a tunnel junction of resistance $R = 1/G$. Left : process of photon absorption at T=0 and equilibrium. Right : spectral noise density of current vs the frequency $\nu$ at T=0 (red line) and T>0 (blue line). The proportionality between the absorption noise and the frequency comes from the fact that the electrons that can be excited in an available state (necessary above the Fermi energy) are in an energy band of width $h\nu$. (b) Separated measurement of emission and absorption voltage noise of a resonant circuit coupled to an on-chip detector, as a function of temperature. Solid lines correspond to the expected temperature dependence of the noises. From ref. [186].

fluctuations, a purely quantum phenomenon.

A manifestation of this asymmetry of the voltage noise at equilibrium has been seen in our group in 2010 [186], measuring both the emission and absorption noises of a resonant circuit. This system was coupled to an on-chip non-symmetrized noise detector based on a SIS junction, a setup almost identical to the one that will be described in the next chapter. The measurement is represented on fig. 6.2 (b) and clearly shows, at zero temperature, that the emission noise is equal to zero and the absorption noise to $2h\nu Re(Z(\nu))$. The temperature evolution is also consistent with formula 6.4.

Note that at room temperature, it is difficult to enter this quantum regime, since it means measuring noise at 6 THz. But at the cryogenic temperatures that we are investigating, it becomes possible : 83 GHz at 4 K and 1 GHz at 50 mK. In the experiment of fig. 6.2 (b), the lowest temperature is 20 mK and the frequency 30 GHz.

From above, we see that as soon as the fluctuation-dissipation theorem is verified, a measure of equilibrium noise is equivalent to a conductance measurement. At high frequency, it however gives access to the high frequency conductance, whose direct measurement is not so trivial. Note that in various systems, equilibrium noise increases at low frequency. This is called $1/f$ noise and can provide information about the dynamics of the system at large time scales [187].

In the next part we will focus on the noise induced by a flow of current, called shot noise, that provides additional information.

## 6.2 Shot noise in a mesoscopic system

This part deals with the noise emitted by a mesoscopic conductor when it is biased by a voltage $V$, inducing a current $I$. We focus for the moment on the low frequency regime, that is sufficient to describe most experiments done in the literature, and already tells us a lot about the interactions in the system.

### 6.2.1 Fluctuations due to charge carriers discreteness

An electrical current can be seen as a large number of charge carriers (in the simplest case, electrons of charge $e$) that are moving from one side of a conductor to the other. During the time $\Delta t$, $N = \frac{I\Delta t}{e}$ electrons cross a transverse section of the conductor (see fig. 6.3). In average, the system has a current $< I >= \frac{e<N>}{\Delta T}$. But of course, this number of electrons N fluctuates. Typically, discrete events like these ones follow a poissonian distribution, provided that the electrons are transferred randomly and independently one from each other. Then the variance is $\Delta N$ such that $\Delta N^2 =< N >$, yielding $\Delta I^2 = \frac{e<I>}{\Delta t}$. Since, for a white noise, $\Delta I^2 = S_I \Delta f$, we obtain the following expression of the noise :

$$S_I = e < I > \tag{6.9}$$

Or the symmetrized expression, that will be used in the following :

$$S_I^{sym}(\nu) = 2e < I > \tag{6.10}$$

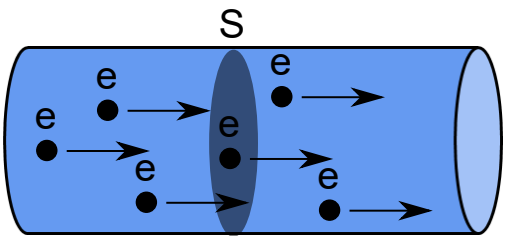


FIGURE 6.3 – Schema of a conductor. The current is proportional to the number of electrons that cross the section S during the time $\Delta t$, divided by this time.

From that, we see that shot noise comes from the discreteness of the charge carriers constituting the current. The ratio between the amplitude of the fluctuations and the average current is proportional to $1/\sqrt{I}$ such that, for large current, shot noise can be neglected compared to other sources of noise (thermal noise in particular). In addition, for samples larger than the electron-phonon length, the Fermi distribution of the electrons is thermalized, hiding the shot noise. Thus, to observe shot noise, one has to measure small currents in small samples.

### 6.2.2 Noise in the scattering matrix formalism

#### 6.2.2.1 Description of the modelization

Of course, this description of shot noise does not take into account the specificities of the mesoscopic system and is valid only for low transmitted systems in absence of any interaction.

We show here that the problem can be treated thanks to scattering matrix formalism, as described in the Blanter and Büttiker review on the subject [15].

Let's consider a mesoscopic system (the blue box on fig. 6.4) connected to two reservoirs, left and right, respectively at electrical potentials $\mu_L$ and $\mu_R$ and assumed to be at the same temperature T. In these reservoirs, the electrons are distributed according to the Fermi distribution :

$$f_{L,R}(E) = \frac{1}{1 + e^{(E-\mu_{L,R})/k_B T}} \tag{6.11}$$

Transport through the sample is assumed to take place through N transverse channels. For each of these channels, we define the operators of creation and annihilation of electrons. We call them $\hat{a}\dagger_{L,R}$ and $\hat{a}_{L,R}$ for electrons moving toward the sample and $\hat{b}\dagger_{L,R}$ and $\hat{b}_{L,R}$ for those going away, for each side R and L (see fig. 6.4). In the following, the calculation is done for only one channel, but it can be generalized to the N channels (see ref. [15]).

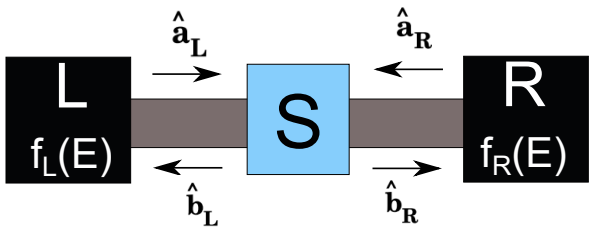


FIGURE 6.4 – Schematics of the situation for which we compute the shot noise, in the case of a single channel.

These creation and annihilation operators are related by the scattering matrix s such that :

$$\begin{pmatrix} \hat{b}_L \\ \hat{b}_R \end{pmatrix} = s(E) \begin{pmatrix} \hat{a}_L \\ \hat{a}_R \end{pmatrix} \text{ with } s(E) = \begin{pmatrix} s_{LL}(E) & s_{LR}(E) \\ s_{RL}(E) & s_{RR}(E) \end{pmatrix} \tag{6.12}$$

#### 6.2.2.2 Current

Within this formalism, it can be shown that the current in the left lead is given by [15] (all the procedure can be similarly reproduced for the right lead) :

$$\hat{I}_L(t) = \frac{e}{h} \int dE dE' e^{i(E-E')t} (\hat{a}_L^\dagger(E,t)\hat{a}_L(E',t) - \hat{b}_L^\dagger(E,t)\hat{b}_L(E',t)) \tag{6.13}$$

To understand this formula, we can remark that the product of creation and annihilation operators $\hat{a}_L^\dagger(E,t)\hat{a}_L(E',t)$ corresponds to the electrons going toward the sample S and $\hat{b}_L^\dagger(E,t)\hat{b}_L(E',t)$ to the ones going away. The current in the lead L is the subtraction of these two contributions. The creation and annihilation operators are taken at different energies E and E', in order to consider all the processes leading to a current, including ones accompanied by the emission or absorption of some energy from the environment. It is interesting to note that for a system at equilibrium (with $\alpha, \beta = L, R$)

$$< \hat{a}_\alpha^\dagger(E,t)\hat{a}_\beta(E',t) >= \delta_{\alpha,\beta}\delta(E-E')f_L(E) \tag{6.14}$$

such that the processes involving different energies E and E' vanish in average. They are indeed related to current fluctuations : $E > E'$ corresponds to absorption processes and $E < E'$ to emission processes.

From the definition of the scattering matrix 6.12, the operators $\hat{b}$ and $\hat{b}^\dagger$ are expressed as a function of $\hat{a}$ and $\hat{a}^\dagger$. After "some algebra" one obtains the general expression for the current :

$$\hat{I}_L(t) = \frac{e}{h}\sum_{\alpha,\beta}\int dEdE' e^{i(E-E')t}\hat{a}_\alpha^\dagger(E)A_{\alpha,\beta}(L;E,E')\hat{a}_\beta(E') \tag{6.15}$$

With the matrix $A$ defined as $A_{\alpha,\beta}(L;E,E') = \delta_{\alpha,L}\delta_{\beta,L} - s_{L,\alpha}^\dagger(E)s_{L,\beta}(E')$.

When computing the current average, from eq. 6.14, we see that only the terms $A$ at the same energy ($E = E'$) remain. In addition to that, the current is conserved : the electrons coming in the system are compensated by the one going out, at any time $t$ [15]. This is related to the fact that $s$ is a unitary matrix, and yields the simple expression :

$$< \hat{I}_L(t) >= \frac{e}{h}\int dE\ Tr[t^\dagger(E)t(E)]\ (f_L(E) - f_R(E)) \tag{6.16}$$

The current in the right electrode $< \hat{I}_R(t) >$ is found, by the same procedure, to be the same (this is of course expected from the current conservation). $Tr[t^\dagger(E)t(E)]$ is the trace of the matrix $t^\dagger(E)t(E)$ defined in eq. 6.12 [2] and can be rewritten as the sum of the eigenvalues of $t^\dagger(E)t(E)$, $T_n$ :

$$< \hat{I}_L(t) >= \frac{e}{h}\sum_n\int dE\ T_n(E)(f_L(E) - f_R(E)) \tag{6.17}$$

$T_n$ is called transmission coefficient of the channel n. At zero temperature, it gives :

$$< \hat{I}_L(t) >= \frac{e}{h}\int_{\mu_L}^{\mu_R} dE\ \sum_n T_n(E) \tag{6.18}$$

For low bias, when the transmission coefficients do not depend on the energy, this leads to

[2] For one channel it is a complex number, for N channels it is a matrix of size N.

the well known Landauer formula of the conductance :

$$G = \frac{dI}{dV}(V=0) = \frac{e^2}{h}\sum_n T_n \tag{6.19}$$

Note that at higher bias voltage, for energy dependent transmissions, the expression of the conductance as a function of the transmission depends on the bias conditions of the experiment. For example, for one channel and a symmetric bias voltage such that $\mu_L = -\mu_R = V/2$ :

$$\frac{dI}{dV}(V) = \frac{e^2}{h}\,\frac{T(V/2)+T(-V/2)}{2} \tag{6.20}$$

While for an asymmetric bias $\mu_L = V$ and $\mu_R = 0$ :

$$\frac{dI}{dV}(V) = \frac{e^2}{h}T(V) \tag{6.21}$$

The conductance is gauge invariant, it depends only on the voltage applied between the electrodes. However, the transmission $T(V)$ and thus the relation between the conductance and the transmission depend on the reference of the potential chosen.

#### 6.2.2.3 Noise

When calculating the noise, we have to chose in which lead, and actually four different components can be distinguished : the intra-lead noises $S_{LL}$ and $S_{RR}$ and the inter-lead noises $S_{RL}$ and $S_{LR}$ defined by :

$$S_{\alpha\beta}(\nu) = \frac{e^2}{h}\int < \delta\hat{I}_\alpha(t)\delta\hat{I}_\beta(t+\tau) > e^{i2\pi\nu\tau}d\tau \tag{6.22}$$

From formula 6.15, it is possible to compute the spectral density of noise according to this definition [15, 21]:

$$S_{\alpha\beta}(\nu) = \frac{e^2}{h}\int dE \sum_{\alpha'\beta'} A_{\alpha',\beta'}(\alpha;E,E+h\nu)A_{\beta',\alpha'}(\beta;E+h\nu,E)\ f_{\alpha'}(E+h\nu)(1-f_{\beta'}(E)) \tag{6.23}$$

At this stage, this formula is valid for any system described by a scattering matrix, for both low and high frequencies. We will see that at low frequency and bias, these different components intra and inter-leads are equal (with a different sign). This is no longer true in the high frequency regime, as it will be detailed in section 7.2.1.

### 6.2.3 Low frequency limit

#### 6.2.3.1 General expression

We now take the limit of low frequencies ($\nu \approx 0$), at zero temperature, in formula 6.23. From ref. [15, 188], we get that intra-lead noise $S_{LL}$ and $S_{RR}$ are positive quantities, while inter-lead ones $S_{LR}$ and $S_{RL}$ are negatives. Moreover, due to current conservation $I_R + I_L = 0$, $S_{LL} = S_{RR} = -S_{RL} = -S_{RL}$.

In the following, we call S the symmetrized intra-lead noise $S(\nu = 0) = S_{LL}(\nu) + S_{LL}(-\nu) = 2S_{LL}$. Its value is given by :

$$S = 2\frac{e^3|V|}{h}\sum_n T_n(1 - T_n) \tag{6.24}$$

If all the channels have a low transmission $T_n \ll 1$, the noise has the Poissonnian value $S^{poiss} = 2e < I >$, naively derived in section 6.2.1. But in general, shot noise is lower than this ; the difference is quantified by the Fano factor :

$$F = \frac{S}{2e < I >} = \frac{\sum_n T_n(1 - T_n)}{\sum_n T_n} \tag{6.25}$$

From that we have the following statements :

- A perfectly transmitted channel ($T = 1$) does not generate noise ($F = 0$).
- A low transmitted channel generates a poissonian noise ($F = 1$).
- Half-transmitted channels ($T = 1/2$) are the most noisy ones.

When $F < 1$, the noise is said to be sub-poissonian. Super-poissonian noise can only be obtained in presence of interactions or inelastic processes, which are totally neglected here.

We present now two examples of informations accessible thanks to shot noise measurements.

#### 6.2.3.2 Fano factor

If the charge of the charge carriers is known (it is not always $e$, see next section), the measurement of shot noise gives additional informations about the number of channels and their transmissions. This will be detailed in the case of Kondo effect, we briefly give here the example of a diffusive conductors.

In this kind of systems, there are a lot of conduction channels, with transmission coefficients

distributed over a distribution function [15]:

$$P(T) = \frac{l}{2L}\frac{1}{T\sqrt{1-T}} \tag{6.26}$$

With $l$ the mean free path of the sample and $L$ its length. It comes that $< T(1-T) >= l(3L)$. This gives a Fano factor F=1/3.

#### 6.2.3.3 Effective charge : example of NS and SNS junctions

Until now, we assumed that the charge carriers were electrons, with a charge $e$. There exists numerous situations in which they carry a different charge $q$. This is for example the case in a SN junction, as represented on fig. 6.5 (a) and (b), describing an experiment done by Jehl *et al.* [18]. There, for low enough currents, electronic transport is achieved through Andreev reflections : an electron arriving at the NS interface is reflected as an hole, and a Cooper pair is transferred in the superconductor (see chapter 4.1). The charge transferred is then $q = 2e$ instead of $e$. In addition, in this experiment the sample is diffusive, such that

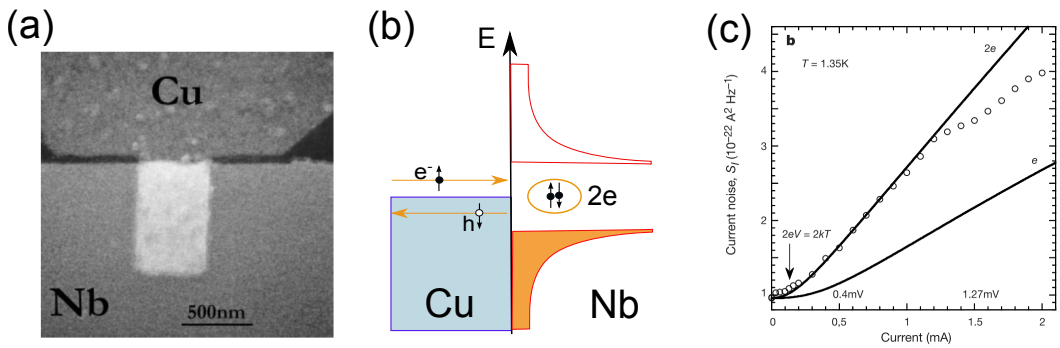


FIGURE 6.5 – (a) Sample measured in ref. [18], a SN junction made of Copper and Niobium. (b) Andreev reflection process that doubles the charge transfered. (c) Measurement of shot noise in the system as a function of the bias current : at low current the noise corresponds to a charge 2e in accordance with Andreev reflection. At higher current, the discrepancy may be due to quasi-particle current.

the expected Fano factor is $F = 1/3$. For a charge $2e$, the noise expected in total is thus $S = 2 \times 2e \times 1/3 \times I = 4/3eI$, as measured on fig. 6.5 (c).

Another example of this enhancement of the effective charge is given by multiple Andreev reflections (MAR) in SNS junctions (see section 4.1.2.5). These processes are represented on fig. 6.6 (a) for a SNS junction biased by a voltage V. If $V = 2\Delta/n$, the electrons must be reflected (n-1) times on a NS interface to participate to transport, each time transferring a Cooper pair. The transfer of charge from one side to the other, *i.e* the effective charge, is $q = n$ and can be measured by shot noise measurements. This has been done in an atomic point contact by Cron *et al.*[189], as represented on fig. 6.6 (b), giving plateaus in the effective

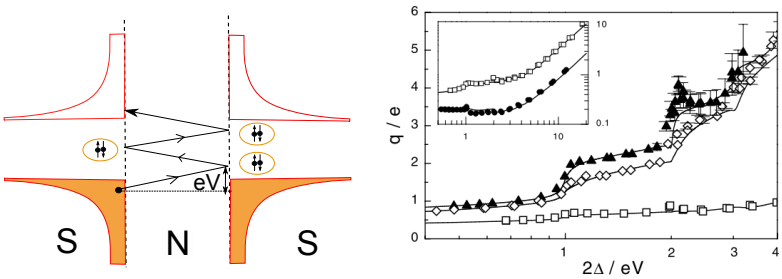


FIGURE 6.6 – (a) Multiple Andreev reflections in a SNS junction biased by a voltage $V$. If $V = 2\Delta/n$, an electrons is reflected (n-1) times on a NS interface, each time transferring a Cooper pair. The transfer of charge from one side to the other is equal to n. (b) Measurement from the experiment by Cron *et al.* [189]. As the voltage is reduced, the effective charge $q/e$ increases.

charge for $q$=1, 2 and 4.

In another context, shot noise measurements provide a direct measurement of fractional charges in the fractional quantum hall effect [17].

## 6.3 Low frequency noise measurement in Kondo regimes

In this part, I describe low frequency noise measurements in a carbon nanotube quantum dot. This work has been realized in the group of Pr. K. Kobayashi in Osaka University, by Meydi Ferrier *et al.* and published in ref. [97]. We made the sample in Orsay and I spent one month in Japan to see how works the experiment and to participate to the measurements and data analysis.

Even though the following work is not strictly speaking part of my PhD work, it is a good introduction to the high frequency noise measurements in the Kondo regime developed in chapter 7. The goal of the experiment is to measure the shot noise in a carbon nanotube in two different regimes : Kondo SU(2) and Kondo SU(4). Each of this situation leads to different channels transmissions, so that the measurement of the Fano factor is a good criterion to distinguish between them. Then, an effective charge is extracted from the non-linear noise, and acts as a direct probe of residual interaction emerging in the non-equilibrium regime between quasi-particles constituting the Fermi liquid.

### 6.3.1 Experimental setup

#### 6.3.1.1 Sample measured : a carbon nanotube quantum dot

Carbon nanotubes are grown on an undoped silicon wafer by chemical vapor deposition. Then, after alignment, one nanotube is chosen and contacted by a bilayer of Palladium (6 nm) and Aluminum (70 nm). The Pd is used to provide a good contact between the electrodes and the nanotube, while aluminum provides superconducting contacts. Actually, all this experiment is done in the normal state, obtained applying a 75 mT magnetic field that is strong enough to destroy superconductivity in the Pd/Al layer.

The distance between the electrodes is $L = 400$ nm and an electrostatic side-gate is deposited nearby. This choice is made instead of using a back-gate in order to prevent any loss of signal at finite frequency (the measurement is done at 2.58 MHz).

#### 6.3.1.2 Noise measurement at low temperature

The sample is cooled down in a dilution fridge of base temperature around 15 mK. The experimental setup is represented on fig. 6.7 and described in details in ref. [190].

DC transport (current and differential conductance) is measured through the SD line with standard lock-in technique. The basic principle of the noise measurement technique is that the LC circuit converts current noise of the sample into voltage fluctuations through a narrow bandwidth around the resonance frequency 2.58 MHz. Then, the cryogenic amplifier transforms this voltage noise in a current noise through the 50Ω output impedance. It

realizes an impedance matching to transport this signal through a coaxial cable up to the room temperature amplifier. Finally this signal is recorded by a digitizer and a fast Fourier transformation is performed. The noise is measured at 2.58 MHz and not below in order to overcome 1/f noise. This frequency corresponds to 0.1 mK, below the temperature of the dilution fridge : the noise is indeed measured in what we called the classical regime.

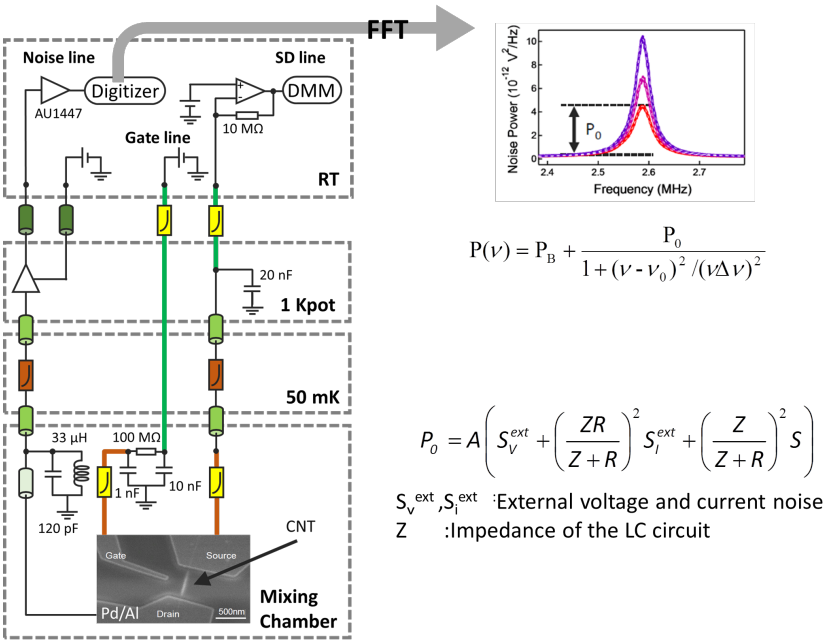


FIGURE 6.7 – Experimental setup used to measure the shot noise, see text for details.

One then obtain a spectrum as the one represented on fig. 6.7, typically a lorentzian peak centered on the frequency of the LC circuit. The proportional coefficient between the height of the peak and the noise is established from a calibration based on the thermal noise of the sample.

The principle of this experimental detection is quite straightforward and has been used by several other groups, such as in ref. [191, 192]. The detection setup used in Japan has a particularly good sensitivity mainly thanks to the homemade cryogenic amplifier at 1K.

Note that in order to suppress some unwanted fluctuations coming from the amplifiers, it is also possible to measure the noise by computing the cross correlation between two physically different lines, such as in ref. [189, 102]. But in any case, what is measured is a symmetrized noise.

### 6.3.2 Linear noise

#### 6.3.2.1 Kondo SU(2)

The stability diagram of the measured carbon nanotube is plotted on fig. 6.8 (a), on top of the zero bias conductance as a function of the temperature. We recognize the typical four-fold degeneracy of carbon nanotubes with Kondo effect for odd occupancies, similarly to fig. 2.19. Since there is no Kondo resonance in the $N = 2$ diamond, the Kondo effect in $N = 1$ and 3 diamonds is of SU(2) symmetry, and opens, in the unitary limit, a perfectly transmitted channel.

For several values of gate voltages, the noise $S_I$ is measured as a function of the current $I_{sd}$ in the sample (see for example fig. 6.8 (b) and (c)). In each case, the Fano factor is extracted from a linear fit as $F = S_I/(2eI_{sd})$ at low current and plotted as a function of $V_g$. If we assume

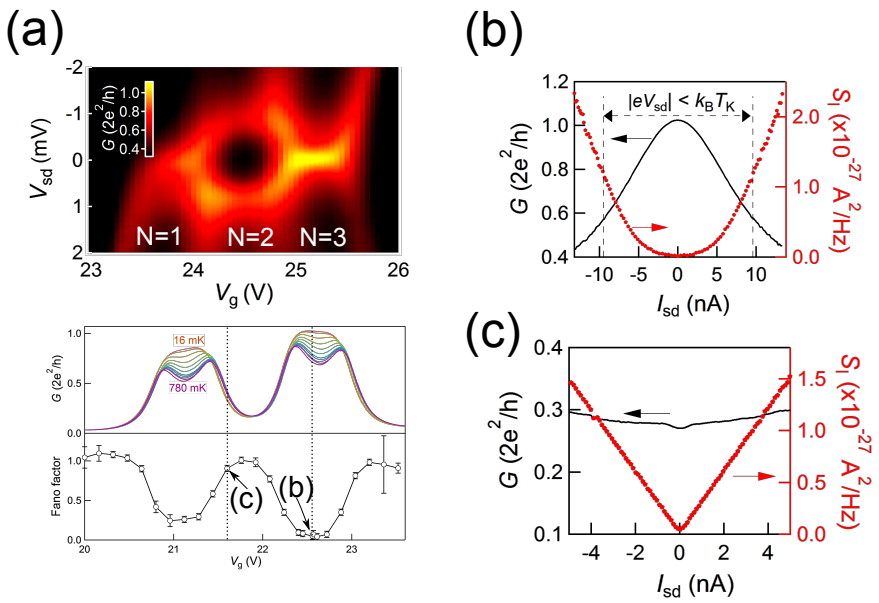


FIGURE 6.8 – (a) Differential conductance as a function of the bias voltage $V_{sd}$ and $V_g$ of the carbon nanotube quantum dot over three Coulomb diamonds. The ones with an odd number of electrons in the last occupied shell are in the SU(2) Kondo regime. At the bottom is represented the temperature dependent conductance at zero bias as well as the measured Fano factor versus the gate voltage. (b) Noise and conductance measurements as a function of the current at the center of a Kondo ridge ($N = 3$ filling factor). (c) Same measurement for N=2 occupancy.

that the system has only one spin degenerate channel of transmission T, the Fano factor is expressed easily as a function T by F=(1-T). Since this transmission is proportional to the conductance $T = \frac{dI/dV}{2e^2/h}$, T and F are expected to have opposed variations, like on fig. 6.8 (a).

We now focus on the Kondo effect present in the diamond with $N = 3$ electrons in the last occupied shell. It is particularly interesting, since the height of the Kondo resonance almost

reaches the maximal value of conductance of the unitary limit $G = 2e^2/h$, meaning that the reservoirs are symmetrically coupled to the nanotube. According to fig. 6.8 (b), at low current, the system generates a very low noise, with a Fano factor close to 0. It means that a SU(2) Kondo effect opens a perfectly transmitted channel ($T = 1$) in the quantum dot, as stated in section 2.3.1.

#### 6.3.2.2 Kondo SU(4)

The same measurement is done for a different range of gate voltage and represented on fig. 6.9. A large resonance at zero bias is observed over the $N = 1$, 2 and 3 occupancies (as on fig. 2.22), denoting SU(4) Kondo effect. In this SU(4) symmetry in the unitary limit, two channels of transmission $T = 1/2$ are open in the $N = 1$ and 3 diamonds, and reach a perfect transmission for $N = 2$.

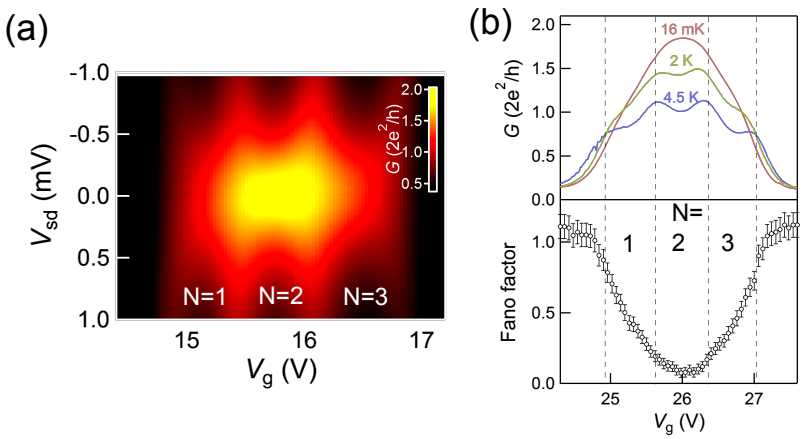


FIGURE 6.9 – (a)Differential conductance as a function of the bias voltage $V_{sd}$ and gate voltage $V_g$ of the carbon nanotube quantum dot over three Coulomb diamonds in the Kondo SU(4) regime. (b)Temperature dependent conductance at zero bias as well as the measured Fano factor versus $V_g$.

Once again, the Fano factor and the conductance have opposite gate voltage dependence. But the configuration of the system is quite different since a second channel participate in transport : the Fano factor is $F = (T_1(1 - T_1) + T_2(1 - T_2))/(T_1 + T_2)$. When two electrons stand in the last occupied shell ($N = 2$) of a symmetrically coupled dot, as stated in sec. 2.3.2.1, the formula 2.14 of the phase shift yields $T_1 = T_2 = 1$. We are here in this situation since the conductance almost reaches $4e^2/h$, and indeed the Fano factor is very low. The case of $N = 1$ and 3 occupancies is more striking. There, the formula 2.14 predicts $T_1 = T_2 = 1/2$. The conductance at zero bias is the same as for Kondo SU(2) ($G = 2e^2/h$), but the system is expected to be very noisy : this is indeed what is measured. Note that an enhancement of noise, attributed to SU(4) Kondo effect, has already been seen by Delattre *et al.* [102].

From this measurement, we see that the shot noise gives valuable informations about the

system : for identical conductance values, it tells us what are the transmission of the various channels involved.

### 6.3.3 Effective charge due to Kondo effect

The measurement of linear noise gives information about the Kondo effect indirectly, through the transmission of the channels. But if one get rid of this linear component, shot noise measurements allow to probe the specific (multiple) scattering between Landau quasi-particles induced by the Kondo correlations.

#### 6.3.3.1 Effective charge of the backscattered current and Fermi liquid theory

When the temperature is lower than $T_K$, a Kondo system in the strong coupling regime (see chapter 1) is a singlet state that can be described as a Fermi liquid [39]. This means that interacting electrons can be described as non-interacting quasi-particles, characterized by a small number of parameters that do not depend on the specific realization of the Kondo effect. In other words, the properties of the system are universal. This is very well understood at equilibrium, but less when a finite bias is applied, where the quasi-particles cannot be considered as non-interacting anymore because of residual interactions.

Out of equilibrium, the Fermi-liquid behavior is hidden in the fluctuations of the backscattered current. This current, that should be equal to zero in absence of interactions, originates from the backscattering of quasi-particles by the Kondo resonance, due to the residual interactions. This backscattered current can be expressed as $I_{bs} = \frac{dI}{dV}(V_{sd} = 0) \times V_{sd} - I_{sd}$, while the backscattered noise is $S_{bs} = S - 2eF|I_{sd}|$. The effective charge is defined as $e^* = S_{bs}/(2I_{bs})$

Backscattering involves different processes, *i.e.* different way of being transferred from the right to the left movers, fig. 6.10 (a)) [193]. Some of these processes are elastic (fig. 6.10 (b)) and involve only one quasi-particles at a time. Some others are inelastic, but are accompanied by the creation of a particle/hole pair so that, again, only one quasi-particle is involved (fig. 6.10 (c)). The interesting processes are the inelastic ones that involve two quasi-particles (fig. 6.10 (d)) : the associated effective charge is $2e$ instead of $e$. We thus have two kinds of processes, that give an effective charge of $e$ or $2e$. The global effective charge $e^*$ of the backscattered noise depends on the ratio between them.

What makes things interesting is that this ratio is universal because of the pinning of the Kondo resonance at the Fermi level, as shown by Nozières in his description of the Kondo effect by the Fermi liquid theory [39]. The calculation gives for SU(2) Kondo effect $e^*_{SU(2)} = \frac{5}{3}e$ and $e^*_{SU(4)} = \frac{3}{2}e$ for SU(4) Kondo effect [193, 194, 195]. According to Sakano et al. [195], $e^*_{SU(N)} \underset{N\to+\infty}{\longrightarrow} 1$. Qualitatively, an electron scattered by a SU(2) Kondo resonance acquires the maximal phase shift possible, $\pi/2$, then two-quasi-particles backscattering processes are likely to occur. According to the formula 1.6, the phase shift associated to the Kondo resonance

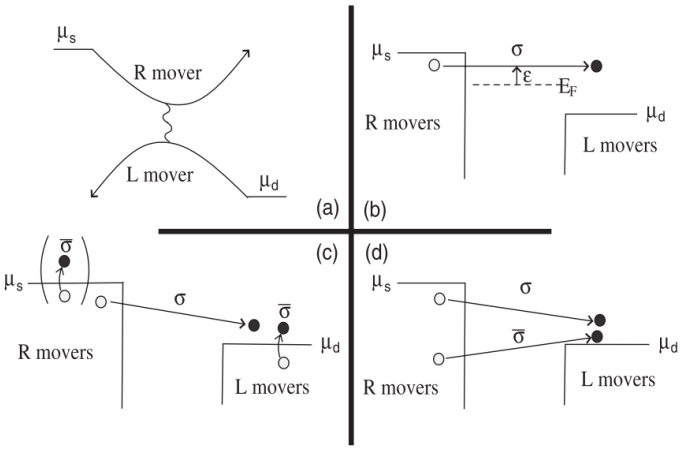


FIGURE 6.10 – Different possible backscattering processes involving one (b) or two (c and d) quasiparticles (see text for details). From [193].

SU(N) is $\delta_N = \pi/N$, that's why two-qp processes become less important as N increases.

#### 6.3.3.2 Experimental measurement

The experimental measurement of this effective charge is not that easy since the backscattered noise is a small signal, whose precision depends crucially on the accuracy of the determination of the linear Fano factor.

The measurement has been done for both SU(2) and SU(4) Kondo effect, and is represented on fig. 6.11.

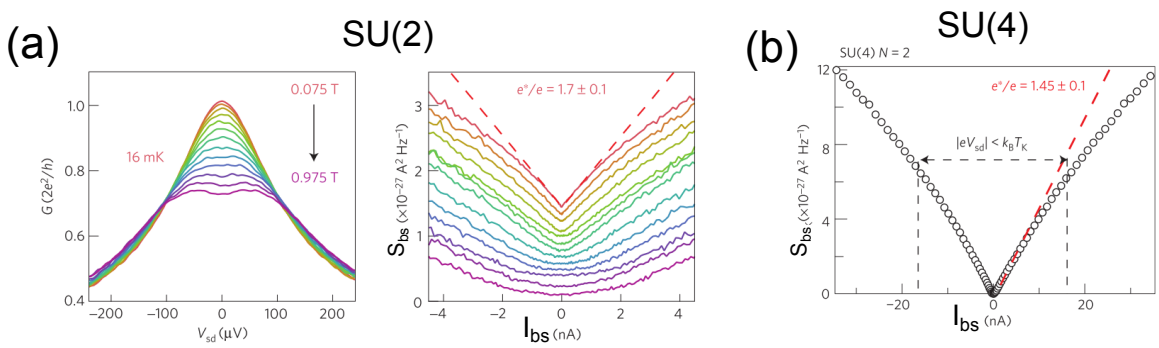


FIGURE 6.11 – Backscattered noise $S_{bs} = S - 2eF|I_{sd}|$ plotted as a function of the backscattered current $I_{bs} = \frac{dI}{dV}(V_{sd} = 0) \times V_{sd} - I_{sd}$ in the case of (a) SU(2) Kondo effect and (b) SU(4) Kondo effect at $N = 2$. (a) For SU(2) Kondo effect the conductance and the backscattered noise are measured at various magnetic fields. As the Kondo resonance is washed out by the magnetic field, the effective charge decreases, proving the Kondo origin of the effect.

In the SU(2) Kondo regime, at low current the noise is linear in the current and the effective

charge is given by the proportionality factor : $e^*/e = 1.7 \pm 0.1$, consistent with the theoretical value. When the magnetic field is increased, the Kondo resonance is washed out and $e^*$ goes to 0, proving that the effect is indeed related to Kondo physics.

In the SU(4) regime at $N = 2$ filling, similarly the effective charge is found to be $e^* = 1.45 \pm 0.1$, again in agreement with the expected value.

These measurements confirm the validity of the Fermi liquid description of the Kondo regime beyond equilibrium. They prove as well that noise measurements enable to distinguish between different kinds of Kondo correlations, without any magnetic field dependence of the conductance.

## Conclusion

- The current noise represents the fluctuations of current in a conductor. We define two regimes of frequencies : the regime of high frequency compared to temperature, where zero-point fluctuations are important, and the low frequency regime, where they are washed out.
- At high frequency, in the quantum regime, the spectral density of noise depends of the sign of the frequency. We have chosen a convention such that the positive frequencies correspond to absorption processes of energy in the form of photons, the negative ones to emission processes.
- When the average current in a mesoscopic conductor is non-zero, the main contribution to the fluctuations come from the shot noise, which originates from the discreteness of the charge.
- The measurement of this shot noise at low frequency gives insights about the system : transmission of the channels, effective charge, interactions.
- In a quantum dot in the Kondo regime, this measurement allows to distinguish between two kinds of Kondo effects : SU(2) and SU(4), which present similar conductance behaviors but distinct shot noise : the first one does not generate noise but the second can be very noisy.
- Extracting the backscattering noise and measuring its effective charge, it is possible to probe the Fermi liquid behavior of the Kondo effect out of equilibrium.

# 7 High frequency noise measurement

In this chapter, I present high frequency noise measurements in a carbon nanotube. In a first part, the measurement setup, based on an on-chip tunnel junction detector, is described. Then, I will develop what is expected from the noise in this limit, that is experimentally almost unexplored. Finally, I will present the experimental results.

## 7.1 High frequency noise measurements

As stated in section 6.3.1.2, the most direct method to measure noise is to acquire the time dependent current and extract the spectral density of noise with a proper analysis or to integrate it analogically (for example with a diode). This kind of measurement remains possible until a few GHz. But beyond and in order to separate emission and absorption processes, on-chip detectors have been proved to be more convenient.

The detection setup used in this thesis is based on such an on-chip detector, made of a superconducting/insulator/superconducting (SIS) junction. In order to measure the noise at some chosen frequencies, this detector is coupled to the source of noise, here the carbon nanotube, through a resonating circuit. After detailing other noise measurement setups, this section aims at describing these different components of the experimental setup.

### 7.1.1 How to measure non-symmetrized noise at high frequency ?

High frequency noise measurements of mesoscopic systems, around a few tens of GHz are not so numerous, because of the technical issue that need to be addressed.

#### 7.1.1.1 High frequency electronics methods

The "natural way" is to follow the low-frequency technique explained in section 6.3.1.2, where the noise is directly extracted from the time dependent signal, using high-frequency electronics

working at the proper frequency (amplifiers, circulators etc.).

This is the technique used first by Schoelkopf *et al.* [191] from 1 to 20 GHz, to measure the frequency dependence of shot noise in a diffusive gold conductor. The measurements, presented on fig. 7.1, showed for the first time the frequency dependence of shot noise. In this experiment, the analysis is based on the symmetrized noise, but the setup does not allow to decide if indeed both emission and absorption are measured, or only emission.

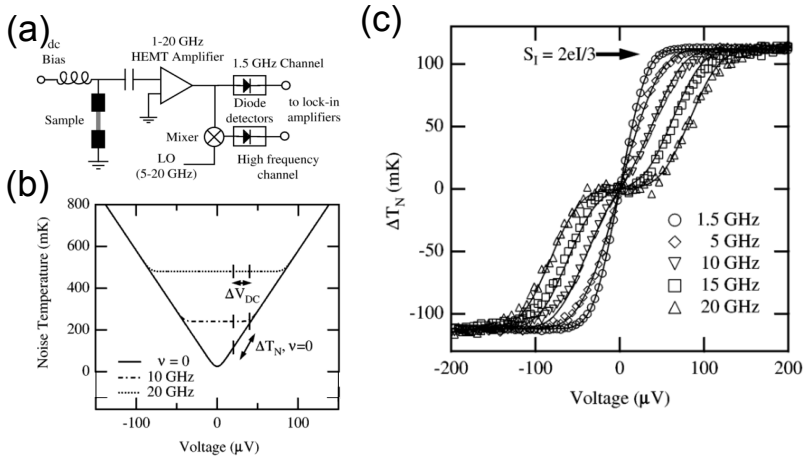


FIGURE 7.1 – (a) Experimental setup used in the experiment by Schoelkopf *et al.* (b) Noise expected as a function of the bias voltage V for various frequencies. (c) Measured derivative of the excess noise, translated as an effective noise temperature $\Delta T_N$, as a function of the bias voltage V for various frequencies (excess noise is the difference between the absolute noise and the noise at $V = 0$). From ref. [191].

A similar method has been used in Saclay to measure the frequency dependence of the shot noise in a quantum point contact [196] and dynamical Coulomb blockade [197]. In these experiments, thanks to a circulator that prevents the mesoscopic system from absorbing photons coming from the detection setup, the authors are able to measure emission noise only. But the frequency measurement is limited by the electronics to 4-8 GHz.

Note that Xue *et al.* proposed an alternative method to measure non-symmetrized noise of a mesoscopic system through a matching circuit [198]. It relies on the fact that the reflexion coefficient of the whole circuit (system+matching circuit) is related to the difference between absorption and emission noise. Added to a measurement of symmetrized noise, it gives access to both components. This method solve the problem of the noise symmetrization, but is still limited by HF electronics.

#### 7.1.1.2 On-chip detectors

To overcome the difficulties inherent to high frequency electronics (symmetrized noise and frequency limitations), the solution that has been proposed in 2000 by R. Aguado and L. P.

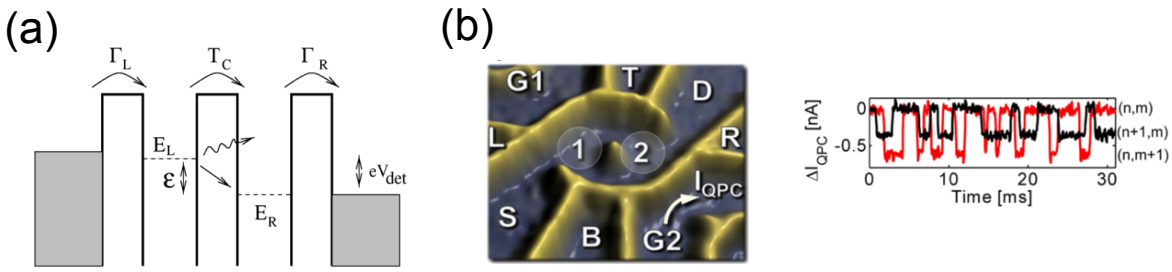


FIGURE 7.2 – (a) Principle of an on-chip detector based on double quantum dot described in ref.[199]. Such a detector is frequency selective and sensitive to non-symmetrized noise. (b) Example of realization of such a detector with a double quantum dot. The transitions from one to the other level are deduced from the real time measurement of the dc current nearby a QPC. From ref. [200].

Kouwenhoven [199] is to use a double-QD on-chip detector. The principle of such a detector is to detect the emission or absorption of photons at the energy $h\nu$ by measuring the inelastic transitions of electrons between two levels separated by an energy $h\nu$ (see fig. 7.2). Such a tunable two-level system can be obtained using a double quantum dot, in which the energy levels is tuned by gate voltages [200, 201] or in a QD [202]. This kind of detector has many advantages : first, it is frequency selective, since one can change the level spacing easily. It is also sensitive to non-symmetrized noise since, knowing the level-configuration of the dot, it is possible to deduce if the measured processes are due to emission or absorption.

The on-chip detector used in this PhD has the same advantages, but is based on a superconducting tunnel junction. This detector will be detailed in the following.

### 7.1.2 SIS junction detector

#### 7.1.2.1 General principle

This noise detection setup is based on the measurement of photo-assisted tunneling (PAT) current in a superconducting tunnel junction, made of a thin layer of insulator (here aluminum oxyde AlOx) between two superconducting layers (typically aluminum) (SIS junction).

The I(V) characteristic of such a system is represented on fig. 7.3 (a) : because of the superconducting gap, one needs to apply a bias voltage $V_d > \frac{2\Delta}{e}$ on the junction to measure a quasi-particle current. Below the gap, all the current is related to Cooper pair tunneling that can be elastic (this is the supercurrent at $V_d = 0$) or inelastic and related to the environment of the junction [203].

Our noise detection is based on the measurement of photo-assisted tunneling (PAT) current of quasi-particles in the junction. For this reason we want to suppress any signal coming from Cooper pair tunneling. To do so, instead of a simple SIS junction, we use two identical SIS junctions in a SQUID geometry. This system is globally equivalent to a junction with

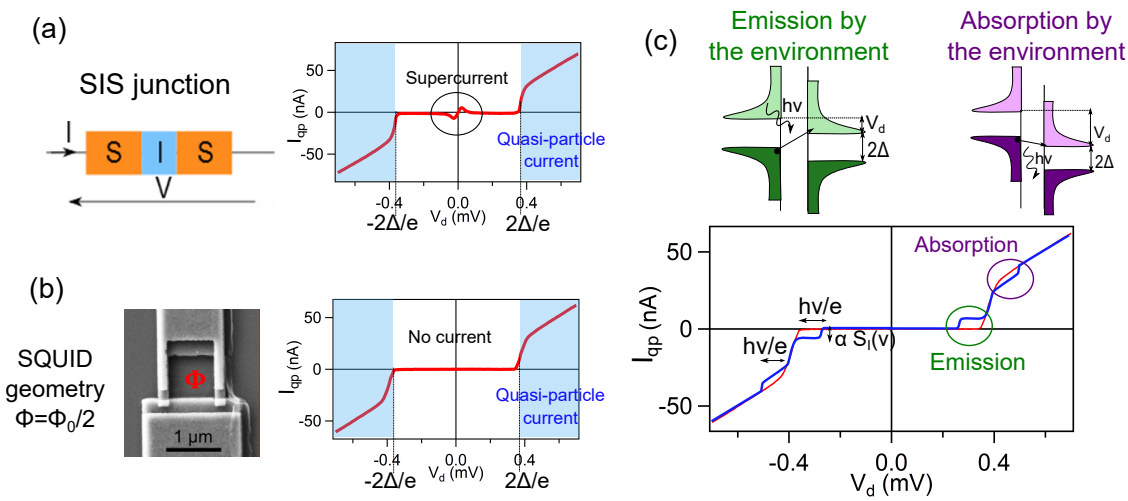


FIGURE 7.3 – Principle of the SIS based on-chip detector. (a) I(V) characteristic of a SIS junction (measurement). If the junction is biased below the superconducting gap ($|V_d| < 2\Delta/e$), there is no current except around $V_d = 0$ due to the supercurrent (the shape of the supercurrent branch is related to the biasing conditions). The quasi-particle current appears for $|V_d| > 2\Delta/e$. (b) In a SQUID geometry, if the proper magnetic flux is applied, the supercurrent features are suppressed (measurement). (c) If the detector emits or absorbs photons (*i.e* if the environment absorbs or emits photons), the quasi-particle current is photo-assisted, the I(V) characteristic is modified (qualitative curve).

a tunable effective critical current. Indeed, the critical current of this symmetric SQUID is equal to $I_c = 2I_0|\cos(2\pi\frac{\Phi}{\Phi_0})|$, with $\Phi_0 = \frac{h}{2e}$ the flux quantum and $I_0$ the critical current of a single junction. If a magnetic flux of $\Phi = 0$ or $\Phi = \frac{\Phi_0}{2}$ is applied in the SQUID, $I_c = 0$ and all the supercurrent-related features vanish (see fig. 7.3 (b)). This has also the advantage of destroying any AC Josephson radiation from the detector, that could disturb the investigated system.

In this supercurrent-less SIS junction, any sub-gap current originates from quasi-particle tunneling, assisted by the absorption of a photon emitted by the environment.

Typical modifications of the I(V) characteristic are represented on fig. 7.3 (c) : when the SIS junction is biased by $|V_d| < 2\Delta/e$, a photo-assisted tunneling current of quasi-particle is possible provided that a photon of energy $h\nu > 2\Delta - |V_d|$ is absorbed. In other words, when the environment emits photons at energy $h\nu$, a current step of width $h\nu/e$ appears in the $I(V)$ characteristic with a height proportional to the amplitude of the irradiation.

Similarly, when the junction is biased above the gap ($|V_d| > 2\Delta/e$) , the SIS junction has enough energy to emit photons of energy $h\nu < |V_d| - 2\Delta$ provided that the environment is able to absorb it. This loss of energy results in a reduction of the quasi-particle current, as represented on fig. 7.3 (c).

#### 7.1.2.2 Expression of the photo-assisted tunneling current with $P(E)$ theory

After this qualitative introduction, we show here the rigorous derivation of the photo-assisted tunneling (PAT) current in the SIS detector.

**Quasi-particle current** To express the PAT current in the detector, we use the $P(E)$ theory that takes into account the electro-magnetic environment to compute the tunneling processes. The derivation follows the review on the subject by Ingold and Nazarov [203].

What is called $P(E)$ is the probability for the junction to absorb or emit the energy $|E|$ in the external circuit (i.e. in the environment). If $E > 0$, the energy is absorbed by the environment, if $E < 0$ it is emitted.

If one knows $P(E)$, it is possible to express the forward tunneling rate in a normal tunnel junction by :

$$\vec{\Gamma}(V_d) = \frac{1}{e^2 R_T} \int_{-\infty}^{\infty} dE dE' f(E)(1 - f(E' + eV_d))P(E - E') \tag{7.1}$$

where it is clear that $P(E - E')$ quantifies the probability that an electron tunnel from the energy $E$ to $E' + eV_d$. In absence of environment, it is not possible to exchange any energy, this probability is reduced to the Dirac function : $P(E - E') = \delta(E - E')$.

In a superconducting tunnel junction, one has in addition to include the superconducting density of states :

$$\frac{N_S(E)}{N(0)} = \begin{cases} \frac{|E|}{\sqrt{(E^2 - \Delta^2)}} & |E| > \Delta \\ 0 & |E| < \Delta \end{cases} \tag{7.2}$$

That gives for the forward tunneling rate in a superconducting tunnel junction :

$$\vec{\Gamma}(V_d) = \frac{1}{e^2 R_T} \int_{-\infty}^{\infty} dE dE' \frac{N_S(E) N_S(E' + eV_d)}{N(0)^2} f(E)(1 - f(E' + eV_d))P(E - E') \tag{7.3}$$

The quasi-particle current is then obtained computing $I_{qp}(V_d) = \vec{\Gamma}(V_d) - \overleftarrow{\Gamma}(V_d) = \vec{\Gamma}(V_d) - \vec{\Gamma}(-V_d)$, with $\overleftarrow{\Gamma}$ is the backward current. After some calculations [203], one gets the expression for the quasi-particle current :

$$I_{qp}(V_d) = \int_{-\infty}^{\infty} dE \frac{1 - e^{eV_d/(k_B T)}}{1 - e^{E/(k_B T)}} P(eV_d - E) I_{qp}^0(E/e) \tag{7.4}$$

Where $I_{qp}^0(V_d)$ is the I(V) characteristic of the SIS junction in absence of environment

$(P(E) = \delta(E))$ (typically, what is represented on fig. 7.3 (b)) :

$$I^0_{qp}(V_d) = \frac{1}{e^2 R_T} \int_{-\infty}^{\infty} dE dE' \frac{N_S(E) N_S(E + eV_d)}{N(0)^2} (f(E) - f(E + eV_d)) \tag{7.5}$$

**Relation between $P(E)$ and voltage fluctuations** For the moment, we have expressed the photo-assisted tunneling current as a function of a quantity related to the environment , $P(E)$. The electrical fluctuations of a mesoscopic system placed close to the detector can be seen as a particular realization of an environment, that can be expressed through $P(E)$. We show here how to do that.

We start defining the phase $\phi(t)$, related to the voltage across the detector by $\phi(t) = \frac{e}{\hbar} \int_{-\infty}^{t} dt' V(t')$. Its auto-correlation function is then :

$$J(t) =< [\phi(t) - \phi(0)]\phi(0) > \tag{7.6}$$

And one can show that $P(E)$ is the Fourier transform of $\exp(J(t))$ :

$$P(E) = \frac{1}{h} \int_{-\infty}^{\infty} dt \exp\left(J(t) + \frac{i}{\hbar} Et\right) \tag{7.7}$$

J(t) represents the fluctuations of phase so, in a limit of low noise, $\exp(J(t)) \approx 1 + J(t)$. Then it is straightforward to express it as a function of the voltage fluctuations across the detector, whose spectral density of noise is called $S_V(\nu)$ [199]:

$$J(t) = \frac{e^2}{2\pi\hbar^2} \int_{-\infty}^{\infty} d\nu \frac{S_V(\nu)}{\nu^2} (e^{-i2\pi\nu t} - 1) \tag{7.8}$$

**Photo-assisted tunneling current** Putting together equations 7.4, 7.7 and 7.8 we obtain the expression of the photo-assisted tunneling current in the SIS junction defined as the difference between the quasi-particle current with and without environment $I_{PAT}(V_d) = I_{qp}(V_d) - I^0_{qp}(V_d)$ [204]:

$$\begin{aligned} I_{PAT}(V_d) = & \int_0^{\infty} d\nu \left(\frac{e}{h\nu}\right)^2 S_V(-\nu) I^0_{qp}\left(V_d + \frac{h\nu}{e}\right) \\ & + \int_0^{eV_d} d\nu \left(\frac{e}{h\nu}\right)^2 S_V(\nu) I^0_{qp}\left(V_d - \frac{h\nu}{e}\right) - \int_{-\infty}^{\infty} d\nu \left(\frac{e}{h\nu}\right)^2 S_V(\nu) I^0_{qp}(V_d) \end{aligned} \tag{7.9}$$

**Monochromatic case** To understand this formula, let's consider a monochromatic source of noise that emits $S_0^-$ and absorbs $S_0^+$ at frequency $\nu_0$ : $S_V(\nu) = S_0^+ \delta(\nu - \nu_0) + S_0^- \delta(\nu + \nu_0)$

(with $0 < h\nu_0 < eV_d$) :

$$I_{PAT}(V_d) = \left(\frac{e}{h\nu_0}\right)^2 \left[S_0^- I_{qp}^0\left(V_d + \frac{h\nu_0}{e}\right) + S_0^+ I_{qp}^0\left(V_d - \frac{h\nu_0}{e}\right) - (S_0^- + S_0^+) I_{qp}^0(V_d)\right] \tag{7.10}$$

- Detector biased below the gap, $V_d < 2\Delta/e$ : $I_{qp}^0(V_d - h\nu_0/e) = I_{qp}^0(V_d) = 0$, yielding $I_{PAT}(V_d) = \left(\frac{e}{h\nu_0}\right)^2 S_0^- I_{qp}^0(V_d + h\nu_0/e)$. With this biasing of the detector, one measures only the emission noise of the source, thanks to the absorption of photons by the detector. $I_{PAT}$ due to frequency $\nu_0$ is measured as a step at $2\Delta > eV_d > 2\Delta - h\nu_0$.
- Detector biased above the gap, $V_d > 2\Delta/e$ : the three terms contribute to $I_{PAT}$ $I_{PAT}(V_d) = \left(\frac{e}{h\nu_0}\right)^2 \left[S_0^- \left(I_{qp}^0\left(V_d + \frac{h\nu_0}{e}\right) - I_{qp}^0(V_d)\right) - S_0^+ \left(I_{qp}^0(V_d) - I_{qp}^0\left(V_d - \frac{h\nu_0}{e}\right)\right)\right]$. We see that in this case, both emission and absorption by the source are detected. But if $eV_d < 2\Delta + h\nu$, $I_{qp}^0\left(V_d - \frac{h\nu_0}{e}\right) = 0$ and thus the contribution related to absorption noise $S_0^+$ is dominant. With such a bias voltage, the $I_{PAT}$ contribution to $I_{qp}$ is negative and mainly related to noise absorbed by the source and emitted by the detector.

At the end, the quasi-particle current, modified by photo-emission and absorption, has the shape represented on fig. 7.3 (c). Note that this kind of detection would work with any system with a non-linear characteristic. It is particularly convenient with SIS junctions, that are also quite simple to fabricate.

#### 7.1.2.3 SIS junctions as high frequency detectors

Since the very beginning of their discovery, superconducting tunnel junction have been shown to be sensitive to microwave radiation, for example by Dayem and Martin in 1962 [205], followed by a theory by Tien and Gordon in 1963 [206]. This first photo-assisted current in a SIS junction was induced by external irradiation. In 1965, Giaever used an SIS junction to detect on-chip the AC Josephson effect emitted by another tunnel Josephson junction [207] (see fig. 7.4).

This kind of detector has also been used as quantum detectors [208], for example for astronomic particles detection [209].

Their use as high frequency non-symmetrized noise detector of mesoscopic systems started in 2003 in Delft and continued in Orsay, laying the foundations for the present work :

- In 2003, the asymmetrized noise of a two-level system, namely a Cooper pair box, was measured by Deblock *et al.* [204].
- In 2006, Onac *et al.* used an SIS detector to measure the noise in a carbon nanotube in the Coulomb blockade regime [210].

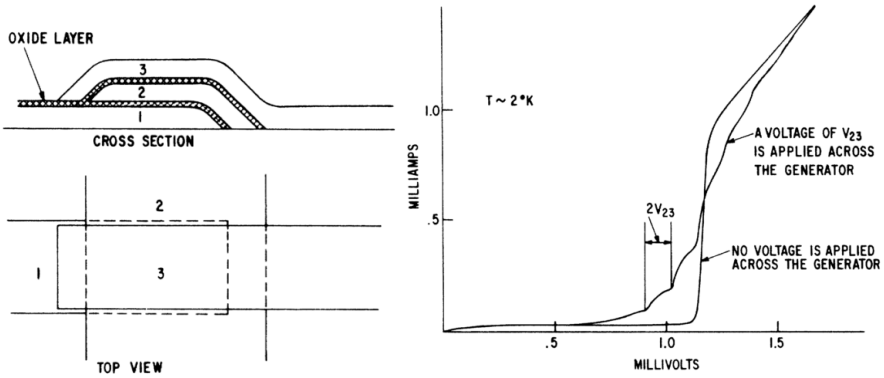


FIGURE 7.4 – Giaever's experiment for the measurement of the AC Josephson effect of a SIS junction with another SIS junction as an on-chip detector. Left : schematics of the sample investigated. Rigth : modification of the I(V) characteristic by AC irradiation. From ref. [207].

- The same year, Billangeon *et al.* use a similar setup to measure the non-symmetrized quasi-particle noise of a tunnel Josephson junction [211]
- In 2007, Billangeon *et al.* measure the AC Josephson effect and resonant Cooper pair tunneling emission of a single Cooper pair transistor [24].

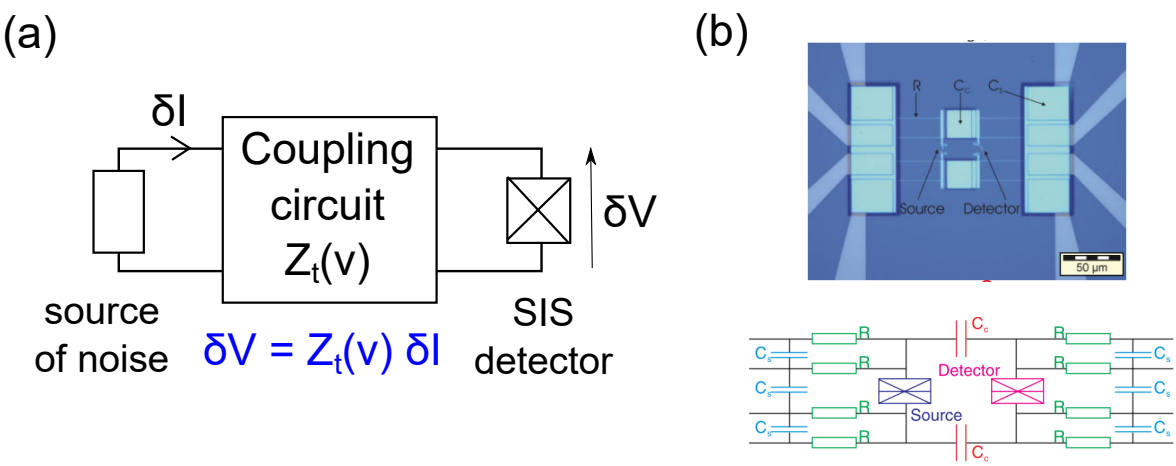


FIGURE 7.5 – (a) Relation between the voltage fluctuations across the detector and the fluctuations of current emitted by the investigated system source. $Z_t(\nu) = \frac{\delta V}{\delta I}$ is called the transimpedance and depends on the coupling circuit. (b) Example of experiment where the coupling is capacitive, from [211].

In all these experiments, the detector is coupled to the noise source by a capacitive coupling such as the one described on fig. 7.5. For a given bias of the detector $V_d$, the measured photo-assisted current results from processes at all the frequencies $h\nu > 2\Delta - V_d$. It is relevant for sources with monochromatic emission or white noise, but is not very convenient for analyzing the frequency dependence of the noise.

That's why, during Julien Basset's PhD [117], a resonant coupling has been developed and gave interesting results :

- In a first experiment, a SIS junction is coupled to the SIS detector through a resonating circuit made of two coupled coplanar transmission lines. The thermal noise of the resonant circuit itself has been measured in both emission and absorption at a fixed frequency as well as their temperature dependence [186] (the result is represented on fig. 6.2).

- This experimental setup allowed as well the measurement of high frequency quasi-particle emission noise of a Josephson junction, as well as its high frequency impedance [19].

- Finally, the source of noise has been replaced by a carbon nanotube quantum dot in the Kondo regime [23]. A first measurement of emission noise has been done at frequencies of the order of the Kondo temperature.

This part of my PhD work is the continuation of this experiment, and will be detailed below. Note that in all these experiments using a resonator, except for the thermal noise of the resonant circuit, the measurement of absorption noise was not possible. The reason for that is the following : it is easier to measure a small deviation from zero of a signal (emission noise, below the gap) than a small variation of a high signal (absorption noise, above the gap). Unfortunately, we still fail to measure the absorption noise with this setup.

### 7.1.3 Coupling through a resonator

Generally, we are interested in the current fluctuations in the system under investigation, called $\delta I$. But the SIS detector is sensitive to the fluctuations of its bias voltage $\delta V$ (see fig. 7.5 (a)). We call trans-impedance $Z_t$ the ratio between these two quantities : $\delta V = Z_t(\nu)\delta I$, such that we have the relation for the noise : $S_V(\nu) = |Z_t(\nu)|^2 S_I(\nu)$ [199]. The question of the coupling between these two components, and thus the value of $Z_t(\nu)$ is crucial for the experiment.

As mentioned above, we want to filter the frequencies at which the noise is detected. To do so, the source and the detector are coupled through a resonant circuit, such that $Z_t(\nu) = \sum_n Z_t^n(\nu - \nu_n)$ with $Z_t^n(\nu - \nu_n)$ a resonance centered around the frequency $\nu_n$, $n^{th}$ harmonic of the resonator. Such examples of resonators are shown on fig. 7.6 with the associated trans-impedance $|Z_t(\nu)|$, whose measurement will be explained soon.

If we assume that the noise does not vary too much over the resonance, then we obtain for the photo-assisted current below the gap (*i.e.* related to emission by the source) :

$$I_{PAT}(2\Delta - h\nu_i < eV_d) = \int_0^\infty d\nu \left(\frac{e}{h\nu}\right)^2 S_I(-\nu) \sum_{n=0}^{\infty} |Z_t^n(\nu - \nu_n)|^2 I_{qp}^0 \left(V_d + \frac{h\nu}{e}\right) \tag{7.11}$$

$$\approx \sum_{n=0}^{\infty} \left(\frac{e}{h\nu_n}\right)^2 K_n S_I(-\nu_n) I_{qp}^0 \left(V_d + \frac{h\nu_n}{e}\right) \tag{7.12}$$

$K_n$ is a coefficient that takes into account the shape of the resonance around frequency $\nu_n$, that has to be determined by a calibration. Note that $I_{PAT}$ is the sum of contributions of the different frequencies, weighted by $\frac{K_n}{\nu_n^2}$. Consequently, for a given bias of the detector, the main contribution comes from the lowest frequency.

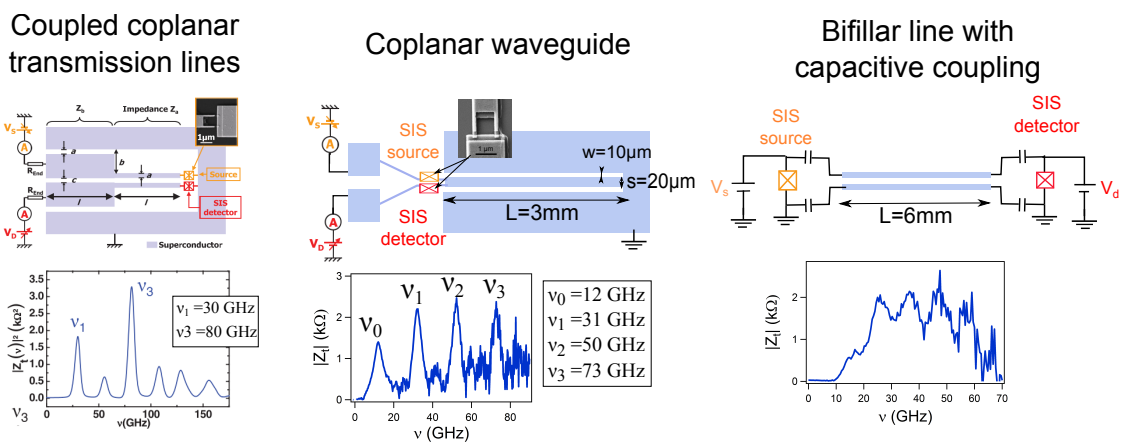


FIGURE 7.6 – Three different designs of resonators and how they are coupling the source and the detector. Below each of them is represented their measured trans-impedance $Z_t(\nu)$. The first one, the coupled coplanar transmission lines, is the one used in ref.[186, 19, 23]. The second one is a coplanar waveguide, that has been used in this work. The last one, bifilar lines with capacitive coupling, is an example of attempt of different design, that did not work. The blue rectangles are made of superconducting aluminum.

### 7.1.4 Characterization of the experimental setup

#### 7.1.4.1 Design of the sample

The first of the resonators represented on fig. 7.6, the coupled coplanar transmission lines, is the one that has been used in the previous experiments, with resonance frequencies around 30 and 80 GHz. In order to decrease the frequency resonance, hoping that we could measure more frequencies with the same setup, we designed a new resonator.

We used a coplanar waveguide geometry, with a transmission line placed between two large ground plane (see center panel of fig. 7.6 and ref. [212], where this kind of resonator is

described). One extremity of the transmission line is grounded while the source and the detector are connected to the other extremity : the length of the resonator L corresponds to the quarter of the wavelength (giving resonance frequencies such that $L = \lambda_n \left(\frac{1}{4} + \frac{n}{2}\right)$ with $n$ an integer). The dimensions of the resonator, made of Aluminum of thickness 200 nm on an undoped silicon wafer are written on fig. 7.6. From all these parameters, it is possible to evaluate the characteristic impedance of the resonator[1] $Z_0 = 46\ \Omega$. To obtain a frequency of the order of 10 GHz, we choose $L \approx 3$ mm.

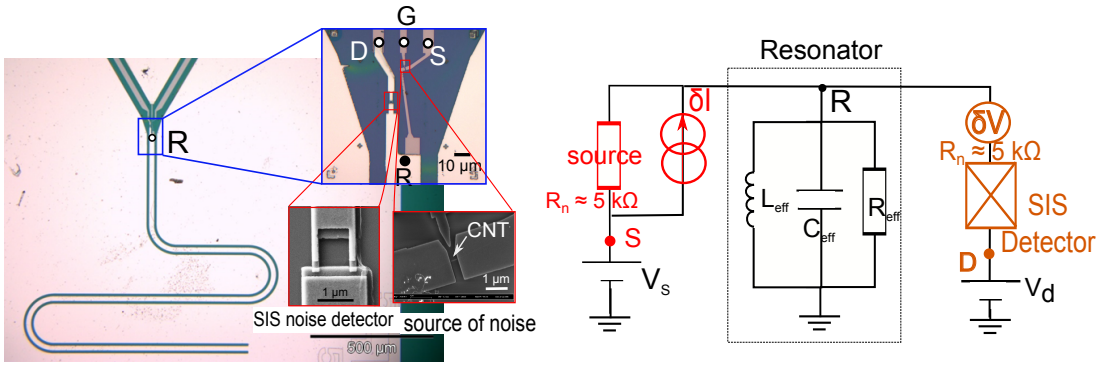


FIGURE 7.7 – Left : picture of the sample used for high frequency measurement. Here the source of noise is a carbon nanotube, it can be replaced by a SIS junction for testing the setup. The equivalent electronic circuit is represented on the right : the coplanar waveguide is equivalent at resonance to a RLC circuit.

The detector and the source are both directly connected to the end of the transmission line. This direct connection is expected to decrease substantially the quality factor. We discuss this question in the following.

#### 7.1.4.2 Characterization with AC Josephson effect of a SIS junction

The usual way for characterizing a resonator (here it means determining the trans-impedance $Z_t$) is to use a vector network analyzer (VNA) and to measure the frequency dependent reflection coefficient. But here, the sample is designed to be addressed by DC measurements, AC signal being confined on-chip. The best way to characterize the resonator (and the detector) seems thus to use an on-chip AC source. A very convenient one is given by the AC Josephson effect of a SIS junction : when biased by the voltage $V_s$, there is a AC current $I(t) = I_C \sin(\frac{2eV_s}{\hbar}t)$ in the junction. The formula 6.2 gives an associated current spectral density $S_I(\nu, V_s) = \frac{I_c^2}{4}\left(\delta\left(\nu - \frac{2eV_s}{h}\right) + \delta\left(\nu + \frac{2eV_s}{h}\right)\right)$. This is the monochromatic situation treated in the section 7.1.2.2, giving the emission contribution to the photo-assisted tunneling current :

$$I_{PAT}(V_d, V_s) = \left(\frac{1}{2V_s}\right)^2 \frac{I_c^2}{4} \left|Z_t\left(\frac{2eV_s}{h}\right)\right|^2 I_{qp}^0(V_d + 2V_s) \tag{7.13}$$

[1] Formula exists to calculate that, I used this website : http://www1.sphere.ne.jp/i-lab/ilab/tool/cpw_e.htm

Thanks to the estimation of the critical current by the Ambegaokar-Baratoff formula [213] and knowing $I_{qp}^0$, the measurement of $I_{PAT}$ at a fixed $eV_d > 2\Delta - h\nu_0$ gives access to $|Z_t(\nu)|$. The measurement is presented on fig. 7.8.

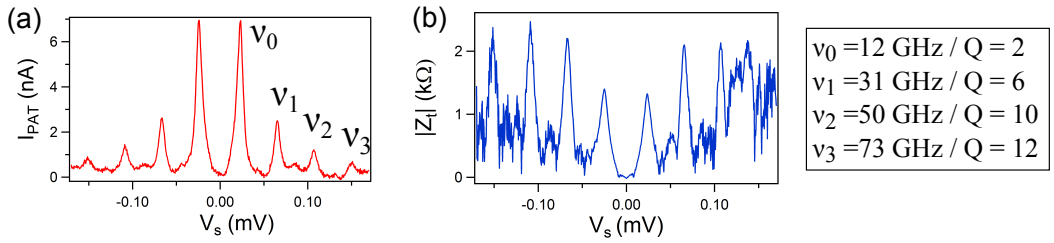


FIGURE 7.8 – (a) Photo-assisted quasiparticle current measured in the detector biased at $2\Delta - h\nu_0 < eV_d < 2\Delta$ as a function of the bias $V_s$ of the source of AC Josephson effect. The frequency of the emission is given by the Josephson frequency $\nu = \frac{2eV_s}{h}$. (b) Trans-impedance $Z_t(\nu)$ extracted from $I_{PAT}$ (see text). The corresponding resonance frequencies and quality factors are given. In this sample, the detector is a SQUID of normal resistance around 5kΩ and the source a simple junction of normal resistance 12kΩ.

#### 7.1.4.3 Width of the resonances

The resonance peaks have roughly all the same width, around 6 GHz (see fig. 7.8). This is unusually large for a resonance peak of a superconducting resonator, and gives very low quality factors ($Q = 2$ for 12 GHz). This could be due to the fact that the detectors and resonators are directly coupled to the transmission line, inducing losses.

To evaluate the expected quality factor of the setup, it is modelized by the RLC circuit represented on fig. 7.7. According to ref. [212], the effective capacitance, inductance and resistance modeling the resonator are (for the fundamental frequency) :

$$L_{eff} = \frac{2L_l L}{\pi^2}, \quad C_{eff} = \frac{C_l L}{2}, \quad R_{eff} = \frac{Z_0}{\alpha L} \tag{7.14}$$

$L_l$ and $C_l$ are respectively the inductance and capacitance per unit of length, $L = 3$ mm the length of the line and $\alpha$ a coefficient that quantifies the losses in the system. Moreover, we know that $Z_0 = \sqrt{\frac{L_l}{C_l}} = 46\ \Omega$ and $\nu_0 = \frac{1}{2\pi\sqrt{L_{eff}C_{eff}}} = 10$ GHz, yielding :

$$L_l = 1.1.10^{-9}\ \text{H/m}, \quad L_{eff} = 0.67\ \text{nH} \tag{7.15}$$

$$C_l = 3.6.10^{-10}\ \text{F/m}, \quad C_{eff} = 0.54\ \text{pF} \tag{7.16}$$

We neglect here the modification of the resonance frequency by the capacitances of the source and detector. In other words, we assume that they are simple resistive conductors. For carbon

nanotubes this assumption is reasonable, less for a SIS junction biased close to the gap [214]. But we neglect this effect in this quick calculation.

Then, the quality factor is simply obtained by

$$Q = 2\pi\nu_0 R_{tot} C_{eff} \text{ with } R_{tot} = \left(R_{eff}^{-1} + R_D^{-1} + R_S^{-1}\right)^{-1} \tag{7.17}$$

$R_{eff}$ represents the internal losses of the resonator, $R_D$ the resistance of the detector and $R_S$ of the source, see fig. 7.7. In ref. [212], $R_{eff} \approx 1.10^8$ Ω. Even though our resonator had a lot of additional losses ($10^4$ times more), we can make the assumption that $R_{tot}$ is dominated in any case by $R_D$ and $R_S$ and not by the intrinsic losses of the resonator. Typically, the normal resistance of the SIS junctions is $R_n^{detector} = 5$ kΩ. For a nanotube, the resistance is always larger than 6 kΩ. Very pessimistically, we take an equivalent resistance $R_{tot} = 2$ kΩ, and obtain a quality factor of $Q = 68$.

From this rough but pessimistic calculation, we see that, at worst, the direct coupling to the resonator would give a quality factor more than 30 times larger than what we measure. Moreover, it seems that whatever the frequency of the resonance or the design of the resonator, the width of the resonance is the same (around 5 GHz, see fig. 7.6). All these clues tell us that this width may be due to the non-monochromaticity of our source (the SIS junction) instead of the resonant circuit itself. This non-monochromaticity may originate from fluctuations of $V_s$ (and thus may be improved by a better filtering) or from the fluctuations of current in the junction [215].

#### 7.1.4.4 Characterization with quasi-particle noise of a SIS junction

There is another way to test the experimental setup : the measurement of the quasi-particle noise of a Josephson junction (*i.e.* a SIS junction biased above the gap). The expression of this noise is given by (see ref. [211] and ref. [216] for the derivation) :

$$S_I(\nu, V_s) = e\left[\frac{I_{qp}^0(\frac{h\nu}{e} + V_s)}{1 - \exp\left(-\frac{\frac{h\nu}{e}+V_s}{k_B T}\right)} + \frac{I_{qp}^0(\frac{h\nu}{e} - V_s)}{1 - \exp\left(-\frac{\frac{h\nu}{e}-V_s}{k_B T}\right)}\right] \tag{7.18}$$

$I_{qp}^0$ is the I(V) characteristic of the junction without environment (see fig. 7.3 (c) and 7.9 (c) in grey).

The derivative of the photo-assisted current as a function of the bias voltage of the source $V_s$ is monitored for three different bias voltages of the detector (defined on fig. 7.9 (b)) : $V_{d,0}$ such that $2\Delta - h\nu_0 < eV_{d,0} < 2\Delta$ (in red), that gives the sum of the contributions at $\nu_0$, $\nu_1$ and $\nu_2$, $V_{d,1}$ such that $2\Delta - h\nu_1 < eV_{d,1} < 2\Delta - h\nu_0$ (in green) giving the sum of $\nu_1$ and $\nu_2$ and $V_{d,2}$ such that $2\Delta - h\nu_2 < eV_{d,2} < 2\Delta - h\nu_1$ (blue) that gives $\nu_2$ alone (and all higher harmonics, that we neglect). Subtracting the proper contributions, we obtain one curve per

frequency, that is integrated to give the noise as a function of the bias voltage fig. 7.9 (b). The amplitude of $I_{PAT}$ is readjusted to fit theoretical curves calculated from formula 7.18 and the measured $I^0_{qp}$ (in grey on fig .7.9).

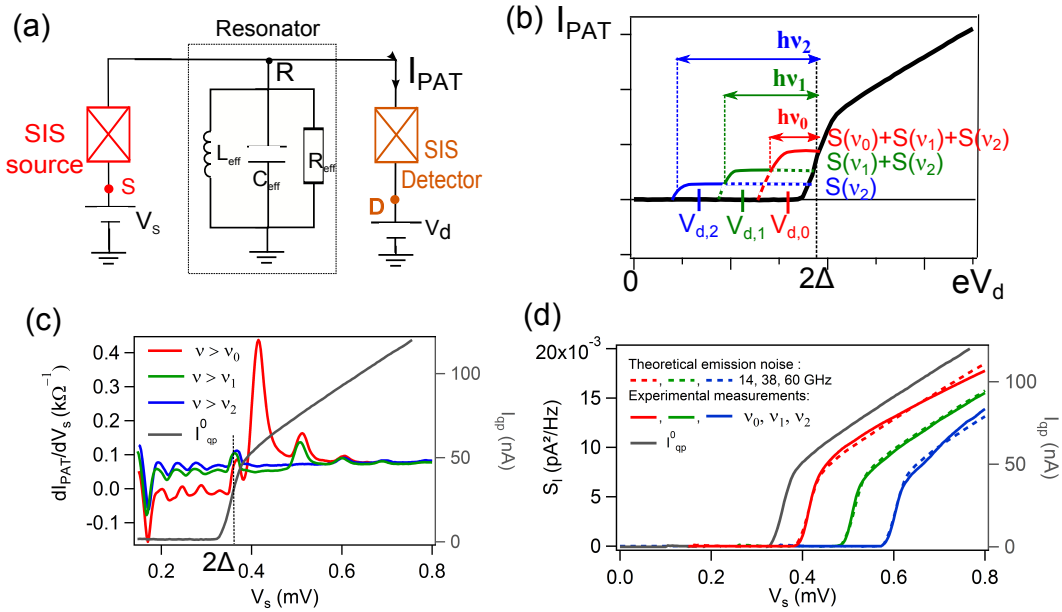


FIGURE 7.9 – (a) Schema of the experimental setup : the source of noise is a tunnel Josephson junction biased by $V_s$, the detector a SIS junction biased by $V_d$. The measured quantity is the photo-assisted current in the detector $I_{PAT}$. (b) Qualitative appearance of $I_{PAT} = f(V_d)$, with three different $V_d$ where the noise has been measured : in red, $2\Delta - h\nu_0 < eV_{d,0} < 2\Delta$, where all the frequencies are present (mainly $\nu_0$, $\nu_1$ and $\nu_2$). In green, $2\Delta - h\nu_1 < eV_{d,1} < 2\Delta - h\nu_0$, giving $\nu_1$ and $\nu_2$. In blue $2\Delta - h\nu_2 < eV_{d,2} < 2\Delta - h\nu_1$, giving only $\nu_2$. Note that the scale is not respected for the amplitudes and the widths of the steps of $I_{PAT}$. (c) Raw measurement of the derivative of $I_{PAT}$ as a function of the source bias voltage $V_s$ for the three values of $V_d$ defined in (b). In addition the I(V) characteristic of the source is represented in grey. (d) In dashed lines (red, green and blue) are represented the expected emission noise at respectively 14, 38 and 60 GHz, that fit better the experimental curves (solid lines at $\nu_0$,$\nu_1$ and $\nu_2$) after calibration. The experimental noise at $\nu_0$ is obtained by integration after subtracting the green curve to the red of (c). $\nu_1$ and $\nu_2$ are obtained similarly. In this sample, the detector is a SQUID of normal resistance around 3.5 kΩ and the source a simple junction of resistance normal 5 kΩ.

From these results, we show that we are able to measure the emission noise of a SIS junction (we know that it is emission noise because absorption or symmetrized noise would be very different, see ref. [211]). The amplitude of the measurement, compared to the one of the prediction, can provide a calibration of the setup. The problem is that, from one sample to the other, the resonator and the junctions may be slightly different (in particular the normal resistance of the junctions vary a lot, and probably as well their capacitance). The value of the frequency resonance of the setup and the value of the transimpedance (*i.e.* the calibration) may vary from one sample to the other.

Note that, in the previous experiment from Julien Basset's PhD, both the transimpedance and

the impedance seen by the detector were measured at the same time, allowing a calibration of the noise (see for example ref. [19] for details). In the present experiment, the environment of the detector seems to be less controlled, preventing us from using this method of calibration.

Consequently, in the following, the amplitude of the measured noises are not known a priori.

To solve the problem, we developed afterward a new design, where three systems are coupled to the resonator : a detector (SIS junction), a source (carbon nanotube) and a calibration source (SIS junction), that can also be used as an on-chip generator (see chapter 8)

### Conclusion

- The direct measurement of noise at frequencies typically larger than a few GHz requires specific high frequency electronics, that has often a limited bandwidth. Moreover, with these setups, it is difficult to separate emission and absorption processes.
- The solution came from on-chip detectors, in which the HF radiation emitted or absorbed by the source is respectively absorbed or emitted by the detector, where it induces a photo-assisted current.
- In this work, we use an on-chip detector based on a tunnel Josephson junction. Depending on the bias voltage applied on the detector, it is *a priori* possible to measure both emission and absorption noise, but separately. This detector is coupled to the source of noise through a resonating circuit, so that we measure the noise at some defined frequencies.
- In order to test our experimental setup, we use another tunnel Josephson junction as a source of noise. With AC Josephson effect, we characterize the resonator (resonance frequency, quality factor). We show as well that the measurement of the emission noise due to quasi-particle current is correctly obtained with this setup.

## 7.2 High frequency noise in a QD : general problematic and theoretical expectations

In this section we will address the problematic of noise in the high frequency regime in a mesoscopic system, focusing on how different it is compared to the low frequency.

The first major difference with low frequency noise is the non-conservation of the current [15]. At zero frequency, the current conservation is given by the unitary of the scattering matrix $s^\dagger(E)s(E') = 1$ with $E = E'$. But as soon as the high frequency fluctuations are concerned, the products of the elements of $s$ matrix are taken at different energies : $s^\dagger(E)s(E + h\nu) \neq 1$. The AC current is not conserved and yields $S_{LL}(\nu) + S_{RR}(\nu) + S_{LR}(\nu) + S_{RL}(\nu) \neq 0$ : the noise inter and intra leads does not necessary have the same value, and can be different in the different electrodes.

In this section, we will first give the finite frequency noise in a system modelized by a scattering matrix, to understand the meaning of the different terms. Then we will see what is expected in the Kondo regime.

### 7.2.1 In the scattering matrix formalism (non-interacting theories)

#### 7.2.1.1 General expression

Let's recall the formula 6.23 derived in sec. 6.2.2.3, which was valid for any frequency :

$$S_{\alpha\beta}(\nu) = \frac{e^2}{h} \int dE \sum_{\alpha'\beta'} A_{\alpha',\beta'}(\alpha; E, E + h\nu) A_{\beta',\alpha'}(\beta; E + h\nu, E)\ f_{\alpha'}(E + h\nu)(1 - f_{\beta'}(E)) \tag{7.19}$$

With the matrix A defined as $A_{\alpha,\beta}(L; E, E') = \delta_{\alpha,L}\delta_{\beta,L} - s^\dagger_{L,\alpha}(E)s_{L,\beta}(E')$.

To go further in the calculation, one needs to express the scattering matrix as a function of the amplitude coefficients of transmission and reflection :

$$s(E) = \begin{pmatrix} r(E) & t(E) \\ t^*(E) & r^*(E) \end{pmatrix} \tag{7.20}$$

This formalism is particularly well suited for the modelization of a quantum dot with a double barrier structure, with an energy dependent transmission that has a Breit-Wigner expression (as done in ref. [217, 21]).

Here, we aim at obtaining an expression that depends only on the energy dependent transmission $T(E) = t^*(E)t(E)$. The calculation has been done by Zamoum *et al.* in ref. [20] using the non-equilibrium Green function technique, independently from the scattering matrix

formalism. The authors assumed symmetric barriers for the system, *i.e.* $\Gamma_L = \Gamma_R$ [2]. The authors then obtain the following formula[3] :

$$S_{\alpha\beta}(\nu) = \frac{e^2}{h}\int_{-\infty}^{\infty} dE \sum_{\alpha'\beta'} M_{\alpha\beta}^{\alpha'\beta'}(E,-\nu)\ f_{\alpha'}(E)(1-f_{\beta'}(E+h\nu)) \tag{7.21}$$

The coefficients $M_{\alpha\beta}^{\alpha'\beta'}(E,\nu)$ are given in the table of fig. 7.10. $T(E)$ is defined such that $T(E) = t^*(E)t(E)$.

| $M_{\alpha\beta}^{\gamma\delta}(\varepsilon,\omega)$ | $\gamma=\delta=L$ | $\gamma=\delta=R$ | $\gamma=L,\ \delta=R$ | $\gamma=R,\ \delta=L$ |
|---|---|---|---|---|
| $\alpha=L$ $\beta=L$ | $\mathcal{T}(\varepsilon)\mathcal{T}(\varepsilon-\hbar\omega)$ $+\lvert t(\varepsilon)-t(\varepsilon-\hbar\omega)\rvert^2$ | $\mathcal{T}(\varepsilon)\mathcal{T}(\varepsilon-\hbar\omega)$ | $\mathcal{T}(\varepsilon-\hbar\omega)[1-\mathcal{T}(\varepsilon)]$ | $\mathcal{T}(\varepsilon)[1-\mathcal{T}(\varepsilon-\hbar\omega)]$ |
| $\alpha=R$ $\beta=R$ | $\mathcal{T}(\varepsilon)\mathcal{T}(\varepsilon-\hbar\omega)$ | $\mathcal{T}(\varepsilon)\mathcal{T}(\varepsilon-\hbar\omega)$ $+\lvert t(\varepsilon)-t(\varepsilon-\hbar\omega)\rvert^2$ | $\mathcal{T}(\varepsilon)[1-\mathcal{T}(\varepsilon-\hbar\omega)]$ | $\mathcal{T}(\varepsilon-\hbar\omega)[1-\mathcal{T}(\varepsilon)]$ |
| $\alpha=L$ $\beta=R$ | $t(\varepsilon)t^*(\varepsilon-\hbar\omega)$ $\times[(1-t^*(\varepsilon))(1-t(\varepsilon-\hbar\omega))-1]$ | $t^*(\varepsilon)t(\varepsilon-\hbar\omega)$ $\times[(1-t(\varepsilon))(1-t^*(\varepsilon-\hbar\omega))-1]$ | $t(\varepsilon)t(\varepsilon-\hbar\omega)[1-t^*(\varepsilon)]$ $\times[1-t^*(\varepsilon-\hbar\omega)]$ | $t^*(\varepsilon)t^*(\varepsilon-\hbar\omega)[1-t(\varepsilon)]$ $\times[1-t(\varepsilon-\hbar\omega)]$ |
| $\alpha=R$ $\beta=L$ | $t^*(\varepsilon)t(\varepsilon-\hbar\omega)$ $\times[(1-t(\varepsilon))(1-t^*(\varepsilon-\hbar\omega))-1]$ | $t(\varepsilon)t^*(\varepsilon-\hbar\omega)$ $\times[(1-t^*(\varepsilon))(1-t(\varepsilon-\hbar\omega))-1]$ | $t^*(\varepsilon)t^*(\varepsilon-\hbar\omega)[1-t(\varepsilon)]$ $\times[1-t(\varepsilon-\hbar\omega)]$ | $t(\varepsilon)t(\varepsilon-\hbar\omega)[1-t^*(\varepsilon)]$ $\times[1-t^*(\varepsilon-\hbar\omega)]$ |

FIGURE 7.10 – Definition of the coefficients $M_{\alpha\beta}^{\alpha'\beta'}(E,\nu)$ used in formula 7.21. From [20].

Note that an expression of noise was already given by Rothstein *et al.* in 2009 [21], but the authors decided to calculate a "net-current" noise, corresponding to $S_- = 1/4(S_{LL} + S_{RR} - S_{RL} - S_{LR})$. This is *a priori* not what is expected to be measured in an experiment.

#### 7.2.1.2 Expression of the different terms

We simplify the formula 7.21, taking its limit at zero temperature (that is qualitatively verified in our systems) and only for emission noise ($\nu < 0$).

We consider that the system under investigation is described by an energy dependent transmission $T(E)$, and we call $\mu_R$ and $\mu_L$ the chemical potentials of each reservoir. One obtains for the intra-leads terms :

$$S_{LL}(\nu) = \frac{e^2}{h}\int_{\mu_R-h\nu}^{\mu_L} T(E+h\nu)\,(1-T(E)) \tag{7.22}$$

$$S_{RR}(\nu) = \frac{e^2}{h}\int_{\mu_R-h\nu}^{\mu_L} T(E)\,(1-T(E+h\nu)) \tag{7.23}$$

As an example, we take $T(E)$ describing a resonance that is centered on the reference of

[2] However, from private communications with the authors, it seems relevant to use these formula aven for asymmetric contacts in our situation, namely for emission noise at low temperature.

[3] The sign of $\nu$ has been changed to take into account different conventions for emission and absorption

potential 0, such as the ones represented on fig. 7.11 (a) and (c). Here, they are simply used as examples, without any consideration about their physical origin [4]. To see what is the associated noise, we need to make some assumptions on how the chemical potentials of the reservoirs are defined.

**Asymmetric biasing** We are considering emission noise, so that all the noise terms vanish if $eV < h\nu$, in the following the formulas are given for $eV > h\nu$. We assume that the potentials are defined such that $\mu_L = -eV > 0$ and $\mu_R = 0$ (see fig. 7.11 (b)), meaning in particular that the resonance in $T(E)$ is pinned to the right contact. We obtain for the derivative of the noise compared to the bias voltage :

$$\frac{S_{LL}}{dV}(\nu, V) = \frac{e^2}{h} T(V + h\nu)(1 - T(V)) \tag{7.24}$$

$$\frac{S_{RR}}{dV}(\nu, V) = \frac{e^2}{h} T(V)(1 - T(V + h\nu)) \tag{7.25}$$

In this case, at finite frequency and for energy dependent transmission, $S_{LL}(\nu, V) \neq S_{RR}(\nu, V)$. Note however that at zero frequency or if the transmission does not depend on energy, one recovers the usual expression for shot noise : $S \propto T(1 - T)$. In the low transmission case, it gives $S_{LL}(\nu) \propto T(V + h\nu)$ and $S_{RR}(\nu) \propto T(V)$ : in one hand, $S_{LL}$ corresponds typically to low frequency shot noise, shifted by the frequency $h\nu$. In the other hand, $S_{RR}$ is not affected by the high frequency.

This general statement is confirmed by the figure 7.11 (d-g) where the two terms $S_{LL}$ and $S_{RR}$ (actually their derivative with respect to the bias voltage, which is the measured quantity in our setup) are plotted for two different energy dependent transmissions and for various frequencies. The temperature is taken into account through the temperature dependence of the Fermi distributions.

**Breaking of the reservoir symmetry** The symmetry between the noise in the different reservoirs is clearly broken because of the finite frequency, the energy dependent transmission as well as the asymmetric biasing [20]. This leads us to ask the question : what does these noises in the "left" and "right" reservoirs represent physically ? The $S_{LL}$ ($S_{RR}$) noise term corresponds to current fluctuations that create an electron/hole pair that recombines in the left (right) electrode (and thus emits a photon of energy $h\nu$ there). Among the four terms $M_{LL}^{LL}$, $M_{LL}^{RR}$, $M_{LL}^{RL}$ and $M_{LL}^{LR}$, the only one that contributes to $S_{LL}$ at T=0 (and thus that gives the greatest contribution at finite T) is one of the crossed terms $M_{LL}^{RL}$ and $M_{LL}^{LR}$ (depending on the sign of the bias voltage). It corresponds to inter-leads processes, involving the passage of an electron from one electrode to the other. In the situation represented on fig. 7.11 (b), electrons

[4] As it will be explained in the following, these energy dependent transmission are extracted from conductance measurements in the Kondo regime.

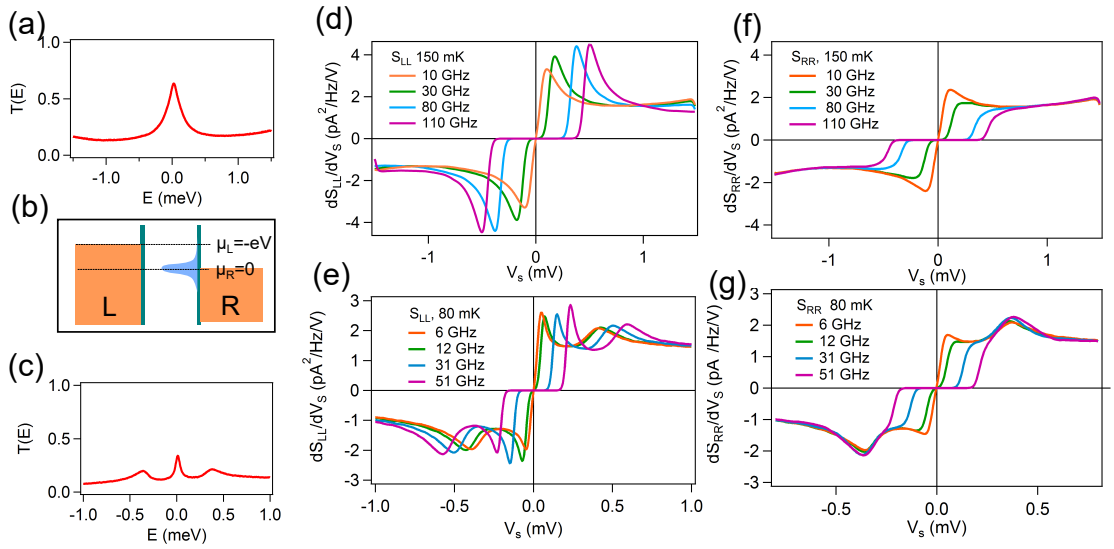


FIGURE 7.11 – Derivative of the noises $S_{LL}$ and $S_{RR}$ with respect to the bias voltage V for two different energy dependent transmissions represented on (a) and (c). The convention used is shown on panel (b) : the resonance is pinned on the right electrode, corresponding to $\mu_R = 0$. The left electrode is such that $\mu_L = eV$. (d) and (f) represent respectively $dS_{LL}/dV$ and $dS_{RR}/dV$ for transmission (a). (e) and (g) are respectively $dS_{LL}/dV$ and $dS_{RR}/dV$ for transmission (c). Here, the temperature is taken into account (150 mK for transmission (a) and 80 mK for (c), but it does not change quantitatively things compared to T=0.)

coming from the left electrode cannot enter in the dot at the potential $-eV$ (since $T(-eV)$ is small) to recombine in the right electrode and emit a photon. However, electrons from the right electrode can easily enter the dot at potential 0 and then relax in the left electrode. That's why the derivative of the noise related to the resonance pinned on the right contact is larger on the left side than on the right one. This can be seen as a general statement : to probe the transmission at energy close to the chemical potential of a contact, one should measure the noise in the other contact.

Note that this difference between the two electrodes is only possible when there exists initially an asymmetry in the system. In a quantum dot, this asymmetry exists as soon as the level in the dot, controlled by the gate voltage, is not centered between the two reservoirs (and thus $T(E)$ does not depend only on the voltage applied between the electrodes). The asymmetry of the barriers between the dot and the reservoirs can also break the left/right asymmetry (see next section where the Kondo effect is involved).

**Symmetric biasing** For a symmetric biasing $\mu_L = -\mu_R = -eV/2 > 0$ with the resonance at $\mu_F = 0$ (*i.e* the resonance between the two reservoirs), one obtains for the two terms :

$$\frac{S_{LL}}{dV}(\nu, V) = \frac{e^2}{h}\left[T(V/2 + h\nu)(1 - T(V/2)) + T(V/2)(1 - T(-V/2 - h\nu))\right] \tag{7.26}$$

$$\frac{S_{RR}}{dV}(\nu, V) = \frac{e^2}{h}\left[T(V/2)(1 - T(V/2 + h\nu)) + T(V/2 - h\nu)(1 - T(-V/2))\right] \tag{7.27}$$

Writing the same quantities for $\mu_L = -\mu_R = eV/2 < 0$, it is possible to show that $\frac{S_{RR}}{dV}(\nu, V)$=-$\frac{S_{LL}}{dV}(\nu, -V)$, the left/right symmetry is recovered.

### 7.2.2 Finite frequency noise in the Kondo regime

#### 7.2.2.1 General problematic

The noise expected in the Kondo regime is *a priori* much more complicated to predict, in the first place because the treatment of the Kondo effect itself requires renormalization group techniques (see section 1.1.2). We are here facing two additional complications. The first one is that we want to investigate the dynamics of the Kondo effect, we are thus interested in measuring the noise at frequencies of the order of $T_K$ or larger, at time scales so short that the Kondo effect may not have time to establish (see section 1.4.2). The second one is that we measure the emission noise such that, we have to apply on the sample a voltage larger than the measurement frequency, here of the order of $T_K$ : the Kondo effect is out-of-equilibrium (see section 1.4.1).

The good point is that these emission noise measurements should be very rich in information about the dynamics of the Kondo effect as well as its out-of-equilibrium behavior, that are very poorly investigated experimentally. The bad point is that these informations are difficult to extract from the measurements, since a theory that which includes at the same time the Kondo effect, its dynamics and out-of-equilibrium decoherence as well as the specific energy dependent transmission of the sample would be very complex and does not exist yet.

#### 7.2.2.2 First measurements and renormalization group calculations

The noise expected in the Kondo regime at finite frequency has been computed thanks to a functional renormalization group (FRG) method by Moca *et al.* [22], as represented on fig. 7.12, for emission noise (a) and symmetrized noise (b). We focus on the emission noise. First, as expected, we remark that there is no noise for $V < h\nu/e$ since the system does not have enough energy to emit a photon at energy $h\nu$. At $eV = h\nu$, the noise exhibits a logarithmic singularity, instead of the linear increase expected for a simple tunnel junction (fig. 7.12 (c)).

Qualitatively, this singularity originates directly from the Kondo effect : the formation of the

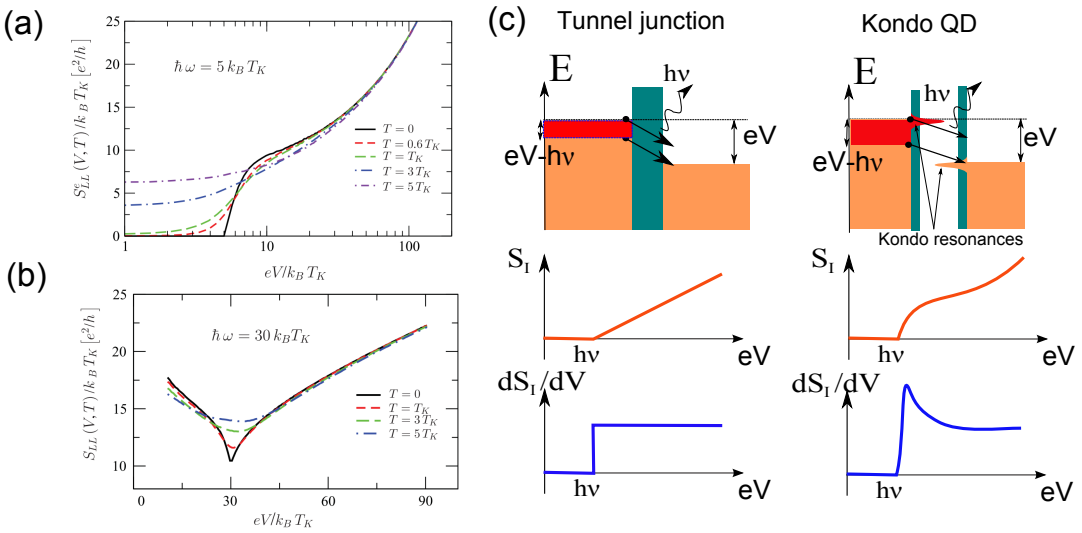


FIGURE 7.12 – (a) and (b) Functional renormalization group calculations in the Kondo regime of the emission noise (a) and the symmetrized noise (b) for various temperatures. From ref. [22]. (c) Qualitative explanation of the emission noise expected in the Kondo regime, compared to the emission noise of a tunnel junction (see text).

out-of-equilibrium Kondo singlet leads to two peaks in the density of state of the system, located at the potentials of each reservoir [95] (we will come back to this point in the following). For this reason, the processes emitting photons at $eV = h\nu$ are greatly favored, inducing an increase of noise, manifested as a peak in the derivative of the noise with respect to $V$.

This manifestation of the Kondo resonance has been first observed in our group in 2012, during Julien Basset's PhD. The noise had been measured in a carbon nanotube in a Kondo region with $T_K = 120$ $\mu$eV $= 1.4$ K, at frequencies of 30 GHz and 80 GHz corresponding respectively to $T_K$ and $2.7T_K$. These measurements are represented on fig. 7.13. At 30 GHz ($h\nu = k_B T_K$),

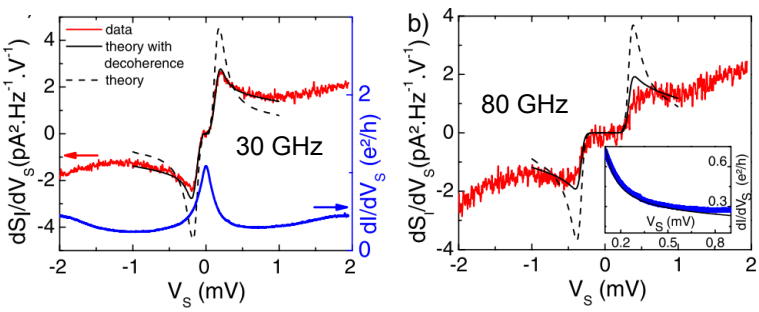


FIGURE 7.13 – Red lines : emission noise measurements in a carbon nanotube in the Kondo regime (the DC conductance is represented in blue) at 30 (left) and 80 GHz (right), corresponding respectively to $T_K$ and $2.7T_K$. Dashed black lines : FRG calculations. Black solid lines : FRG calculations with additional decoherence introduced in the model. From ref. [23].

this feature is visible in the noise. But at 80 GHz ($h\nu = 2.7k_BT_K$), it is completely washed out. These curves are compared to FRG calculations (dashed lines) : in both cases, the theory predicts a resonance much more pronounced than measured, with however a better agreement for the lowest frequency. To reproduce the measurement, the authors had to put, by hand, an additional decoherence (black solid lines). The origin of this decoherence, that destroys insidiously the Kondo resonance, remains unknown. Since the dynamics of the Kondo effect is taken into account, we can speculate that it is related to out-of equilibrium effects, which may not be included properly. In particular, the asymmetry of the contacts (equal here to $\Gamma_L/\Gamma_R = 5$) is not taken into account.

An important conclusion of this experiment is that, actually, this measurement of emission noise at frequencies of the order of $T_K$ is not able to tell us about the dynamics of the Kondo effect since another source(s) of decoherence dominates.

Note that a theory based on another renormalization group method has been compared to these measurements by Müller et al.[218]. There the agreement is very good, without any adjustable parameter.

In order to have a better understanding of the decoherence effects and maybe discover their origin, we intended to perform a new experiment to probe the noise in the Kondo regime on a wider range of frequency and thus ratios $h\nu/(k_BT_K)$.

#### 7.2.2.3 Out of equilibrium Kondo effect and influence of the contact asymmetry.

**What happens to the Kondo effect out-of-equilibrium ?** When a quantum dot in the Kondo regime is biased by a voltage $V$ applied between the two contacts, the system is driven out-of-equilibrium. Then, a finite current in the system induces current fluctuations that dephase the coherent spin-flip processes [46, 50]. In other words, the decoherence is induced by inelastic scattering of electrons and, as soon as $eV \approx k_BT_K$, the Kondo resonance may be qualitatively affected.

The first effect of a voltage bias between the two reservoirs of a QD in the Kondo regime is the splitting of the Kondo resonance in the density of states, giving one peak pinned at the potential of each reservoir (see symmetric case on fig. 7.14 and fig. 7.15 (a)). The second one is a weakening of these resonances due to decoherence.

From the experimental point of view, the weakening of the Kondo resonance indirectly affects the shape of the Kondo resonance in the $dI/dV$ of the sample. However, the splitting of the Kondo resonance cannot be observed through conductance measurements : De Franceschi *et al.* had to introduce a third electrode to induce an additional splitting [93]. Et few years later, Leturcq *et al.* [219] used a three terminals setup, including a weakly coupled one. These two experiments, probing the DC density of states of the system, are the only ones which put forward the consequences of non-equilibrium on the Kondo effect.

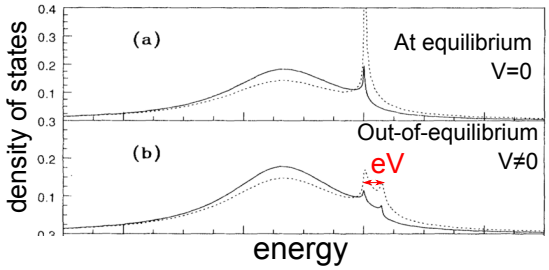


FIGURE 7.14 – Splitting of the Kondo resonance in the density of states and weakening of the Kondo resonance in an out-of-equilibrium situation. The full and dashed lines correspond to two different calculation methods, but give qualitatively the same results. Taken from [95].

**Influence of the contact asymmetry** Until now, we implicitly assumed that the coupling of the dot to both reservoirs are the same. But experimentally, this is hardly the case. Actually, it is a parameter that varies strongly in a nanotube sample when the gate voltage is tuned (see section 2.2.1.1). What can be the effect of the contact asymmetry on the Kondo effect and its decoherence ? In the following, we define $\Gamma_{L,R}$ as the coupling of each reservoir to the dot, as represented on fig. 7.15.

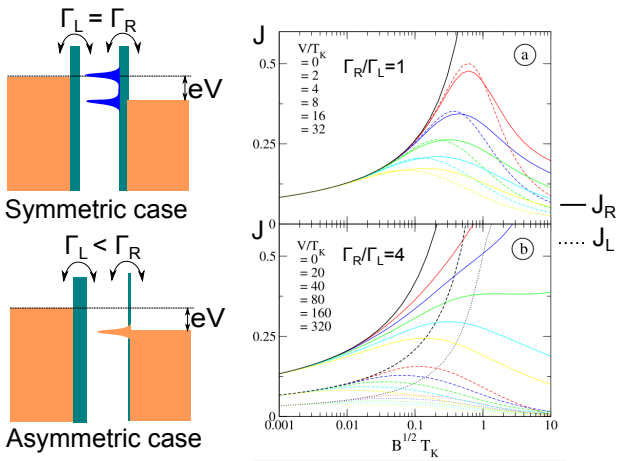


FIGURE 7.15 – Left : Schematic representation of an asymmetrically coupled quantum dot in the Kondo regime. Right : flow renormalization diagrams in the case of symmetric contacts (a) and asymmetric ones (b), taken from [220]. $B$ on the bottom axis is a renormalization parameter which increases during the renormalization process and the different colors represent the various bias voltages applied on the system (given as insets on each graph). On panel (a), the effective coupling J is the same for both reservoirs such that $J_R$ and $J_L$ are superimposed. The strong coupling ($J \to \infty$) is accessible only for very small V ($eV < 2k_BT_K$, black continuous line). (b) If $\Gamma_R = 4\Gamma_L$, $J_L \neq J_R$, for some quite large finite V, the strong coupling is reached, but only for the right contact (namely, $J_R \to \infty$ for $V/T_K \leq 40$ but $J_L \to \infty$ only for $V/T_K = 0$).

In the case of symmetric contacts, the channel coupled to the dot is a combination of both reservoirs. But for asymmetric contacts, the well coupled contact is more involved in the Kondo many-body state that the poorly-coupled one. This can be understood from [220] and

fig. 7.15 : on fig. 7.15(a), the effective coupling J is the same for both reservoirs. The strong coupling ($J \to \infty$) is accessible only for very small V ($eV < 2k_BT_K$). In a situation of one contact better coupled than the other, here the right one is four times more coupled than the left ($\Gamma_R = 4\Gamma_L$, see fig. 7.15(b)), the effective coupling is different in both contacts $J_L \neq J_R$. For quite large finite V, the strong coupling is reached, but only for the right contact.

Lebanon *et al.* [221] show that, in the density of states, the Kondo resonance pinned on the poorly coupled contact is strongly reduced compared to the one on the well coupled contact, and even disappears in the $\Gamma_L/\Gamma_R \ll$ or $\gg 1$ limit (corresponding typically to STM measurements).

For these reasons, when the reservoirs are asymmetrically coupled, the Kondo resonance should be more resistant to decoherence. This is related to the fact that the Kondo singlet is mainly formed between the dot and the best coupled reservoir, and is therefore less affected by the voltage applied on the other contact (we can say that thanks to the asymmetry, the Kondo singlet is "less out-of-equilibrium").

An other way to see that is to consider that, in a dot asymmetrically coupled to the reservoirs, the conductance is reduced by a factor $\frac{4\Gamma_R\Gamma_L}{(\Gamma_R+\Gamma_L)^2}$ compared to the symmetric case [38]. Then, for the same applied bias voltage, the current is lower and thus the decoherence is reduced as well (the decoherence rate is shown to be proportional to the current [220]).

### 7.2.3 Non-interacting theories and Kondo effect ?

We have at our disposal two kinds of theories for describing finite frequency noise measurements in the Kondo regime :

1. Theories based on renormalization group, that take into account the specificities of the Kondo effect (resonance, dynamics). But these theory deal with pure Kondo effect and cannot take into account the specificities of the quantum dot, in particular the non-zero conductance at high bias which is not related to Kondo effect itself but to cotunneling processes. Moreover, it is not clear how these theory take into account the effect of asymmetrically coupled reservoirs.

2. Non-interacting theories, able to describe the noise of a QD whose energy dependent transmission T(E) is known. This theory can take into account the Kondo effect only through its manifestation in T(E). In particular, the decoherence effect and the dynamics are not included nor the multiple scattering processes probed in the low frequency experiment of section 6.3.

In the following, we chose to compare our measurements to the second one, the scattering matrix theory, that has the advantage of being easily implementable and gives to some extent

the noise expected without decoherence/dynamics effects. The difficulty is the extraction of T(E) from the only quantity we have access to : the DC conductance $dI/dV$.

This problem will be tackled during the analyze of the experimental results, but we can however make some general statements. In a QD in the Kondo regime, the position of the resonance is not determined by the gate voltage (unlike in a Breit-Wigner case). Indeed, whatever is $V_g$, if the left and right barriers are symmetric ($\Gamma_R/\Gamma_L = 1$), one Kondo resonance is pinned at each reservoir's Fermi level. Then, the system does not have any spatial asymmetry, giving $S_{LL} = S_{RR}$. On the other hand, if $\Gamma_R/\Gamma_L \neq 1$, there is only one resonance, pinned on the best coupled contact : $S_{LL}$ and $S_{RR}$ have different expressions.

Remark on the analyze of the first measurement in the Kondo regime (fig. 7.13) : After doing these considerations, it seems obvious that in any high frequency measurement one has to think about which noise has to be considered : $S_{LL}$, $S_{RR}$ or, why not, a mix of both (depending on the experimental setup). In the experiment of fig. 7.13, the asymmetry of the contacts is shown to be equal to $\Gamma_L/\Gamma_R = 5$ (or $\Gamma_R/\Gamma_L = 5$, we don't know), but the noise computed by FRG does not take this into account and gives the same result in left and right contacts. The conclusion of the comparison experiment/theory is thus not clear...

### Conclusion

- The problematic of noise at finite frequency in a mesoscopic system is more complex than the low frequency one since some symmetries can be broken : the symmetry between emission and absorption noise but, in addition to that, the noise is sensitive to any spatial asymmetry between the left and right electrodes.

- In the Kondo regime, renormalization group methods show that the derivative of the emission noise at frequency $\nu$ is predicted to exhibit a singularity at $eV_s = h\nu$, that is directly related to the Kondo resonance in the density of state. This singularity can be seen as a probe of the Kondo resonance at high frequency and out-of-equilibrium.

- In a previous PhD work, one first measurement was performed in a CNT QD in the Kondo regime. When compared to RG theory, the measurement was shown to exhibit more decoherence than expected.

- Unfortunately, RG methods cannot take into account the specificities of the quantum dot sample that is measured (as for example residual differential conductance at high voltage). Moreover, this theory presently does not include all the consequences of asymmetrically coupled reservoirs, in particular the noise in left and right reservoirs are predicted to be the same.

- However, these effects can be included in a non-interacting, which does not take into account the specificities of the Kondo effect (dynamics, decoherence...). At last, we will

compare our experimental data with these non-interacting theories, that can be seen as the noise expected in absence of any decoherence or dynamics effect of the Kondo effect.

## 7.3 Experimental results : finite frequency noise in carbon nanotube quantum dot

In this section, we present high frequency noise measurement of a carbon nanotube, using the setup describe in part 7.1, summarized on fig. 7.16. The main actor of the setup, the carbon

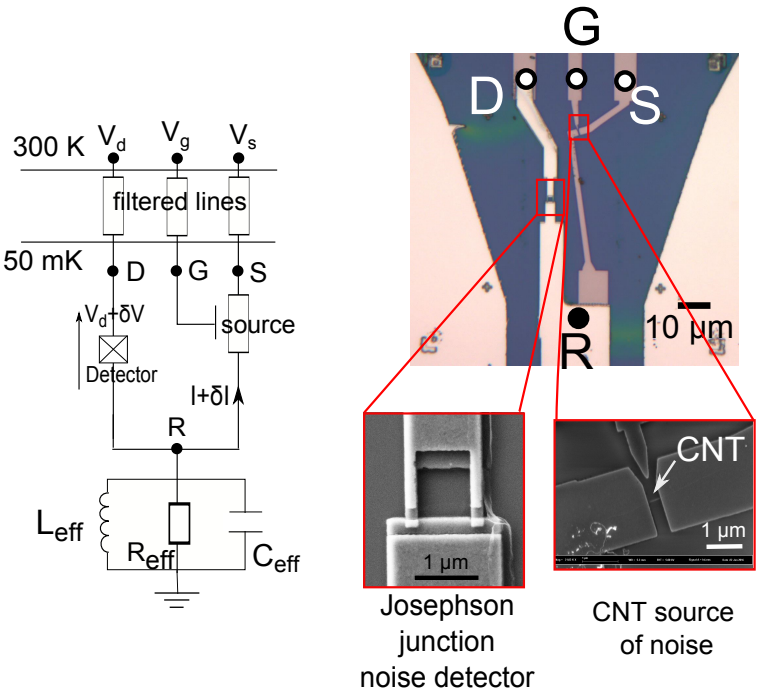


FIGURE 7.16 – Measurement setup used in this part. A carbon nanotube is coupled to a SIS detector through a resonant circuit, and cooled down to 50 mK.

nanotube, can be DC biased by a voltage $V_s$ and an electrostatic gate $V_g$ is placed nearby to tune the energy level in the dot. It is coupled to a SIS detector through a resonant circuit, as described in the previous part. The SIS detector is biased by a voltage $V_d$.

Depending on the gate voltage and on the run of experiment (the nanotube has been cooled down three times), the nanotube can exhibit different transport regimes : SU(2) Kondo effect, Coulomb blockade and SU(4) Kondo effect. We first focus on the SU(2) Kondo effect regime, and discuss more briefly the other cases.

### 7.3.1 Noise in the Kondo SU(2) regime

#### 7.3.1.1 Characterization of the CNT sample : DC measurement

We start measuring the DC conductance of the nanotube as a function of the gate voltage. Such a measurement is represented on fig. 7.17 for a large range of gate voltage. Note the

discontinuities when the gate voltage is swept : they may indicate that a charge was trapped by an impurity in the sample. This kind of things induce hysteresis in the system and make CNT sample sometimes difficult to measure.

We have focused on three interesting ranges of $V_g$, where SU(2) Kondo effect is observed, plotted on fig. 7.18.

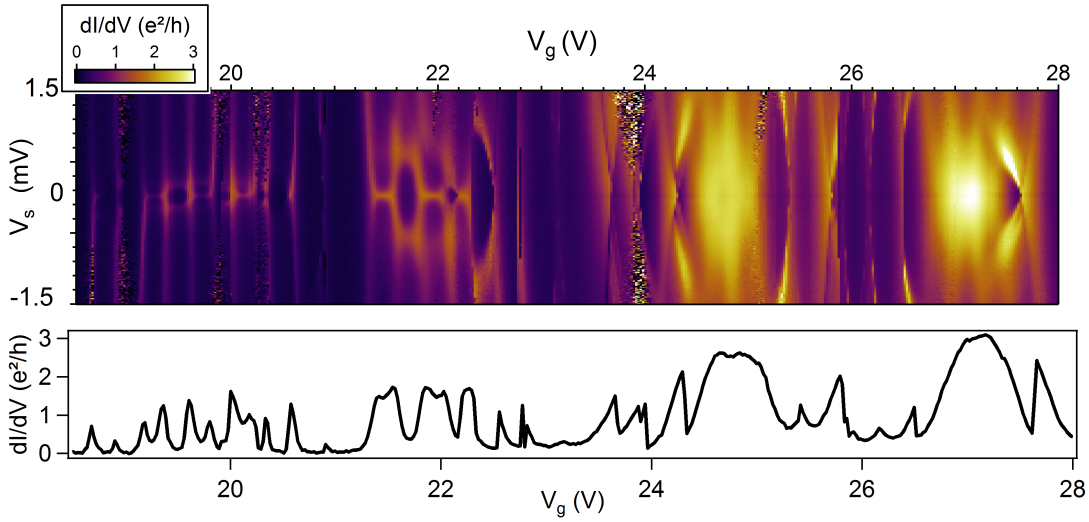


FIGURE 7.17 – Color plot : differential conductance $dI/dV$ of the carbon nanotube quantum dot as a function of the bias voltage $V_s$ and the gate voltage $V_g$ for a large range of gate voltage. Below is represented an horizontal cut at $V_s = 0$ of the color plot.

In table 7.1 are given the parameters of the quantum dot in each zone.

- Kondo ridge A is the one measured during Julien Basset's PhD. It is represented here as in the following so that it can be compared to the new measurements. For a detailed investigation of this Kondo ridge, see ref. [117].
- Zones B exhibits clearly non-zero conductance at zero bias, typical of the Kondo effect. Two satellite peaks are also visible at $V_s = \pm 0.35$ meV, indicating a breaking of the orbital degeneracy of the nanotube : the zero bias peak comes from SU(2) Kondo physics (and not SU(4)). The Kondo temperature is determined from the temperature dependence of the resonance represented on fig. 7.22, as described in section 2.3.1.2. The asymmetry is given by the height of the Kondo peak according to formula 2.15. The charging energy U is evaluated from the size of the Coulomb diamonds and the coupling $\Gamma$ calculated from formula 2.13 that relates $T_K$, U and $\Gamma$.
- Zone C includes actually a whole shell of the nanotube, with three diamonds corresponding to electronic occupancies N=1, 2 and 3. For N=1 and 3 filling, the conductance increases at zero bias, indicating again that we are in a SU(2) Kondo regime. The

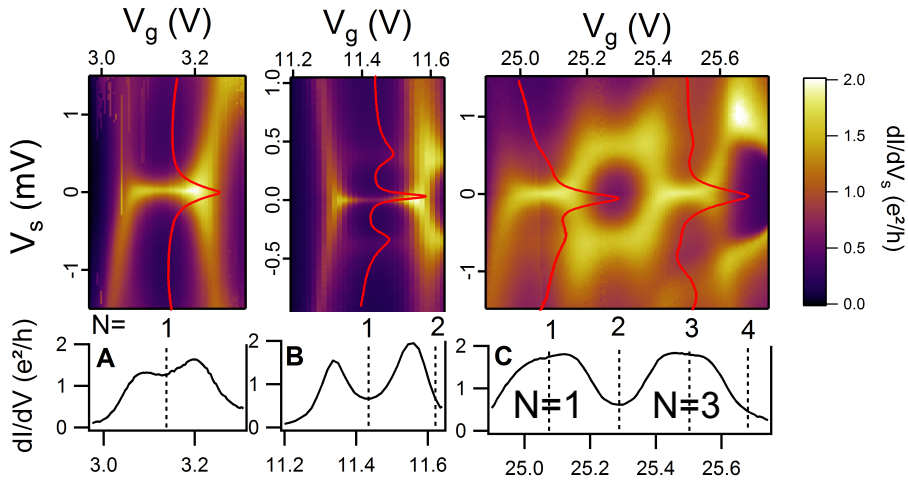


FIGURE 7.18 – Color plot : differential conductance of the carbon nanotube quantum dot as a function of the bias voltage and the gate voltage $\frac{dI}{dV_s}(V_s, V_g)$ in three ranges of gate voltage where SU(2) Kondo effect is observed (non zero conductance at zero bias inside the Coulomb diamonds). Below are represented horizontal cuts at $V_s = 0$ of the color plot. In red are plotted vertical cuts of the color plots at the gate voltages indicated by dashed lines. The Kondo ridge A is the one that had been measured during Julien Basset's PhD, for comparison. B and C have been measured on the new sample. (see text)

breaking of the orbital degeneracy is $\delta E \approx 0.6$ meV, evaluated from the position of the inelastic cotunneling peaks. The temperature dependence of the conductance is the one represented on fig. 2.19, and the other parameters are extracted like in zone B and are measured identical for both N=1 and N=3.

From table 7.1, we see that we have at our disposal three different Kondo ridges (actually four, but N=1 and N=3 of the zone C are very similar), in three different regimes of asymmetry : a very asymmetric Kondo effect for zone B, with $\Gamma_L/\Gamma_R = 11$, an almost symmetric Kondo in zone C ($\Gamma_L/\Gamma_R = 1.5$) and an intermediately symmetric one with zone A : $\Gamma_L/\Gamma_R = 5$. This will allow to investigate the influence of the asymmetry on the decoherence of the Kondo effect.

| Kondo ridge | U (meV) | $T_K$ ($\mu$eV) | $\Gamma$ (meV) | $\Gamma_L/\Gamma_R$ |
|---|---|---|---|---|
| A | 2.5 | 120 | 0.52 | 5 |
| B | 1.8 | 30 | 0.25 | 11 |
| C | 1.7 | 130 | 0.43 | 1.5 |

TABLE 7.1 – Parameters of the carbon nanotube quantum dot in the three Kondo regions investigated. U is the charging energy, $T_K$ the Kondo temperature, $\Gamma_L/\Gamma_R$ the coupling asymmetry between left and right contacts and $\Gamma = \Gamma_L + \Gamma_R$ the total coupling.

#### 7.3.1.2 Noise measurements

**Description of the measurement procedure** After having identified the interesting gate voltage region mentioned above, we measure the associated noise according to the following procedure :

- We start by choosing the proper bias voltages for the detector. A first measurement in made with $2\Delta - \nu_0 < V_d < 2\Delta$ ($V_d$ chosen such that the measured photo-assisted current is maximal), so that both the signals corresponding to $\nu_0$ and $\nu_1 = 3\nu_0$ are measured (the signal corresponding to higher harmonics is very low, we neglect it). A second measurement is made at $2\Delta - \nu_1 < V_d < 2\Delta - \nu_0$, giving the signal at frequency $\nu_1$.
- For both $V_d$, we measure the derivative of the photo-assisted current in the detector with respect to the bias voltage of the source for various gate voltage ($\frac{dI_{PAT}}{dV_S}(V_S, V_g)$). This measurement is assumed to be proportional to the emission noise by the nanotube, that is represented for both zones B and C, respectively on fig. 7.19 (a) and 7.20 (a).

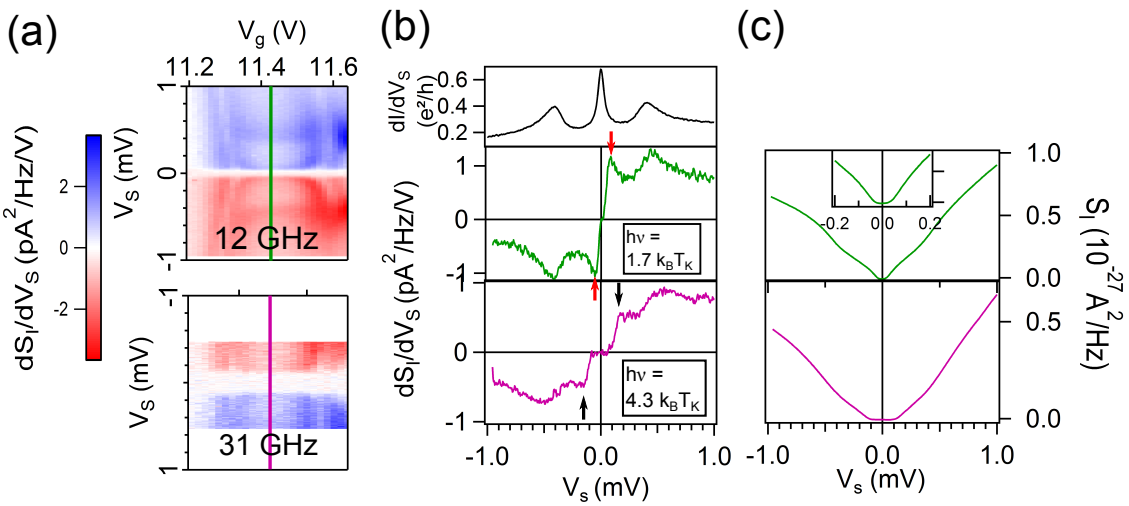


FIGURE 7.19 – Measurement of the derivative of the emission noise with respect to the bias voltage of the nanotube for Kondo ridge B, with a Kondo temperature $k_B T_K = 30$ $\mu$eV, *i.e* 0.35 K, and an asymmetry of $\Gamma_L/\Gamma_R = 11$. The noise is measured here at the two frequencies allowed by the resonator : $\nu_0 = 12$ GHz and $\nu_1 = 31$ GHz. In (a), the measurement is presented all over the Kondo ridge. Note that, at 30 GHz, the measurement has been done only on a smaller range of $V_s$ than at 12 GHz. On (b) is presented the same measurement taken at the center of the Kondo ridge. (c) gives the noise as a function of $V_s$, integrated from (b). Red arrows indicate Kondo related singularities in the derivative of the noise, black arrows indicate where these singularities are washed out (see text).

Since our goal is to investigate the Kondo effect, we chose to focus on gate voltages corresponding to the center of the Coulomb diamonds of each Kondo ridge, at half filling. From a

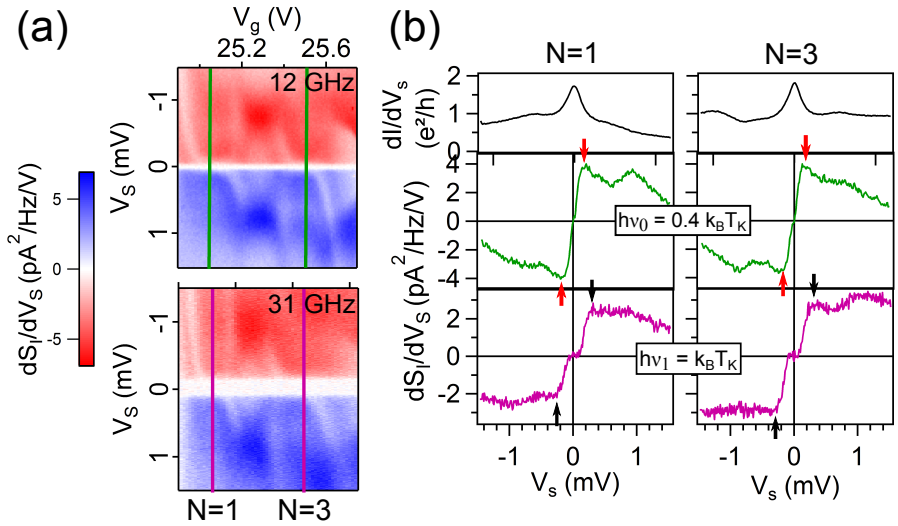


FIGURE 7.20 – Measurement of the derivative of the emission noise with respect to the bias voltage of the nanotube for Kondo ridges C, with a Kondo temperature $k_BT_K = 130$ $\mu$eV *i.e* 1.5 K, and an asymmetry $\Gamma_L/\Gamma_R = 1.5$. The noise is measured here at the two frequencies allowed by the resonator : $\nu_0 = 12$ GHz and $\nu_1 = 31$ GHz. In (a), the measurement is presented all over the three diamonds N=1, 2 and 3. On (b) is presented the same measurement taken at the center of the Kondo ridges N=1 and 3. Red arrows indicate Kondo related singularities in the derivative of the noise, black arrows indicate where these singularities are washed out (see text).

theoretical point of view, this is for this gate voltage that the Kondo effect is the simplest to analyze since the occupation is well defined there, minimizing the effect of the other charge states. We thus plot the derivative of the noise on fig. 7.19 (b) and fig. 7.20 (b) respectively for the centers of Kondo ridges B and C. They can be compared to the data for ridge A on fig. 7.13. For Kondo ridge B, the noise itself (instead of its derivative) is shown, in order to convince the reader that the derivative is more appropriate for data analysis.

**Qualitative analysis** For both ridges B and C, we can see that for low $V_s$ there is no noise, as expected for emission noise. For the first frequency $\nu_0$, this zero plateau is of the order of 100 $\mu$eV, in agreement with $\nu_0 = 12$ GHz. For the second frequency the plateau has a width around 250 $\mu$eV, in agreement with $\nu_1 = 31$ GHz[5]. The interesting features are the ones around $eV_s = h\nu$, where the Kondo resonance is involved :

- Ridge B, with a contact asymmetry $\Gamma_L/\Gamma_R = 11$ : The measurement at 12 GHz corresponds to $h\nu_0 = 1.7k_BT_K$. A singularity in the derivative of the noise is clearly seen (see red arrow on fig. 7.19 (b)), as a manifestation of the Kondo resonance. The interesting point is that, at 31 GHz corresponding to $h\nu_1 = 4.3k_BT_K$, this singularity

[5]Note that the size of the plateau is not precise enough to give these values of 12 and 31 GHz. We assume that the circuit resonates at the same frequencies as the one of fig. 7.8 (since we cannot use AC Josephson effect to characterize the resonator).

has disappeared (black arrows on fig. 7.19 (b)). This statement, in agreement with what has been measured for the Kondo ridge A, shows that at $h\nu_0 = 1.7T_K$ (corresponding to a voltage $V_s = 1.7T_K/e$ applied on the system), the Kondo resonance still exists, but not if $eV_s = 4.3k_BT_K$

- Ridges C, with a contact asymmetry $\Gamma_L/\Gamma_R = 1.5$ : there, the Kondo temperature is higher, therefore 12 GHz corresponds to $h\nu_0 = 0.4k_BT_K$ and 31 GHz to $h\nu_1 = 1k_BT_K$. At 12 GHz, the singularity in the noise derivative is not as clear as for ridge B, but is still present. The reason for the singularity to be so soft is probably that in the conductance, the Kondo resonance lies on a conductance background around $e^2/h$ (T=1/2), that is very noisy (since the shot noise is typically proportional to $T(1-T)$). However, at 31 GHz, the noise derivative is completely flat. It seems that, at $eV_s = 0.4k_BT_K$, the Kondo resonance still contributes to noise, but not at $eV_s = k_BT_K$.

From these measurements, it qualitatively seems that while for a very asymmetric coupling of the electrodes the Kondo resonance participates to noise when biased by $V_s = 1.7k_BT_K$, it is completely destroyed when biased by $V_s = 1k_BT_K$ for almost symmetric contacts.

#### 7.3.1.3 Quantitative analysis

To support these qualitative analysis, we now compare the noise measurements with the noise expected from the theory described in section 7.2.3 (noise calculated from the energy dependent transmission). The difficulty is to extract $T(E)$ from the conductance measurement. We detail the procedure we followed in the two limit cases : symmetric and asymmetric contacts.

**Asymmetric Kondo effect $\frac{\Gamma_R}{\Gamma_L} = 5$ and 11.** From the considerations about Kondo effect with asymmetric contacts, in absence of any decoherence, we can consider $T(E)$ as a resonance, similar to the Kondo one in the conductance, pinned on the best coupled contact (here the right one, but note that this choice of "left" and "right" is, here, completely arbitrary). Assuming that the right contact is the best coupled one, we can chose the potentials $\mu_L = -eV$ and $\mu_R = 0$, such that whatever the value of the bias voltage, $T(V) = \frac{h}{2e^2}\frac{dI}{dV}(V)$. This is exactly the situation described on fig. 7.11. We assume that $S_{LL}$ or $S_{RR}$ computed with this method give the noise expected if there is absolutely no decoherence of the Kondo effect.

It worths emphasizing that the noise measured is different depending on if we measure the noise in the well coupled electrode or in the poorly coupled (the right or left one). We have no idea which side of the junction indeed corresponds to "left" and "right", and we are actually not sure that we measure the noise only from the left or the right. That's why, on fig. 7.21, we represent both of them for each frequency, as well as $S_- = S_{LL} + S_{RR} - S_{RL} - S_{LR}$, a mixed of all inter and intra leads noise terms (this quantity is the one calculated by Rothstein *et al.* [21]).

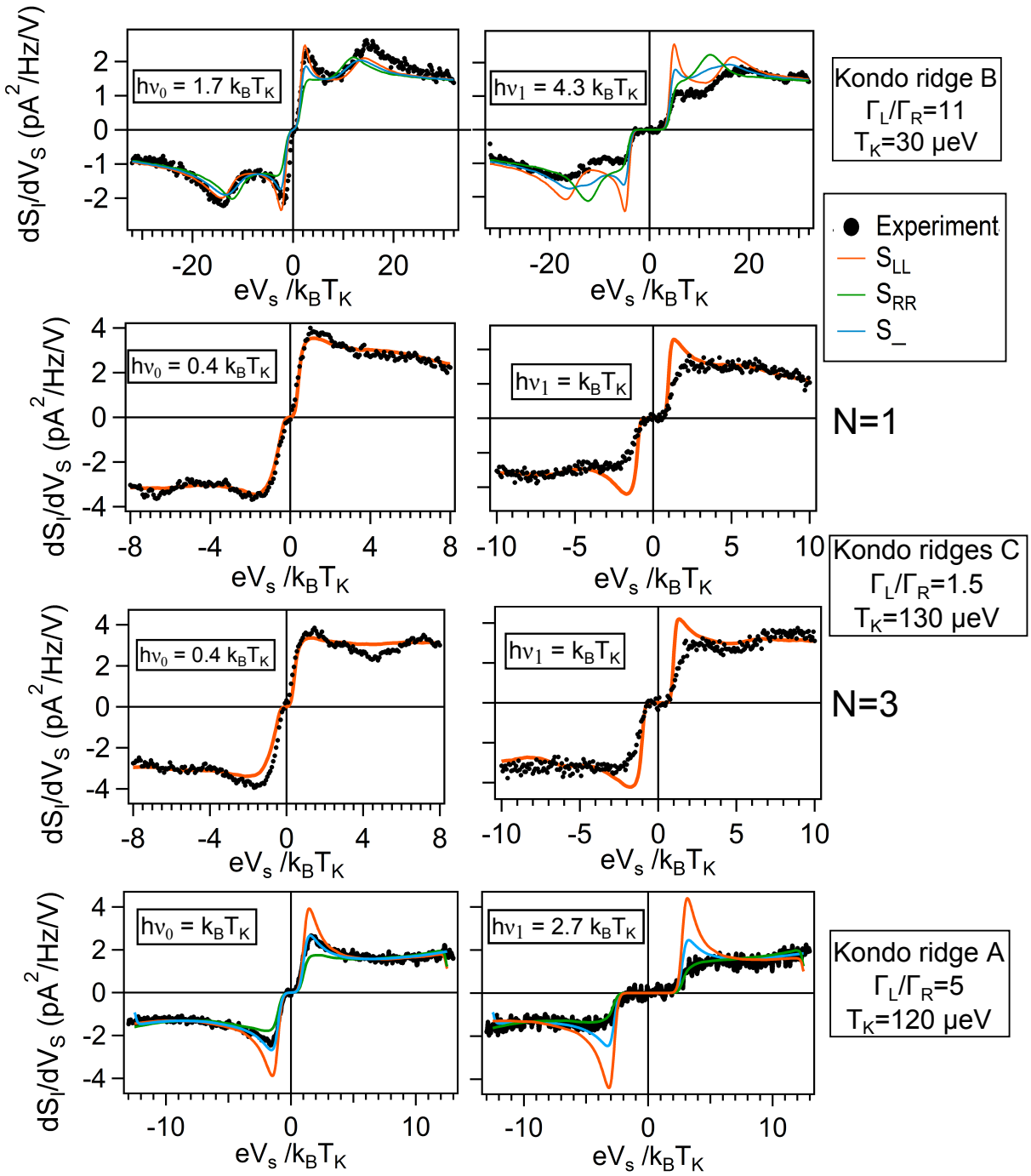


FIGURE 7.21 – Comparison of the different terms of the noise derivative predicted in the scattering matrix formalism with experimental data, as a function of $eV_s/k_BT_K$. For each ridge, B, C and A, and each frequency, three terms are compared to the experiment. These terms are the intra-lead terms $S_{LL}$ and $S_{RR}$ as well as $S_- = S_{LL} + S_{RR} - S_{RL} - S_{LR}$, the noise of the net current [21]. The electronic temperature for the theory is 80 mK, a temperature a bit higher than the base temperature of the fridge (50 mK).

**Symmetric Kondo effect $\frac{\Gamma_L}{\Gamma_R} = 1.5$.** This case is more tricky since, instead of one resonance pinned to one reservoir, there are two resonances, one on each contact (see fig. 7.15). $T(E)$ thus depends on the bias applied and cannot be extracted from the dc conductance. But we can solve this problem in a first approximation from the following considerations. Roughly, from the discussion of the asymmetric case, we can say that $S_{LL}$ probes the resonance pinned on the right contact and $S_{RR}$ probes the one on the left contact. If the resonances are identical and the current background of the QD is energy independent, we recover $S_{RR} = S_{LL}$. In the following, we will make a very strong assumption. We don't know $T(E)$, but we know that it contains a resonance centered on $\mu_R$ (that we define to be $\mu_R = 0$) that looks like, in absence of decoherence, to the Kondo resonance observed in the conductance. In addition, we know that $S_{LL}$ only probes the resonance of the right contact, and does not depend on the one of the left contact. That's why we assume that $S_{LL}$ calculated with $T(V) = \frac{h}{2e^2}\frac{dI}{dV}$ and $\mu_L = -eV$, $\mu_R = 0$ is a good approximation of the noise expected in this symmetric Kondo regime. The same result would be obtained if the resonance was pinned on the left contact and $S_{RR}$ was calculated. For this reason, we plot only $S_{LL}$ on fig. 7.21 (in this approximation, $S_{LL}$, $S_{RR}$ and $S_-$ are identical).

**Comparison experiment/theory** In both cases, the quantities compared to the experiment on fig. 7.21 typically represents the noise that would be measured if *all* the informations about the Kondo effect (interactions, decoherence, dynamics) were included in the conductance. In other words, any deviation could be attributed to out-of-equilibrium decoherence, dynamics effects or both together. Note that, in the absence of a reliable calibration, the amplitude of the noise derivative has been chosen to obtain the best adequacy with theory at high voltages (where there is no Kondo correlations anymore).

We now detail this comparison for the three different asymmetries :

- Kondo ridge B, strong asymmetry $\Gamma_R/\Gamma_L = 11$. For the lowest frequency, the noise in the left electrode $S_{LL}$ fits quite well with the experiment, unlike $S_{RR}$. It means that we are probably measuring the noise in the less coupled electrode and that the Kondo resonance, pinned on the well coupled contact, is not very affected by the bias voltage and the high frequency ($eV_s = h\nu = 1.7k_BT_K$). But when $eV_s = h\nu = 4.3k_BT_K$, $S_{LL}$ doesn't fit anymore the experiment where the singularity at $eV_s = h\nu$ is completely washed out : there, the Kondo resonance is strongly suppressed by the voltage bias.
- Kondo ridges C, $\Gamma_R/\Gamma_L = 1.5$, almost symmetric contacts. For the lowest frequency, the experiment is well fitted by $S_{LL/RR}$, meaning that the Kondo resonance is present. But this time, it corresponds to $eV_s = h\nu = 0.4k_BT_K$, that is very low (and thus indeed, the Kondo resonance should not be affected). But as soon as $eV_s = h\nu = k_BT_K$, $S_{LL}$ does not fit anymore the experiment, the Kondo resonance is suppressed.
- Kondo ridge A, less asymmetric than B $\Gamma_R/\Gamma_L = 5$. There, $S_{LL}$ does not fit very well for both $eV_s = h\nu = k_BT_K$ and $2.7k_BT_K$, even though it is better for the lower frequency.

It means certainly that the resonance is weaken by the voltage bias, but could be either due to the fact that this theory is no well suited for this asymmetry regime. Note the good agreement with $S_-$ (accidental ?).

This quantitative analysis meets the qualitative one : the Kondo effect in a quantum dot that is symmetrically coupled to the reservoirs is less resistant to a bias voltage than in an asymmetrically coupled QD.

#### 7.3.1.4 Attempt of interpretation

The dependence of out-of-equilibrium decoherence on contact asymmetry is not surprising, even though never measured before. What is more striking is the value of frequencies (or equivalently speaking, of bias voltages) at which the Kondo features completely disappear : between 1.7 and $4.3k_BT_K$ for $\Gamma_L/\Gamma_R = 11$, between 1 and $2.7k_BT_K$ for $\Gamma_L/\Gamma_R = 5$ and between 0.4 and $k_BT_K$ for $\Gamma_L/\Gamma_R = 1.5$. According to Leturcq *et al.* [219] who measured the out-of-equilibrium density of states of a quite symmetric Kondo effect ($\Gamma_L/\Gamma_R = 1.5$), even if a voltage $V = 4.5k_BT_K$ is applied between the electrodes, the Kondo resonance is split but not completely washed out. It means that the decoherence we measure cannot be entirely accounted for by the effect of a bias voltage on the DOS of the system {dot+reservoirs}.

To account for this decoherence, we can invoke the background of conductance which is always present, and which reaches almost $e^2/h$ in the symmetric case (partly because of large inelastic cotunneling peaks) : it may be the manifestation of a second conduction channel, which brings some additional decoherence. It is also likely that this decoherence is associated to the high frequency nature of the measurement : the high frequency emission noise is more sensitive to out-of-equilibrium decoherence of the Kondo effect than the DC DOS.

#### 7.3.1.5 Temperature dependence

As a complementary measurement, we present here the temperature dependence of the noise at the center of the Kondo ridge B. In principle, this measurement is complicated because temperature affects as well the superconductivity of the detector at the same time as the Kondo effect. That's why this was relevant only for the Kondo ridge with the lowest $T_K = 30$ $\mu$eV $= 0.35$ K, such that the Kondo resonance is affected before the noise detection.

The measurement is presented on fig. 7.22 : the temperature dependence of both the conductance and the noise are plotted. When the temperature increases, the Kondo resonance is affected, its height decreases. Logically, the singularity in noise, direct consequence of the Kondo resonance, decreases as well. Note that at high voltages, the noise is not affected.

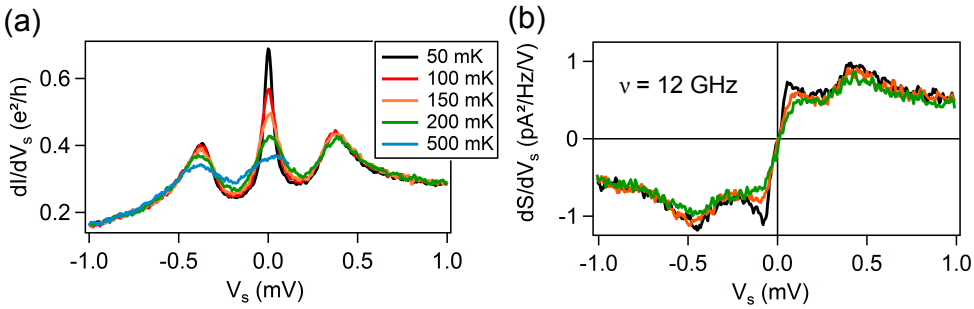


FIGURE 7.22 – Temperature dependence of the conductance and the noise derivative as a function of $V_s$ for various temperatures, measured at the center of the Kondo ridge B, with $T_K = 30$ $\mu$eV. The noise measurement is realized at 12 GHz.

### 7.3.2 Noise in other regimes

#### 7.3.2.1 Coulomb blockade peak

Measuring the noise due to Coulomb blockade peaks would be a very good test of our setup and of the scattering matrix theory. Unfortunately, we faced experimental difficulties. The Coulomb peaks are often very poorly conducting, so that the induced noise is very weak and difficult to measure. The solution could be to average a lot of measurements, but this was made difficult (almost impossible) by a drift of gate voltage : it was difficult on this sample to stay at $V_g = cste$ with a high precision. It was thus difficult to resolve properly Coulomb blockade peaks.

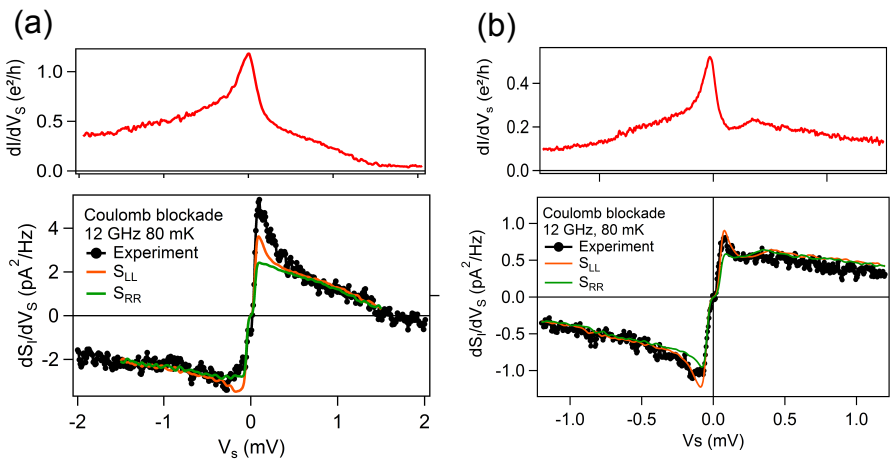


FIGURE 7.23 – Noise derivative and differential conductance in the Coulomb blockade regime, plotted as a function of the bias voltage $V_s$. (a) and (b) represent two different Coulomb peaks, measured at 12 GHz.

We present however on fig. 7.23 the noise measured on two different Coulomb peaks, compared to scattering matrix theory. The measurement is presented only for 12 GHz, at 31 GHz

the signal was too weak to be reliable. Note that this situation is very different from the Kondo regime since the potential are defined compared to the energy level in the dot. These measurements are taken on the edges of two diamonds, where the energy level in the dot is aligned with one of the reservoirs. That's why the same quantity as for the asymmetric Kondo regime has been plotted (the resonance is centered on the Fermi level of the right reservoir), but we don't know in which reservoir we are measuring the noise. The comparison between theory and experiment is not very convincing, and we are missing the higher frequencies.

#### 7.3.2.2 SU(4) Kondo effect

We find a zone in gate voltage where the coupling between the dot and the reservoirs is large enough to observe SU(4) Kondo effect ($\Gamma > \delta E$). The conductance map is represented on fig. 7.24 and is actually the one described in section 2.3.2.1.

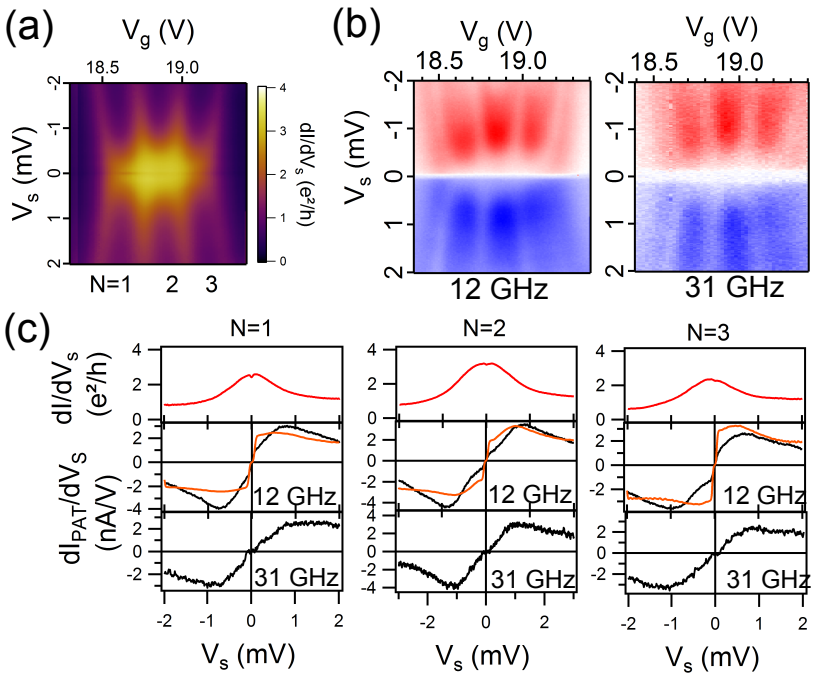


FIGURE 7.24 – Noise measurement in the SU(4) Kondo regime. (a) Differential conductance as a function of $V_s$ and $V_g$ in a region where the coupling of the QD to the electrodes is large enough to allow SU(4) Kondo effect. See section 2.3.2.1 for details. (b) Derivative of the photo-assisted noise in the detector, proportional to the noise derivative, as a function of $V_s$ and $V_g$, in the Kondo SU(4) region. (c) Vertical cuts at the centers of the N=1, 2 and 3 diamonds of each of the three color plots.

As for SU(2) Kondo effect, we measure the noise derivative as a function of the bias and gate voltage, all over the three diamonds of the SU(4) Kondo region (N=1, 2 and 3 diamonds). The frequencies at which the noise is measured are still 12 GHz and 31 GHz, but the Kondo temperature here is of the order of 500 $\mu$eV ($T_K \approx 6$ K), corresponding to 125 GHz. The measurement is thus in a low frequency regime such that, except the width of the emission

noise plateau at low voltage, the noise is the same at both frequencies. A quantitative analyze of SU(4) Kondo effect at low frequency is presented in section 6.3.

Moreover, in this regime it is difficult to compare the experimental data with the scattering matrix theory. Indeed, since two channels are involved, there is no way for extracting the energy dependent transmissions from the conductance. We try to do it assuming that the two channels were equally transmitted (see orange lines on fig. 7.24), but the agreement with the experiment is so poor that this hypothesis may be wrong.

### 7.3.3 Conclusion

- In this part, we have presented measurements of emission noise in a carbon nanotube quantum dot at frequencies 12 and 31 GHz. We investigate this emission noise mainly in two SU(2) Kondo regions, but we also measured this quantity in the Coulomb blockade regime and in SU(4) Kondo regime.
- We have access to the noise in SU(2) Kondo regions in different regimes of coupling : reservoirs symmetrically coupled to the QD or, on the contrary, very asymmetrically. This parameter is very relevant here since it can break the symmetry between the reservoirs, important in the context of finite frequency noise, and because it may affect the decoherence of the Kondo effect due to a bias voltage.
- The measurements in the SU(2) Kondo regime are compared to the one of the previous work from Basset *et al.* and to a theory based on the energy dependent transmission, that roughly gives the expected noise in absence of any decoherence specific to Kondo effect.
- The result of this comparison is that, at low frequency, a singularity is present in the experimental noise derivative and fits quite well with the theory. At higher frequency, the expected singularity disappears, because of out-of-equilibrium decoherence pf the Kondo effect. The point is that, the more symmetric are the contacts, the lower is the frequency (*i.e* the lower is the bias voltage) at which the Kondo resonance is destroyed. In other words, out-of-equilibrium decoherence of the Kondo effect is weaker when one reservoir is less coupled to the QD than the other.
- The comparison of these data with out-of-equilibrium DOS measurements show that the high frequency emission noise is more sensitive to out-of-equilibrium decoherence of the Kondo effect than the DC DOS.

# Part IV

# AC Josephson effect in a carbon nanotube in the Kondo regime

# 8 AC Josephson effect in a carbon nanotube in the Kondo regime

In this part, we combine the two first experiments presented in this PhD : we couple a carbon nanotube quantum dot Josephson junction to the noise detector presented in chapter 7. The DC Josephson effect has been investigated in details in chapter 5, by measuring the current-phase relation. In this new experiment, instead of phase biasing the junction, we bias it with a voltage such that it emits a high frequency radiation, this is the AC Josephson effect. It can be measured by the SIS detector at the resonance frequencies of the coupling circuit.

What is the effect of Coulomb blockade and Kondo effect on this AC Josephson effect ? What happens to the 0-$\pi$ transition ? There are very few theoretical or experimental investigations of these questions. We present in this chapter the issues associated with AC Josephson effect, before exposing experimental results and attempts of explanations.

## 8.1 Why measuring AC Josephson effect ?

### 8.1.1 Definition and experimental manifestation

**AC Josephson effect** If a constant voltage $V$ is applied across a Josephson junction, the evolution of the phase difference across the junction is given by :

$$\frac{d\varphi}{dt} = \frac{2eV}{\hbar} \tag{8.1}$$

On the other hand, the DC Josephson effect yields the current-phase relation $I = I(\varphi) = \sum_{n=1}^{\infty} I_{c,n} \sin(n\varphi)$. The combination of these equations show that the Josephson junction generates an alternative non dissipative current at the Josephson frequency $f_J = \frac{2eV}{h}$ and its harmonics :

$$I(t) = \sum_{n=1}^{\infty} I_{c,n} \sin(2\pi n f_J t) \tag{8.2}$$

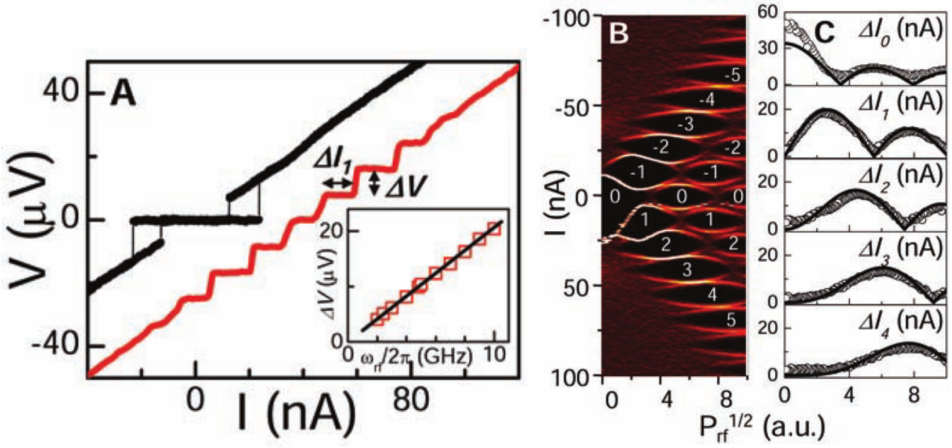


FIGURE 8.1 – **A** In red, Shapiro steps measured in an InAs nanowire by Doh *et al.* [68] under irradiation at 4 GHz (to compare with the black curve, without irradiation). **B** Derivative of **A** curve with respect to the current for various power of the external radiation. On the right is plotted the width of the steps as a function of the exciting power : it is quite consistent with a Bessel function fit (black lines).

This AC Josephson emission has been detected in tunnel Josephson junctions as soon as 1965 for example by Yanson *et al.* [222] or Giaever [207]. This phenomenon is now used to fabricate high frequency radiation generator, see for example ref. [223] where BSCCO materials are used as intrinsic high-$T_c$ Josephson junctions to produce a coherent THz emission.

More recently, for mesoscopic physics, the experimental setup described in chapter 7 has been used to measure the Josephson emission of a superconducting Cooper pair transistor [24]. Note as well that it is the Josephson emission of a superconducting tunnel junction that we use to characterize our experimental setup (ref. [19] and fig. 7.8). Very recently, Deacon *et al.* have measured the emission of a HgTe Josephson junction using high frequency electronics[224].

However, the frequencies involved are relatively high : $\nu_J \approx 5$ GHz for a bias $V = 10$ $\mu$eV, and the emitted power is quite low[225]. For these reasons, the most common way to investigate AC Josephson effect is actually to irradiate the junction and to measure its DC current.

**Shapiro steps** To understand the effect of an rf irradiation, we can include it as an alternative component in the voltage bias, added to a continuous one [111, 225]:

$$V = V_0 + V_{ac}\cos(\omega_{ac}t + \phi_0) \tag{8.3}$$

According to formula 8.1, the phase evolves as :

$$\varphi(t) = \omega_0 t + \frac{2eV_{ac}}{\hbar\omega_{ac}}\sin(\omega_{ac}t + \phi_0) \tag{8.4}$$

where $\omega_0 = \frac{2eV_0}{\hbar}$ is the Josephson frequency associated to the voltage $V_0$. To obtain the current in the junction, we now have to insert this expression into the current-phase relation. In the simplest case of a tunnel junction (sinusoidal CPR), it can be expressed as a function of Bessel functions $J_n$ such that [111]:

$$I = I_c \sum (-1)^n J_n \left( \frac{2eV_{ac}}{\hbar\omega_{ac}} \right) \sin(\omega_0 t - n\omega_{ac} t + \phi_0) \tag{8.5}$$

It follows that, if $\omega_0 = n\omega_{ac}$ *i.e.* $V_{0,n} = n\hbar\omega_{ac}/2e$, there are DC contributions to the current $I_n = I_c J_n \left(\frac{2eV_{ac}}{\hbar\omega_{ac}}\right) \sin(\phi_0)$, showing up as peaks in the I(V) characteristic. In the case of a DC current bias of the junction, together with RF irradiation, it leads to steps in the V(I) characteristic. An example of measurement of these steps, called Shapiro steps, is shown on fig. 8.1 (taken from ref. [68]). Shapiro steps can be seen as a locking of the dynamics of the junction on the irradiation frequency.

Another way of understanding these steps is to see them as photo-assisted tunneling of Cooper pairs [225]: when a voltage $V$ is applied on the junction, there is an energy difference $2eV$ between the Cooper pairs on one side and on the other of the junction. Consequently, to tunnel through the junction, the pair has to acquire or loose the energy amount $2eV$. This process is associated with the absorption or emission of a photon of energy $\hbar\omega = 2eV$, and generates copies of the supercurrent branch at finite bias.

### 8.1.2 AC Josephson effect used as a probe of the Josephson effect

#### 8.1.2.1 Probe of the harmonics of the CPR

If we consider now the general case, the dc CPR can have harmonics :

$$I(\varphi) = \sum_{n=1}^{\infty} I_{c,n} \sin(n\varphi) \tag{8.6}$$

These harmonics induce Josephson emission at harmonics of the Josephson frequency. In the Shapiro steps, new steps appear at voltages $V_{n,m} = \frac{m}{n}\frac{\hbar\omega_{ac}}{2e}$ ($m$ being an integer) : these are fractional Shapiro steps [226]. It is even possible for Josephson junctions to emit sub-harmonics, giving additional steps.

The analysis of the Shapiro steps has been proven to be useful in the context of 0-$\pi$ transitions in SFS junctions. The goal was to know the harmonic content of the current-phase relation at the transition : does the critical current vanish or is there a second harmonic ? To answer this question, Sellier *et al.* measured the Shapiro steps in a junction at the 0-$\pi$ transition, and demonstrated the presence of half-integer Shapiro steps [166]. These steps demonstrate the presence of a $\pi$-periodic contribution to the CPR, *i.e.* $I = I_c \sin(\varphi/2)$.

Another recent use of Shapiro steps is the search for topological superconductivity (and thus

Majorana fermions). Then, it has been predicted that the CPR should become $4\pi$-periodic [227]. But this $4\pi$-periodic CPR involves an unstable energy branch, from which the system may relax for various reasons [228], making this phenomenon difficult to observe from a stationary current-phase relation measurement. However, this difficulty can be overcome investigating the AC Josephson effect at frequencies larger than the inverse of the relaxation times in the system [229]. Then, the $4\pi$ periodicity should manifest as the disappearance of

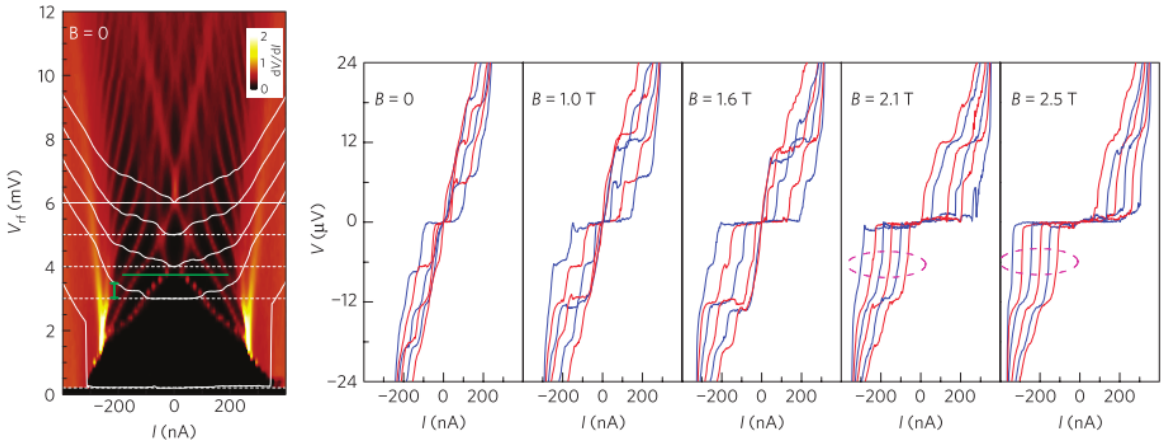


FIGURE 8.2 – Shapiro steps measured by Rokhinson *et al.* [229] in a InSb semi-conducting wire. When the magnetic field is increased, one can see a disappearance of the first Shapiro step (indicated by the dashed violet ellipses). This is attributed to the topological phase transition induced by the magnetic field in presence of spin-orbit coupling.

the first Shapiro step (or, in other words, as a doubling of the voltage height of the step). This is what has been observed by Rokhinson *et al.* [229] in a InSb semi-conducting wire contacted with Nb (fig. 8.2). They show that, when an in-plane magnetic field larger than 2 T is applied, the first step indeed disappears, consistently with a topological phase transition.

Wiedenmann *et al.* performed a similar experiment in HgTe quantum wells Josephson junctions [228]. They also measured this disappearance of the first Shapiro steps, but showed that this observation was only possible for frequencies not too high. Otherwise, due to the dynamics of the junction, the first step is recovered. Very recently, they confirmed these results with a direct AC Josephson emission measurement in the same system [224]. The experiment has been performed with high frequency electronics and has been made possible in particular thanks to the use of a cryogenic amplifier.

We see that the investigation of AC Josephson effect can provide informations about the harmonics of the current-phase relation. However, as suggested by the frequency dependence of the HgTe experiment, these results can be strongly affected by the phase dynamics. This is what we address now.

#### 8.1.2.2 Probe of the dynamics of the system

**Landau-Zener transitions** The dramatic effect of phase dynamics on AC Josephson effect can be understood from the study of a simple system by Averin and Bardas [230]: a superconducting point contact, modelized by a channel of arbitrary transmission $T$. In the case of a transmission close to 1, the Andreev bound states look like the one represented on fig. 8.3 (a) : around $\varphi = \pi$, the positive (unstable) and negative (stable) branches are very close. Then, if a voltage is applied across the junction, the phase evolves with a velocity $2eV/h$ and the probability for the system to make a transition to the excited level is non-zero, this is a Landau-Zener (LZ) transition. The consequence on the Josephson emission is dramatic since the CPR probed is $4\pi$ instead of $2\pi$-periodic : the amplitude of the emission at $f_J$ is reduced (see fig. 8.3 (b)) and the one at $f_J/2$ increased.

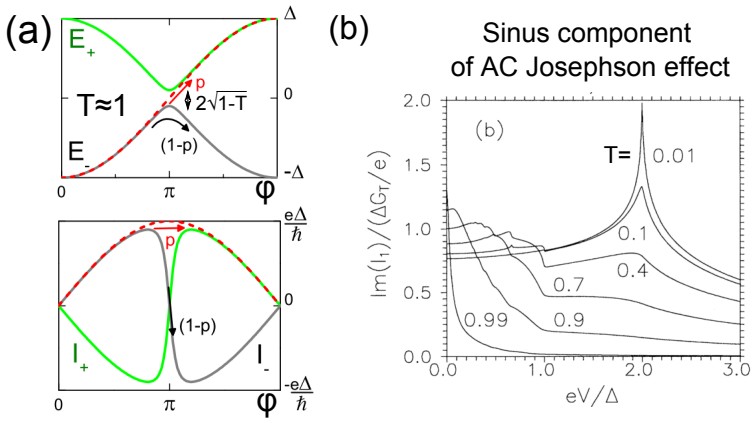


FIGURE 8.3 – (a) Schema of ABS levels in a situation where the level spacing at $\pi$ is very small, such that Landau-Zener (LZ) transition are very likely to happen. Adapted from ref. [231] where the authors investigated this issue measuring the I(V) characteristic of a superconducting quantum point contact. (b) Amplitude of the Josephson emission at $f_J$ as a function of the bias voltage for various transmission coefficients T. From ref. [230].

The Landau-Zener probability can be expressed as

$$p = \exp\left(-\frac{\pi(1-T)\Delta}{eV}\right) \tag{8.7}$$

The higher is the transmission, the closer are the Andreev levels, favoring Landau-Zener transitions. On the other hand, the larger is the bias voltage, the faster is the variation of the phase, the more likely is the Landau-Zener transition. This is figured on fig. 8.3, where for small transmissions, the amplitude of the emission at $f_J$ is constant until large bias voltages while it is quickly reduced for high transmissions.

This dynamics-induced doubling of the period has been observed in a superconducting Cooper pair transistor (SCPT) by Billangeon *et al.* [24] (see fig. 8.4). In this experiment, the SCPT can be seen as a device where the spacing between the ABS depends on the gate voltage. The

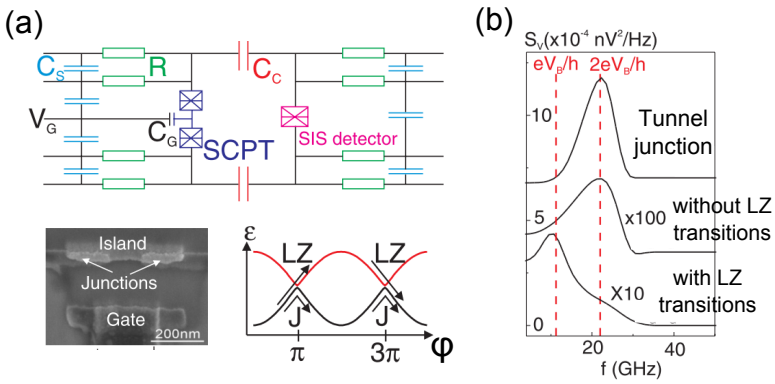


FIGURE 8.4 – (a) Experimental setup used to measured AC Josephson emission in a superconducting Copper pair transistor (SCPT), from ref. [24]: the SCPT is capacitively coupled to a SIS detector, such as the one described in the previous chapter. (b) Measurement of Josephson emission as a function of frequency in three different situations : in a simple tunnel junction (reference), in the SCPT at a gate voltage where one do not expect Landau-Zener (LZ) transition and at another gate voltage, where LZ is expected.

authors have shown that, indeed, when the ABS are very close and LZ transitions expected, a signal is mainly emitted at $f_J/2$ instead of $f_J$, as it is the case in the reference situation, with a tunnel junction where no LZ transition is expected.

**Landau-Zener transitions in the Kondo regime** The dynamics of the Andreev states in the Kondo regime has also been investigated by Levy Yeyati *et al.* [232]. The main difference with the superconducting point contact is that the Andreev states are detached from the continuum (see fig. 4.13), which leads to interference effects in the DC current. In ref. [233], this theory is shown to explain the shape of the zero bias peak of conductance observed in a S-QD-S junction made of a CNT, provided that an inelastic relaxation rate is taken into account. These effects have certainly consequences on the AC Josephson effect but, unfortunately, the authors only considered the dc current due to MAR processes and not the ac emission.

**Conclusion on Josephson dynamics** From these examples, we see that interpreting AC Josephson measurements is not easy and that these experiments are more complex than DC Josephson effect measurements. Besides, one should not forget that this kind of measurement requires a voltage biasing of the system. This is even more true for Shapiro steps, where the system is excited at high frequency. As a consequence this is an out-of-equilibrium measurement.

Note that it is possible to investigate the dynamics of a Josephson junction in an equilibrium situation. This is for example what has been done in refs. [234, 235], where an SNS junction is formed in an isolated ring, excited by a high frequency magnetic flux, and measured thanks

to its coupling to a resonator. The advantage of this method compared to AC Josephson effect is that the high frequency excitation is controlled and can be chosen in order to access the linear response of the system at equilibrium. Its drawback is that DC transport is not available. This is a real problem when working with CNTs, which need to be characterized via a stability diagram that implies applying a bias voltage.

### 8.1.3 AC Josephson effect in a superconducting QD

In the preceding parts of this manuscript, two experiments have been presented. In the first one, we investigate the influence of the Kondo effect on the current-phase relation of a quantum dot Josephson junction : if the Kondo effect is strong enough compared to the superconducting correlations ($T_K \gg \Delta$), it can induce a $\pi$ to 0 transition. If it is of the same order of magnitude ($T_K \approx \Delta$), then the CPR is strongly anharmonic. On the other hand, we presented emission noise measurements at high frequency in a CNT in the Kondo regime. We showed that if the frequency is too high compared to $T_K$ (which is equivalent, in an emission measurement, to a large applied voltage bias), the Kondo resonance is weaken and does not participate in the emission process.

The question we can naturally ask is what is expected from an emission noise measurement if the CNT is contacted with superconducting leads ? Then, depending on if the CNT is voltage biased below or above the gap, its high frequency emission corresponds either to AC Josephson effect or quasi-particle noise. We will focus on the AC Josephson emission, that is related to the DC current-phase relation. What happens to the 0-$\pi$ transition driven by the ratio $T_K/\Delta$ ? Is it possible to observe it in the Josephson emission ? At frequencies of the order of $T_K$, which is the timescale at which the Kondo screening takes place ($hf_J \approx k_B T_K$), is the Kondo effect still able to induce a 0-junction ? If the transition exists, is it possible to detect the non-harmonicity of the CPR analyzing the frequency of the Josephson emission ?

These question are open since, to our knowledge, there is neither theoretical prediction nor experiment about AC Josephson effect in the Kondo regime.

The only predictions, given by Hiltscher *et al.* [236], concerns a single-level QD in the atomic limit ($\Delta \to \infty$), thus without Kondo correlations. We can still notice the following points :

- Just as for high frequency noise, if the spatial asymmetry between the electrodes is broken, the Josephson emission is *a priori* different in the two leads. In particular, the AC Josephson effect in the weakly coupled reservoir probes the proximity effect induced by the strongly coupled reservoir.
- Like in DC Josephson effect, AC Josephson effect is suppressed in the regions where the dot is occupied by an odd number of electrons. However, the gate dependence of this suppression depends on the voltage bias (which also determines the Josephson frequency) : the amplitude of the Josephson emission is therefore *a priori* not proportional to the

DC critical current of the system.

Note that there exists a measurement of Shapiro steps in a carbon nanotube, performed by Cleuziou *et al.* [84]. However, in their experiment, the nanotube is very well coupled to the electrodes, such that it is in a Fabry-Pérot regime. This experiment shows a gate dependence of the Josephson emission in this regime, as well as different dynamics regimes.

## 8.2 AC Josephson effect measurement

I present here our measurement of the AC Josephson emission of a carbon nanotube quantum dot in the Kondo regime. I first present the experimental setup (which is actually the same as the one used for high frequency noise measurements), before showing the experimental results and an attempt of interpretation.

### 8.2.1 Experimental setup

#### 8.2.1.1 Description and fabrication of the sample

The experimental setup is represented on fig. 8.5. The source of Josephson emission is a carbon nanotube contacted with superconducting electrodes. The noise detection is performed using the same SIS detector as in the previous experiment. Both are directly connected to the end of the central line of a coplanar waveguide resonator, whose other end is grounded, so that they are coupled at the resonant frequencies of the circuit.

In addition, a second Josephson tunnel junction, actually a SQUID identical to the SIS detector but with a different loop area, is connected as well on the resonator (between the points R and C on fig. 8.5). The objective of this third junction is to provide a controlled source of Josephson emission, either to calibrate the setup or to on-chip irradiate the CNT.

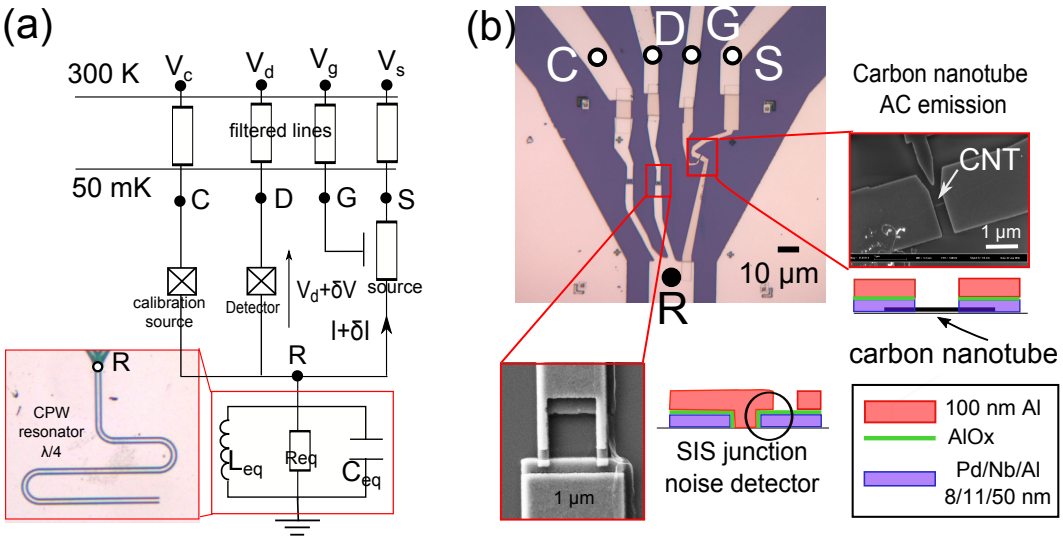


FIGURE 8.5 – (a) Experimental setup used to measure the AC Josephson emission of a CNT QD. The source of emission, the CNT Josephson junction, is directly connected to a resonant circuit, as well as two tunnel Josephson junctions, which can be used as noise detectors and on-chip generators. (b) Image of the sample and description of the metallic layers of the contacts.

The CNT are first grown by CVD, as explained in chapter 3. On top of the nanotubes, the contacts, the resonator and the tunnel junctions are deposited in one step. A layer of 8 nm of

Pd, 11 nm of Nb and 50 nm of Al is first deposited with an angle of 15°. This layer is oxidized under oxygen pressure and covered by a 100 nm layer of Al, deposited at -15° (see fig. 8.5). As in the current-phase relation experiment, Pd is necessary for a good coupling between the CNT and the contacts, and aluminum is required to form the oxide layer of the tunnel junctions. The niobium increases the superconducting gap seen by the CNT to $\Delta \approx 150$ $\mu$eV. The tunnel junctions have total area of $600 \times 200$ nm$^2$, with normal resistances of 2.3 k$\Omega$ and 2.5 k$\Omega$.

As indicated on fig. 8.5, the detector is biased by the voltage $V_d$, the nanotube by $V_s$, and $V_g$ is the gate voltage applied on an electrostatic side-gate placed close to the nanotube. $V_c$ is the voltage applied on the additional tunnel Josephson junction. The design of the resonator is exactly the same as the previous one, with resonances expected around $\nu_0 = 12$ GHz, $\nu_1 = 31$ GHz and $\nu_2 = 51$ GHz.

#### 8.2.1.2 Measured quantity

The principle of the experiment is exactly the same as described in section 7.1.4.2 (in the previous chapter), where the AC Josephson emission of a tunnel Josephson junction has been used to characterize the resonator. If we assume that the CNT has a sinusoidal CPR $I = I_c \sin(\varphi)$ (which has been shown in the preceding to be often the case experimentally), when biased by $V_s$, the junction emits a radiation $I_c \sin(2\pi f_J(Vs)t)$ with $f_J(V_s) = 2eV_s/h$. The resulting photo-assisted tunneling current in the detector should be, for a fixed $V_d = V_0$ such that $2\Delta - h\nu_0 < eV_d < 2\Delta$ :

$$I_{PAT}(V_s) = \left(\frac{1}{2V_s}\right)^2 \frac{I_c^2}{4} \left| Z_t\left(\frac{2eV_s}{h}\right)\right|^2 I_{qp}^0(V_0 + 2V_s) \tag{8.8}$$

Thanks to the coupling through the resonator, we get that, for a given bias of the detector $V_d$, $I_{PAT}(V_s)$ is a succession of peaks at $V_s = h\nu_n/(2e)$, of height proportional to the square of $I_c$ and to a factor $k_n = \left(\frac{e|Z_t(\nu_n)|}{h\nu_n}\right)^2 I_{qp}^0(V_0 + h\nu_n/e)\Delta\nu_n$ which depends on the resonance $n$ (but is constant for a given bias voltage of the detector) :

$$I_{PAT}(V_s) \approx \frac{I_c^2}{4} \sum_{n=0}^{\infty} k_n \delta\left(\frac{2eV_s}{h} - \nu_n\right) \tag{8.9}$$

At the end, the quantity measured in this experiment is exactly the same as the one obtained by Deacon *et al.* in ref. [224] when the bias voltage of the junction is swept at a fixed frequency measurement. The difference is that we have only a few frequencies available, determined by the design of the resonator (but not limited by high frequency electronics).

#### 8.2.1.3 Effect of the second Josephson junction

In this setup, there is another tunnel Josephson junction. It can be used to irradiate the CNT Josephson junction while measuring its high frequency emission. The crucial point is to check that it is possible to choose a biasing of this additional junction such that it does not affect the measurement of the emission of the nanotube.

We made a test sample containing three tunnel Josephson junctions : one used as a detector, the other as a source and the last one as an on-chip generator. We have checked that, if the generator junction is biased below the gap corresponding to a Josephson frequency above 100 GHz (not coupled by the resonator), the measured quasi-particle noise of the source JJ is as expected.

### 8.2.2 Detail of one measurement

#### 8.2.2.1 Differential conductance in the normal state

As in each experiment in a quantum dot, we first try to characterize the sample by measuring its differential conductance as a function of the bias voltage $V_s$ and the gate voltage $V_g$ in the normal state. This is what is represented on fig. 8.6, at 30 mK [1] and with a 1T perpendicular field. This quantity is also represented for more range of gate voltage on fig. 8.9.

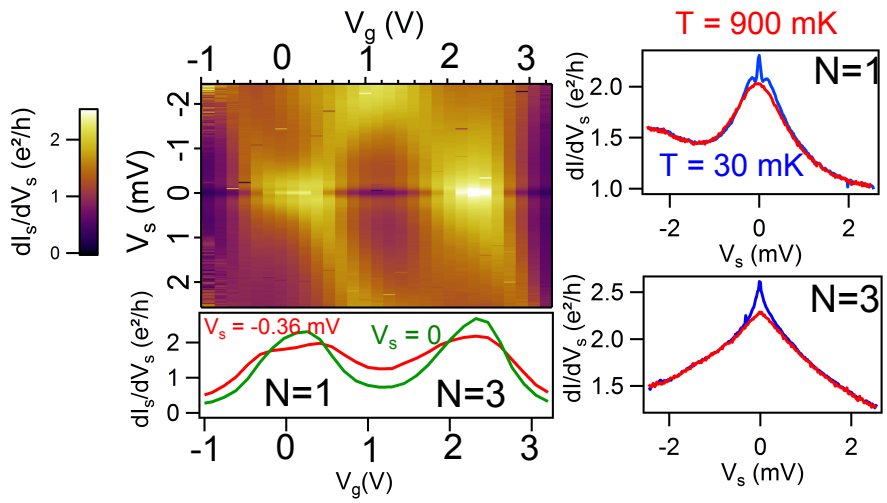


FIGURE 8.6 – Differential conductance of the CNT in a 1T perpendicular magnetic field. Below the color plot representing $dI_s/dV_s(V_s, V_g)$, horizontal cuts are shown at zero bias voltage and -0.36 mV (see text). On the right, vertical cuts are shown at 30 and 900 mK at the center of the $N = 1$ ($V_g = 0.1$ V) and $N = 3$ ($V_g = 2.4$ V) diamonds.

[1] The base temperature of the dilution fridge has been improved since the previous experiment by slightly increasing the mixture quantity and changing its composition.

Just as in the current-phase relation measurement, the contacts are partially made of niobium, we are thus facing the same problem : at the maximum magnetic field that we can apply in this setup, 1T, superconductivity is not completely destroyed. This can be seen on fig. 8.6 where there is a dip around zero bias for all gate voltages. This measurement however reveals the presence of Coulomb structures in the nanotube, with the 1-3-1 alternation of big and small diamonds. The diamonds which can be identified as oddly occupied present a non-zero conductance at zero bias due to the Kondo effect.

On the right are represented two vertical cuts of the color plot at the middle of the $N = 1$ and 3 diamonds. The first striking feature is the sharp peak at zero bias at 30 mK, which disappears at 900 mK : this may be a supercurrent peak, strong enough to resist to a 1T magnetic field (probably a 0-junction).

To overcome these features due to superconductivity, below the color plot is represented in red a horizontal cut at $V_s = -0.36$ meV instead of zero bias (that is represented in green for comparison). We see however that, in the $N = 3$ diamond, the conductance is higher than $2e^2/h$ : a second channel may participate partially to transport. This statement is confirmed by the non-zero conductance in the $N = 2$ diamond, which is however not high enough to be considered as a full SU(4) Kondo effect. Moreover, the zero-bias structure is very large, suggesting a large Kondo temperature and thus a large coupling $\Gamma$, which favors the two-level regime. Note that the $T_K$ could be itself enhanced by the two-level regime and that the central structure may be enlarged by cotunneling peaks, making very complicated any determination of $\Gamma$ and $T_K$.

#### 8.2.2.2 DC supercurrent

We now current bias the carbon nanotube in order to obtain its critical current as a function of the gate voltage (actually it is a switching current, we will however use the denomination "critical"). This measurement is presented on fig. 8.7 : the color plot represents the differential resistance of the sample as a function of the bias current. The critical current is extracted as the current at which the resistance increases abruptly, namely when the resistance reaches half the difference between the resistance at zero current and at the largest current. As suggested by the conductance measurements above, the supercurrent is quite high, especially in the N=3 diamond, where it reaches almost 10nA. The two odd diamonds are clearly in a 0-junction state, made possible by the Kondo effect (without Kondo, a $\pi$-junction is *a priori* expected).

#### 8.2.2.3 AC Josephson amplitude measurement

We now present the measurement of AC Josephson emission. In order to measure all the frequencies available ($\nu_0$, $\nu_1$, $\nu_2$ etc.), we bias the detector to a voltage $V_d$ such that $2\Delta - h\nu_0 < eV_d < 2\Delta$, fixed during a measurement. On the other hand, the additional tunnel junction is biased below the gap such that it emits a radiation at a frequency too large to be coupled

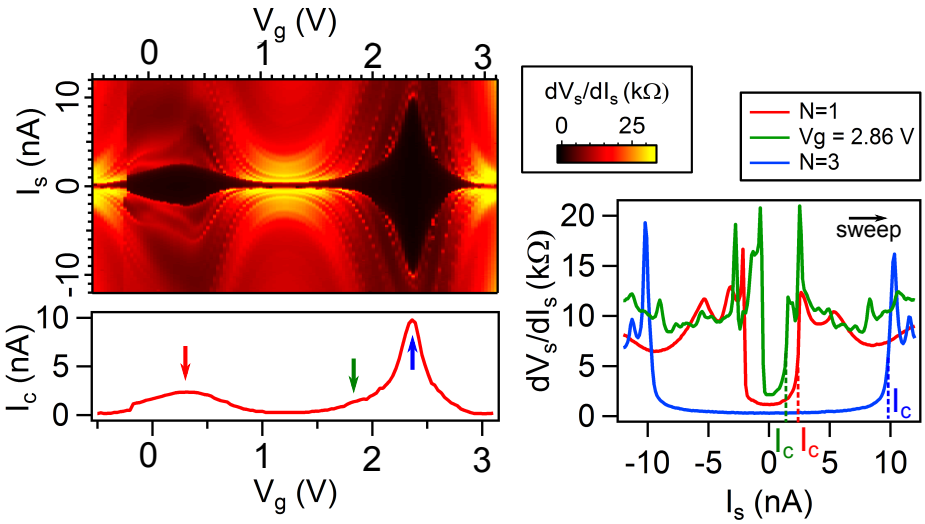


FIGURE 8.7 – Differential resistance of the CNT as a function of the biasing current, in the same region of gate voltage as above. On the right are represented vertical cuts of the color plot at three gate voltages, indicated by the colored arrows, from which is extracted the switching current, represented below the color plot.

through the resonator (typically 100 GHz). The signal measured on the detector due to this junction is checked to be very small. Then, we bias the CNT with a DC voltage $V_s$ added to an alternative one, at a frequency of the order of a few tens of Hz (to perform the lock-in detection) and with an amplitude of 2 $\mu$V. Three quantities are measured : the DC current in the detector, the alternative current (at the excitation frequency) in the nanotube and in the detector. The two latter quantities represent respectively the differential conductance of the nanotube in the superconducting state and the derivative of the photo-assisted tunneling current in the detector with respect to the bias voltage of the CNT. They are represented on fig. 8.8 (a) and (b).

Panel (c) represents the photo-assisted tunneling current, obtained by integration of the panel (b) with respect to $V_s$. Note that this quantity has been corrected of a background of parasitic currents which was attributed to the fact that the detector is biased very close to the gap. Indeed, there, a small quasi-particle current may be superimposed to $I_{PAT}$, and this current is very sensitive to any variation in the bias conditions of the detector, that can be modified by a high current in the nanotube. We checked that, if the detector is biased such that $2\Delta - h\nu_1 < eV_d < 2\Delta - h\nu_0$, this parasitic current disappears.

The measurement of the conductance of the nanotube confirms the information given by previous measurement : there is a strong supercurrent in the Kondo regions. At the center of the diamonds, the peak at zero bias is so high that it merges the MAR structures. This is generally observed when there is one almost perfectly transmitted channel [189].

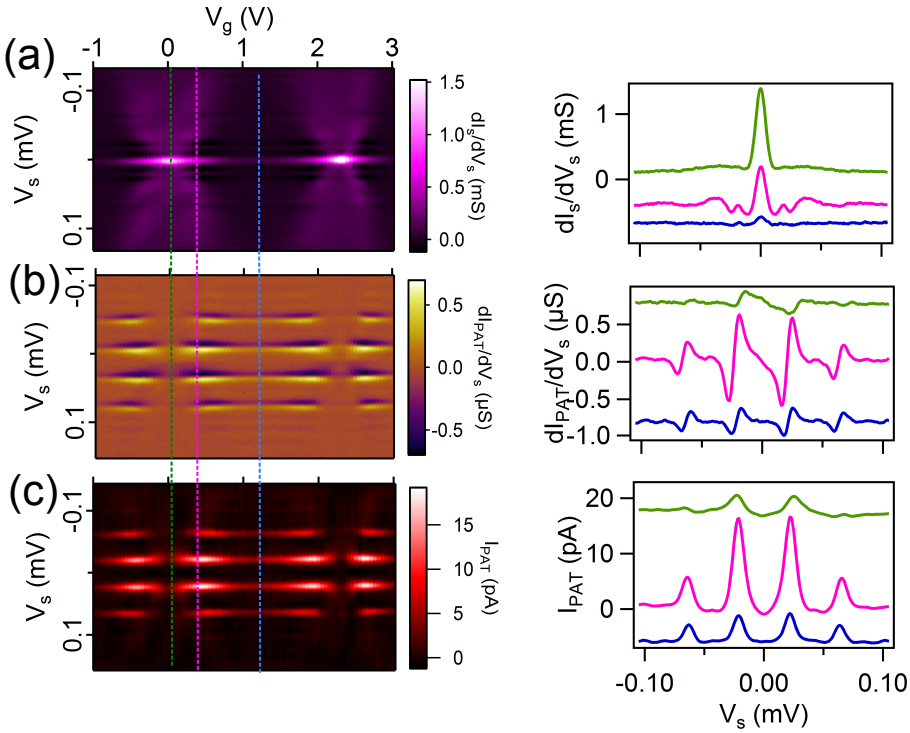


FIGURE 8.8 – (a) Differential conductance of the CNT as a function of its bias voltage $V_s$ in the superconducting state in the gate voltage region investigated above. (b) Derivative of the photo-assisted tunneling current. (c) Quantity represented on (b) integrated over $V_s$, yielding $I_{PAT}(V_s, V_g)$. Vertical cuts of the three color plots are given on the right at the gate voltages indicated by the dashed color lines.

The photo-assisted tunneling current exhibits four peaks, symmetric in $\pm V_s$. They are centered around $V_s = \pm 22$ $\mu$eV and $V_s = \pm 64$ $\mu$eV. These values correspond to Josephson frequencies $f_J = 11$ GHz and $f_J = 31$ GHz, which are resonances frequencies expected for our resonator. It means that we are measuring conventional Josephson effect, *a priori* without significant frequency doubling or halving. It is the case for all the gate voltage regions (data not shown). Note that small peaks are also visible at $V_s = \pm 100$ $\mu$eV for some gate voltage, corresponding to 48 GHz, but they are not high enough to be measurable.

As in the experiment of characterization of the resonator with AC emission of a Josephson tunnel junction, the peaks are quite large ($\Delta V_s \approx 10$ $\mu$eV $\approx 2.5$ GHz). We believe that this is due to the linewidth of the emission itself instead of the quality factor of the resonator, due to an imperfect voltage biasing. Note that, in ref. [224] where the frequency selection is expected to be very good, the width of the AC Josephson emission peaks is of the same order of magnitude.

The main qualitative observation is that, for the gate voltages where the critical current is the highest in DC (thanks to the Kondo effect), the AC Josephson effect collapses. Moreover,

it seems to decrease on a wider gate voltage range at 31 GHz than at 11 GHz. The amplitude of the AC Josephson emission is thus clearly not proportional to the DC critical current.

### 8.2.3 Quantitative analysis and attempts of explanations

#### 8.2.3.1 Description of the results

To provide a more quantitative analysis, we plot the amplitude of the Josephson emission, chosen as the square root of the height of the $I_{PAT}$ peak (since the detector is quadratic). This quantity is plotted for each frequencies 11 GHz and 31 GHz as a function of the gate voltage on fig. 8.9 (b), superimposed with the DC critical current as well as the zero bias conductance in the superconducting state. The signal at 31 GHz is renormalized by a numerical factor to compensate the fact that the ratio between $I_{PAT}$ and the amplitude of the Josephson emission depends on the frequency. This numerical factor has been chosen such that, outside from the oddly occupied diamonds, the emission have the same amplitude at both frequencies.

The qualitative remark is confirmed : the maxima of DC critical current correspond to minima of AC Josephson emission, and this minimum is lower for the highest frequency.

To understand the origin of this collapse of AC Josephson emission, this quantity is represented as well for three other gate voltage regions, where there is also Kondo effect in oddly occupied diamonds on fig. 8.9. Each of these diamonds is designated by a letter from A to G. Note that the renormalization factors between 11 and 31 GHz amplitudes are slightly different depending on the measurements : this may be due to different biasing of the detector. Fig. 8.10 shows the same quantity, but compared to the superconducting state differential conductance. At zero bias, this quantity is related to the supercurrent. At finite bias and below the gap, in the case of symmetric contacts, it is governed by the multiple Andreev reflections. We now review the different zones.

The differential conductance of diamond A exhibits a non zero-value around zero bias around $1.4\, e^2/h$, indicating a not perfectly transmitted channel and thus an asymmetric coupling between left and right reservoirs. From my experience, it seems that such a contact asymmetry is generally (but not necessary) related to a lower Kondo temperature. There, the critical current becomes very small at the center of the Kondo ridge but it is however difficult to say if the junction turns $\pi$ or not. As for diamonds B and C, the AC emission decreases in the odd diamond, but here it is also the case for the critical current. An unexpected effect remains : while the amplitudes at 11 and 31 GHz coincide outside the oddly occupied diamond, the emission is lower at 31 GHz than at 11 GHz inside the diamond.

The diamond D and E present a behavior relatively similar to diamonds B and C : AC Josephson emission decreases when the critical current is maximum, and this decrease is more severe at 31 GHz than at 11 GHz. Again, no $T_K$ can be extracted from the "normal" state measurement, but the conductance in the normal state exceeds $2e^2/h$ and is quite high at

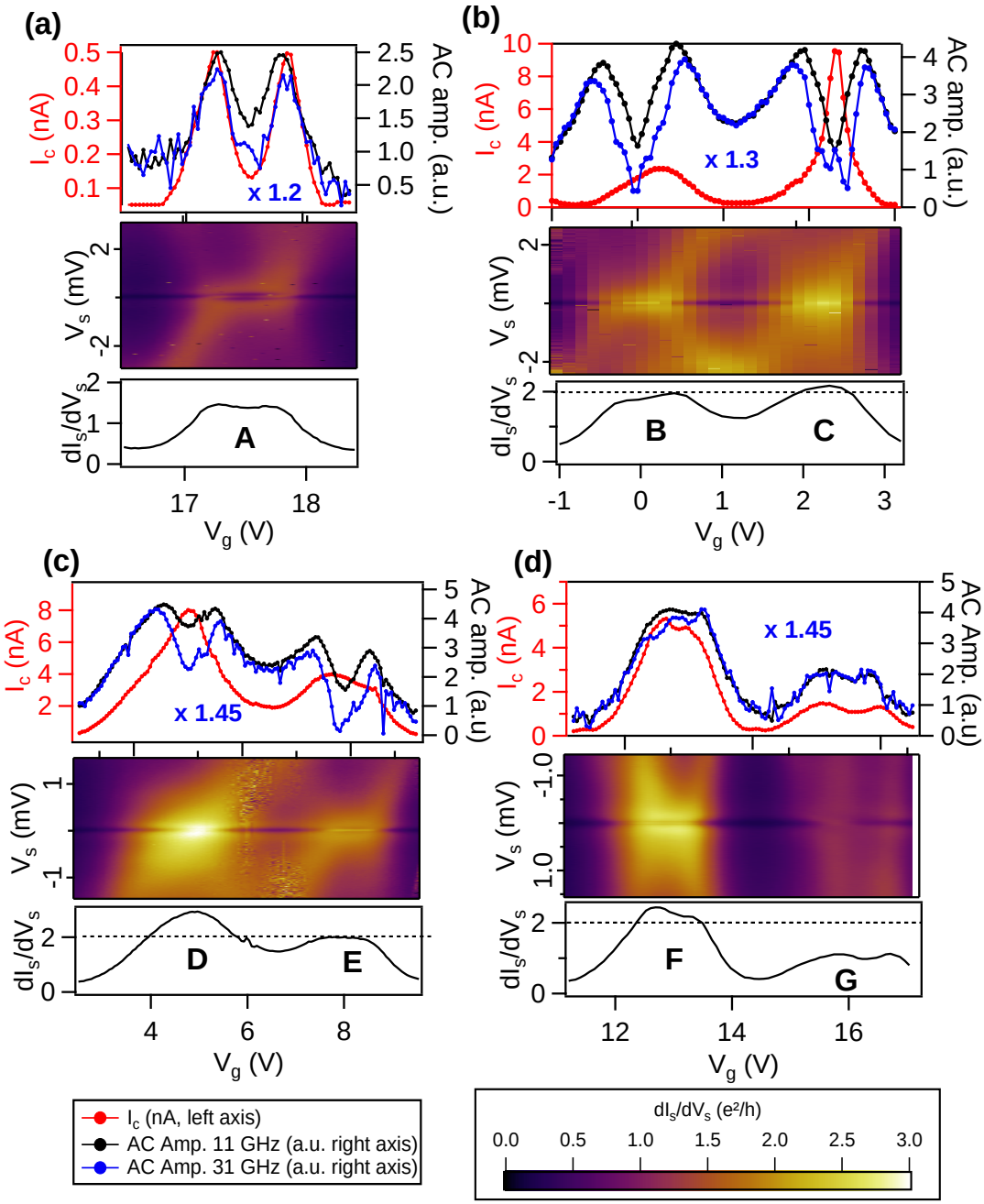


FIGURE 8.9 – Comparison between the AC Josephson amplitudes at 11 and 31 GHz and the critical current in seven oddly occupied diamonds. The AC amplitudes (11 GHz in black, 31 GHz in blue) are represented in arbitrary unit (right axes), which is the same for the four plots. However, the 31 GHz one is renormalized by a factor written in blue, to compensate the fact that the ratio between $I_{PAT}$ and the amplitude of the Josephson emission depends on the frequency. The critical current is plotted in red, the scale is indicated on the left axes. Below each plot is represented the differential conductance in presence of a 1 T magnetic field as a function of the bias and gate voltages. Horizontal cuts of these color plots are given for $V_s \approx -0.3$ mV, outside from the superconducting dip.

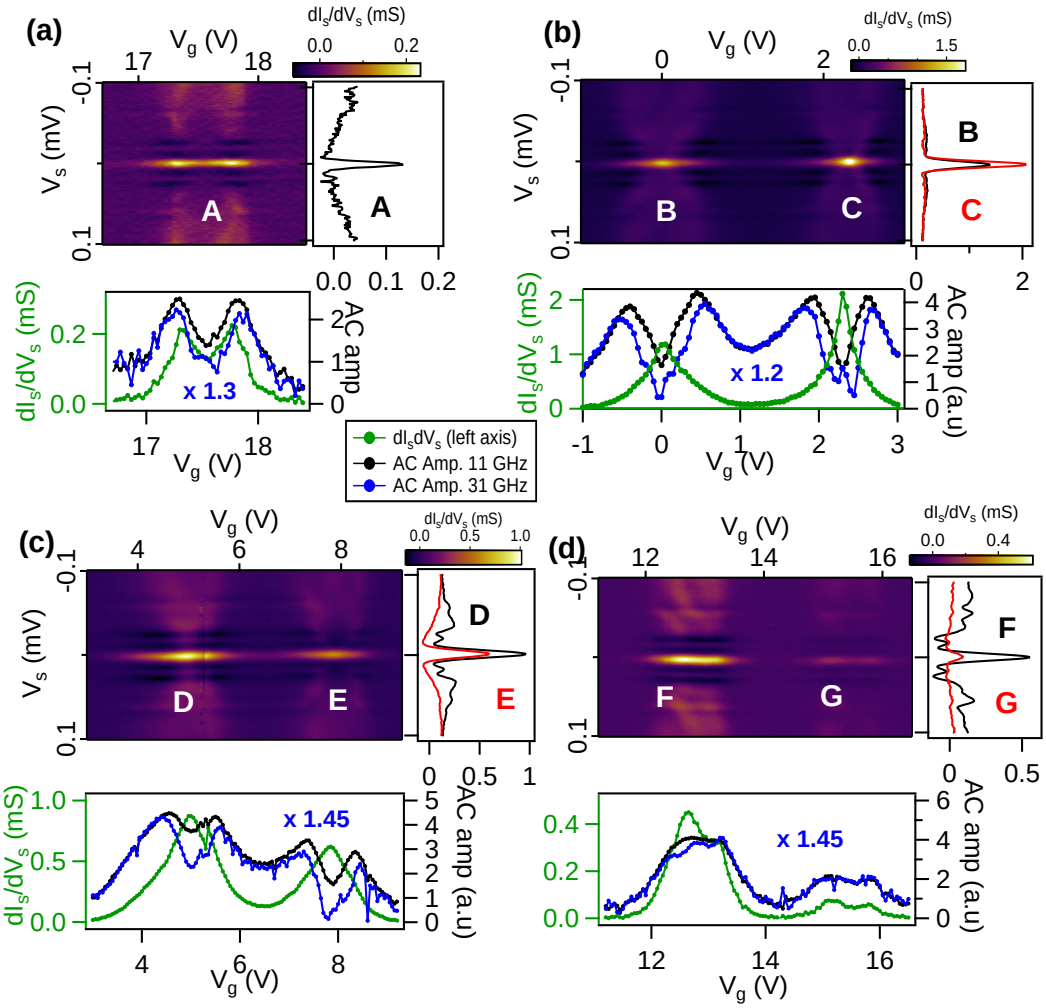


FIGURE 8.10 – Comparison between the AC Josephson amplitudes at 11 and 31 GHz and the conductance in the superconducting state ($B = 0$) for seven oddly occupied diamonds. The differential conductance in the superconducting state is plotted as a function of the gate and bias voltages. On the right of each colorplot are represented vertical cuts at the center of each diamond (indicated by the letters). The AC amplitudes (11 GHz in black, 31 GHz in blue) are represented in arbitrary units. The 31 GHz one is renormalized by a factor written in blue, to compensate the fact that the calibration depends on the frequency. The zero bias conductance is plotted in green (left axis).

N=2, suggesting the presence of a second transmission channel. The differential conductance in the superconducting state of diamond D exhibits MAR structures, suggesting that these channels are not as well transmitted as in diamonds B, C and E. This "bad" transmission is accompanied by a collapse of the Josephson emission that is not as strong as in B, C and E diamonds.

The diamonds E and F present a different behavior : the emission at both frequencies approximatively coincide all over the three diamonds, even in the oddly occupied ones, following the evolution of the critical current. Once again, the normal state is difficult to interpret, since the conductance is not qualitatively different from the one in B-F (maximum close to $2e^2/h$, large structure centered around zero). Note however that the conductance at N=2 filling is quite low, suggesting that there is no second energy level participating to transport. The conductance in the superconducting state provide more informations : especially in diamond F, strong MAR structures are visible, indicating a non perfectly transmitted channel.

If we try to summarize, we could say that the collapse of the AC Josephson effect in the oddly occupied diamonds is correlated with both very high supercurrent and no MAR structure in the conductance in the superconducting state.

#### 8.2.3.2 A measurement problem ?

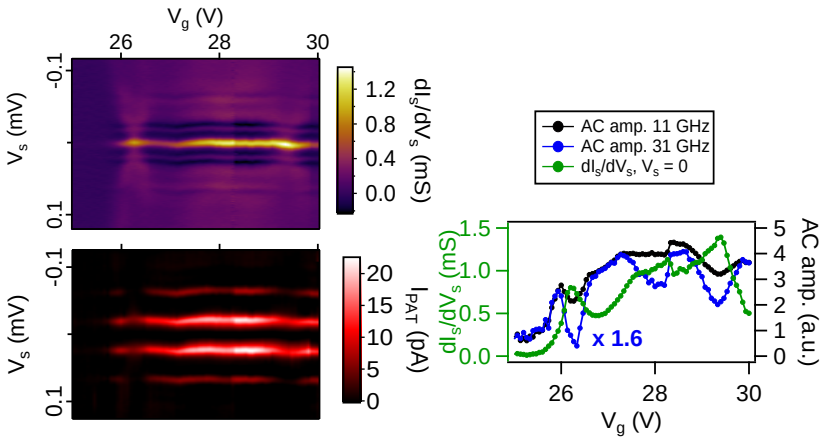


FIGURE 8.11 – Comparison of the differential conductance in the superconducting state and the AC Josephson emission in the case of a "Fabry-Pérot" region of the nanotube. On the right is represented the zero-bias conductance superimposed with the AC Josephson amplitude at 11 and 31 GHz (the square root of the height of the peaks at each frequency, in arbitrary units). The 31 GHz one has been multipled by 1.6 in order to take into account that the calibration is not the same for both frequencies.

The effect observed is correlated to a relatively low resistance of the nanotube, which could modify the electromagnetic environment seen by the detector. Could the suppression of AC Josephson emission be due to a modification of the measurement due to the high current

flowing in the nanotube and its high conductance in this region ? There are three reasons which contradict this hypothesis :

- In the zone F, where this effect is not observed, the conductance is of the same order as in zone E, where a collapse of the AC emission is observed.
- We have also measured the AC Josephson emission in a Fabry-Pérot region, with less Coulomb features (fig. 8.11), in particular between $V_g = 27$ V and 29 V. There, the conductance is quite high (comparable do the Kondo diamonds), but the AC emission is not clearly affected. It is affected around $V_g = 26$ V and 30 V but, there, some Coulomb interactions may remain.
- We have measured the AC emission of the additional Josephson tunnel junction in the presence of the highly conducting carbon nanotube. We checked that this measurement did not depend on the gate voltage in the range $[-1\,V, 3\,V]$, where the effect on the AC Josephson effect of the nanotube is the most striking.

#### 8.2.3.3 Frequency induced 0-$\pi$ transition ?

The AC Josephson emission in Kondo regions B and C qualitatively looks like what could be expected in a quantum dot in the Coulomb blockade regime, but in absence of the Kondo effect. At these frequencies, it seems that the nanotube Josephson junction behaves like a $\pi$-junction, instead of the 0-junction expected from the DC critical current measurement. The fact that this effect is more prominent at 31 GHz than at 11 GHz suggests that the frequency (or the corresponding applied bias) plays a major role.

In this experiment, the Kondo effect has the same reasons for being weaken as in the high frequency emission noise experiment : because of the high frequency dynamics and the out-of-equilibrium situation. Here, unfortunately, we cannot extract any Kondo temperature (see the analyze of the normal state differential conductance). We can however say that, except for the diamond A where there may be a $\pi$-junction, the diamonds B to G exhibit 0-junctions in the superconducting state, and thus $k_B T_K > \Delta = 0.15$ meV : the Kondo temperature corresponds to a frequency larger than 3.5 GHz. The fact that a temperature of 1K does not affect the zero-bias structure in the normal state added to the large width of this structure suggests that the Kondo temperature is probably larger than 30 GHz, but this is not certain. In this experimental setup where 11 and 31 GHz are measured, the measurement frequency is probably lower than $T_K$.

In the high frequency noise measurement in the normal state, we have seen that the decoherence of Kondo effect at these frequencies is dominated by out-of-equilibrium effects, and not by the dynamics of the Kondo effect. Here, thanks to the Josephson nature of the emission, the bias corresponding to 31 GHz corresponds only to 64 $\mu$eV (instead of 128 $\mu$eV in the noise experiment). Therefore, a weakening of the Kondo resonance itself is less likely.

#### 8.2.3.4 Landau-Zener transition ?

In our experiment, the vanishing of the AC emission is correlated to high critical currents, where the Kondo effect opens an almost perfectly transmitted channel. Then the Andreev bound states are very close in energy at $\varphi = \pi$, which can lead to Landau-Zener transitions and to a $4\pi$-periodic CPR [230]. This explanation seems to be consistent with our data : as it can be seen on fig. 8.10, when the AC Josephson emission collapses, the superconducting conductance exhibits only a large central peak, without any MAR feature, signature of a transmission close to 1 (diamonds A, B and E). On the contrary, the effect is less clear when MAR structures are visible in the conductance, suggesting imperfect transmissions (diamonds D, F and G).

The problem is that Landau-Zener transitions would manifest as a change in frequency from $f_J = 2eV_s/h$ to $f_J/2$. In other words, there should be less signal at $V_s = h\nu_{0,1}/2e$ and the appearance of peaks at 22 and 62 GHz (similarly to experiments from ref. [24, 224]). But this is not the case in this experiment, which makes this interpretation not very convincing.

#### 8.2.3.5 Effect of the barrier asymmetry ?

According to Hiltscher *et al.* [236], "The AC Josephson current between QD and left reservoir only probes the proximity effect induced by the right superconducting reservoir, held at a different potential". If the barriers are asymmetric, the Kondo effect develops mainly on the well coupled electrode, and the other one does not contribute to the Kondo correlations. Then, if we measure the AC Josephson emission in the well coupled contact, we probe the AC emission in the poorly coupled one, where there is no Kondo effect (or a weaker one). That could explain why the AC emission is weaker than expected in some diamonds. This point is however very speculative and deserves deeper theoretical investigations.

## 8.3 Conclusion

- When a Josephson junction is biased by a voltage $V$, the superconducting phase across it changes at the speed $d\varphi/dt = 2eV/\hbar$, leading to the high frequency emission of a radiation whose harmonics depend on the ones of the current-phase relation : this is the AC Josephson effect.
- The AC Josephson effect is not only a probe of the dc current-phase relation : because of its dynamical nature, it can give access to information different from the dc Josephson effect (in particular related to Landau-Zener transitions).
- If the Josephson junction is irradiated (or excited at high frequency), the AC Josephson effect manifests itself as steps in the dc V(I) characteristic (or peaks in the I(V) characteristic), called Shapiro steps, which are easier to measure than direct AC Josephson emission.

- Using the same experimental setup as for the high frequency noise measurements, we can measure directly the AC Josephson emission from any Josephson junction, here a carbon nanotube contacted with superconducting electrodes.
- We measure this Josephson emission at 11 and 31 GHz for various gate voltage regions, focusing on the Kondo regime. We show that, in some diamonds, the AC Josephson emission follows the dc critical current. In some others, where the supercurrent is strongly enhanced by the Kondo effect in dc, the AC emission collapses, the effect being stronger at 31 than at 11 GHz.
- Comparing these results with the normal and superconducting conductances, we try to understand this effect and propose several interpretations.

# General conclusion

To conclude this manuscript, I recall the main results of my PhD and give some perspectives.

**DC Josephson effect** Investigating the DC Josephson effect of a carbon nanotube quantum dot, we provide the first measurement of the current-phase relation all over the 0-$\pi$ transition induced by a level crossing, putting forward a phase-driven 0-$\pi$ transition (here controlled by the competition between the Kondo effect and the superconductivity). In perfect agreement with Quantum Monte Carlo calculations, the obtained CPR have unusual shapes, with a strong anharmonicity which is characteristic of junctions whose ground state, 0 or $\pi$, depends on the superconducting phase. This behavior is observed for all the 0-$\pi$ transitions in the single-level regime of the sample, and is shown to be described by a universal phase diagram. We measure as well the current-phase relation in the unexplored regime where two-levels of the quantum dot participate in the transport of Cooper pairs. Then, we show experimentally that the 0-$\pi$ transitions which do not involve a change of magnetic state are completely different from the first order transition since they exhibit a complete vanishing of the critical current and remain harmonic.

The supercurrent in a carbon nanotube in the two-level regime had never been measured before. Therefore, it would be interesting to reproduce this experiment in different regimes, in particular in the presence of two-level Kondo effects (SU(4) for example), in order to explore a phase diagram predicted to be very rich[11, 12]. Moreover, because of the presence of a non-negligible spin-orbit and thanks to the presence of a second channel, the magnetic field dependence of the current-phase relation is very promising [152, 155]. Indeed, in addition to a singlet-triplet transition, this system is predicted to exhibit $\varphi_0$-junction. It may be possible to develop a detection setup working in a magnetic field of a few tens or hundreds Gauss, which would be sufficient to observe the effect, thanks to an enhancement of the effect in quantum dots, due to Coulomb interactions [14].

**High frequency emission noise** Following the work of Julien Basset, we have measured the high frequency emission noise of a carbon nanotube quantum dot, focusing on the Kondo regime. These new measurements allowed us to access a larger range of parameters, in order to understand the decoherence of the Kondo effect induced by a bias voltage. In particular,

we have measured the noise at frequencies around the Kondo temperature in two limits : a situation in which the left and right reservoirs are symmetrically coupled to the nanotube and another where one of the reservoirs is ten times better coupled than the other. From these measurements, we show that when the reservoirs are symmetrically coupled, the Kondo singlet equally spreads on both of them and is thus more strongly weaken by a bias voltage than when the reservoirs are asymmetrically coupled. Indeed, in the latter case the Kondo resonance involves mainly the best coupled contact and is not affected by the bias voltage. Moreover, we show that the high frequency emission noise is more sensitive to out-of-equilibrium decoherence of the Kondo effect than the DC density of state.

The breaking of the spatial symmetry of the system raises also the question of the asymmetry of the noise : should the noise be the same in both electrodes ? What is measured in the experiment ? This point, very specific to finite frequency, has never been addressed experimentally until now. To answer, one should design a setup where the noise of an asymmetric system (a quantum dot seems to be a good candidate) could be measured simultaneously in both electrodes. Maybe a high frequency electronic setup such as the one used in ref. [237] would be more appropriate for that than our on-chip measurement, which has spatial constraints.

With our setup, the greatest challenge would be to access as well the absorption noise. Indeed, absorption processes are also possible at equilibrium and would give insights into the dynamics of the system, without providing any energy to the system. Moreover, while emission noise can also be measured with high frequency electronics, it is not the case of absorption noise. Unfortunately, it is for the moment very difficult to detect such a signal. We need to improve the coupling between the source and detector, to increase the number of photons absorbed by the system which are coming from the detector.

Another challenge is to adapt this noise measurement setup in order to make it work in presence of a magnetic field. This requires to make a non-superconducting resonator (which should be possible since we don't need a very good quality factor, between 50 and 100 is ok), and above all a SIS detector with a larger critical field (this may be possible using niobium). Our attempt to do it, with a gold resonator, failed because gold damaged the oxide layer of the junctions. Maybe copper would be more appropriate.

**AC Josephson effect** For the third and last experiment, we used the same setup, the only difference being that the nanotube is contacted with superconducting electrodes. Contacted with normal electrodes and under biasing, the nanotube emits a polychromatic radiation associated to the current fluctuations. In the case of superconducting contacts, this emission is (approximately) monochromatic and strongly related to the current-phase relation, itself depending on the correlations in the system (here the Kondo effect). We show that, strikingly, when the DC Josephson current is enhanced by the Kondo effect, the AC Josephson effect is not necessary enhanced as well, especially for the highest frequency. It seems that we are facing a frequency-induced 0-$\pi$ transition, but the reason for that is not clear, mainly because

of a difficult determination of the Kondo temperatures in the normal state. We can however invoke some potential explanation : the dynamics of the Kondo effect, the fact that it is out of-equilibrium, the dynamics of the junction itself (Landau-Zener transitions) or effects of the contact asymmetry.

To go further in the interpretation, we would need more theoretical insights into what is expected for AC Josephson effect in a quantum dot in the Kondo regime. Moreover, it may be useful to measure new samples, where the normal state conductance measurement would provide more information on the parameters of the system.

# List of publications

- In preparation : R. Delagrange, J. Basset, R. Weil, H. Bouchiat and R. Deblock. "Out-of-equilibrium Kondo effect probed by quantum noise".
- In preparation : R. Delagrange, R. Weil, A. Kasumov, H. Bouchiat and R. Deblock. "AC Josephson effect in a carbon nanotube QD in the Kondo regime".
- [9] R. Delagrange, R. Weil, A. Kasumov, M. Ferrier, H. Bouchiat and R. Deblock. "0-$\pi$ quantum transition in a carbon nanotube Josephson junction : universal phase dependence and orbital degeneracy". Phys. Rev. B **93**, 195437 (2016).
- [97] M. Ferrier, T. Arakawa1, T. Hata, R. Fujiwara, R. Delagrange, R. Weil, R. Deblock, R. Sakano, A. Oguri and K. Kobayashi. "Universality of non-equilibrium fluctuations in strongly correlated quantum liquids". Nat. Phys. **12**, 3556 (2015), pp. 230-235.
- [8] R. Delagrange, D. J. Luitz, R. Weil, A. Kasumov, V. Meden, H. Bouchiat and R. Deblock. "Manipulating the magnetic state of a carbon nanotube Josephson junction using the superconducting phase". Phys. Rev. B **91**, 241401 (2015).
- [6] J. Basset, R. Delagrange, R. Weil, A. Kasumov, H. Bouchiat and R. Deblock. "Joint measurement of current-phase relations and transport properties of hybrid junctions using a three junctions superconducting quantum interference device". J. Appl. Phys. **116**, 024311 (2014).

# Bibliography


[1] I. Garate. "Charge-Kondo effect in mesoscopic superconductors coupled to normal metals". *Phys. Rev. B* **84**, 085121 (2011).

[2] B. Béri and N. R. Cooper. "Topological Kondo effect with Majorana fermions". *Phys. Rev. Lett.* **109**, 156803 (2012).

[3] S. De Franceschi, L. P. Kouwenhoven, C Schonenberger, and W. Wernsdorfer. "Hybrid superconductorâquantum dot devices". *Nat. Nanotechnol.* **5**, 10 (2010), pp. 703–711.

[4] J. A. van Dam, Y. V. Nazarov, E. P. A. M. Bakkers, S. De Franceschi, and L. P. Kouwenhoven. "Supercurrent reversal in quantum dots". *Nature* **442**, 7103 (2006), pp. 667–670.

[5] M. L. Della Rocca, M. Chauvin, B. Huard, H Pothier, D. Esteve, and C. Urbina. "Measurement of the current-phase relation of superconducting atomic contacts". *Phys. Rev. Lett.* **99**, 127005 (2007).

[6] J. Basset, R Delagrange, R Weil, A. Kasumov, H. Bouchiat, and R. Deblock. "Joint measurement of current-phase relations and transport properties of hybrid junctions using a three junctions superconducting quantum interference device". *J. Appl. Phys.* **116**, 024311 (2014).

[7] J.-P. Cleuziou, N. V. N'Guyen, S. Florens, and W. Wernsdorfer. "Interplay of the Kondo Effect and Strong Spin-Orbit Coupling in Multihole Ultraclean Carbon Nanotubes". *Phys. Rev. Lett.* **111**, 136803 (2013).

[8] R Delagrange, D. Luitz, R Weil, A. Kasumov, V Meden, H. Bouchiat, and R. Deblock. "Manipulating the magnetic state of a carbon nanotube Josephson junction using the superconducting phase". *Phys. Rev. B* **91**, 241401 (2015).

[9] R Delagrange, R Weil, A. Kasumov, M. Ferrier, H Bouchiat, and R. Deblock. "0-$\pi$ quantum transition in a carbon nanotube Josephson junction: universal phase dependence and orbital degeneracy". *Phys. Rev. B* **93**, 195437 (2016).

[10] D. Luitz and F. F. Assaad. "Weak-coupling continuous-time quantum Monte Carlo study of the single impurity and periodic Anderson models with s-wave superconducting baths". *Phys. Rev. B* **81**, 024509 (2010).

[11] A. Zazunov, R. Egger, T. Jonckheere, and T Martin. “Anomalous josephson current through a spin-orbit coupled quantum dot”. *Phys. Rev. Lett.* **103**, 147004 (2009).

[12] M. Lee, T. Jonckheere, and T Martin. “Josephson effect through a multilevel quantum dot near a singlet-triplet transition”. *Phys. Rev. B* **81**, 155114 (2010).

[13] T. S. Jespersen, K Grove-Rasmussen, J. Paaske, K. Muraki, T Fujisawa, J Nygård, and K. Flensberg. “Gate-dependent spin-orbit coupling in multielectron carbon nanotubes”. *Nat. Phys.* **7**, 1880 (2011), pp. 348–353.

[14] A. Brunetti, A. Zazunov, A. Kundu, and R. Egger. “Anomalous Josephson current, incipient time-reversal symmetry breaking, and Majorana bound states in interacting multilevel dots”. *Phys. Rev. B* **88**, 144515 (2013).

[15] Y. Blanter and M Buttiker. “Shot Noise in Mesoscopic Conductors”. Vol. 336. Physics Report, 2000, pp. 1–166.

[16] L. Saminadayar, D. Glattli, Y. Jin, and B. Etienne. “Observation of the e/3 Fractionally Charged Laughlin Quasiparticle”. *Phys. Rev. Lett.* **79**, 13 (1997), pp. 2526–2529.

[17] R. de Picciotto, M. Reznikov, M Heiblum, V Umansky, G Bunin, and D Mahalu. “Direct observation of a fractional charge”. *Phys. E Low-dimensional Syst. Nanostructures* **3**, 1-3 (1998), pp. 47–51.

[18] X Jehl, M. Sanquer, R Calemczuk, and D Mailly. “Detection of doubled shot noise in short normal-metal/superconductor junctions”. *Nature* **405**, 6782 (2000), pp. 50–3.

[19] J. Basset, H. Bouchiat, and R. Deblock. “High-frequency quantum admittance and noise measurement with an on-chip resonant circuit”. *Phys. Rev. B* **85**, 085435 (2012).

[20] R. Zamoum, M. Lavagna, and A. Crépieux. “Nonsymmetrized noise in a quantum dot: Interpretation in terms of energy transfer and coherent superposition of scattering paths”. *Phys. Rev. B* **93**, 235449 (2016).

[21] E. A. Rothstein, O Entin-Wohlman, and A Aharony. “Noise spectra of a biased quantum dot”. *Phys. Rev. B* **79**, 075307 (2009).

[22] C. P. Moca, P. Simon, C. H. Chung, and G. Zaránd. “Nonequilibrium frequency-dependent noise through a quantum dot: A real-time functional renormalization group approach”. *Phys. Rev. B* **83**, 201303 (2011).

[23] J. Basset, A. Kasumov, C. P. Moca, G. Zaránd, P. Simon, H. Bouchiat, and R. Deblock. “Measurement of Quantum Noise in a Carbon Nanotube Quantum Dot in the Kondo Regime”. *Phys. Rev. Lett.* **108**, 046802 (2012).

[24] P.-M. Billangeon, F. Pierre, H. Bouchiat, and R. Deblock. “Ac Josephson effect and resonant cooper pair tunneling emission of a single cooper pair transistor”. *Phys. Rev. Lett.* **98**, 216802 (2007).

[25] J. W. G. Van Den Berg and J. de Nobel. “Les propriétés à basses températures des alliages des métaux "normaux" avec des solutés de transition”. fr. *J. Phys. le Radium* **23** (1962), pp. 665–671.

[26] J. Kondo. “Resistance Minimum in Dilute Magnetic Alloys”. *Prog. Theor. Phys.* **32**, 1 (1964), pp. 37–49.

[27] A. Georges. “The beauty of impurities: Two revivals of Friedel’s virtual bound-state concept”. *Comptes Rendus Phys.* **17** (2016), pp. 430–446.

[28] K. G. Wilson. “The renormalization group: critical phenomena and the Kondo Problem”. *Rev. Mod. Phys.* **47** (1975), pp. 773–839.

[29] S. De Franceschi and W. G. van der Wiel. “Kondo Effect in Quantum Dots”. *Handb. nanophysics nanoparticles quantum dots.* 2012. Chap. 37, pp. 20–37.

[30] L. P. Kouwenhoven and L. Glazman. “Revival of the Kondo effect”. *Phys. World* **14**, 1 (2001), pp. 33–38.

[31] P. Jarillo-Herrero, J. Kong, H. S. J. van der Zant, C. Dekker, L. P. Kouwenhoven, and S. De Franceschi. “Orbital Kondo effect in carbon nanotubes.” *Nature* **434**, 7032 (2005), pp. 484–8.

[32] P. W. Anderson. “A poor man’s derivation of scaling laws for the Kondo problem”. *J. Phys. C Solid State Phys.* **3**, 12 (1970), pp. 2436–2441.

[33] T. Costi, A. C. Hewson, and V Zlatic. “Transport coefficients of the Anderson model via the numerical renormalization group”. *J. Phys. Condens. Matter* **6** (1994), p. 2519.

[34] P. W. Anderson. “Localized Magnetic States in Metals”. *Phys. Rev.* **124**, 1 (1961), pp. 41–53.

[35] J. Schrieffer and P. A. Wolff. “Relation between the Anderson and Kondo Hamiltonians”. *Phys. Rev.* **149**, 2 (1966), pp. 491–492.

[36] E. Dupont. *Effet Kondo et Poor man’s scaling.* 2004. URL: http://www.physique.usherb.ca/{~}edupont/.

[37] A. C. Hewson. *The Kondo Problem to Heavy Fermions.* Cambridge, UK: Cambridge University Press, 1993.

[38] M. Pustilnik and L. Glazman. “Kondo effect in quantum dots”. *J. Phys. Condens. Matter* **16**, 16 (2004), R513–R537.

[39] P. Nozières. “A "fermi-liquid" description of the Kondo problem at low temperatures”. *J. Low Temp. Phys.* **17**, 1-2 (1974), pp. 31–42.

[40] L. Glazman and M. E. Raikh. *Resonant Kondo transparency of a barrier with quasilocal impurity states.* 1988.

[41] Z. Iftikhar, S. Jezouin, A Anthore, U. Gennser, F. D. Parmentier, A. Cavanna, and F. Pierre. “Two-channel Kondo effect and renormalization flow with macroscopic quantum charge states”. *Nature* **526**, 7572 (2015), pp. 233–236.

[42] D. Goldhaber-Gordon, H. Shtrikman, D. Mahalu, D. Abusch-Magder, U. Meirav, and M. a. Kastner. “Kondo effect in a single-electron transistor”. *Nature* **391**, 6663 (1998), pp. 156–159.

[43] S. M. Cronenwett, T. H. Oosterkamp, and L. P. Kouwenhoven. "A Tunable Kondo Effect in Quantum Dots". *Science* **281**, 5376 (1998), pp. 540–544.

[44] J Nygård, D. H. Cobden, and P. E. Lindelof. "Kondo physics in carbon nanotubes." en. *Nature* **408**, 6810 (2000), pp. 342–346.

[45] T. S. Jespersen, M. Aagesen, C. Sørensen, P. E. Lindelof, and J Nygård. "Kondo physics in tunable semiconductor nanowire quantum dots". *Phys. Rev. B* **74**, 233304 (2006).

[46] J. Paaske, A. Rosch, J Kroha, and P. Wölfle. "Nonequilibrium transport through a Kondo dot: Decoherence effects". *Phys. Rev. B* **70**, 155301 (2004).

[47] S. Hershfield, J. H. Davies, and J. W. Wilkins. "Probing the Kondo resonance by resonant tunneling through an Anderson impurity". *Phys. Rev. Lett.* **67**, 26 (1991), pp. 3720–3723.

[48] P. Nordlander, M. Pustilnik, Y. Meir, N. S. Wingreen, and D. C. Langreth. "How Long Does It Take for the Kondo Effect to Develop?" *Phys. Rev. Lett.* **83**, 4 (1999), pp. 808–811.

[49] A. Kogan, S. Amasha, and M. A. Kastner. "Photon-induced Kondo satellites in a single-electron transistor." *Science* **304**, 5675 (2004), pp. 1293–5.

[50] A. Kaminski, Y. V. Nazarov, and L. Glazman. "Suppression of the Kondo Effect in a Quantum Dot by External Irradiation". *Phys. Rev. Lett.* **83**, 2 (1999), pp. 384–387.

[51] M. R. Buitelaar, T Nussbaumer, and C Schonenberger. "Quantum dot in the Kondo regime coupled to superconductors." *Phys. Rev. Lett.* **89**, 256801 (2002).

[52] V. Barzykin and L. P. Gor'Kov. "Competition between phonon superconductivity and Kondo screening in mixed valence and heavy fermion compounds". *Phys. Rev. B* **71**, 214521 (2005).

[53] E. Müller-Hartmann and J. Zittartz. "Kondo effect in superconductors". *Phys. Rev. Lett.* **26**, 8 (1971), pp. 428–432.

[54] L. Levy. *Magnétisme et supraconductivité*. EDP Science, 1997.

[55] L Dumoulin, E Guyon, and P Nedellec. "Etude de films d'alliages kondo par résistivité et proximité supraconductrice ( températures critiques )". *Le J. Phys.* **34** (1973), p. 1021.

[56] K. J. Franke, G Schulze, and J. I. Pascual. "Competition of superconducting phenomena and Kondo screening at the nanoscale." *Science* **332**, 6032 (2011), pp. 940–944.

[57] J.-C. Charlier, X. Blase, and S. Roche. "Electronic and transport properties of nanotubes". *Rev. Mod. Phys.* **79**, 2 (2007), pp. 677–732.

[58] A. H. Castro Neto, F. Guinea, N. M. R. Peres, K. S. Novoselov, and A. K. Geim. "The electronic properties of graphene". *Rev. Mod. Phys.* **81**, 1 (2009), pp. 109–162.

[59] E. A. Laird, F Kuemmeth, G. Steele, K Grove-Rasmussen, J Nygård, K. Flensberg, and L. P. Kouwenhoven. "Quantum transport in carbon nanotubes". *Rev. Mod. Phys.* **87** (2014), pp. 703–764.

[60] Y. Kasumov, A Shailos, I. I. Khodos, V. T. Volkov, V. I. Levashov, V. N. Matveev, S Gueron, M Kobylko, M Kociak, H. Bouchiat, V Agache, A. S. Rollier, L Buchaillot, A. M. Bonnot, and A. Kasumov. "CVD growth of carbon nanotubes at very low pressure of acetylene". *Appl. Phys. A* **88**, 4 (2007), pp. 687–691.

[61] B Huard, A Anthore, N. O. Birge, H Pothier, and D. Esteve. "Effect of Magnetic Impurities on Energy Exchange between Electrons". *Phys. Rev. Lett.* **95**, 36802 (2005).

[62] E Akkermans and G. Montambaux. *Mesoscopic Physics of Electrons and Photons.*

[63] R. A. Webb, S. Washburn, C. P. Umbach, and R. B. Laibowitz. "Observation of h/e Aharonov-Bohm Oscillations in Normal-Metal Rings". *Phys. Rev. Lett.* **54** (1985).

[64] S. Datta. *Electronic Transport in Mesoscopic Systems.* 2007.

[65] G. Montambaux and E Akkermans. *Mesoscopic Physics of Electrons and Photons.*

[66] N. D. Mermin and N. W. Ashcroft. *Solid State Physics.*

[67] L. P. Kouwenhoven, C. M. Marcus, P. L. McEuen, S. Tarucha, R. M. Westervelt, and N. S. Wingreen. "Electron transport in quantum dots". *Mesoscopic Electron Transp.* Ed. by G. S. L.L. Sohn L.P. Kouwenhoven. Kluwer, 1997. Chap. 1, pp. 1–110.

[68] Y.-J. Doh, J. A. van Dam, A. L. Roest, E. P. A. M. Bakkers, L. P. Kouwenhoven, and S. De Franceschi. "Tunable Supercurrent Through Semiconductor Nanowires". *Science* **309**, 5732 (2005), pp. 272–275.

[69] L. C. Venema, J. W. G. Wildoer, J. W. Janssen, S. J. Tans, H. L. J. T. Tuinstra, L. P. Kouwenhoven, and C. Dekker. "Imaging Electron Wave Functions of Quantized Energy Levels in Carbon Nanotubes". *Science* **283**, 1999 (1999), pp. 52–55.

[70] H. J. Joyce, C. J. Docherty, Q. Gao, H. H. Tan, C. Jagadish, J. Lloyd-Hughes, L. M. Herz, and M. B. Johnston. "Electronic properties of GaAs, InAs and InP nanowires studied by terahertz spectroscopy." *Nanotechnology* **24**, 214006 (2013).

[71] M. S. Purewal, B. H. Hong, A. Ravi, B. Chandra, J. Hone, and P. Kim. "Scaling of Resistance and Electron Mean Free Path of Single-Walled Carbon Nanotubes". *Phys. Rev. Lett.* **98**, 18 (2007), p. 186808.

[72] F Kuemmeth, S Ilani, D. C. Ralph, and P. L. McEuen. "Coupling of spin and orbital motion of electrons in carbon nanotubes." *Nature* **452**, 7186 (2008), pp. 448–52.

[73] H. A. Nilsson, P. Caroff, C. Thelander, M. Larsson, J. B. Wagner, L.-E. Wernersson, L. Samuelson, and H. Q. Xu. "Giant, Level-Dependent g Factors in InSb Nanowire Quantum Dots". *Nano Lett.* **9**, 9 (2009), pp. 3151–3156.

[74] S. Nadj-Perge, V. S. Pribiag, J. W. G. Van Den Berg, K. Zuo, S. R. Plissard, E. P. A. M. Bakkers, S. M. Frolov, and L. P. Kouwenhoven. "Spectroscopy of spin-orbit quantum bits in indium antimonide nanowires". *Phys. Rev. Lett.* **108**, 166801 (2012).

[75] M. Marganska, P. Chudzinski, and M. Grifoni. "The two classes of low-energy spectra in finite carbon nanotubes". *Phys. Rev. B* **92**, 075433 (2015).

[76] J. Cao, Q. Wang, M. Rolandi, and H. Dai. "Aharonov-Bohm interference and beating in single-walled Carbon-nanotube interferometers". *Phys. Rev. Lett.* **93**, 216803 (2004).

[77] D. R. Schmid, S. Smirnov, M. Marganska, A. Dirnaichner, P. L. Stiller, M. Grifoni, K. H. Andreas, and C. Strunk. "Broken SU(4) symmetry in a Kondo-correlated carbon nanotube". *Phys. Rev. B* **91**, 155435 (2015).

[78] A Makarovski, J Liu, and G Finkelstein. "Evolution of Transport Regimes in Carbon Nanotube Quantum Dots". *Phys. Rev. Lett.* **99**, 66801 (2007).

[79] J. Svensson and E. E. B. Campbell. "Schottky barriers in carbon nanotube-metal contacts". *J. Appl. Phys.* **110**, 111101 (2011).

[80] A. Javey, J. Guo, Q. Wang, M. Lundstrom, and H. Dai. "Ballistic carbon nanotube field-effect transistors". *Nature* **424**, 6949 (2003), pp. 654–657.

[81] J.-P. Cleuziou. "Propriétés de transport électronique de nanotubes de carbone : des nanotubes hybrides au nano-SQUID". PhD thesis. Université de Toulouse, 2007.

[82] W. Liang, M. W. Bockrath, D. Bozovic, J. H. Hafner, M. Tinkham, and H. Park. "Fabry - Perot interference in a nanotube electron waveguide". *Nature* **411**, 6838 (2001), pp. 665–669.

[83] H. I. Jørgensen, K Grove-Rasmussen, T Novotný, K. Flensberg, and P. E. Lindelof. "Electron Transport in Single-Wall Carbon Nanotube Weak Links in the Fabry-Perot Regime". *Phys. Rev. Lett.* **96**, 207003 (2006).

[84] J.-P. Cleuziou, W. Wernsdorfer, S. Andergassen, S. Florens, V. Bouchiat, T Ondarçuhu, and M. Monthioux. "Gate-Tuned High Frequency Response of Carbon Nanotube Josephson Junctions". *Phys. Rev. Lett.* **99**, 117001 (2007).

[85] S. De Franceschi, S. Sasaki, J. M. Elzerman, W. G. van der Wiel, S. Tarucha, and L. P. Kouwenhoven. "Electron Cotunneling in a Semiconductor Quantum Dot". *Phys. Rev. Lett.* **86**, 5 (2001), pp. 878–881.

[86] C. W. J. Beenakker. "Theory of Coulomb-blockade oscillations in the conductance of a quantum dot". *Phys. Rev. B* **44**, 4 (1991), pp. 1646–1656.

[87] D. V. Averin and Y. V. Nazarov. "Virtual electron diffusion during quantum tunneling of the electric charge". *Phys. Rev. Lett.* **65**, 19 (1990), pp. 2446–2449.

[88] D. Goldhaber-Gordon, J Göres, M. A. Kastner, H. Shtrikman, D. Mahalu, and U. Meirav. "From the Kondo Regime to the Mixed-Valence Regime in a Single-Electron Transistor". *Phys. Rev. Lett.* **81**, 23 (1998), pp. 5225–5228.

[89] B. Babić, T. Kontos, and C Schonenberger. "Kondo effect in carbon nanotubes at half halfing". *Phys. Rev. B* **70**, 235419 (2004).

[90] W. G. Van Der Wiel. "Electron transport through double quantum dots". *Rev. Mod. Phys.* **75** (2003), pp. 1–22.

[91] R. Maurand, T. Meng, E. Bonet, S. Florens, L. Marty, and W. Wernsdorfer. "First-Order 0-$\pi$ Quantum Phase Transition in the Kondo Regime of a Superconducting Carbon-Nanotube Quantum Dot". *Phys. Rev. X* **2**, 011009 (2012).

[92] A. V. Kretinin, H. Shtrikman, D. Goldhaber-Gordon, M. Hanl, A. Weichselbaum, J. von Delft, T. Costi, and D. Mahalu. "Spin-1/2 Kondo effect in an InAs nanowire quantum dot: Unitary limit, conductance scaling, and Zeeman splitting". *Phys. Rev. B* **84**, 245316 (2011).

[93] S. De Franceschi, R Hanson, W. G. van der Wiel, J. M. Elzerman, J. J. Wijpkema, T Fujisawa, S. Tarucha, and L. P. Kouwenhoven. "Out-of-equilibrium Kondo effect in a mesoscopic device." *Phys. Rev. Lett.* **89**, 156801 (2002).

[94] A Eichler, R. Deblock, M Weiss, C Karrasch, V Meden, C Schonenberger, and H. Bouchiat. "Tuning the Josephson current in carbon nanotubes with the Kondo effect". *Phys. Rev. B* **79**, 161407 (2009).

[95] Y. Meir, N. S. Wingreen, and P. A. Lee. "Low-Temperature Transport Through a Quantum Dot: The Anderson Model Out of Equilibrium". *Phys. Rev. Lett.* **70**, 17 (1993), pp. 2601–2604.

[96] C. H. L. Quay, J. Cumings, S. J. Gamble, R. de Picciotto, H. Kataura, and D. Goldhaber-Gordon. "Magnetic field dependence of the spin- 1 2 and spin-1 Kondo effects in a quantum dot". *Phys. Rev. B* **76**, 245311 (2007).

[97] M. Ferrier, T. Arakawa, T. Hata, R. Fujiwara, R Delagrange, R Weil, R. Deblock, R. Sakano, A. Oguri, and K. Kobayashi. "Universality of non-equilibrium fluctuations in strongly correlated quantum liquids". *Nat. Phys.* **12**, 3556 (2015), pp. 230–235.

[98] J. V. Holm, H. I. Jørgensen, K Grove-Rasmussen, J. Paaske, K. Flensberg, and P. E. Lindelof. "Gate-dependent tunneling-induced level shifts observed in carbon nanotube quantum dots". *Phys. Rev. B* **77**, 161406 (2008).

[99] J. S. Lim, M.-S. Choi, M. Y. Choi, R. López, and R. Aguado. "Kondo effects in carbon nanotubes: From SU(4) to SU(2) symmetry". *Phys. Rev. B* **74**, 205119 (2006).

[100] A Makarovski, A Zhukov, J Liu, and G Finkelstein. "SU(2) and SU(4) Kondo effects in carbon nanotube quantum dots". *Phys. Rev. B* **75**, 241407 (2007).

[101] M. Filippone, C. P. Moca, G. Zaránd, and C. Mora. "The Kondo Temperature of SU(4) Symmetric Quantum Dots". *Phys. Rev. B* **90**, 121406 (2014).

[102] T. Delattre, C Feuillet-Palma, L. G. Herrmann, P. Morfin, J.-M. Berroir, G. Fève, B. Plaçais, D. C. Glattli, M.-S. Choi, C. Mora, and T. Kontos. "Noisy Kondo impurities". *Nat. Phys.* **5**, 1186 (2009), pp. 208–212.

[103] M. R. Galpin, F. W. Jayatilaka, D. E. Logan, and F. B. Anders. "Interplay between Kondo physics and spin-orbit coupling in carbon nanotube quantum dots". *Phys. Rev. B* **81**, 75437 (2010).

[104] M.-S. Choi, R. López, and R. Aguado. "SU(4) Kondo Effect in Carbon Nanotubes". *Phys. Rev. Lett.* **95**, 067204 (2005).

[105] A. Kogan, G. Granger, M. Kastner, D. Goldhaber-Gordon, and H. Shtrikman. "Singlet-triplet transition in a single-electron transistor at zero magnetic field". *Phys. Rev. B* **67**, 113309 (2003).

[106] N. Roch, S. Florens, V. Bouchiat, W. Wernsdorfer, and F. Balestro. "Quantum phase transition in a single-molecule quantum dot." *Nature* **453**, 7195 (2008), pp. 633–7.

[107] W. G. van der Wiel, S. De Franceschi, J. M. Elzerman, S. Tarucha, L. P. Kouwenhoven, J Motohisa, F Nakajima, and T Fukui. "Two-Stage Kondo Effect in a Quantum Dot at a High Magnetic Field". *Phys. Rev. Lett.* **88**, 126803 (2002).

[108] P Petit, C Feuillet-Palma, M. L. Della Rocca, and P Lafarge. "Universality of the two-stage Kondo effect in carbon nanotube quantum dots". *Phys. Rev. B* **89**, 115432 (2014).

[109] Y. Bomze, I Borzenets, H Mebrahtu, A Makarovski, H. U. Baranger, and G Finkelstein. "Two-stage Kondo effect and Kondo-box level spectroscopy in a carbon nanotube". *Phys. Rev. B* **82**, 161411 (2010).

[110] J. Paaske, A. Rosch, P. Wölfle, N. Mason, C. M. Marcus, and J Nygård. "Non-equilibrium singletâtriplet Kondo effect in carbon nanotubes". *Nat. Phys.* **2**, 340 (2006), pp. 460–464.

[111] M. Tinkham. *Introduction to superconductivity.* McGraw-Hill, Inc., 1996.

[112] B. Josephson. "Possible new effects in superconductive tunnelling". *Phys. Lett.* **1**, 7 (1962), pp. 251–253.

[113] R. P. Feynman, R. B. Leighton, and M. Sands. *The Feynman Lectures on Physics, Vol. III : Quantum Mechanics.* 1965.

[114] Y. V. Nazarov and Y. Blanter. *Quantum Transport- Introduction to Nanoscience.* Cambridge University Press, 2009.

[115] B. J. Van Wees and H. Takayanagi. "The superconduting proximity effect in semiconductor-superconductor systems : ballistic transport, low dimensionality and sample specific properties". *Mesoscopic Electron Transp.* 1997, pp. 469–501.

[116] J.-D. Pillet, C. H. L. Quay, P. Morfin, C. Bena, A. L. Yeyati, and P. Joyez. "Andreev bound states in supercurrent-carrying carbon nanotubes revealed". *Nat. Phys.* **6**, 12 (2010), pp. 965–969.

[117] J. Basset. "High frequency quantum noise of mesoscopic systems and current-phase relation of hybrid junctions." PhD thesis. Universite Paris-Sud, 2011.

[118] A. A. Golubov, M. Y. Kupriyanov, and E. Il'ichev. *The current-phase relation in Josephson junctions.* 2004.

[119] T. Meng. "Andreev bound states in Josephson quantum dot devices". PhD thesis. Institut Néel, Grenoble, 2009.

[120] C. W. J. Beenakker and H. van Houten. "The Superconducting Quantum Point Contact". *Nanostructures Mesoscopic Syst.* (1992), pp. 1–8.

[121] A. F. Morpurgo, T. M. Klapwijk, and B. J. Van Wees. "Hot electron tunable supercurrent". *Appl. Phys. Lett.* **72**, 8 (1998), pp. 966–968.

[122] J. J. A. Baselmans, B. J. Van Wees, and T. M. Klapwijk. "Reversing the direction of the supercurrent in a controllable Josephson junction". *Nature* **397** (1999), pp. 1998–2000.

[123] K. Flensberg, J. B. Hansen, and M. Octavio. "Subharmonic energy-gap structure in superconducting weak links". *Phys. Rev. B* **38**, 13 (1988), pp. 8707–8711.

[124] T. M. Klapwijk, G. Blonder, and M. Tinkham. "Explanation of subharmonic energy gap structure in superconducting contacts". *Physica* **109-110** (1982), pp. 1657–1664.

[125] J. C. Cuevas, A. Martín-Rodero, and A. L. Yeyati. "Shot Noise and Coherent Multiple Charge Transfer in Superconducting Quantum Point Contacts". *Phys. Rev. Lett.* **82**, 20 (1999), pp. 4086–4089.

[126] A. Kasumov, M. Kociak, M. Ferrier, R. Deblock, S. Guéron, B. Reulet, I. Khodos, O. Stéphan, and H. Bouchiat. "Quantum transport through carbon nanotubes: Proximity-induced and intrinsic superconductivity". *Phys. Rev. B* **68**, 214521 (2003).

[127] Y. Yang, G. Fedorov, S. E. Shafranjuk, T. M. Klapwijk, B. K. Cooper, R. M. Lewis, C. J. Lobb, and P. Barbara. "Electronic transport and possible superconductivity at van Hove singularities in carbon nanotubes". *Nano Lett.* **15**, 12 (2015), pp. 7859–7866.

[128] A. Kasumov, R. Deblock, M Kociak, B. Reulet, H. Bouchiat, I. I. Khodos, Y. Gorbatov, V. T. Volkov, C Journet, and M Burghard. "Supercurrents through single-walled carbon nanotubes". *Science* **284**, 5419 (1999), pp. 1508–1511.

[129] C. W. J. Beenakker and H. van Houten. "Resonant Josephson current through a quantum dot". *Single-Electron Tunneling and Mesoscopic Devices* (1992), p. 175.

[130] P. Dubos, H Courtois, B Pannetier, F. K. Wilhelm, A. D. Zaikin, and G Schon. "Josephson critical current in a long mesoscopic S-N-S junction". *Phys. Rev. B* **63**, 064502 (2001).

[131] B. I. Spivak and S. A. Kivelson. "Negative local superfluid densities: The difference between dirty superconductors and dirty Bose liquids". *Phys. Rev. B* **43**, 4 (1991), pp. 3740–3743.

[132] I. O. Kulik. "The Josephson tunnel effect in superconductors with paramagnetic impurities". *Sov Phys JETP* **23**, 3 (1966).

[133] T Novotný, A. Rossini, and K. Flensberg. "Josephson current through a molecular transistor in a dissipative environment". *Phys. Rev. B* **72**, 224502 (2005).

[134] L. Glazman and A Matveev. "Resonant Josephson current through Kondo impurities in a tunnel Barrier". *JETP* **49** (1989), p. 659.

[135] J.-P. Cleuziou, W. Wernsdorfer, V. Bouchiat, T Ondarçuhu, and M. Monthioux. "Carbon nanotube superconducting quantum interference device". *Nat. Nanotechnol.* **1**, 1 (2006), p. 53.

[136] H. I. Jørgensen, T Novotný, K Grove-Rasmussen, K. Flensberg, and P. E. Lindelof. "Critical current 0-$\pi$ transition in designed Josephson Quantum Dot junctions." *Nano Lett.* **7**, 8 (2007), pp. 2441–5.

[137] A. V. Rozhkov, D. P. Arovas, and F Guinea. "Josephson coupling through a quantum dot". *Phys. Rev. B* **64**, 233301 (2001).

[138] A. Clerk and V. Ambegaokar. "Loss of $\pi$-junction behavior in an interacting impurity Josephson junction". *Phys. Rev. B* **61**, 13 (2000), pp. 9109–9112.

[139] J.-D. Pillet, P. Joyez, R. Žitko, and M. F. Goffman. "Tunneling spectroscopy of a single quantum dot coupled to a superconductor: From Kondo ridge to Andreev bound states". *Phys. Rev. B* **88**, 045101 (2013).

[140] B.-K. Kim, Y.-H. Ahn, J.-J. Kim, M.-S. Choi, M.-H. Bae, K. Kang, J. Lim, R. López, and N. Kim. "Transport Measurement of Andreev Bound States in a Kondo-Correlated Quantum Dot". *Phys. Rev. Lett.* **110**, 076803 (2013).

[141] W Chang, V. E. Manucharyan, T. S. Jespersen, J Nygård, and C. M. Marcus. "Tunneling Spectroscopy of Quasiparticle Bound States in a Spinful Josephson Junction". *Phys. Rev. Lett.* **110**, 217005 (2013).

[142] E. J. H. Lee, X. Jiang, M. Houzet, R. Aguado, C. M. Lieber, and S. De Franceschi. "Spin-resolved Andreev levels and parity crossings in hybrid superconductor-semiconductor nanostructures." *Nat. Nanotechnol.* **9**, 1 (2014), pp. 79–84.

[143] C Karrasch, A. Oguri, and V Meden. "Josephson current through a single Anderson impurity coupled to BCS leads". *Phys. Rev. B* **77**, 024517 (2008).

[144] J Bauer, A. Oguri, and A. C. Hewson. "Spectral properties of locally correlated electrons in a Bardeen-Cooper-Schrieffer superconductor". *J. Phys. Condens. Matter* **19**, 48 (2007), p. 486211.

[145] J. Schindele. "Observation of Cooper Pair Splitting and Andreev Bound States in Carbon Nanotubes". PhD thesis. Universität Basel, 2014.

[146] E. Vecino, A. Martín-Rodero, and A. Levy Yeyati. "Josephson current through a correlated quantum level: Andreev states and $\pi$ junction behavior". *Phys. Rev. B* **68**, 035105 (2003).

[147] M.-S. Choi, M. Lee, K. Kang, and W. Belzig. "Kondo effect and Josephson current through a quantum dot between two superconductors". *Phys. Rev. B* **70**, 020502 (2004).

[148] F. Siano and R. Egger. "Josephson current through a nanoscale magnetic quantum dot". *Phys. Rev. Lett.* **93**, 047002 (2004).

[149] Y. Shimizu, H. Horii, Y. Takane, and Y. Isawa. "Multilevel Effect on the Josephson Current through a Quantum Dot". *J. Phys. Soc. Japan* **67**, 5 (1998), pp. 1525–1528.

[150] D. B. Szombati, S. Nadj-Perge, D. Car, S. R. Plissard, E. P. A. M. Bakkers, and L. P. Kouwenhoven. "Josephson $\phi$0-junction in nanowire quantum dots". *Nat. Phys.* 3742 (2016).

[151] Y Yu, Q. F. Liang, and J. M. Dong. "0-pi Transition in a Superconductor/Carbon Nanotube Quantum Dot/Superconductor Junction". *J. Phys. Soc. Japan* **79**, 094712 (2010).

[152] S. Droste, S. Andergassen, and J. Splettstoesser. "Josephson current through interacting double quantum dots with spin-orbit coupling". *J. Phys. Condens. Matter* **24**, 415301 (2012).

[153] C Karrasch, S. Andergassen, and V Meden. "Supercurrent through a multilevel quantum dot close to singlet-triplet degeneracy". *Phys. Rev. B* **84**, 134512 (2011).

[154] A. Zazunov, A. Levy Yeyati, and R. Egger. "Josephson effect for SU(4) carbon-nanotube quantum dots". *Phys. Rev. B* **81**, 1 (2010), p. 12502.

[155] J. S. Lim, R. Lopez, M.-S. Choi, and R. Aguado. "Josephson current in carbon nanotubes with spin-orbit interaction". *Phys. Rev. Lett.* **107**, 196801 (2011).

[156] G. Blatter, V. B. Geshkenbein, and L. B. Ioffe. "Design aspects of superconducting-phase quantum bits". *Phys. Rev. B* **63**, 174511 (2001).

[157] A. V. Ustinov and V. K. Kaplunenko. "Rapid single-flux quantum logic using $\pi$-shitters". *J. Appl. Phys.* **94**, 8 (2003), pp. 5405–5407.

[158] A. I. Buzdin. "Proximity effects in superconductor-ferromagnet heterostructures". *Rev. Mod. Phys.* **77** (2005), pp. 935–976.

[159] M. Eschrig. "Spin-polarized supercurrents for spintronics". *Phys. Today* **64**, 1 (2011), p. 43.

[160] T. Yokoyama, M. Eto, and Y. V. Nazarov. "Anomalous Josephson effect induced by spin-orbit interaction and Zeeman effect in semiconductor nanowires". *Phys. Rev. B* **89**, 195407 (2014).

[161] T. Kontos, M Aprili, J. Lesueur, F. Genêt, B. Stephanidis, and R. Boursier. "Josephson Junction through a Thin Ferromagnetic Layer: Negative Coupling". *Phys. Rev. Lett.* **89**, 13 (2002), p. 137007.

[162] S. M. Frolov, D. J. Van Harlingen, V. A. Oboznov, V. Bolginov, and V. V. Ryazanov. "Measurement of the current-phase relation of superconductor/ferromagnet/superconductor $\pi$ Josephson junctions". *Phys. Rev. B* **70**, 144505 (2004).

[163] W Guichard, M Aprili, O Bourgeois, T. Kontos, J. Lesueur, and P Gandit. "Phase sensitive experiments in ferromagnetic-based Josephson junctions". *Phys. Rev. Lett.* **90**, 167001 (2003).

[164] V. V. Ryazanov, V. A. Oboznov, A. Y. Rusanov, A. V. Veretennikov, A. A. Golubov, and J Aarts. "Coupling of Two Superconductors through a Ferromagnet: Evidence for a $\pi$ Junction". *Phys. Rev. Lett.* **86**, 11 (2001), pp. 2427–2430.

[165] A. V. Samokhvalov and A. I. Buzdin. "First order 0-$\pi$ phase transitions in superconductor/ferromagnet/superconductor trilayers". *Phys. Rev. B* **92**, 054511 (2015).

[166] H. Sellier, C. Baraduc, F. Lefloch, and R. Calemczuk. "Half-Integer Shapiro Steps at the 0-$\pi$ Crossover of a Ferromagnetic Josephson Junction". *Phys. Rev. Lett.* **92**, 257005 (2004).

[167] J. J. A. Baselmans, T. Heikkilä, B. J. Van Wees, and T. M. Klapwijk. "Direct Observation of the Transition from the Conventional Superconducting State to the $\pi$ State in a Controllable Josephson Junction". *Phys. Rev. Lett.* **89**, 207002 (2002).

[168] M. Vojta. "Impurity Quantum Phase Transitions". *Philos. Mag.* **86**, 13-14 (2006).

[169] I. G. Rau, S. Amasha, Y. Oreg, and D. Goldhaber-Gordon. "Quantum Phase Transitions in Quantum Dots". *Underst. Quantum Phase Transitions.* Ed. by C. Press. 2010, p. 33.

[170] H Mebrahtu, I. V. Borzenets, D. E. Liu, H. Zheng, Y. V. Bomze, A. I. Smirnov, H. U. Baranger, and G Finkelstein. "Quantum phase transition in a resonant level coupled to interacting leads." *Nature* **488**, 7409 (2012), pp. 61–4.

[171] M. H. Devoret, J. M. Martinis, and J. Clarke. "Measurements of Macroscopic Quantum Tunneling out of the Zero-Voltage State of a Current-Biased Josephson Junction". *Phys. Rev. Lett.* **55**, 18 (1985), pp. 1908–1911.

[172] I. Petkovic. "Phase dynamics of the ferromagnetic Josephson junctions." PhD thesis. Université Paris-Sud, 2009.

[173] Y. Ota, N. Nakai, H. Nakamura, M. Machida, D. Inotani, Y. Ohashi, T. Koyama, and H. Matsumoto. "Ambegaokar-Baratoff relations for Josephson critical current in heterojunctions with multigap superconductors". *Phys. Rev. B* **81**, 214511 (2010).

[174] D. Luitz, F. F. Assaad, T Novotný, C Karrasch, and V Meden. "Understanding the Josephson Current through a Kondo-Correlated Quantum Dot". *Phys. Rev. Lett.* **108**, 227001 (2012).

[175] M. Žonda, V. Pokorný, V. Janiš, and T Novotný. "Perturbation theory for an Anderson quantum dot asymmetrically attached to two superconducting leads". *Phys. Rev. B* **93**, 024523 (2016).

[176] A. L. Yeyati, J. C. Cuevas, A. López-Dávalos, and A. Martín-Rodero. "Resonant tunneling through a small quantum dot coupled to superconducting leads". *Phys. Rev. B* **55**, 10 (1997), R6137–R6140.

[177] B. M. Andersen, K. Flensberg, V. Koerting, and J. Paaske. "Nonequilibrium Transport through a Spinful Quantum Dot with Superconducting Leads". *Phys. Rev. Lett.* **107**, 256802 (2011).

[178] A Eichler, M Weiss, S Oberholzer, C Schonenberger, A. L. Yeyati, J. C. Cuevas, and A. M. Rodero. "Even-Odd Effect in Andreev Transport through a Carbon Nanotube Quantum Dot". *Phys. Rev. Lett.* **99**, 126602 (2007).

[179] T Sand-Jespersen, J. Paaske, B. M. Andersen, K Grove-Rasmussen, H. I. Jørgensen, M Aagesen, C. B. S\orensen, P. E. Lindelof, K. Flensberg, and J Nygård. "Kondo-Enhanced Andreev Tunneling in InAs Nanowire Quantum Dots". *Phys. Rev. Lett.* **99**, 126603 (2007).

[180] R. S. Deacon, Y. Tanaka, A Oiwa, R. Sakano, K Yoshida, K Shibata, K Hirakawa, and S. Tarucha. "Tunneling Spectroscopy of Andreev Energy Levels in a Quantum Dot Coupled to a Superconductor". *Phys. Rev. Lett.* **104**, 076805 (2010).

[181] A. Clerk, M. H. Devoret, S. M. Girvin, F. Marquardt, and R. J. Schoelkopf. "Introduction to quantum noise, measurement, and amplification". *Rev. Mod. Phys.* Vol. 82. 2. 2010, pp. 1155–1208.

[182] U. Gavish, Y. Levinson, and Y. Imry. "Detection of quantum noise". *Phys. Rev. B* **62**, 16 (2000), R10 637.

[183] H. Nyquist. "Thermal agitation of electric charge in conductors". *Phys. Rev.* **32**, 1 (1928), pp. 110–113.

[184] M. H. Devoret. "Quantum fluctuations in electrical circuits". Ed. by Elsevier. 1997. Chap. 10, pp. 351–386.

[185] R Kubo. "The fluctuation-dissipation theorem". *Rep. Prog. Phys.* **29** (1966), p. 255.

[186] J. Basset, H. Bouchiat, and R. Deblock. "Emission and Absorption Quantum Noise Measurement with an On-Chip Resonant Circuit". *Phys. Rev. Lett.* **105**, 166801 (2010).

[187] M. B. Weissman. "1/f Noise and Other Slow, Nonexponential Kinetics in Condensed Matter". *Rev. Mod. Phys.* **60**, 2 (1988), pp. 537–571.

[188] M Buttiker. "Scattering theory of current and intensity noise correlations in conductors and wave guides". *Phys. Rev. B* **46**, 19 (1992), pp. 12485–12507.

[189] R. Cron, M. F. Goffman, D. Esteve, and C. Urbina. "Multiple-Charge-Quanta Shot Noise in Superconducting Atomic Contacts". *Phys. Rev. Lett.* **86**, 18 (2001), pp. 4104–4107.

[190] T. Arakawa, Y. Nishihara, M. Maeda, S. Norimoto, and K. Kobayashi. "Cryogenic amplifier for shot noise measurement at 20 mK". *Appl. Phys. Lett.* **103**, 17 (2013), pp. 0–4.

[191] R. J. Schoelkopf, P. J. Burke, A. A. Kozhevnikov, D. E. Prober, and M. J. Rooks. "Frequency Dependence of Shot Noise in a Diffusive Mesoscopic Conductor". *Phys. Rev. Lett.* **78**, 17 (1997), pp. 3370–3373.

[192] M. Dolev, Y. Gross, Y. C. Chung, M. Heiblum, V. Umansky, and D. Mahalu. "Dependence of the tunneling quasiparticle charge determined via shot noise measurements on the tunneling barrier and energetics". *Phys. Rev. B* **81**, 161303 (2010).

[193] E. Sela, Y. Oreg, F. von Oppen, and J. Koch. "Fractional Shot Noise in the Kondo Regime". *Phys. Rev. Lett.* **97**, 086601 (2006).

[194] C. Mora, X. Leyronas, and N. Regnault. "Current Noise through a Kondo Quantum Dot in a SU(N) Fermi Liquid State". *Phys. Rev. Lett.* **100**, 036604 (2008).

[195] R. Sakano, T. Fujii, and A. Oguri. "Kondo crossover in shot noise of a single quantum dot with orbital degeneracy". *Phys. Rev. B* **83**, 075440 (2011).

[196] E. Zakka-Bajjani, J. Ségala, F. Portier, P. Roche, D. C. Glattli, A. Cavanna, and Y. Jin. "Experimental Test of the High-Frequency Quantum Shot Noise Theory in a Quantum Point Contact". *Phys. Rev. Lett.* **99**, 236803 (2007).

[197] C. Altimiras, O. Parlavecchio, P. Joyez, D. Vion, P. Roche, D. Esteve, and F. Portier. "Dynamical Coulomb Blockade of Shot Noise". *Phys. Rev. Lett.* **112**, 236803 (2014).

[198] W. W. Xue, Z Ji, F Pan, J Stettenheim, M. P. Blencowe, and a. J. Rimberg. "Measurement of quantum noise in a single-electron transistor near the quantum limit". *Nat. Phys.* **5**, 1339 (2009), pp. 660–664.

[199] R. Aguado and L. P. Kouwenhoven. "Double Quantum Dots as Detectors of High-Frequency Quantum Noise in Mesoscopic Conductors". *Phys. Rev. Lett.* **84**, 9 (2000), pp. 1986–1989.

[200] S. Gustavsson, M. Studer, R. Leturcq, T. Ihn, K. Ensslin, D. C. Driscoll, and A. C. Gossard. "Frequency-selective single-photon detection using a double quantum dot". *Phys. Rev. Lett.* **99**, 206804 (2007).

[201] N. Ubbelohde, C. Fricke, C. Flindt, F. Hohls, and R. J. Haug. "Measurement of finite-frequency current statistics in a single-electron transistor". *Nat. Commun.* **3** (2012), p. 612.

[202] E Onac, F. Balestro, L. H. W. Van Beveren, U. Hartmann, Y. V. Nazarov, and L. P. Kouwenhoven. "Using a quantum dot as a high-frequency shot noise detector". *Phys. Rev. Lett.* **96**, 176601 (2006).

[203] G.-L. Ingold and Y. V. Nazarov. "Charge Tunneling Rates in Ultrasmall Junctions". *Single Charg. tunneling* **294** (2005), pp. 21–107.

[204] R. Deblock, E Onac, L. Gurevich, and L. P. Kouwenhoven. "Detection of quantum noise from an electrically driven two-level system." *Science* **301**, 5630 (2003), pp. 203–6.

[205] A. H. Dayem and R. J. Martin. "Quantum interaction of microwave radiation with tunneling between superconductors". *Phys. Rev. Lett.* **8**, 10 (1962), pp. 2–5.

[206] P. K. Tien and J. P. Gordon. "Multiphoton Process Observed in the Interaction of Microwave Fields with the Tunneling between Superconductor Films". *Phys. Rev.* **129**, 2 (1963), pp. 647–651.

[207] I. Giaever. "Detection of the ac Josehson effect". *Phys. Rev. Lett.* **14**, 22 (1965), pp. 904–906.

[208] J. R. Tucker and M. J. Feldman. "Quantum detection at millimeter wavelengths". *Rev. Mod. Phys.* **57**, 4 (1985), pp. 1055–1113.

[209] D. Twerenbold. "Cryogenic particle detectors". *Reports Prog. Phys.* **59** (1996).

[210] E Onac, F. Balestro, B Trauzettel, C. F. J. Lodewijk, and L. P. Kouwenhoven. "Shot-Noise Detection in a Carbon Nanotube Quantum Dot". *Phys. Rev. Lett.* **96**, 026803 (2006).

[211] P.-M. Billangeon, F. Pierre, H. Bouchiat, and R. Deblock. "Emission and Absorption Asymmetry in the Quantum Noise of a Josephson Junction". *Phys. Rev. Lett.* **96**, 136804 (2006).

[212] M Göppl, A Fragner, M Baur, R Bianchetti, S Filipp, J. M. Fink, and P. J. Leek. "Coplanar waveguide resonators for circuit quantum electrodynamics". *J. Appl. Phys.* **104**, 113904 (2008).

[213] V. Ambegaokar and A. Baratoff. "Tunneling Between Superconductors". *Phys. Rev. Lett.* **10**, 11 (1963), pp. 486–489.

[214] A. Worsham, N. Ugras, D Winkler, D. Prober, N. Erickson, and P. Goldsmith. "Quantum tunneling currents in a superconducting junction." *Phys. Rev. Lett.* **67**, 21 (1991), pp. 3034–3037.

[215] A. J. Dahm, A Denenstein, D. N. Langenberg, W. H. Parker, D Rogovin, and D. J. Scalapino. "Linewidth of the Radiation Emitted by a Josephson Junction". *Phys. Rev. Lett.* **22**, 26 (1969), pp. 1416–1420.

[216] P.-M. Billangeon. "Détection de bruit quantique mésoscopique à très haute-fréquence". PhD thesis. Université Paris-Sud, 2008.

[217] J. Hammer and W. Belzig. "Quantum noise in ac-driven resonant-tunneling double-barrier structures: Photon-assisted tunneling versus electron antibunching". *Phys. Rev. B* **84**, 085419 (2011).

[218] S. Y. Müller, M. Pletyukhov, D. Schuricht, and S. Andergassen. "Magnetic field effects on the finite-frequency noise and ac conductance of a Kondo quantum dot out of equilibrium". *Phys. Rev. B* **87**, 245115 (2013).

[219] R. Leturcq, L. Schmid, K. Ensslin, Y. Meir, D. C. Driscoll, and A. C. Gossard. "Probing the Kondo density of states in a three-terminal quantum ring". *Phys. Rev. Lett.* **95**, 126603 (2005).

[220] S. Kehrein. "Scaling and Decoherence in the Nonequilibrium Kondo Model". *Phys. Rev. Lett.* **95**, 056602 (2005).

[221] E. Lebanon and A. Schiller. "Measuring the out-of-equilibrium splitting of the Kondo resonance". *Phys. Rev. B* **65**, 035308 (2001).

[222] I. Yanson, V. Svistunov, and I. Dmitrenko. "Experimental Observation of the Tunnel Effect for Cooper Pairs with the Emission of Photons". *Sov. Phys. JETP* **21**, 1933 (1965), p. 650.

[223] L. Ozyuzer, A. E. Koshelev, C. Kurter, N. Gopalsami, Q. Li, M. Tachiki, K. Kadowaki, T. Yamamoto, H. Minami, H. Yamaguchi, T. Tachiki, K. E. Gray, W.-K. Kwok, and U. Welp. "Emission of Coherent THz Radiation from Superconductors". *Science* **318**, 5854 (2007), pp. 1291–1293.

[224] R. S. Deacon, J. Wiedenmann, E. Bocquillon, T. M. Klapwijk, P. Leubner, C. Brüne, S. Tarucha, K. Ishibashi, H. Buhmann, and L. W. Molenkamp. "Josephson radiation from gapless Andreev bound states in HgTe-based topological junctions". *arxiv* **1603**, 09611 (2016).

[225] A Barone and G Paterno. *Physics and Applications of the Josephson Effect*. Ed. by J. W. &. Sons. Wiley-interscience, 1982.

[226] J. C. Cuevas, J Heurich, A Martín-Rodero, A. Levy Yeyati, and G. Schön. "Subharmonic shapiro steps and assisted tunneling in superconducting point contacts." *Phys. Rev. Lett.* **88**, 157001 (2002).

[227] R. M. Lutchyn, J. D. Sau, and S. Das Sarma. "Majorana fermions and a topological phase transition in semiconductor-superconductor heterostructures". *Phys. Rev. Lett.* **105**, 077001 (2010).

[228] J. Wiedenmann, E. Bocquillon, R. S. Deacon, S. Hartinger, T. Herrmann, T. M. Klapwijk, L. Maier, C. Ames, C. Brüne, K. Ishibashi, S. Tarucha, H. Buhmann, L. W. Molenkamp, O. Herrmann, T. M. Klapwijk, L. Maier, C. Ames, C. Brüne, C. Gould, A. Oiwa, K. Ishibashi, S. Tarucha, H. Buhmann, and L. W. Molenkamp. "$4\pi$-periodic Josephson supercurrent in HgTe-based topological Josephson junctions". *Nat. Commun.* **10**, 10303 (2015).

[229] L. P. Rokhinson, X. Liu, and J. K. Furdyna. "The fractional a.c. Josephson effect in a semiconductor-superconductor nanowire as a signature of Majorana particles". *Nat. Phys.* **8**, 11 (2012), pp. 795–799.

[230] D. V. Averin and A. Bardas. "ac Josephson effect in a single quantum channel". *Phys. Rev. Lett.* **75**, 9 (1995), pp. 1831–1834.

[231] M. Chauvin, P. vom Stein, D. Esteve, C. Urbina, J. C. Cuevas, and A. L. Yeyati. "Crossover from Josephson to Multiple Andreev Reflection Currents in Atomic Contacts". *Phys. Rev. Lett.* **99**, 067008 (2007).

[232] A. Levy Yeyati, A. Martín-Rodero, and E. Vecino. "Nonequilibrium Dynamics of Andreev States in the Kondo Regime". *Phys. Rev. Lett.* **91**, 266802 (2003).

[233] E. Vecino, M. R. Buitelaar, A. Martin-Rodero, C Schonenberger, and A. L. Yeyati. "Conductance properties of nanotubes coupled to superconducting leads: Signatures of Andreev states dynamics". *Solid State Commun.* **131**, 9-10 SPEC. ISS. (2004), pp. 625–630.

[234] F. Chiodi, M. Ferrier, K. Tikhonov, P. Virtanen, T. Heikkilä, M. Feigelman, S. Guéron, and H. Bouchiat. "Probing the dynamics of Andreev states in a coherent Normal/Superconducting ring". *Sci. Rep.* **1** (2011), p. 251.

[235] B. Dassonneville, M. Ferrier, S. Guéron, and H. Bouchiat. "Dissipation and supercurrent fluctuations in a diffusive normal-metal-superconductor ring". *Phys. Rev. Lett.* **110**, 217001 (2013).

[236] B. Hiltscher, M. Governale, and J. König. "Ac Josephson transport through interacting quantum dots". *Phys. Rev. B* **86**, 235427 (2012).

[237] O. Parlavecchio, C. Altimiras, J.-R. Souquet, P. Simon, I. Safi, P. Joyez, D. Vion, P. Roche, D. Esteve, and F. Portier. "Fluctuation-Dissipation Relations of a Tunnel Junction Driven by a Quantum Circuit". *Phys. Rev. Lett.* **114**, 126801 (2015).

ÉCOLE DOCTORALE
Physique en Île-de-France (EDPIF)

**Titre** : Effet Josephson et émission haute fréquence dans un nanotube de carbone dans le régime Kondo.

**Mots clés** : *Effet Kondo, effet Josephson, bruit quantique, boîte quantique, nanotube de carbone*

**Résumé** : Cette thèse est consacrée au transport quantique à travers une impureté Kondo, formée dans une boîte quantique réalisée dans un nanotube de carbone. L'effet Kondo est ainsi sondé à travers deux situations : en compétition avec l'effet Josephson induit dans le nanotube par des contacts supraconducteurs et à travers son émission haute fréquence.

Dans une première série d'expériences, nous avons introduit un nanotube dans un SQUID, afin de mesurer la relation entre son supercourant et la différence de phase supraconductrice à ses bornes. Nous avons mesuré cette relation lorsque les corrélations Kondo et supraconductrices sont du même ordre de grandeur et montré que l'état du système, singulet ou doublet (correspondant respectivement à une jonction 0 ou π) peut alors être contrôlé par la phase supraconductrice. Nous avons également montré que, si un deuxième niveau d'énergie participe au transport des paires de Cooper, la transition 0-π n'est plus une transition du premier ordre comme c'est le cas quand un seul niveau est impliqué.

Dans la deuxième partie de la thèse, le nanotube de carbone est couplé, aux fréquences déterminées par un résonateur, à une jonction tunnel supraconductrice servant de détecteur on-chip de bruit haute fréquence. Ceci nous a permis de mesurer le bruit en émission de la boîte quantique dans le régime Kondo avec des couplages aux réservoirs plus ou moins symétriques. Nos mesures posent le problème de l'asymétrie spatiale du bruit mesuré et semblent montrer que, plus le couplage aux réservoirs est symétrique, plus la résonance Kondo est affaiblie dans une situation hors équilibre.

Enfin, ce dispositif a été utilisé afin de mesurer l'émission Josephson AC d'un nanotube avec des électrodes supraconductrices, afin de voir ce que devient la compétition entre l'effet Kondo et la supraconductivité à haute fréquence. Ces mesures révèlent une diminution de l'émission Josephson alors que l'on a un maximum de supercourant.

**Title :** Josephson effect and high frequency emission in a carbon nanotube in the Kondo regime.

**Keywords :** *Kondo effect, Josephson effect, quantum noise, quantum dot, carbon nanotube*

**Abstract :** This thesis is dedicated to quantum transport through a Kondo impurity, formed in a carbon nanotube quantum dot. We probe the Kondo effect in two situations: in competition with the Josephson effect induced in the nanotube by superconducting contacts and through its high frequency emission.

In a first experiment, we have introduced a nanotube in a SQUID in order to measure its supercurrent as a function of the superconducting phase across it. We have measured this quantity in the regime where the Kondo and superconducting correlations are of the same order of magnitude and shown that the ground state of the system, singlet or doublet (corresponding respectively to 0 and π junctions), is then controlled by the superconducting phase. We have also demonstrated that, if a second energy level participate in the transport of Cooper pairs, the 0-π transition is not anymore a first order one as it is the case when only one level is involved.

In the second part of the thesis, the carbon nanotube is coupled, at some frequencies determined by a resonator, to a tunnel superconducting junction which is used as an on-chip high-frequency noise detector. This enables the measurement of the emission noise of the quantum dot in the Kondo regime, with reservoirs coupled either symmetrically or not to the dot. Our measurements raise the problem of the spatial asymmetry of the measured noise and seem to show that, the more symmetric is the coupling of the reservoirs to the dot, the more the Kondo resonance is weaken in an out-of-equilibrium situation.

Finally, this setup has been used in order to measure the AC Josephson emission of a nanotube contacted with superconducting electrodes, in order to extend our investigation of the competition between the Kondo effect and superconductivity at high frequency. These measurements reveal a decrease of the Josephson emission observed together with a maximum of supercurrent.

**Université Paris-Saclay**
Espace Technologique / Immeuble Discovery
Route de l'Orme aux Merisiers RD 128 / 91190 Saint-Aubin, France